Ferroelectrets: from material science to energy harvesting and sensor applications

Zur Erlangung des akademischen Grades Doktor-Ingenieur (Dr.-Ing.)
Genehmigte Dissertation von Omar Ben Dali aus Sousse, Tunesien
Tag der Einreichung: 29. November 2022, Tag der Prüfung: 10. Mai 2023

1. Gutachten: Prof. Dr. mont. Mario Kupnik
2. Gutachten: Prof. Dr.-Ing. Heinz von Seggern
Darmstadt, Technische Universität Darmstadt

TECHNISCHE UNIVERSITÄT DARMSTADT

Department of Electrical Engineering and Information Technology

Measurement and Sensor Technology Group

Ferroelectrets: from material science to energy harvesting and sensor applications

Accepted doctoral thesis by Omar Ben Dali

Date of submission: 29. November 2022
Date of thesis defense: 10. Mai 2023

Darmstadt, Technische Universität Darmstadt

Bitte zitieren Sie dieses Dokument als:
URN: urn:nbn:de:tuda-tuprints-240744
URL: http://tuprints.ulb.tu-darmstadt.de/24074
Jahr der Veröffentlichung auf TUprints: 2023

Dieses Dokument wird bereitgestellt von tuprints,
E-Publishing-Service der TU Darmstadt
http://tuprints.ulb.tu-darmstadt.de
tuprints@ulb.tu-darmstadt.de

Erklärungen laut Promotionsordnung

§ 8 Abs. 1 lit. c PromO

Ich versichere hiermit, dass die elektronische Version meiner Dissertation mit der schriftlichen Version übereinstimmt.

§ 8 Abs. 1 lit. d PromO

Ich versichere hiermit, dass zu einem vorherigen Zeitpunkt noch keine Promotion versucht wurde. In diesem Fall sind nähere Angaben über Zeitpunkt, Hochschule, Dissertationsthema und Ergebnis dieses Versuchs mitzuteilen.

§ 9 Abs. 1 PromO

Ich versichere hiermit, dass die vorliegende Dissertation selbstständig und nur unter Verwendung der angegebenen Quellen verfasst wurde.

§ 9 Abs. 2 PromO

Die Arbeit hat bisher noch nicht zu Prüfungszwecken gedient.

Darmstadt, 29. November 2022

O. Ben Dali

Acknowledgment

Special thanks to my esteemed supervisor Prof. Kupnik for having made this PhD journey possible. I greatly appreciate his challenging expectations, which undoubtedly led me to a better version of myself.

Words cannot express my gratitude to Prof. von Seggern for the invaluable patience and feedback. Additionally, I would like to express my deepest gratitude to my colleague Dr. Zhukov, without whom this endeavor would not have been possible.

I am also grateful to Prof. Sessler who generously provided not only knowledge and expertise, but also laboratory equipment.

I would like to thank Prof. Zhang and her group at Tongji University for the continuous exchange of experiences and productive collaboration.

I would like to further extend my sincere thanks to my friends and colleagues at the measurement and sensor technology group. The regular discussions were oftentimes a source of inspiration. Special thanks go to my longtime fellow warriors Bastian Latsch and Romol Chadda for their unconditional support. I also appreciate all the support I received from my undergraduate students who helped turn my concepts into reality.

Grateful sentiments go to my spouse Fatma Souissi for her unwavering support and belief in me. You have brought me back from the brink of giving up every single time. Without you, I would not be the person I am today.

Lastly, I would be remiss in not mentioning my family, especially my brother Malek Ben Dali back home for standing by my side throughout my years of study despite the distance. Their belief in me has kept my spirits and motivation high during this process.

Abstract

The purpose of this thesis is to develop innovative ferroelectrets that can be used in energy harvesting devices as well as mechanical sensors. In the first stage, the focus lies on the application of ferroelectrets as energy harvesters. The inability to control the environment where the energy harvesters will be applied, requires the use of materials that can be utilized in harsh environment such as high temperature or humidity. Therefore, new ferroelectrets based on polymers with excellent electret properties, such as fluoroethylene propylene (FEP) are developed. Two types of ferroelectrets are considered, one optimized for the longitudinal piezoelectric effect and the other one optimized for the transverse piezoelectric effect in these materials. Hereby, new void structures are achieved through thermally fusing such films so that parallel tunnels (parallel-tunnel ferroelectrets) are formed between them, or by fusing round-section FEP tubes together so that they form a band or membrane.

The FEP tube configuration is optimized based on a finite element model showing that implementing a single tube structure ($25\,\mathrm{mm} \times 1.5\,\mathrm{mm}$) as the energy harvester exhibits the largest output power. By building the energy harvester and modeling it analytically, it is demonstrated that the generated power is highly dependent on parameters such as wall thickness, load resistance, and seismic mass. Utilizing a seismic mass of 80 g at resonance frequencies around 80 Hz and an input acceleration of $1\,g$ ($9.81\,\mathrm{m\,s^{-2}}$), output powers up to 300 µW are reached for a transducer with 25 µm thick walls.

The parallel-tunnel ferroelectrets ($40\,\mathrm{mm} \times 10\,\mathrm{mm}$) are characterized and used in an energy harvester device based on the transverse piezoelectric effect. The energy harvesting device is an air-spaced cantilever arrangement produced by additive manufacturing technique (3D-printing). The device is tested by exposing it to sinusoidal vibrations with an acceleration a, generated by a shaker. By placing the ferroelectret at a defined distance from the neutral axis of the cantilever beam and using a proper pre-stress of the ferroelectret, an output power exceeding 1000 µW at the resonance frequency of approximately 35 Hz is reached. This demonstrates a significant improvement of air-spaced vibrational energy harvesting with ferroelectrets and greatly exceeds previous performance data for ferroelectret energy harvester of maximal 230 µW.

In the second stage of the dissertation, the focus is shifted to develop ferroelectrets for chosen applications such as force myography, ultrasonic transducer and smart insole. Hereby, new arrangements and manufacturing methods are investigated to build the ferroelectret sensors. Furthermore, and following the recent requirements of eco-friendlier sensors, ferroelectrets based on polylactic acid (PLA) are investigated. PLA is a biodegradable and bioabsorbable material derived from renewable plant sources, such as corn or potato starch, tapioca roots, and sugar canes.

This work relays a promising new technique in the fabrication of ferroelectrets. The novel structure is achieved through sandwiching a 3D-printed grid of periodically spaced thermoplastic polyurethane (TPU) spacers and air channels between two 12.5 µm-thick FEP films. Due to the ultra-soft TPU sections, very high quasi-static ($22.000\,\mathrm{pC\,N^{-1}}$) and dynamic ($7500\,\mathrm{pC\,N^{-1}}$) d_{33}-coefficients are achieved. The isothermal stability of the d_{33}-coefficients showed a strong dependence on poling temperature. Furthermore, the thermally stimulated discharge currents revealed well-known instability of positive charge carriers in FEP, thereby

offering the possibility of stabilization by high-temperature poling. A similar approach is taken by replacing the environmentally harmful FEP by PLA. Large piezoelectric d_{33}-coefficients of up to 2850 pC N^{-1} are recorded directly after charging and stabilized at about 1500 pC N^{-1} after approximately 50 days under ambient environmental conditions. These ferroelectrets when used for force myography to detect the slightest muscle movement when moving a finger, resulted in signal shapes and magnitudes that can be clearly distinguished from each other using simple machine learning algorithms known as Support Vector Machine (SVM) with a classification accuracy of 89.5%.

Following the new manufacturing route using 3D-printing, an insole is printed using pure polypropylene filament and consists of eight independent sensors, each with a piezoelectric d_{33} coefficient of approximately 2000 pC N^{-1}. The active part of the insole is protected using a 3D-printed PLA cover that features eight defined embossments on the bottom part, which focus the force on the sensors and act as overload protection against excessive stress. In addition to determining the gait pattern, an accelerometer is implemented to measure kinematic parameters and validate the sensor output signals. The combination of the high sensitivity of the sensors and the kinematic movement of the foot, opens new perspectives regarding diagnosis possibilities through gait analysis.

By 3D-printing a PLA backplate and using it in combination with a bulk PLA film, a new possibility to build ultrasonic transducers is presented. The ultrasonic transducer consists of three main components all made from PLA: the film presenting the vibrating plate, the printed backplate with well-defined groves, and the printed holder. The PLA film and the printed backplate build together the ferroelectret with artificial air voids. The printed holder clamps the film on the backplate and fixes the ferroelectret together. The resulting sound pressure is measured with a calibrated microphone (Type 4138, Bruel & Kjaer) at a distance of 30 cm. The biodegradable ultrasonic transducer exhibits a large bandwidth of approximately 45 kHz and fractional bandwidth of 70%. The resulting sound pressure at the resonance frequency can be increased from 98 dB up to 106 dB for driving voltages from 30 to 70 V, respectively.

The obtained theoretical and experimental results are an excellent base for further optimizing ferroelectrets to be accepted in the field of energy harvesting and mechanical sensors, where flexibility and high sensitivity are mandatory for the applications.

Kurzfassung

Ziel dieser Arbeit ist die Entwicklung innovativer Ferroelektrete, die als Energy Harvester sowie auch als mechanische Sensoren genutzt werden können. Im ersten Teil der Arbeit mit dem Schwerpunkt der Energiegewinnung werden neuartige Ferroelektrete auf der Grundlage von Polymeren mit hervorragenden Elektret Eigenschaften, wie beispielsweise Fluorethylenpropylen (FEP), entwickelt. Diese eignen sich aufgrund ihrer Einsatzmöglichkeit bei harschen Umgebungsbedingungen, wie z.B. hohe Temperatur oder Luftfeuchtigkeit. Es werden zwei Arten von Ferroelektreten untersucht, die auf Hohlraumstrukturen basieren. Einerseits werden zwei FEP-Folien gezielt thermisch miteinander verschmolzen, sodass zwischen ihnen definierte parallele Tunnel (Paralleltunnel-Ferroelektrete) entstehen. Andererseits werden FEP-Röhren mit rundem Querschnitt miteinander verschmolzen, sodass sich ein Band oder eine Membran bildet. Dabei ist die FEP-Röhren Konfiguration auf den longitudinalen piezoelektrischen Effekt und die FEP-Folien Konfiguration auf den transversalen piezoelektrischen Effekt optimiert.

Die FEP-Röhrenkonfiguration wird auf der Grundlage eines Finite-Elemente-Modells optimiert. Es zeigt sich, dass die Implementierung einer einzigen Röhrenstruktur ($25\,\mathrm{mm} \times 1.5\,\mathrm{mm}$) als Energy Harvester die größte Ausgangsleistung aufweist. Der damit aufgebaute Energy Harvester und dessen analytische Modellierung weisen große Abhängigkeiten zwischen der erzeugten Leistung und der Wandstärke, Lastwiderstand und seismischer Masse auf.

Für einen Wandler mit einer Wandstärke von 25 µm unter Verwendung einer seismischen Masse von 80 g und einer wirkenden Beschleunigung a von $1\,g$ ($9.81\,\mathrm{m\,s^{-2}}$) lassen sich Ausgangsleistungen von bis zu 300 µW bei einer Resonanzfrequenz von 80 Hz erreichen.

Der Energy Harvester mit Paralleltunnel-Ferroelektret ($40\,\mathrm{mm} \times 10\,\mathrm{mm}$) Konfiguration basiert auf einer Biegebalkenanordnung. Hierbei wird die Ferroelektretstruktur auf einem additiv gefertigten Biegebalken (3D-Druckverfahren) in einem definierten Abstand zur neutralen Faser des Balkens angebracht. Die Charakterisierung dieses Systems erfolgt durch die Messung des Ausgangssignals infolge einer sinusförmigen Schwingungsanregung mit einer Beschleunigung a, die mit Hilfe eines Schwingerregers erzeugt wird. Durch die Platzierung des Ferroelektrets in einem definierten Abstand und die Verwendung einer geeigneten Vorspannung des Ferroelektrets wird eine Ausgangsleistung von über 1000 µW bei der Resonanzfrequenz von etwa 35 Hz erreicht. Dies zeigt eine signifikante Erhöhung der gewonnenen Energie mit Ferroelektreten und übertrifft bei weitem frühere Leistungsdaten von maximal 230 µW.

Im zweiten Teil dieser Arbeit werden neue Herstellungsmethoden und Anordnungen solcher Ferroelektret-Sensoren untersucht. Der Fokus liegt auf ausgewählten Anwendungen, wie beispielsweise Kraftmyographie, Ultraschallwandlern und intelligenten Einlegesohlen. Darüber hinaus werden Ferroelektrete auf der Basis von Polymilchsäure (PLA) untersucht, um den aktuellen Anforderungen an umweltfreundlicheren Sensoren gerecht zu werden. PLA ist ein biologisch abbaubares und bioabsorbierbares Material, das aus erneuerbaren pflanzlichen Quellen wie Mais- oder Kartoffelstärke, Tapiokawurzeln und Zuckerrohr produziert wird.

Als eine neuartige Möglichkeit zur Herstellung von Ferroelektret-Sensoren, wird eine vielversprechende Sandwichstruktur vorgestellt. Dabei wird ein additiv gefertigtes Gitter aus periodisch angeordneten Abstandshalten aus thermoplastischem Polyurethan (TPU) und Luftkanälen zwischen zwei FEP-Folien mit einer Dicke von 12.5 µm platziert. Aufgrund der sehr weichen TPU-Abschnitte werden sehr hohe quasistatische (22.000 $\mathrm{pC\,N^{-1}}$) und dynamische (7500 $\mathrm{pC\,N^{-1}}$) d_{33}-Koeffizienten erreicht. Die isotherme Stabilität der d_{33}-Koeffizienten zeigt eine starke Abhängigkeit von der Polungstemperatur. Darüber hinaus zeigen die thermisch stimulierten Entladeströme die bekannte Instabilität positiver Ladungsträger in FEP, was die Möglichkeit einer Stabilisierung durch Hochtemperatur-Polung bietet. Ein ähnlicher Ansatz wird verfolgt, indem das umweltschädliche FEP durch PLA ersetzt wird. Dabei lassen sich hohe piezoelektrische d_{33}-Koeffizienten von bis zu 2850 $\mathrm{pC\,N^{-1}}$ direkt nach dem Aufladen messen, die sich nach etwa 50 Tagen bei Laborbedingungen auf etwa 1500 $\mathrm{pC\,N^{-1}}$ stabilisieren. Diese hohe Empfindlichkeit ermöglicht die Detektion von sehr kleinen Verformungen der neuartigen Ferroelektret-Sensoren, die in einer Kraftmyographie Anwendung gezeigt wird. Hierbei werden vier solcher Ferroelektret-Sensoren um den Unterarm gespannt, um kleinste Muskelbewegungen beim Beugen der Finger zu erkennen. Dabei lassen sich Signalformen und -amplituden messen, die mit einfachen Algorithmen des maschinellen Lernens klassifizierbar sind. Durch die Nutzung einer Support Vector Machine als Klassifikator lässt sich eine Klassifizierungsgenauigkeit von 89,5% der verschiedenen Fingerbeugungen einer Hand erreichen.

Mit dieser neuen Herstellungsmöglichkeit der additiver Fertigung wird eine Einlegesohle für eine Anwendung in der Ganganalyse aus reinem Polypropylen Filament gedruckt. Diese besteht aus acht voneinander unabhängigen Sensoren, die jeweils einen piezoelektrischen d_{33}-Koeffizienten von etwa 2000 $\mathrm{pC\,N^{-1}}$ aufweisen. Der aktive Teil der Einlegesohle wird durch eine weitere 3D-gedruckte PLA-Hülle geschützt, die auf der Unterseite acht definierte Prägungen aufweist. Über diese Prägungen lässt sich die Kraft fokussiert auf die Sensoren einleiten, die gleichzeitig bei zu hohen Belastungen als Überlastschutz fungieren. Zusätzlich zur Bestimmung des Gangbildes wird ein Beschleunigungssensor eingesetzt, um kinematische Parameter zu messen und die Ausgangssignale der Sensoren zu validieren. Die Kombination aus der hohen Empfindlichkeit der Sensoren und der kinematischen Bewegung des Fußes eröffnet neue Perspektiven hinsichtlich der Diagnosemöglichkeiten bei der Ganganalyse.

Als letzte Anwendung wird der Einsatz solcher Ferroelektrete als Ultraschallwandler auf PLA-Basis untersucht. Hierbei wird ein Ultraschallwandler auf Basis einer 3D-gedruckten PLA-Rückplatte mit definierten Rillen und einer PLA-Folie, die die vibrierende Platte darstellt, aufgebaut. Die PLA-Folie bildet gemeinsam mit der Rückplatte den Ferroelektret-Wandler mit künstlichen Luftlöchern. Beide Elemente werden durch einen ebenfalls 3D-gedruckter Halter miteinander fixiert. Der resultierende Schalldruck wird mit einem kalibrierten Mikrofon (Typ 4138, Bruel & Kjaer) in einem Abstand von 30 cm gemessen. Der biologisch abbaubare Ultraschallwandler weist eine hohe Bandbreite von etwa 45 kHz und eine relative Bandbreite von 70% auf. Der resultierende Schalldruck bei der Resonanzfrequenz kann von 98 dB auf bis zu 106 dB für Steuerspannungen von 30 bis 70 V erhöht werden.

Die erzielten theoretischen und experimentellen Ergebnisse stellen eine hervorragende Grundlage für die weitere Optimierung von Ferroelektreten dar. Die Ferroelektret-Wandler können in den Bereichen Energy Harvesting und mechanische Sensorik eingesetzt werden, bei den eine hohe Flexibilität sowie hohe Empfindlichkeit gefordert ist.

List of publications

2023

- X. Ma, S. Zhukov, H. von Seggern, G. M. Sessler, **O. Ben Dali**, M. Kupnik, Y. Dai, P. He, X. Zhang "Biodegradable and Bioabsorbable Polylactic Acid Ferroelectrets with Prominent Piezoelectric Activity", *Advanced Electronic Materials*, 2201070, 2023.
- X. Xiang, X. Ma, L. Zhou, G. M. Sessler, H. von Seggern, **O. Ben Dali**, M. Kupnik, H. Pengfei Y. Dai and X. Zhang "Threadlike Piezoelectric Sensors Based on Ferroelectrets and Their Application in Washable and Breathable Smart Clothing", Advanced Materials Technologies, 2202130, 2023

2022

- **O. Ben Dali**, Y. Sellami, S. Zhukov, H. von Seggern, N. Schäfer, B. Latsch, G. M. Sessler, P. Beckerle, and M. Kupnik "Ultrasensitive and low-cost insole for gait analysis using piezoelectrets",in 2022 *IEEE Sensors*, IEEE, 2022.
- **O. Ben Dali**, S. Zhukov, R. Chadda, A. Kasanski, H. von Seggern, X. Zhang, G. M. Sessler, and M. Kupnik, "Eco-Friendly High Sensitive Piezoelectrets for Force Myography," in *IEEE Sensors Journal*, 2022.
- M. Rutsch, **O. Ben Dali**, P. Downing, G. Allevato, C. Haugwitz, J. Hinrichs, and M. Kupnik, "Optimization of thin film protection for waveguided ultrasonic phased arrays", in 2022 *IEEE International Ultrasonics Symposium (IUS)*, IEEE, 2022.
- R. Chadda, M. Link, T. Engel, C. Hartmann, **O. Ben Dali**, J. Probst, H. Merschroth, E. Abele, M. Weigold, and M. Kupnik, "Evaluation of Additively Manufactured Parts in Disruptive Manner as Deformation Elements for Structural Integrated Force Sensors," in *IEEE Sensors Journal*, vol. 22 , no. 20 , pp. 19249-19258, 2022.
- **O. Ben Dali**, H. von Seggern, G. M. Sessler, P. Pondrom, S. Zhukov, X. Zhang, M. Kupnik, "Ferroelectret energy harvesting with 3D-printed air-spaced cantilever design", Nano Select, vol. 3, no. 3, pp. 713–722, 2022.

2021

- H. von Seggern, S. Zhukov, **O. Ben Dali**, C. Hartmann, G. M. Sessler, and M. Kupnik, "Highly efficient piezoelectrets through ultra-soft elastomeric spacers", Polymers, vol. 13, no. 21, p. 3751, 2021.
- **O. Ben Dali**, S. Zhukov, M. Rutsch, C. Hartmann, H. von Seggern, G. M. Sessler, and M. Kupnik "Biodegradable 3d-printed ferroelectret ultrasonic transducer with large output pressure", in 2021 IEEE International Ultrasonics Symposium (IUS), IEEE, 2021, pp. 1–4.
- **O. Ben Dali**, S. Zhukov, C. Hartman, H. von Seggern, G. M. Sessler, and M. Kupnik, "Biodegradable additive manufactured ferroelectret as mechanical sensor", in 2021 IEEE Sensors, IEEE, 2021, pp. 1–4.

2020

- S. Zhukov, H. von Seggern, X. Zhang, Y. Xue, **O. Ben Dali**, P. Pondrom, G. M. Sessler, and M. Kupnik, "Microenergy harvesters based on fluorinated ethylene propylene piezotubes", Advanced Engineering Materials, 22(5), 1901399, 2020.
- X. Ma, H. von Seggern, G. Sessler, S. Zhukov, **O. Ben Dali**, M. Kupnik, and X. Zhang, "High performance fluorinated polyethylene propylene ferroelectrets with an air-filled parallel-tunnel structure", to appear in IOP Journal Smart Materials and Structures, pp. 1–16, 2020.
- **O. Ben Dali**, P. Pondrom, G. M. Sessler, S. Zhukov, H. von Seggern, X. Zhang, and M. Kupnik, "Cantilever-based ferroelectret energy harvesting", Applied Physics Letters, vol. 116, no. 24, p. 243 901, 2020.
- Zhukov, X. Ma, H. von Seggern, G. M. Sessler, **O. Ben Dali**, M. Kupnik, and X. Zhang, "Biodegradable cellular polylactic acid ferroelectrets with strong longitudinal and transverse piezoelectricity", Applied Physics Letters, vol. 117, no. 11, p. 112 901, 2020.

2019

- **O. Ben Dali**, S. Zhukov, R. Chadda, P. Pondrom, X. Zhang, G. Sessler, H. von Seggern, and M. Kupnik, "Modeling of piezoelectric coupling coefficients of soft ferroelectrets for energy harvesting", in Proc. IEEE International Ultrasonics Symposium (IUS), pp. 147– 150, 2019.
- M. Rutsch, **O. Ben Dali**, A. Jager, G. Allevato, K. Beerstecher, J. Cardoletti, A. Radetinac, L. Alff, and M. Kupnik, "Air-coupled ultrasonic bending plate transducer with piezoelectric and electrostatic transduction element combination", in Proc. IEEE International Ultrasonics Symposium (IUS), pp. 147– 150, 2019.

Abbreviations

IoT Internet of things

CAGR compound annual growth rate

PZT lead zirconate titanate

PVDF polyvinylidene fluoride

PP polypropylene

FEP fluorinated polyethylene propylen

SiO_2 silicon dioxide

Si_3N_4 silicon nitride

PTFE polytetrafluoroethylene

TSDC thermally stimulated discharge currents

EMF electromechanical films

SEM scanning electron micrograph

PETP polyethylene terephthalate

PEI polyetherimide

PEEK polyether ether ketone

COP cyclo-olefin polymers

COC cyclo-olefin copolymers

ePTFE expanded polytetrafluoroethylene

fPTFE fibrous polytetrafluoroethylene

IXPP radiation-crosslinked polypropylene

EVA ethylene-vinyl acetate

THV tetrafluoroethylene–hexafluoropropylene–vinylide

PDMS polydimethylsiloxane

BT barium titanate

FEA finite element analysis

ST Sawyer-Tower-Method

PEN polyethylene-naphthalate

PE cellular polyethylene

FDM fused deposition modeling

PLA polylactide acid

TPU thermoplastic polyurethane

PGS poly(glycerol sebacate)

CO_2 carbon dioxide

ABS acrylonitrile butadiene styrene

HMI Human Machine Interface

EMG electromyography

FMG force myography

SVM Support Vector Machine

CA classification accuracy

MAV mean absolute value

SPI serial peripheral interface

UDP user datagram protocol

AI artificial intelligence

ML machine learning

DL deep learning

ANN artificial neural network

NN Neural Network

ReLU rectified linear unit function

FFNN feed forward neural network

RNN recurrent neural network

LSTM long short-term memory

BoPET biaxially-oriented polyethylene terephthalate

PET polyethylene terephthalate

SSHI synchronized switch harvesting on inductor

Contents

1 Introduction

In recent decades, the need for sensors has grown drastically. Through the new topics such as Internet of things (IoT), industry 4.0, which includes the automation of various industries, the sensor market is expected to reach 238 billion dollars by 2025 with a compound annual growth rate (CAGR) of 9.1% from 2021 to 2026 [1]. The growing demands for reliability and the tendency to produce more lightweight and flexible structures is also associated with the growing new fields of applications such as the wearable technology, which is expected to grow from 116.2 billion US-dollars in 2021 to 265.4 billion US-dollars by 2026 [2].

With the growth of the number of sensors arises the challenge of their electrical supply. Although it is theoretically possible to power each sensor with a battery, powering numerous sensors over a long period of time presents some problems: these batteries need to be replaced or recharged on a regular basis, which proves complicated when they are located in difficult-to-reach locations such as sensor networks used to monitor widely distributed production and process engineering plants, or embedded and implanted sensors for medical applications. In order to reduce the associated maintenance requirements and to supply these electronic devices with energy in places where electric power is not readily available, energy harvesting systems have become a steadily growing alternative. Hereby renewable energy sources can be utilized wisely and, thus, cover the growing demand and the need to use ”clean” energy sources. One more alternative is the development of sensors that feature output signals large enough to be self-sufficient.

Energy harvesting is defined as the extraction of electrical energy from ambient sources such as heat, vibration or air currents for low power consumption devices[3]–[9]. Although energy harvesters have been investigated and even commercialized, more compact and efficient solutions are required.

In vibrational energy harvesting, piezoelectric transducers utilizing the direct piezoelectric effect have been investigated for the last 20 years, where piezoceramics such as lead zirconate titanate (PZT) have been the dominating materials [10]–[14]. After the classification of lead as a toxic material, the restrictions to its use have been increased. This, in turn, offered the opportunity for research of new lead-free materials such as ferroelectric polymers represented dominantly by polyvinylidene fluoride (PVDF) and its copolymers [15]–[17].

Other polymer categories that can be considered piezoelectric are the voided charged polymers, also called ferroelectrets or piezoelectrets [18]–[20]. The early ferroelectrets were polarized cellular polymers, foremost polypropylene (PP), exhibiting high piezoelectric activity that exceeds PVDF [21]–[25]. Drawbacks of polarized cellular PP are the missing thermal charge stability and the absence of a significant d_{31} activity. Due to these limitations, alternative ferroelectret materials, mostly fluorocarbons, have been investigated [26]–[39]. As a rule, these systems are characterized by a significant and thermally more stable d_{33} piezoelectric response. This makes it possible to implement rather efficient vibration-based micro-energy harvesters [40]–[45]. A promising new development are parallel-tunnel films [46]–[50]. These consist, for example, of two fluorinated polyethylene propylen (FEP) films partly fused together at elevated temperatures with enclosed air-filled tunnels and surface metallization. Beside their superior electret properties as well as their far better thermal stability than PP, these structures exhibit not only similar longitudinal piezoelectric

coefficients as piezoceramics but also have a large d_{31}-activity. This allows their use in energy harvesters based on the transverse piezoelectric effect, including cantilever systems. The present work is dedicated to such materials and their applications. Starting from the physical and technical fundamentals of these materials, new ferroelectrets have been developed that show significant improvement compared with state of the art at present date. This allows their use in several applications such as energy harvesting, human machine interface, and ultrasonic transducer.

1.1 Structure of this thesis

The main objective of this thesis is the development of new ferroelectrets with improved piezoelectric properties in order to use them in energy harvesting and other applications, where high sensitivity and stability is required. Therefore, this thesis can be devided into three main topics: ferroelectrets for energy harvesting, novel ferroelectret arrangements and some sensor applications.

In Chapter 2, the fundamentals required for a better understanding of this work are briefly discussed. In this context, a brief definition of electrets, their preparation and characterization methods as well as the origin of their piezoelectricity are discussed.

In Chapter 3, the development, characterization and optimization of ferroelectrets built with materials known for their temperature stability are introduced. These ferroelectrets are optimized for their application in energy harvesting devices based on longitudinal and transversal piezoelectric effect.

In Chapter 4, novel ferroelectrets are presented. Here, new ferroelectret arrangements to enhance the piezoelectric effect are introduced. Furthermore, a biodegradable material is presented that can be used to manufacture eco-friendlier ferroelectrets. Additionally, further manufacturing routes are demonstrated.

In Chapter 5, some transducer applications, such as mechanical sensors and ultrasonic transducers, are presented using the new developed ferroelectret materials showing the great potential to be investigated.

1.2 Original work and contributions

In the author opinion the main contributions carried out through this thesis are fourfold:

1. The optimization and characterization of the newly developed ferroelectrets based on FEP in cooperation with Prof. von Seggern group at TU Darmstadt and Prof. Zhang at Tongji University. These ferroelectrets were used in energy harvesting devices, that featured output powers exceeding known ferroelectret energy harvesters with at least an order of magnitude. Furthermore, analytical models are introduced that describe the energy harvester devices based on the longitidunal as well as the transversal piezoelectric effect of the ferroelectrets.

2. The introduction of new ferroelectret arrangement using soft 3D-printed spacers. The main advantage of such structures is the possibility of improving the mechanical and electrical properties of the ferroelectrets independently. In this context, an analytical model is introduced that predicts the reachable piezoelectric coefficients based on the material parameters as an excellent base for further optimizing ferroelectrets with such an arrangement.

3. The introduction of biodegradable materials that can be used to build ferroelectrets, which is PLA. Since this material is available in different forms: cellular film, bulk film, and filament, three manufacturing techniques were introduced. The three forms were investigated regarding isothermal charge stability as well as their piezoelectric effect. Furthermore, the possibility of combining two material forms, i.e. bulk films and 3D-printed filament, is demonstrated.
4. In addition to the presented possibility of 3D-printing a ferroelectret ultrasonic transducer as well as 3D-printing a piezoelectric insole that features a high sensitivity, an eco-friendly ferroelectret for force myography was introduced. This eco-friendly ferroelectret can be regarded as a milestone for these sensors to be accepted in the field of human machine interfaces as an eco-friendly alternative to the conventional piezoelectric sensors.

2 Fundamentals

In this chapter, the physical fundamentals of electrets are discussed. Afterwards, as the focus of this work requires, different types of piezoelectric electrets are presented including their manufacturing processes. Subsequently, some application fields of such materials are discussed.

2.1 Electrets: a brief history and introduction

An electret is a dielectric material with the ability to exhibit an electrical charge over a long period of time. This term was first used by Oliver Heaviside in 1885 as an analogy to the at the time well known term magnet [51]. This property of exhibiting an electric field after treatment of particular waxes was already described by Gray in 1732 [52] and theorized by Faraday in 1839. Despite the fact that enough studies on electrostatic phenomena have been conducted, the first systematic studies on electrets were carried out starting from 1919 by Mototari Eguchi.

At that time it was known that some waxes and resinous materials exhibit a different conductivity depending on their physical state: a moderate conductivity in liquid state and very good insulation in solid state. Eguchi used a mixture of waxes such as Carnauba wax and beeswax, and let them solidify while applying a strong electric field. After cooling, the solidified wax showed very strong electric polarities on its two surfaces, which could be destroyed neither when touched by Bunsen flame, exposed to X-rays nor after the lapse of many years [54]. After further studies, it has become evident that this electret property is not a superficial nature, but is achieved through a permanent internal change within the material. After investigating the first electrets, it was realized that two different types of polarization were present. The first type consists of electric charges

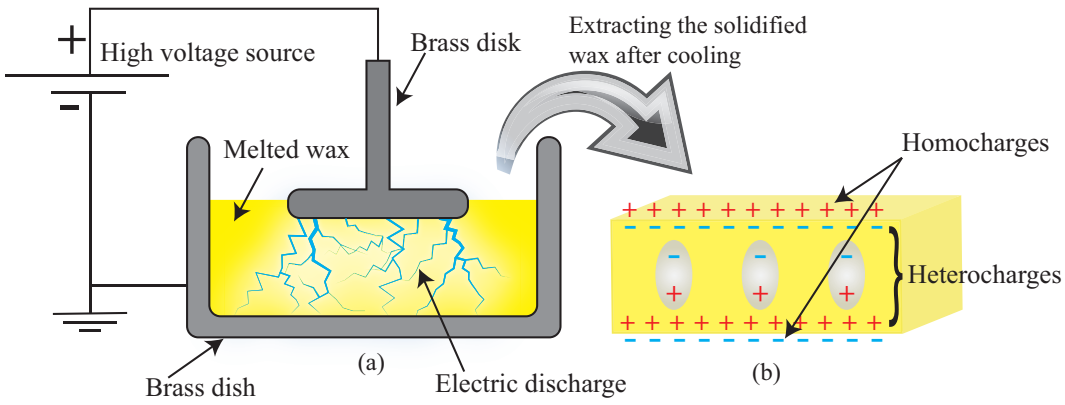

Figure 2.1: Schematic representation of configuration described by Gemant [53]. (a) The polarization of the melted wax at 130 °C and (b) charged and solidified wax after a period of time.

formed by free ions and molecular dipoles in the composite which were later called heterocharges. These feature an opposite polarization as the polarizing electrodes. The other type features the same polarization as the electrodes and were later called homocharges [55]–[58]. In the following years, many investigations were carried out to answer the general question: under what conditions are the dielectric materials permanently polarized and which type of permanent polarisation is attained [53], [59], [60]. These efforts came to fruition at the hand of Bernhard Gross as he outstandingly demonstrated the difference between space charge and dipole polarisation [61], [62]. The concepts of heterocharge and homocharge as suggested by Gross are summarized in Figure 2.2 [63]. Heterocharges can be found in any capacitor material when set under electric voltage resulting in internal polarisation. Depending on the material, these heterocharges can be space charges, interfacial charges if the material consists of different phases, orientational molecular dipoles with different sizes, ionic dipoles or atomic dipoles. The homocharges are deposited or injected from outside and keep their polarity. These can be surface charges that exhibit the same polarity as the poling electrodes, internal charges or bipolar cavity charge.

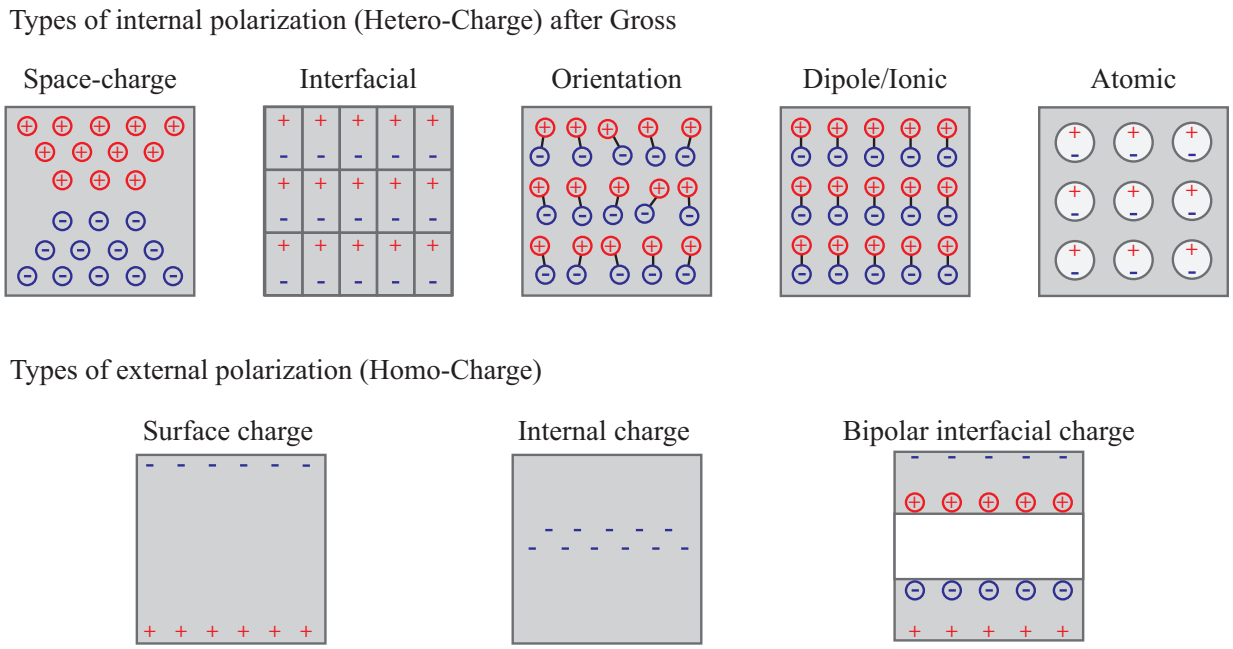

Figure 2.2: Summary of all different polarizations as defined by Gross and adapted by Reimund Gerhard [64].

As a way to distinguish between true electrets and materials that are only electrostatically charged for a short time, a broader definition of the term electret was introduced by Sessler [52]. The charge in an electret must be ”sufficiently stable not to change during the experimental period”, which is also referred to as ”quasi-permanent” [52]. If a material does not possess this property and discharges within a very short time, it is not considered an electret. Thus, in general, only dielectric materials can be called electrets, since conductive materials are not able to store the additional charge. Using this definition, electret materials can be further classified as good or bad electrets, depending on its temporal charge stability as well as temperature stability.

The first electrets, which were mainly made from wax, rosin and sulfur, showed a relatively low temperature stability (<60 °C) and relatively short lifetime [65] and were therefore bad electrets. Alternative materials that showed better charge stability and high surface charge density were the inorganic electrets based on silicon dioxide (SiO_2) and silicon nitride (Si_3N_4). These were compatible with microelectronics, however, exhibited a relatively high young’s modulus which didn’t allow them to be used as flexible transducers. Thus,

more research efforts were oriented towards polymers, that can be tuned and improved regarding their electret and mechanical properties.

2.2 Charges in real electrets

Regardless of the material and manufacturing method, electrets can be classified by the type of charge storage. All real electrets have several charge types and consist of a superposition of mono- and heterocharges.

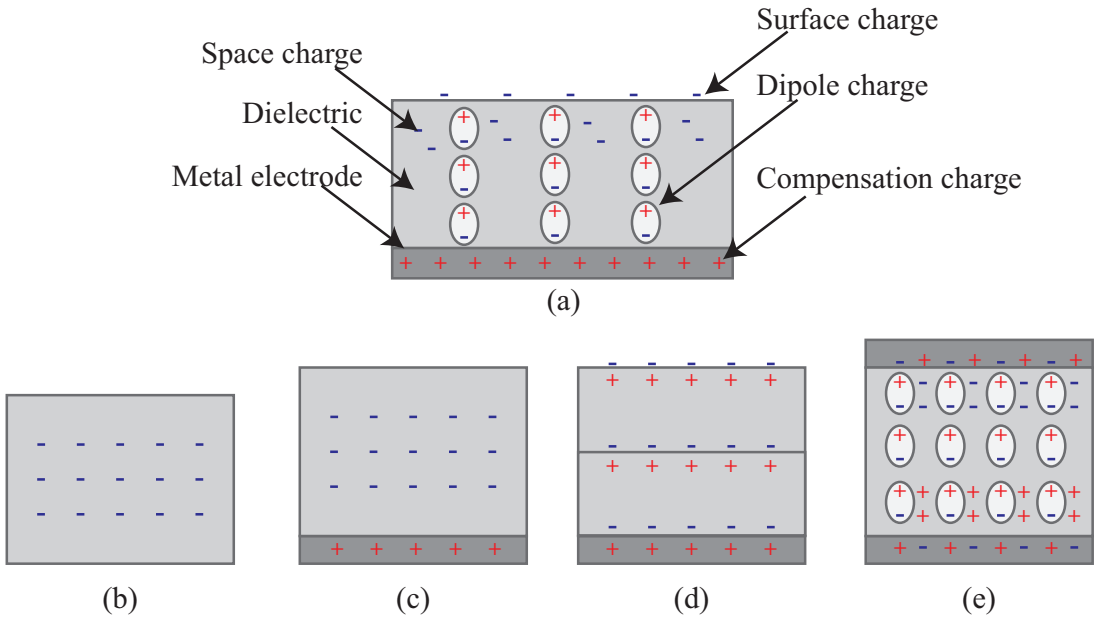

Figure 2.3: Schematic representaion of some typical electrets without electrodes or with grounded electrodes: (a) one-sided metallized electret having deposited surface charges, injected space charges, aligned dipolar charges (or microscopically displaced charges), and compensation charges, (b) nonmetallized monocharge electret, (c) one-sided metallized electret with surface and space charges, (d) one-sided metallized electret with surface charges and charges displaced within domains (Maxwell-Wagner effect) and (e) two-sided metallized electret with dipolar and space charges [66].

Heteropolar charges, also called dipole charges, always have the opposite polarity than the generating source. These are the main charges found in semi-crystalline and polar polymers such as PVDF [-(C2H2F2)n-], that have a positive and a negative center of charge due to their chemical structure [58]. The origin of polarity is the type of atomic bond. Nonpolar bonds produce nonpolar molecules and polar bonds or ionic bonds produce polar molecules.

Homocharges are stored charges that are either positive or negative in the form of an excess or lack of electrons and exhibit the same polarity as the generating source. Depending on their location in the material, they can be divided into volume or space charges and surface charges. The charges are stored in the material in so-called energetic traps [66]. This type of charges is mainly found in polarized non-polar polymers such as FEP and polytetrafluoroethylene (PTFE).

The storage of charges can be explained or interpreted using the energy band model known in solid-state physics as shown in Figure 2.4 [52], [67]. Due to the imperfect structure of materials, there are additional energetic states in the band gap. Charges can be stored in these so-called traps. Depending on the energetic distance of these additional states from the valence or conduction band, the charges are bound stronger or weaker. By supplying energy, for example by radiation or heat, the charge carriers stored in the traps can be released. Since materials often have many defects near the surface, more of these storage sites tend to be superficial and less in the interior of the material. It is believed that the volume traps can be caused by structural anomalies, such as impurities, defects of the monomer units, irregularities of the chains and imperfections of the crystallites, whereas surface traps are caused by chemical impurities, oxidation or chains breakage [66], [68].

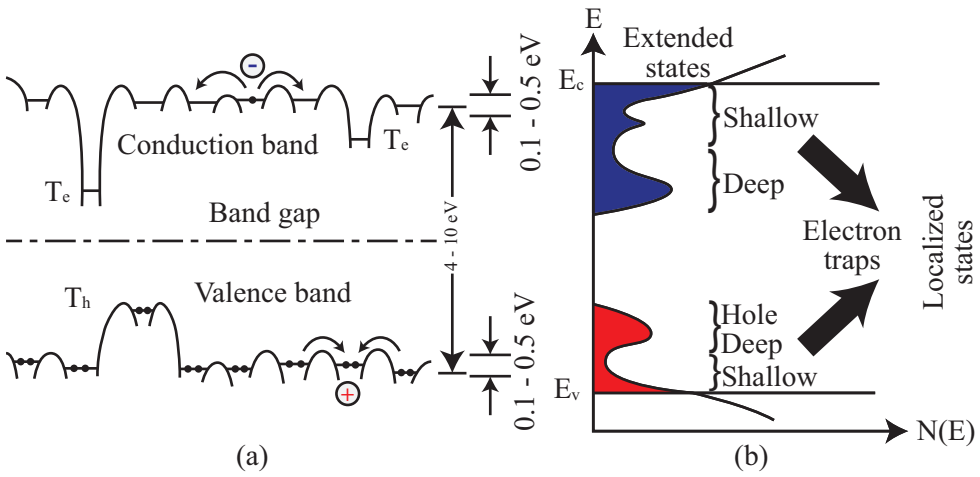

Figure 2.4: (a) Valence and conduction bands of an electret with energetic defects as well as (b) equivalent energy band diagram with location of energetically shallow and deep vacancies according to Sessler and Bauer [66], [67]. Possible states between valence and conduction band can serve as storage sites for charges where the depth of the vacancies indicates the long-term storage capability.

The total charge density in an electret can be described as the difference of homocharges and heterocharges. A material with a large amount of both charge types can have a relatively low external field since these charge types compensates each other. Since an electret has to exhibit a strong electric field, it is desirable for an electret material to posses only one of the two charge types. Therefore several charging methods have been investigated for forming space-charge electrets and dipolar electrets, which differ frequently.

The charging of the dipolar electret such as PVDF is generally achieved through application of an electric field to the material at a relatively high temperature with a subsequent cooling while maintaining the electric field. Otherwise very high electric field ($400\,\mathrm{MV\,m^{-1}}$) accros the sample is needed [69]. The charging of space-charge (or surface-charge) electrets is mostly achieved by injecting (or depositing) charge carriers. This can be achieved for example by using corona discharges, particle beams, or contact electrification through (or onto) a non-metallized surface. The non-metallization of the electret is not mandatory if relatively high fields can be achieved. Other methods consist in the generation of carriers within the dielectric by light, radiation or heat and simultaneous charge separation by a field.

2.3 Charging and polarizing methods of electrets

Even though the physical properties of a material are largely responsible for the potential of its electret properties, the method of charging also has a major influence on how well this potential is exploited. The charging method, for instance, determines which type of charge, i.e. heteropolar or homopolar, how much charge is stored, and in which energy level. Furthermore, the environmental conditions, such as elevated temperature [70] or a different atmosphere [71], strongly influence the long-term stability of the electret. In this section, the charging methods relevant for this work are briefly explained.

2.3.1 Thermal charging methods

The polarization of electrets by applying an electric field to the sample at an elevated temperature with subsequent cooling without removing the electric field is referred to as thermal charging method. This method is mainly used to polarize polar polymers such as PVDF, because of the very high electric field required for polarization at room temperature. This can be significantly reduced by heating such materials at a suitable temperature. For waxes, a temperature above the melting point is needed, whereas for polymers a temperature just above the glass transition temperature and lower than the melting point is needed. The elevated temperature leads to a sufficient mobility of the molecules or molecular chains. When the heated material is exposed to an electric field, the polar molecules are aligned along the field. By slowly lowering the temperature, the materials solidify while maintaining the alignment of the dipoles, resulting in a permanent polarization. This type of polarization is, however, one of three phenomena that can occur in thermal charging. In addition to the polarization due to dipole alignment or charge separation within the dielectric, known as dielectric absorption resulting in heterocharges, the discharges in the air gaps between the electrode and the sample, if external electrodes are used, result in homocharge deposition or injection in the case of contacting electrodes [52].

2.3.2 Corona charging method

Corona charging is currently one of the most used methods for forming electrets, due to the uniformity of deposited charges as well as the simplicity of its implementation (Figure 2.5). In general, the setup consists of a high voltage source, a fine corona needle and a back electrode, which is also the sample holder. When a sufficiently high voltage is applied between asymmetric electrodes such as a point or fine wire and a plate or cylinder, a corona discharge occurs [72]. The ionization near the corona needle is limited to a small volume near the point where ions and excited molecules are created, causing the gas to move due to many collisions between charged particles and neutral molecules. The drift region, extends from the corona point to the planar grounded electrode and is characterized by the presence of charge carriers of only one polarity with mobilities of the order of a few cm/Vs [73]. Positive or negative ions are created depending on the polarity of the corona. In air, negative polarity of the needle mostly produce CO_3^- ions, whereas positive polarity of the needle primarily produce $(H_2O)_nH^+$ ions [74]. These ionized air molecules move along the field lines towards the sample. Due to the low energy of corona ions at atmospheric pressure, the corona ions do not penetrate the bulk of the materials, but they transfer their charge to the surface. The excess charge supplied by corona ions is either trapped on the surface in the shallow traps or injected and trapped in bulk traps, resulting in an electric field in the sample's bulk. The charge penetration into the bulk depends on charge polarity, charge density and surface characteristics of the used electret material [52].

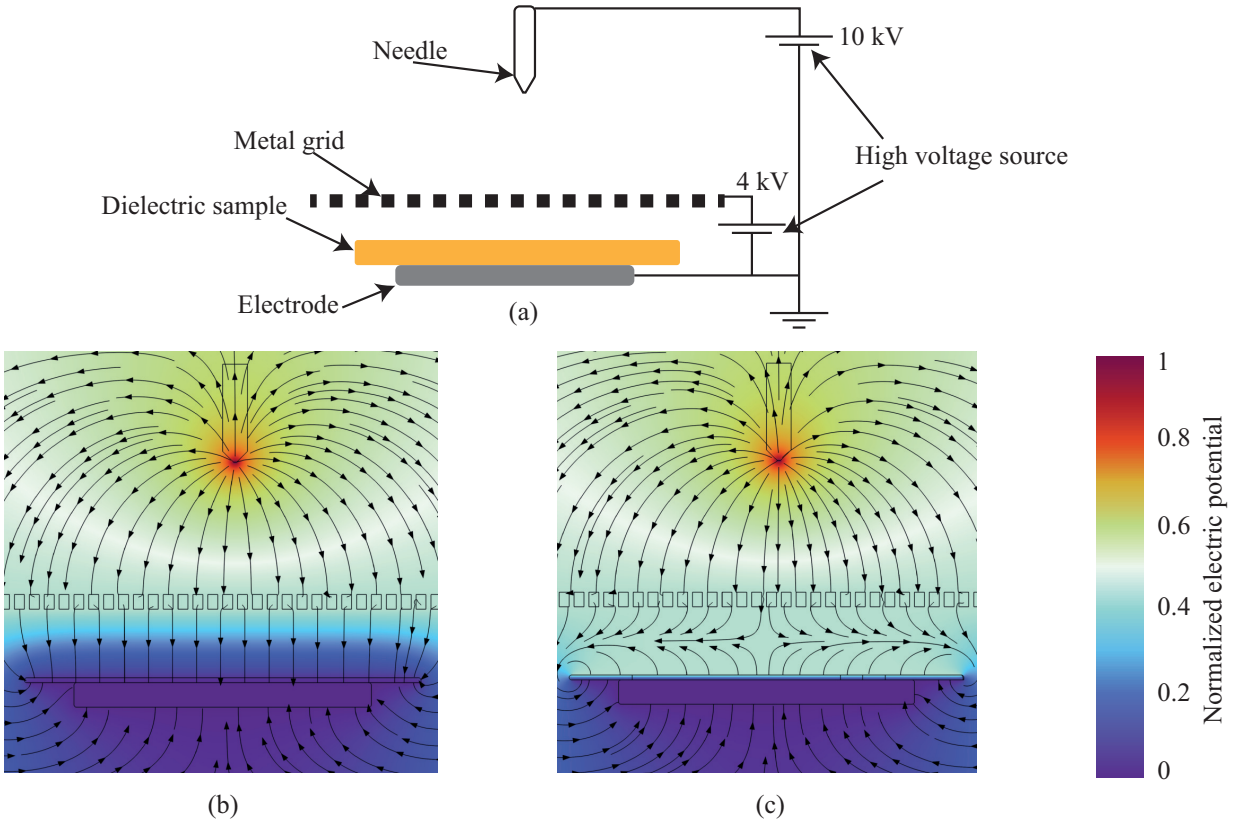

Figure 2.5: (a) Schematic representation of corona charging. The high-voltage source generates a strong electric field, which ionizes the air close to the needle tip. (b) The ions generated move along the E-Field in direction of the metal grid and dielectric film. The ions that reach the dielectric film result in the charging process and building the surface potential. (c) When the surface potential of the electret reaches the grid potential, the ions can not be accelerated towards the electret anymore and the charging process is then terminated.

If the sample is charged, a surface potential $V_s(t)$ can be measured under open circuit conditions. Considering the electric field $E(x,t)$ inside the dielectric with a thickness d, the surface potential can be defined as:

$$V_s(t) = \int_0^d E(x,t)\,dx. \tag{2.1}$$

While the total current $I(t)$ across the sample is given by

$$I(t) = I_c + A\frac{\partial D(x,t)}{\partial t} = I_c + A\frac{\partial\left(\varepsilon E(x,t) + P(x,t)\right)}{\partial t}, \tag{2.2}$$

with D being the electric displacement, $I_c(x,t)$ the conduction current, ε the material permittivity, $P(x,t)$ the electric polarization, and A the sample area facing the electric field.

In order to control the charging process, an improvement of the corona setup was introduced by Gross [75]. The main idea behind this improvement is to place a grid or a wire mesh between the poling needle and

the sample to be charged, which allows the measurement of the charging current and the sample surface potential during the charging process [76]. The surface potential can be determined through two techniques. The first one is by measuring the vibrating capacitor consisting of the grid and the sample by means of the Kelvin technique [77]. The grid is set into vibration using a loudspeaker, generating an AC-signal which can be measured using a lock-in amplifier. When the surface potential of the electret matches the grid potential, the measured AC voltage drops to zero. The second method is achieved by a fixed grid and controlling its voltage V_G to always keep the charging current constant. Hereby the potential of the grid is adjusted to always match the surface potential of the sample by ΔV as

$$V_G = V_s(t) + \Delta V. \tag{2.3}$$

By knowing the potential difference between the grid and the sample surface, while keeping the charging current constant, the surface potential $V_s(t)$ of the electret is determined as the difference between V_G and ΔV [78].

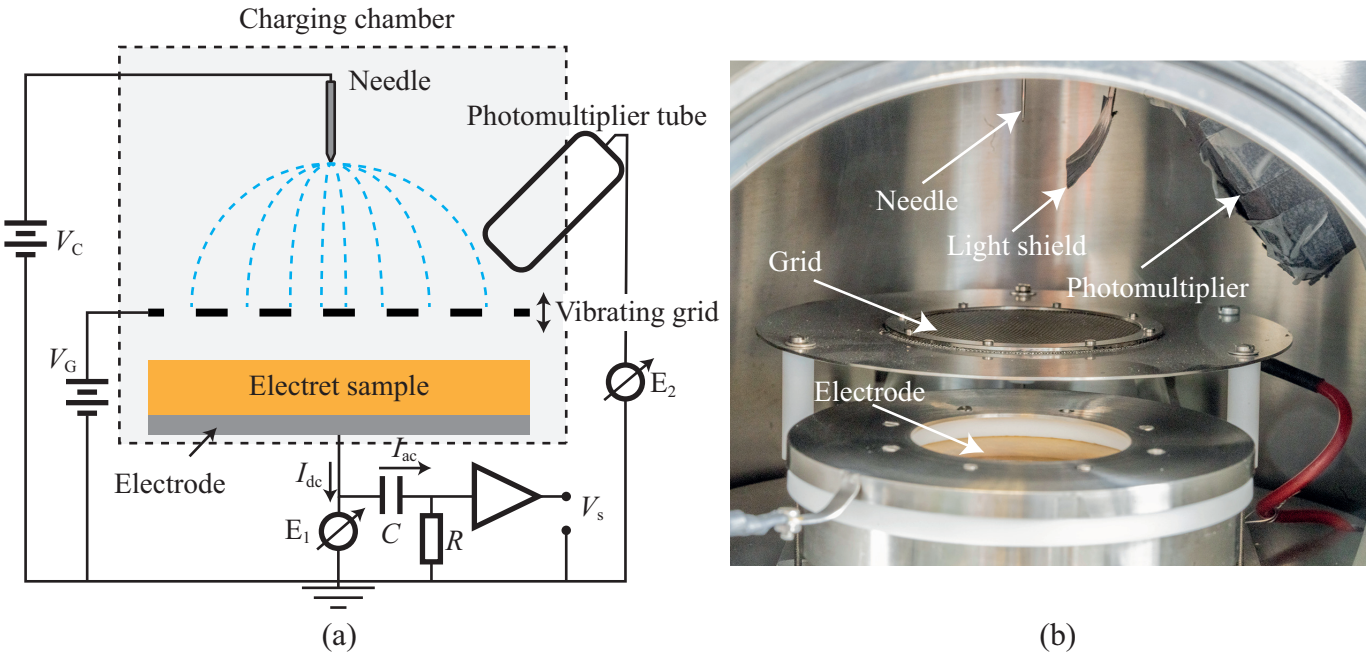

Figure 2.6: Corona triode experimental setup consisting of a point-to-plane corona discharge and a grid between the needle and a sample with additional light emission measurement facility. (a) Schematic representation of the setup [79] and (b) a photograph of the setup without electret sample.

During charging, the current can be described as a function of the surface potential $V_s(t)$, i.e.

$$I(t) = I_c(t) + C\frac{dV_s(t)}{dt}, \tag{2.4}$$

and the conduction current $I_c(t)$ can be defined as

$$I_c(t) = \frac{A}{t}\int_0^d i_c(x,t)\,dx, \tag{2.5}$$

where i_c is the conduction current density, A the area of the back electrode (ground electrode), t the thickness of the sample and C its capacitance. When fully charged, the displacement current is almost zero and the conduction current, which is a leakage current, approximately equals the total current. Additionally, it was shown that if corona charging is carried out at higher temperatures, energetically deeper traps can be charged, which increases the long-term stability of the electrets [80].

The corona setup used in this work is shown in Figure 2.6. The needle is fixed at a distance of 5 cm from the grid, whereas the grid is at a distance of 5 mm from the sample. The grid is mounted on a loudspeaker in order to be set into sinusoidal vibration and allow the measurement of the surface potential V_s of the sample by means of the Kelvin technique. In order to measure the light emission during sample poling, a photomultiplier (Hamamatsu R6094) is incorporated into the charging chamber (Figure 2.6). During the charging process three parameters can be recorded: the DC-charging current I_{dc} measured by the electrometer E_1 (Keithley 610C), the surface potential V_s measured by the AC-current I_{ac}, and the light intensity measured by a photomultiplier and the electrometer E_1. The electrode, on which the electret sample is placed, can be heated using cartridge heater in combination with current controller. This allows the charging process to be conducted at different temperatures. The light shield is used to minimize the contribution of the corona light to the photomultiplier output current and to allow a better measurement of the light emission due to electrical breackdown in the electret sample during the charging process. Since the corona light, mainly produced by the needle tip and grid, is constant during the whole charging process, it can be subtracted from the total photomultiplier output current. This allows a better measurement of the breakdown related photomultiplier currents, that is responsible for the charging process of the electret sample. When the sample is fully charged, the light emission caused by the breakdown in the electret disappears.

2.3.3 Contact Charging method

In case of two-sided metallized electrets, a sandwich contact poling can be achieved by applying a high voltage to both electrodes. The discharges within the material result in the creation of trapped micro-dipoles. This method however, features several drawbacks. The metallization of the electret films should only cover the middle section of the film so that the edges remain isolating. Otherwise, by increasing the poling voltage an electric flashover occurs between the edge of the upper and lower electrodes. If the electret structure features some defects such as inhomogeneous thickness or holes, the electric field would be concentrated at such sites, preventing further charging of the electret sample due to electrical breakdown. Therefore, corona charging method exhibits some advantages compared with contact charging such as:

- Poling without deposited electrodes or with only one electrode.
- Poling of thin films in spite of defects. This is possible due to the limitation of destructive breakdown phenomena only to small sample areas.
- Large electric fields are needed in the case of sandwich contact poling.

2.4 Characterization methods

In this work, the main quantities considered for the characterization of the electrets are: amplitude and polarity of the surface potential and stability of charges [81], which can be determined using Kelvin probe and thermally stimulated discharge currents, respectively.

2.4.1 Surface potential measurement using the Kelvin probe

The relation between the volumetric charge distribution ρ and the electric potential V_s can be expressed using Poisson´s equation as:

$$\Delta V_s(x,y,z) = \frac{-\rho(x,y,z)}{\varepsilon_0 \varepsilon},$$
$$V_s = \iiint_V -\frac{\rho(x,y,z)}{\varepsilon_0 \varepsilon}\, dx\, dy\, dz. \tag{2.6}$$

However, the measured surface potential only confirms the existence of charges within the material without any information regarding their local distribution.

The surface potential measurement is usually performed by a vibrating Kelvin probe with a frequency of a few hundred Hertz. In fact, a capacitance C_k is formed between the Kelvin (vibrating) probe and the charged surface of the electret as

$$C_k = \frac{Q}{V_s - V_{sk}}, \tag{2.7}$$

where Q corresponds to charges of the electret and V_{sk} is the potential applied to the Kelvin probe.

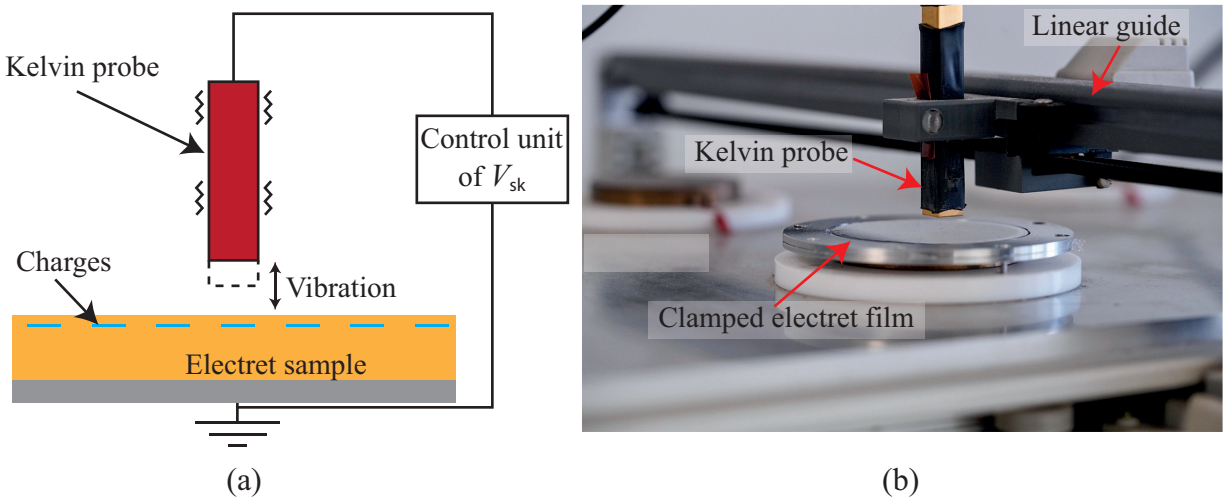

Figure 2.7: (a) Schematic representation of the Kelvin probe method for determining the surface potential of electret materials. (b) Photograph of the measurement setup using 244 ISOPROBE electrostatic voltmeter (Monroe Electronics, Inc.).

Due to the vibration, a periodic current I_{sk} flows through the probe that can be expressed as

$$I_{sk} = (V_s - V_{sk})\frac{dC_k}{dt}. \tag{2.8}$$

By applying a proper DC-voltage V_{sk} to the moving probe that compensates the field in the air gap, the current I_{sk} is canceled. In this case, the applied voltage V_{sk} corresponds to the surface potential of the sample V_s. The

advantage of this method is that the surface potential, and, thus, the charge in the material can be measured without contact and without being affected by the measurement [81].

The measurement setup used in this work consists of a Kelvin probe mounted on a linear $xy-$stage. The samples to be measured are placed on grounded electrodes with a diameter of 42 mm in defined positions [Figure 2.7(b)]. The measurement device controlling the Kelvin probe is a 244 ISOPROBE electrostatic voltmeter (Monroe Electronics, Inc.).

2.4.2 Thermally stimulated discharge currents

Two types of thermally stimulated discharge currents (TSDC) are of interest for the characterization of electrets. The first type is TSDC with shorted electrodes, where the current released by a shorted bilaterally

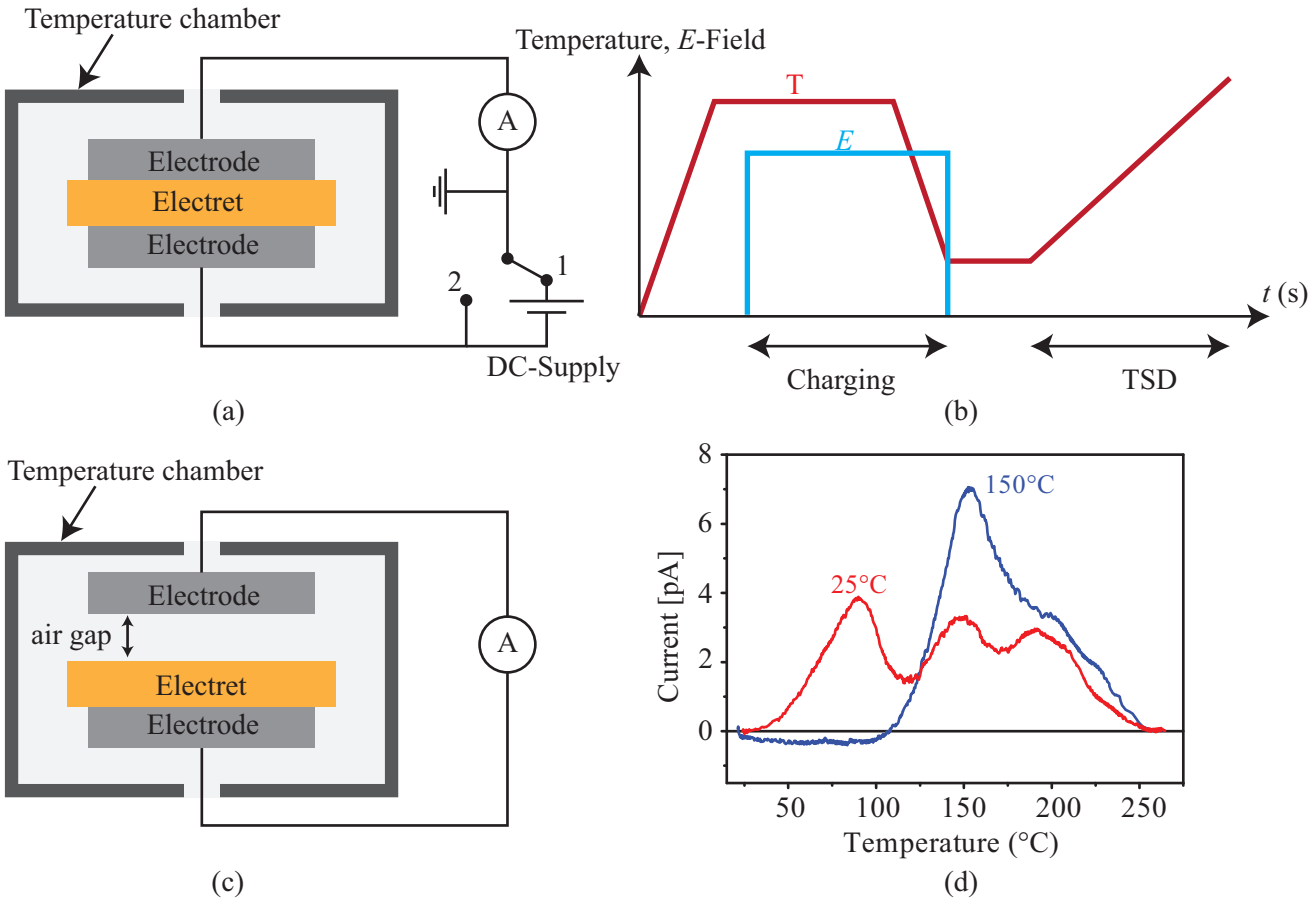

Figure 2.8: (a) Electret charging and TSDC unit, where position 1 and 2 correspond to charging and TSDC measurement, respectively. (b) Field and temperature program during charging and TSDC [52]. (c) Measurement setup of TSDC with an air gap (open-circuit TSDC). (d) Exemplary measurement of open-circuit TSDC of FEP samples charged in a corona triode at different temperatures [33].

metallized electret is measured during heating [Figure 2.8(a)]. beforehand, it is necessary that the electret is charged. Therefore, in the case of TSDC with shorted electrodes it is possible to design the experiment in two steps: first, the charging of the electret through contact charging method or thermal charging method and

second, conducting the TSDC measurement [Figures 2.8(a) and (b)]. Hereby, the material is heated slowly with a temperature ramp of the order of a few degrees Celsius per minute, and the current flowing between the two electrodes is measured [Figure 2.8(b)]. The measured current peaks are generally related to the dipolar properties and to the phenomena of discharging in the material.

The second type is TSDC with an adjacent air gap to the electret, where the charge remaining on the nonmetallized side of an electret is measured during heating in open circuit. This is achieved by placing an electrode in front of the charged surface of the sample and separating them by an air gap [Figure 2.8(c)]). The sample is heated with a temperature ramp of a few degrees Celsius per minute and the current flowing between the upper and lower electrodes is measured. Here as well the measurement shows peaks of depolarization current. The analysis of these peaks reveals detailed information on the type of traps (deep or shallow) in which the charges are placed. In fact, the analysis of the TSDC provides information about the charge stability of the structures and elucidates the role of the air/solid film interface in the discharging process. The higher the temperature of the peak, the more the traps are energetically deep and stable.

2.5 Piezoelectric electrets: piezoelectrets/ferroelectrets

Electret based electromechanical films (EMF) consist of two-sided metallized electret material that feature positive and negative electric charge pairs that are quasi-permanently trapped and build therefore macroscopic ”quasi-dipoles” within the material. Upon mechanical excitation, these films exhibit analogous behaviour to those of piezoelectric crystals/ceramics, and are referred to as a ”piezoelectret” in later use [23], [82]–[85]. Since such films show a hysteresis effect upon charging and charge reversal, a synonymous term frequently used is ferroelectret. In the rest of this document the term ferroelectrets will be used.

The first ferroelectrets were based on PTFE and PVDF, which still belong to the most stable space charge and dipole electrets, respectively. A further development in ferroelectrets of high interest is the discovery of the large piezoelectric activity of heterogeneous non-polar space charge electrets. This triggered more focused efforts for developement of new ferroelectrets based on porous and cellular polymers with remanent charges.

The new ferroelectrets exhibited strong piezoelectric properties after electric charging [18], [23], [24], [86]. The polymer-air composites, in contrast to the well-known bulk ferroelectric materials, are elastically soft due to their high air content and the low Young’s modulus of the polymer walls. The elastic properties of the structure and the quasi-permanent trapping of electric charges inside the polymer walls are key for the working principle of ferroelectrets. During charging, a large electric field E is applied to the both-side-metallized cellular polymer generating large electric fields in the air-filled voids. These electric fields, when strong enough, initialize Paschen breakdown [87]. Generated positive and negative charges are separated by the applied electrostatic field and move towards the polymer walls, where they are quasi-permanently trapped. Such trapped charges induce a surface charge density in the electrodes which redistributes under mechanical compression and under short circuit conditions, while the trapped charge density stays constant. This principle is called the direct piezoelectric effect [18], [86]. The ability to efficiently convert mechanical energy into electrical energy favours ferroelectrets to be used in energy harvesters and in various mechanically based sensors. A first review of this class of materials was published in 2002 by Gerhard-Multhaupt [85]. Since then, significant progress in understanding, design, characterization and possible applications of these materials has been achieved [88], [89]. Thereby the aforementioned systems can be roughly divided into three classes: ferroelectrets with statistically distributed air-filled voids, ferroelectrets with an open-pore structure (statistically distributed fibers), and ferroelectrets with artificially introduced air voids.

2.5.1 Classes of polymer ferroelectrets and their manufacturing methods

Ferroelectrets hybrids with statistically distributed air-filled voids:
The development of ferroelectrets began in 1990 with the use of cellular PP with statistically distributed closed pores [23]. All the pores are lens-like shaped, but their size varies over a wide range, as shown in the scanning electron micrograph (SEM) in Figure 2.9(d). Other materials with such a structure are polyethylene terephthalate (PETP), polyetherimide (PEI), polyether ether ketone (PEEK), cyclo-olefin polymers (COP) and cyclo-olefin copolymers (COC) [88], [89]. Among these materials, cellular PP features outstanding quasi-static and low-frequency dynamic d_{33}-coefficients up to 300 $\mathrm{pC\,N^{-1}}$, but rather low thermal stability concerning charge storage.

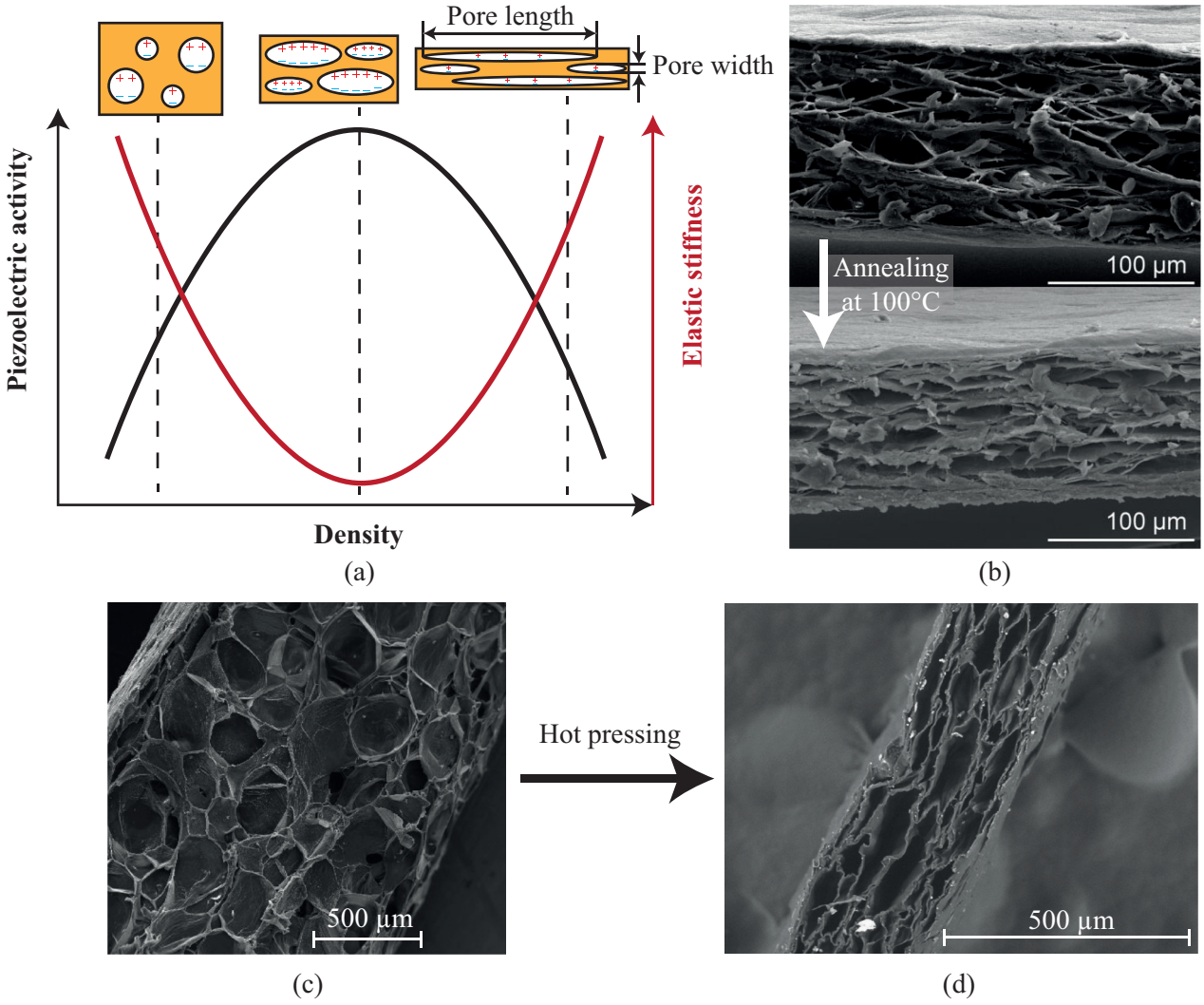

Figure 2.9: (a) Relationship between piezoelectric activity (black line), the elastic stiffness (red line) and density [90]. (b) SEM of cross sections from PETP films [90], (c) and (d) SEM of irradiation-cross-linked PP films before hot pressing and after, respectively [91].

The manufacturing of the ferroelectrets of this class is generally based on foaming technologies such as injection moulding and extrusion foaming, cross-linked polyolefin foaming [40], and by mixing blowing agents

with a polymer solution [92]. Depending on the foaming conditions such as pressure and temperature as well as the polymer viscosity and composition, the size of the voids can be adjusted [93], [94].

The piezoelectric effect of such ferroelectrets depends on the geometry of the pores. For instance, pores featuring a pore width smaller than 10 µm or larger than 100 µm require large electric fields to reach Paschen breakdown [87]. Furthermore, the elastic stiffness of the films, which directly contributes to the piezoelectric response, depends on the pore shapes as well (Figure 2.9). It was shown, that the elastic stiffness of foamed PP depends on its density. Upon decreasing the inflation of the voids, i.e. increasing the density of the film, a local minimum of the film stiffness can be reached [Figure 2.9(a)] [19]. This local minimum of the stiffness corresponds to the local maximum of the measured piezoelectric coefficients of the ferroelectret film [19].

Ferroelectrets sandwich with an open-pore structure (statistically distributed fibers):
This class of ferroelectret materials is based on polymer foams with an open-pore structure sandwiched between two solid polymer layers. So far, expanded polytetrafluoroethylene (ePTFE), also known as fibrous polytetrafluoroethylene (fPTFE), is used exclusively as an open-pore layer [28], [33], [42], [95], [96], whereas FEP is used as solid layer. For manufacturing such ferroelectrets, the layers are stacked on top of each other (Figure 2.10). Since after charging such structures the layers are bond together due to electrostatic forces, only some groups [42] used hot pressing at approximately 280 °C prior to the charging process .

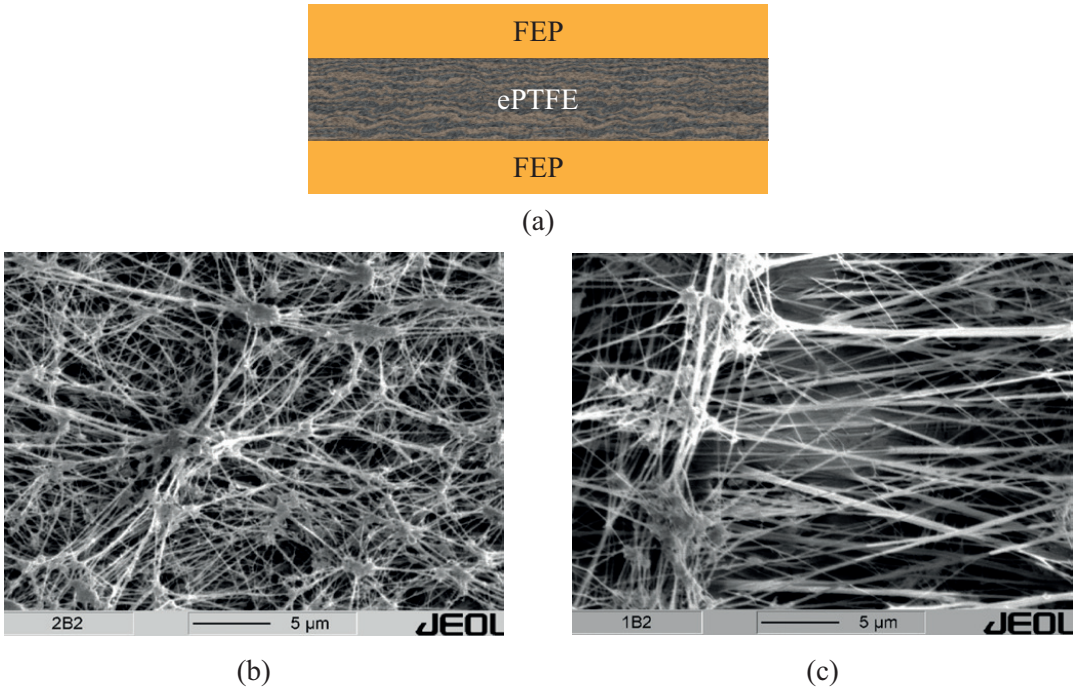

Figure 2.10: (a) Schematic illustration of the FEP/ePTFE/FEP structure, (b) SEM of the porous ePTFE film with nominal porosities of 98% and (c) 91% [95].

Investigations of surface potential decay and TSDC of individual ePTFE films demonstrate outstanding charge storage stability [97]. While individual ePTFE films exhibit rather small d_{33}-coefficients of about 20 pC N^{-1}, FEP/ePTFE/FEP sandwiches possess remarkable d_{33}-coefficients (100 - 1600 pC N^{-1}) depending on geometry and charging conditions [28], [98]. Such properties are combined with good thermal stability [33], but rather unstable mechanical properties, mainly linked to the ePTFE layer.

Ferroelectrets with artificially introduced air voids:
These ferroelectret systems with artificially introduced air-filled voids have been studied intensively in recent years [27], [32], [34], [39], [47], [99], [100]. Generally these ferroelectrets consist of arrays with well-controlled, geometrically defined microstructures. Hereby, several manufacturing techniques were introduced. One of the most utilized fabrication methods is using patterned rigid template to permanently deform the films under the influence of heat, followed with fusion bonding. This results in a good mechanical bond between different layers [34], [39], [99]. Further fabrication possibilities involve the use of perforated intermediate structure between two flat films. These fabrication methods are utilized in this work and will be explained in more detail in upcoming sections. The main advantages of this class of ferroelectrets are the design freedom regarding the geometry of the pores as well as the variety of electret films that can be employed. Although the charge stability, and, thus, the electric property, depends on the films utilized. The mechanical properties are defined by the interplay of the geometry and Young's modulus of the films. This implies an enhancement of ferroelectret mechanical stability based on FEP/ePTFE combinations, featuring the main disadvantage of the class of ferroelectrets with open-pore structure (Figure 2.11). The obtained structures with defined air-filled channels or spherical caps, can be charged to deliver d_{33}-coefficients up to 3000 pC N^{-1}, while exhibiting high thermal charge stability.

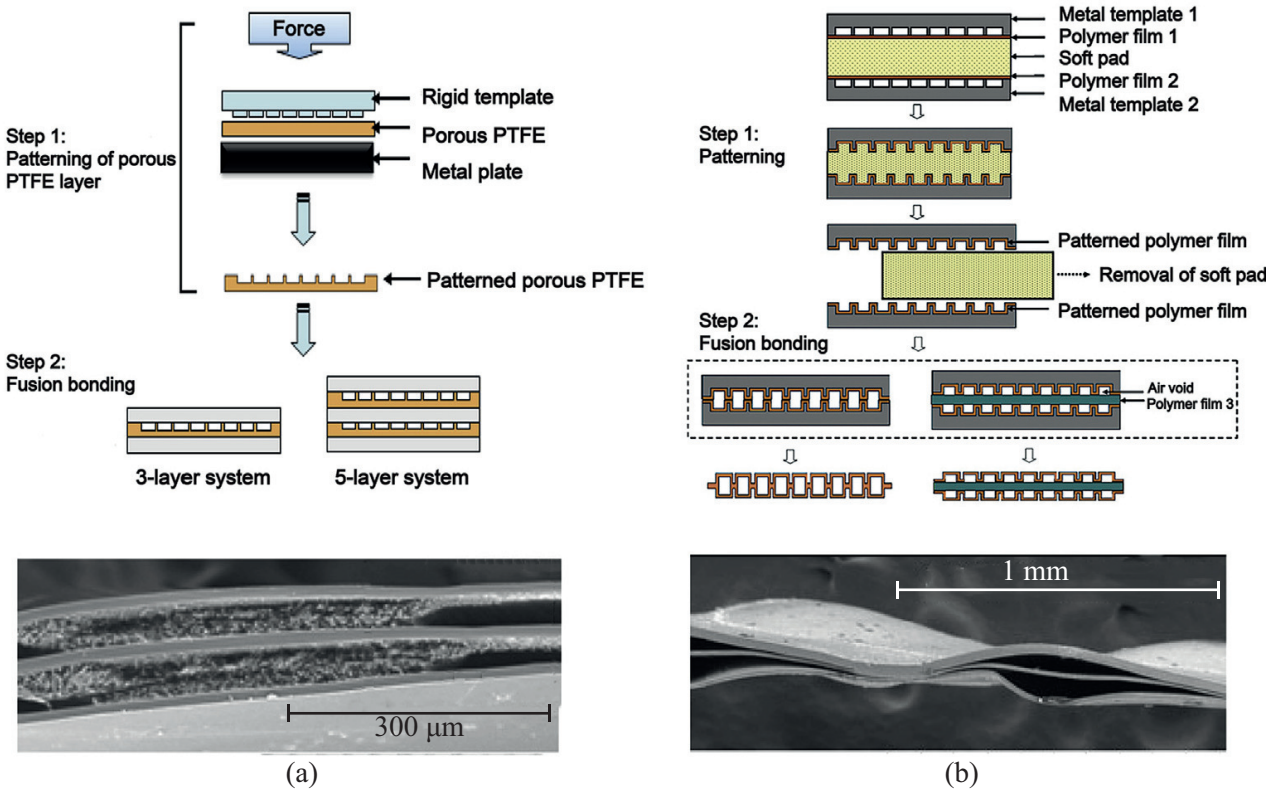

Figure 2.11: (a) Schematic illustration of the fabrication process using a structured template to prepare multi-layer laminated FEP/PTFE films with a photograph of a cross section of the produced ferroelectret [99]. (b) A schematic illustration of a similar fabrication method using the same materials: FEP/PTFE, however, with different fabrication steps [36].

2.5.2 Modeling of ferroelectrets: Origin of piezoelectricity

From a formal perspective, the piezoelectricity is defined by the laws of thermodynamics. Hereby, the piezoelectric constant d_{ij} is defined as the derivative of the Gibbs free energy G with respect to the electric field vector E and stress tensor T at constant temperature [101], i.e

$$d_{ij} = \frac{\partial^2 G(E,T)}{\partial E_i \partial T_j} \rightarrow d_{ij} = \left(\frac{\partial D_i}{\partial T_j}\right)_{E=\text{const}} = \left(\frac{\partial S_j}{\partial E_i}\right)_{T=\text{const}}, \tag{2.9}$$

where S is the strain and D is the electric displacement. If the second derivative shows measurable values, the material can be considered piezoelectric [101]. The subscripts i and j ($1 \leq i \leq 3$ and $1 \leq j \leq 3$) denote the geometric directions of the electric and mechanical quantity, respectively. At this point, it should be pointed out that the relations in equation (2.9) describe thermodynamic quantities: E-field and mechanical stress, that are not directly measurable. The derivatives are assumed to be at constant stress or E-field, which do not entirely correspond to constant force and constant voltage in the case of ferroelectrets. Several models have been developed for a better description of ferroelectrets and understand the influence of stored charges, in order to relate the measurable quantities force and voltage to the equation quantities E-field and stress.

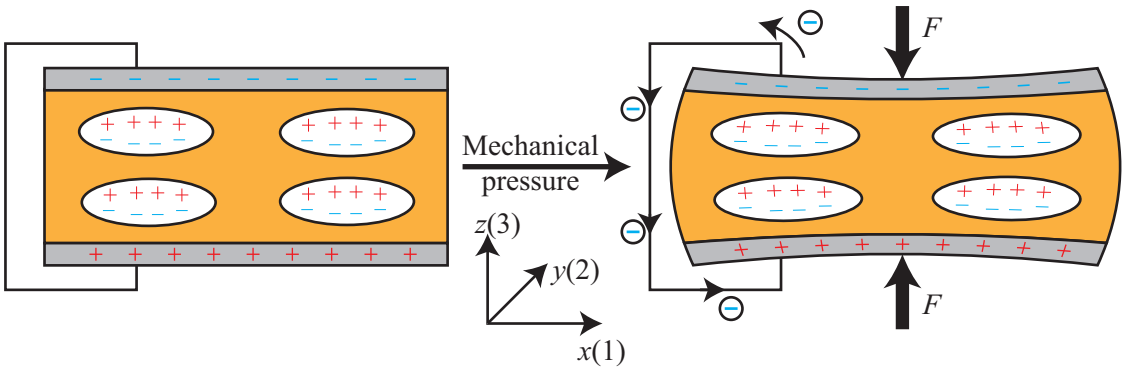

Figure 2.12: Charge flow in a ferroelectret upon mechanical stress resulting in thickness change [52].

If an electrically short-circuited ferroelectret is deformed under the influence of mechanical pressure, the pores are deformed and the micro-dipoles move closer to each other. To maintain the zero potential due to the short circuit, charges flow between the electrodes (Figure 2.12). This behaviour corresponds to the general definition of piezoelectricity in polymers shown theoretically and experimentally for electrets with ordered dipoles by Adams [60].

A model that illustrates the piezoelectric behaviour of ferroelectrets has been introduced by Hillenbrand and Sessler [52], [83] by simplifying the structure of a cellular film [Figures 2.13(a) and (c)] to plane parallel solid layers alternating polymer and air. This model was extended by considering the different layers as capacitors in series, where the polymer layer is a fixed capacitor and the air layer is a variable capacitor as shown in Figure 2.13(d) [44]. The latter approach is based on the assumption that the air layers are much softer than the polymer layers and experience therefore a much larger deformation upon mechanical stress.

For modeling the structure, it can be assumed that the cellular film consists of a total number N of solid layers, each layer with a thickness t_{1n}, and each two solid layers confine one air layer with a thickness t_{2m} as shown in Figure 2.13(c). A further assumption is that the air layers do not contain any volume charges and the solid

layers on both sides of each air layer feature an equal charge density of $\pm\sigma_m$ that includes all permanent charges. The same magnitude is assumed, since the charges should originate from discharges in the air gap during poling.

The relation of the E-fields in the solid layer, with a permittivity ε, and air layers, with a permittivity $\varepsilon_{\text{air}} = 1$, can be described by Gauss's law and Kirchhoff's second law for short circuit conditions as [83]

$$E_{1i} = -\left[\varepsilon_0 \left(t_1 + \varepsilon t_2\right)\right]^{-1} \sum_i t_2 \sigma_i, \tag{2.10}$$

$$E_{2i} = \frac{\sigma_1}{\varepsilon_0} - \left[\varepsilon_0 \left(t_1 + \varepsilon t_2\right)\right]^{-1} \varepsilon \sum_i t_{2i}, \sigma_i, \tag{2.11}$$

$$\text{with } t_1 = \sum_i t_{1i} \text{ and } t_2 = \sum_i t_{2i}. \tag{2.12}$$

Assuming the solid layers do not deform, it applies that $E_{1i} = E_1$. The charge σ_0 on the electrode can be expressed as [83]

$$\sigma_0 = -\varepsilon_0 \varepsilon E_1. \tag{2.13}$$

Under short circuit conditions, when a mechanical stress is applied on the ferroelectret causing mechanical deformation, the charge on the electrodes changes accordingly. Under the assumption that the thickness change occurs mainly due the compression of the air layers, and follow the equations (2.10) and (2.13), the charge change can be expressed as [83]

$$\frac{\partial \sigma_0}{\partial t_2} = \varepsilon \frac{t_i \sum_i t_{2i} \sigma_i}{t_2 \left(t_1 + \varepsilon\right)^2}, \text{ with } \frac{\partial \sigma_{2i}}{\partial t_2} = \frac{t_{2i}}{t_2}. \tag{2.14}$$

In a quasi-static case and assuming a linear elastic behaviour with Y being the Young's modulus of the ferroelectret, the stress-strain relation can be expressed as [83]

$$\frac{\Delta t_2}{t_1 + t_2} = \frac{\Delta T}{Y}, \tag{2.15}$$

where T denotes the mechanical stress and t_1 and t_2 are the total thickness of the solid layers and air layers, respectively. Based on equations (2.14) and (2.15), the piezoelectric charge constant d_{33} can be expressed as [83]

$$d_{33} = \frac{\Delta \sigma_0}{\Delta T} = \frac{\varepsilon \left(t_1 + t_2\right)}{Y} \frac{t_i \sum_i t_{2i} \sigma_i}{t_2 \left(t_1 + \varepsilon t_2\right)^2}. \tag{2.16}$$

The piezoelectric response can be described in open circuit conditions as well, by assuming that the electrode charge σ_0 and consequently E_1 and E_{2i} remain constant upon mechanical deformation. Thus, a thickness change induces a voltage ΔV that can be described as [83]

$$\Delta V = \sum_i \Delta t_{2i} E_{2i}, \tag{2.17}$$

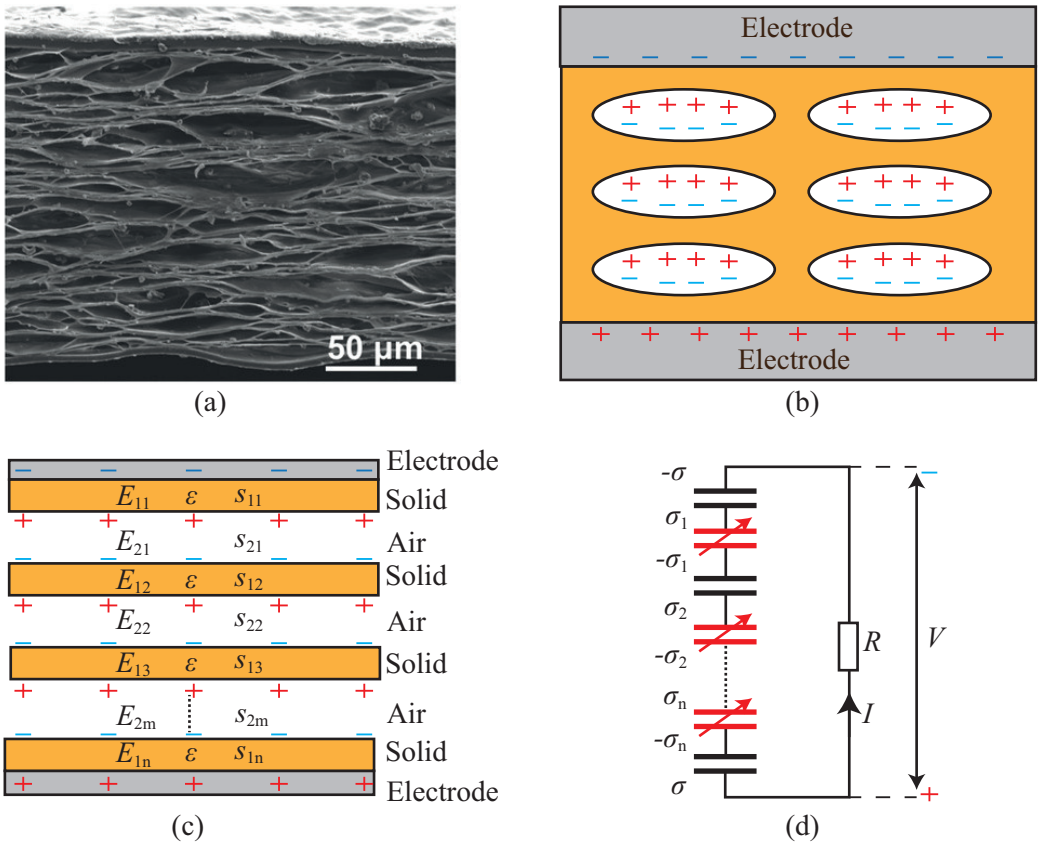

Figure 2.13: . (a) Cross-sectional SEM image of cellular polypropylene [44]. (b) Schematic illustration that simplifies the cellular structure and based, on which the equivalent parallel plane structure (c) and equivalent circuit model (d) are based [44], [83].

which corresponds to an electric field ΔE as [83]

$$\Delta E = -\frac{1}{t_1 + t_2} \sum_i \Delta t_{2i} E_{2i}. \tag{2.18}$$

The piezoelectric voltage coefficient g_{33} can be calculated as [83]

$$g_{33} = \frac{\Delta E}{\Delta T} = \frac{1}{\varepsilon_0 Y} \frac{t_i \sum_i t_{2i}\sigma_i}{t_2(t_1 + \varepsilon t_2)}, \text{ with } t_i = t_{1i} + t_{2i}. \tag{2.19}$$

Both piezoelectric d and g coefficients are considered to be equivalent piezoelectric coefficients to those of linear materials such as ceramics. In this context, the polymers being generally non linear materials, their Young's modulus can be considered nearly linear only for small stresses and strains. Furthermore, the piezoelectric coefficients being directly dependent on the Young's modulus, can not be assumed to be constant coefficients as normally done for conventional piezoelectric ceramics.

Due to the lightweight, flexibility and fascinating sensitivity as well as the obvious improvement potential, ferroelectrets have been intensively investigated and tailored for several applications such as energy harvesting,

human-machine interactions, human healthcare and human motion detection. In the following, few ferroelecret applications are discussed.

2.5.3 Application fields of ferroelectrets

A very attractive application field for flexible and very sensitive ferroelectrets is vibration based energy harvesting. In vibrational energy harvesting, piezoelectric transducers utilizing the direct piezoelectric effect have been investigated for the last 25 years, where piezoceramics such as PZT have been the dominating materials [10]–[14]. After the classification of lead as a toxic material, the restrictions to its use have been increased. This, in turn, offered the opportunity for research of new lead-free materials such as ferroelectric polymers represented dominantly by PVDF and its copolymers [15], [16], [102]. Energy harvesting with ferroelectrets was first described in 2012 by Anton [103]. The first device consisted essentially of a PP ferroelectret film with electrodes on both sides and topped with a seismic mass. When put on a vibrating substrate, power is generated through a load resistance between the two electrodes due to the longitudinal piezoelectric effect of the ferroelectret. The early ferroelectret based energy harvesting devices delivered small output powers, typically in the range of several µW with a seismic mass of one kilogram and load resistances in the MΩ range. To improve the performance of the harvesters, new and better ferroelectrets were investigated. Pondrom et al. investigated an energy harvester by stacking layers of enhanced PP films. The used PP film features a piezoelectric d_{33}-coefficient of approximately 600 pC N^{-1} [41]. A harvester consisting of nine layers reached an output power of 5 µW with a seismic mass of 8 g. Even though the seismic mass is significantly reduced compared to prior ferroelectret energy harvesters, the output power is still small. Later, Zhang et al. introduced ferroelectrets based on radiation-crosslinked polypropylene (IXPP) [104] that resulted in an output power of 120 µW by using a seismic mass of approximately 34 g. Due to the poor thermal stability of PP ferroelectrets, ferroelectrets based on FEP have been improved and used for energy harvesting. By introducing the third class of ferroelectrets (see section 2.5.1), new possibilities for energy harvesting were made possible, which are based on the transverse piezoelectric effect. Thereby, output power exceeding 200 µW was achieved [47], [105].

A further source of mechanical energy is human body movement. In fact, it was shown that the human body is an enormous energy reservoir that generates over 100 W during normal daily activities such as breathing and walking [107]. Only 5 % of this power would be sufficient to cover the energy to supply most portable electronics [108]. The mechanical energy available in a human body that can be harvested with ferroelectrets is either with high amplitude at low frequency such as walking or low amplitude with relatively high frequency such as physiological signals. Investigating the latter type of mechanical energy in the human body opened a new application field, which is human healthcare monitoring. For this application as well, PP was very popular and was used to detect several physiological signals such as coughing action, arterial pulses [25] and active voiceprint to realize voiceprint recognition [109]. Since a higher sensitivity is required, more artificial ferroelectret systems have been developed. Chen et al. demonstrated a heartbeat and respiration monitoring system based on a flexible hollow micro-structured ethylene-vinyl acetate (EVA) and FEP films [110]. Wang et al. used a sandwich consisting of two structured FEP/e-PTFE films which confine an FEP film [111] to monitor wrist motion, facial muscle contraction, eye blinking, and breathing. The reached piezoelectric d_{33}-coefficient was approximately 7380 pC N^{-1}, which is far above conventional piezoelectric polymers.

Ferroelectrets are also used as tactile sensors for human machine interaction. By using PP in combination with a paper substrate and 2D grid-printed electrodes, it was possible to locate the touch point and record the pressure information in real time [112]. Furthermore, and again using PP, a self-powered 30-key keyboard was developed [113]. The hybrid systems are also present in the development of pressure sensors since they

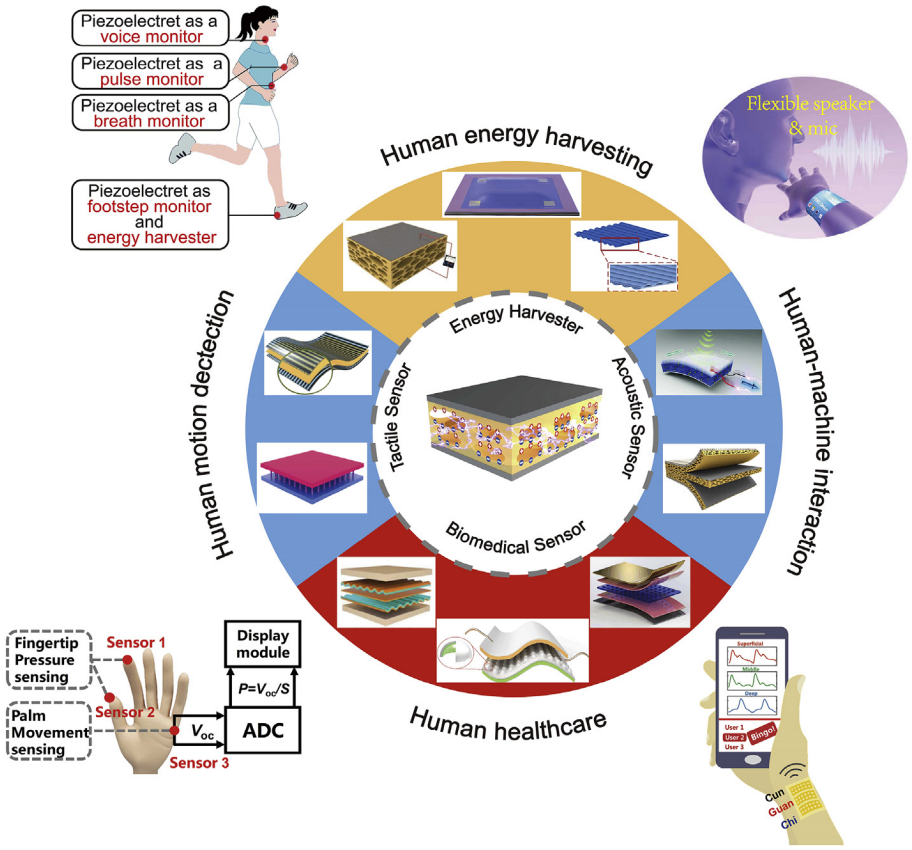

Figure 2.14: Application fields of ferroelectrets including some ferroelectret structures [106].

offer further design freedom. It was shown that the combination of materials that store different polarity of charges is a great approach to increase the stability of ferroelectrets. Li et al. suggested an interesting combination using tetrafluoroethylene–hexafluoropropylene–vinylide (THV) and COC to build the electric part of the ferroelectret, while using polydimethylsiloxane (PDMS) to enhance the mechanical stability [114]. The choice of THV and COC can be explained by the fact, that THV is known for its good positive charges storage ability, while COC stores negative charges. In addition to the linear behaviour of the tactile sensor up to 150 kPa, this ferroelectret showed a sensitivity of 30 mV kPa^{-1}, which is 10 times larger that of PP. The application field of ferroelectrets has been very wide showing a great potential of these flexible piezoelectric materials. However, several enhancements of ferroelectrets have to be made in order to make them usable in practicable applications as sensors and energy harvesters. The introduced energy harvesters in literature reached an output power in the range of several microwatt, which is not sufficient for supplying most of electronic devices when considering the losses caused by energy management circuits. On the other hand, while developing the sensors, only the sensitivity was in focus without taking into account other important properties such as the response range, mechanical stability, and linearity. Furthermore, the significant signal interference with the ferroelectret sensors in combination with wearable electronics and data processing has been hardly addressed. Additional aspects that need further improvement are the fabrication processes, that are currently not suitable for mass production. Furthermore, the long-term stability of ferroelectrets and their reliability under real life conditions such as high work intensity and harsh environment have to be addressed. Hereby, a better understanding of the storage mechanism has to be given more attention while investigating further dielectric materials regarding their application as ferroelectrets, that are environmentally friendlier.

3 Ferroelectrets for energy harvesting

The following chapter was published in [48]–[50], [115], [116].

The new communication technologies such as the internet standard 5G and IoT will influence almost all aspects of daily life. The dramatic increase of connected widely distributed devices creates new challenges regarding their energy supply. Even though conventional batteries can be used as energy source, their replacement in several applications located in remote areas or in harsh environments is inconvenient and expensive. In order to supply these electronic devices with energy in places where electric power is not readily available, energy harvesting systems have become a steadily growing alternative (Figure 3.1). Energy harvesting is defined as the extraction of electrical energy from ambient sources such as heat, vibration or air currents for low power consumption devices.

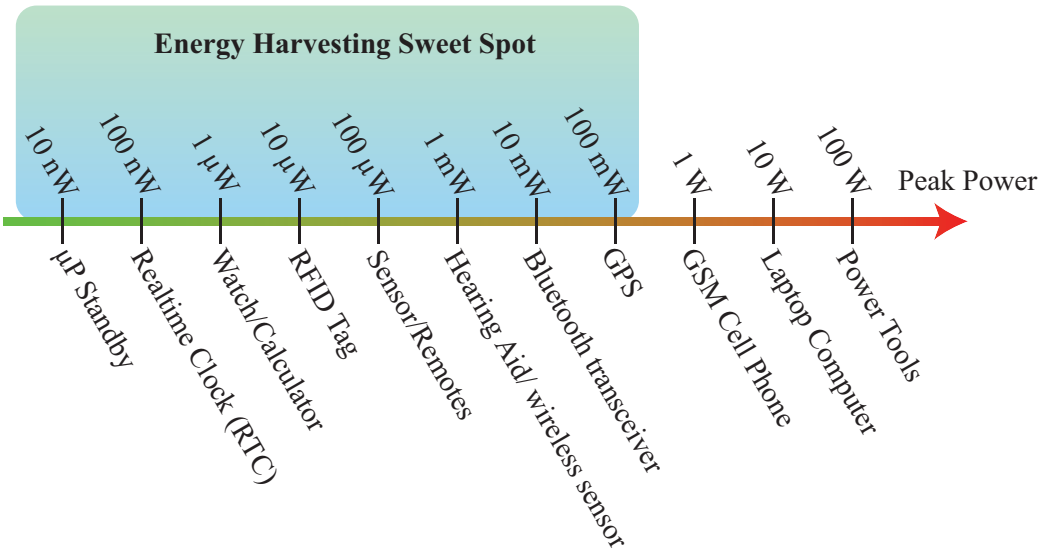

Figure 3.1: Energy harvesting application possibilities for various electronic devices based on their power consumption [117].

Vibration-based energy harvesting, as the name suggests, is a method of energy harvesting from mechanical sources, which consists of converting energy from vibrating mechanical sources into electrical energy. Three main transduction mechanisms are suitable for this purpose, which are electro-magnetic, electrostatic and piezoelectric transducers.

Electromagnetic energy harvesters usually consist of a permanent magnet oscillating near a coil by means of a spring [118], [119]. The relative motion between the magnet and the coil generates a voltage accros the coil, according to Faraday's law of induction. This type of energy harvester is particularly well suited for low

frequencies below 20 Hz [120]. The main disadvantages of electromagnetic harvesters are their relatively large volume and the difficulty of miniaturizing them [118].

Electrostatic energy harvesting corresponds to the use of a capacitor arrangement that changes its capacity when set into vibration. The two main arrangements used for this purpose are often referred to as ”in-plane” and ”out-of-plane” methods. In the ”in-plane” method, the capacitance change occurs by changing the overlap area of the condenser plates while maintaining a constant air gap thickness [121]–[124], while in the ”out-of-plane” method, the air gap thickness is dynamically changed and the overlap of the electrodes remains constant [125], [126]. The main disadvantage of the first electrostatic energy harvesters was the required DC voltage between the electrodes, which was modulated by the modification of the geometry of the capacitor due to vibration. This problem was solved by using an electret attached to a capacitor plate [125].

Piezoelectric energy harvesters, as mentioned in the introduction, are generally based on piezoelectric materials such as the ceramics barium titanate (BT) and PZT as well as PVDF [11], [127]–[130]. In many of these harvesters, the piezoelectric material is deformed using a seismic mass or through bending devices equipped with a seismic mass. Energy harvesting based on ferroelectrets as active materials, belongs into the categories of electrostatic or piezoelectric harvesting devices, since ferroelectrets are basically electrets. Although energy harvesting devices have been investigated and even commercialized, more efficient solutions are required. In the following, the development of ferroelectret based energy harvesters is discussed. Thereby, the very recent developed ferroelectrets: tubular-array [39] and parallel-tunnel structures [105] are optimized and characterized for better exploiting their potential.

3.1 Ferroelectrets based on FEP tubes: tubular-array ferroelectrets

The main disadvantage of the hybrid systems is a strong lateral inhomogeneity of the piezoelectric d_{33} coefficient. Obviously, the high piezoelectricity is derived only from highly compressible porous areas of arrays while binding zones show no piezoelectric effect at all. Therefore, to maximize the overall piezoelectric response, it is important to design a structure with high ratio between the active and non-active areas. In this context, a promising structure consisting of tubular commercial fluoroethylenepropylene is presented by Zhukov et al. [39], [131]. It reached a piezoelectric d_{33} coefficient of 60 pC N^{-1} and 160 pC N^{-1} when using a wall thickness of 120 µm and 50 µm, respectively. It is obvious that the piezoelectric response of such ferroelectrets is influenced by the interplay of dielectric, electrical and mechanical properties.

In a previous work [132], the mechanical properties of the tubular-array configuration have been determined and the needed material parameters in COMSOL Multiphysics have been defined. Based on these results, a generalized model for predicting the piezoelectric behaviour of the tubular-array ferroelectrets is introduced. In the following, a brief introduction regarding the preparation of such ferroelectrets as well as the steps for the finite element analysis (FEA) modeling towards a targeted optimization of the tubular-array ferroelectrets is presented.

3.1.1 Preparation of the tubular-array ferroelectrets

For manufacturing the tubular-array ferroelectrets, 7 cm long FEP tubes from ZEUS ltd (USA) with a diameter of 1 mm are mounted on a structured frame and compressed between two hotplates. The FEP tubes are deformed such that they are in lateral physical contact with each other. Through heating up to 270 °C for approximately 10 min, the contact surfaces of the tubes melt into each other to form the tubular-array

ferroelectrets. The thickness of the resulting array is controlled by inserting spacers with a defined thickness between the two hotplates. After cooling the structure to room temperature, the sample is metallized on both sides by sputtering a uniform silver electrode using K950X turbo evaporator (EMITECH Group, Montigny-le-Bretonneux, France). The sample is then clamped between two electrodes and polarized with contact charging at 6 kV using a high voltage power supply (HCN 35-6 500, FuG Elektronik, Schechen, Germany). The preparation steps are summarized in Figure 3.2

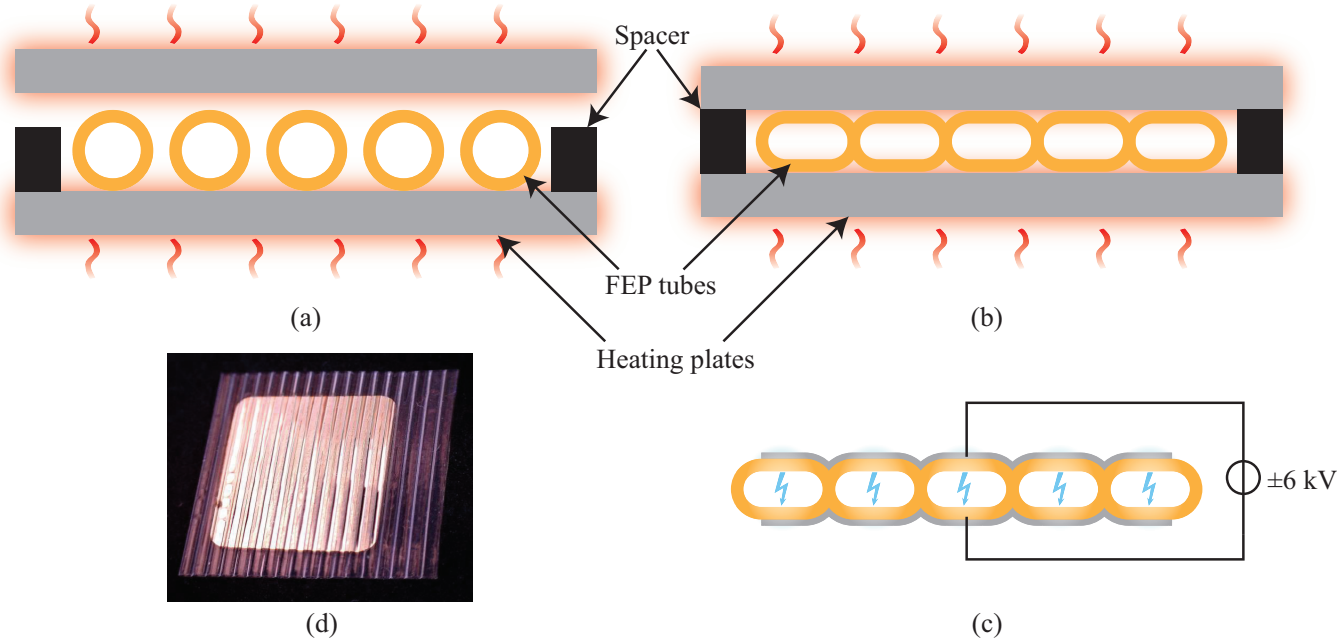

Figure 3.2: Schematic illustration of the preparation steps of a tubular-array from FEP tubes: (a) arrangement of the FEP tubes on the heating plate, (b) compression of FEP tubes to build a stadium-like shape structure, (c) charging process of the structure after metallizing its two sides and (d) a photograph of the tubular-array ferroelectret.

Zhukov et al. [131] demonstrated an approach to analytically predict the piezoelectric d_{33} response of the tubular-array ferroelectrets, by simplifying the geometry as a sandwich consisting of one air layer with a thickness t_2 sandwiched between two equally thick solid FEP layers with a thickness t_1. For a known Young's modulus Y_{total} of the whole device, the piezoelectric d_{33} can be calculated as [131]

$$d_{33} = \frac{\varepsilon_0 \varepsilon_1 \Delta E_1}{Y_{\text{total}} \cdot \left(\frac{\Delta t_2}{2t_1 + t_2}\right)}, \tag{3.1}$$

where E_1 is the electric field in the FEP wall. When an external force F is applied to the structure, the thickness of the air layer as well as the electric field E_1 change and can be described as [131]

$$\frac{\Delta E_1}{\Delta t_2} = \frac{\varepsilon_0 \varepsilon_2 \frac{2t_1}{t_2^2} \sigma_{\text{int}}}{\left(\varepsilon_0 \varepsilon_1 + \varepsilon_0 \varepsilon_2 \frac{2t_1}{t_2}\right)^2}, \tag{3.2}$$

where σ_{int} is the trapped charge density at the air/FEP interfaces after the charging process. Since the assumed sandwich structure differs from the real structure, a correction factor α was required. Considering

the equations 3.2 and 3.1 as well as the geometrical correction factor α, the d_{33} coefficient can be expressed as [131]

$$d_{33} = \alpha \cdot \frac{\varepsilon_1 \varepsilon_2 \sigma_{\text{int}}}{Y_{\text{total}}} \cdot \frac{1 + \left(\frac{t_2}{2t_1}\right)}{\left[\varepsilon_2 + \varepsilon_1 \left(\frac{t_2}{2t_1}\right)\right]^2}. \tag{3.3}$$

From equation 3.3, it becomes obvious that the piezoelectric d_{33} coefficient of ferroelectrets with artificial voids is directly proportional to the amount of trapped charges σ_{int} and inversely proportional to the Young's modulus Y_{total} of the whole structure. The ability of trapping charges is mainly defined by the electret material. On the other hand the Young's modulus of such structures depends not only on the used material but also on the geometry of the voids. The analytical model is only useful if the elastic modulus is known and the geometry is very similar to the assumed one. A better optimization of the tubular-array ferroelectret can be attained, when the Young's modulus itself can be predicted based on the geometry of the tunnels. This can be achieved by using FEA. For modeling the structure of the ferroelectrets, the resulting stadium-like shape is approximated as shown in Figure 3.3.

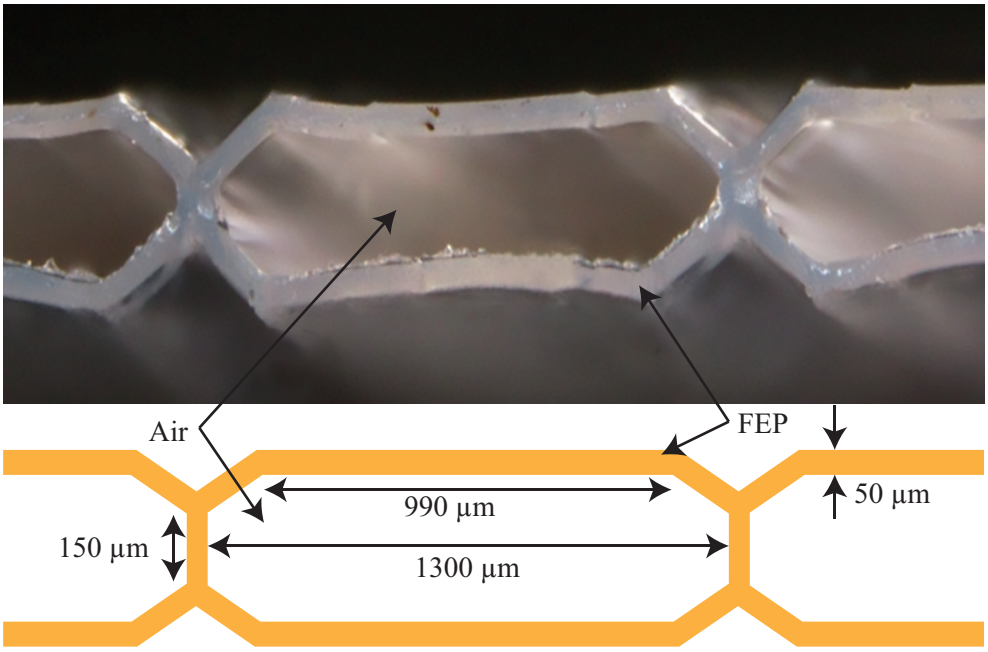

Figure 3.3: Comparison of the structure geometry corresponding to one of the measured samples with the geometry simulated. The modeled structure geometry in COMSOL Multiphysics features a 50 µm thick FEP layer, which reproduces the manufactured geometry [115].

3.1.2 Modeling of the electrical properties of tubular-array ferroelectrets

The piezoelectricity of the tubular-array specifically and ferroelectrets generally is due to the dipoles created by the poling process. During polarization, charges generated by Paschen breackdown move toward the polymer/air interfaces where they remain trapped. For modeling the ferroelectrets as charged entities, the trapped charges can be defined as an remanent charge density σ_{int} at the inner FEP/air interfaces or as

permanent polarization of the air volume. In this work, the software COMSOL Multiphysics is used. For defining the charging hysteresis caused by the remanent polarization, the AC/DC module is required. On the other hand, the definition of σ_{int} does not necessitate any additional modules to the electrostatics interface. Therefore, the focus will be on how to determine σ_{int}.

According to previous work on charging properties of ferroelectrets [95], the charging of the structure begins when the poling voltage reaches the breakdown voltage V_B. For devices consisting of two parallel solid blocking layers with a thickness t_1 and permittivity ε_1 separated by a t_2 thick porous layer with permittivity ε_2, the breakdown voltage V_{B} can be determined as [95]

$$V_{\text{B}} = E_{\text{B}} \left(t_2 + \frac{2\varepsilon_2 t_1}{\varepsilon_1} \right), \tag{3.4}$$

where E_{B} is the breakdown electric field. An increase in poling voltage across the entire sandwich results in the build-up of an electric field across the sample with an electric field strength E_1 in the solid layers and E_2 in porous layer. When E_2 reaches the threshold value E_{B}, a build-up of an interface charge density σ_{int} starts, which can be described as [35]

$$\sigma_{\text{int}}(V) = \begin{cases} 0 & V \leq V_{\text{B}} \\ \varepsilon_0 \left[\frac{\varepsilon_1}{2t_1} V - \left(\varepsilon_2 + \frac{\varepsilon_1 t_2}{2t_1} \right) E_{\text{B}} \right] & V \geq V_{\text{B}} \end{cases}. \tag{3.5}$$

The maximum remanent interface charge $\sigma_{\text{int}}^{\text{max}}$ that can be reached after short circuiting the ferroelectret, however, corresponds to a poling voltage $V \geq 2V_{\text{B}}$ and according to equations (3.5) and (3.4) can be described as

$$\sigma_{\text{int}}^{\text{max}} = E_B \left(\varepsilon_0 \varepsilon_2 + \varepsilon_0 \varepsilon_1 \frac{t_2}{2t_1} \right). \tag{3.6}$$

Further increase of the poling voltage does not result in higher remanent polarization because of the back-switching during short−circuiting of the sample [95].

In the case of tubular-array ferroelectrets, the two solid layers are represented by the FEP walls of the tubes with a thickness t_{FEP} and a permittivity ε_{FEP}, and the porous layer is replaced by an air gap t_{air} featuring a permittivity ε_{air}.

The remanent interface charge σ_{int} in turn induces a surface charge density σ_0 on the surface of the electrode, which can be determined by analyzing the electric displacement field at the boundary FEP/air using Gauss' law as

$$\int_{\partial V} \vec{D} \cdot \mathrm{d}\vec{A} = (\vec{D_{\text{FEP}}} \cdot \vec{n_1} + \vec{D_{\text{air}}} \cdot \vec{n_2}) \cdot \mathrm{d}A \tag{3.7}$$

$$D_{\text{FEP}} - D_{\text{air}} = \sigma_{\text{int}}. \tag{3.8}$$

This equation (3.8) can be rewritten as a function of the electric fields in air and FEP layers in one FEP/air boundary layer as

$$\varepsilon_0 \varepsilon_{\text{FEP}} E_{\text{FEP}} - \varepsilon_0 \varepsilon_{\text{air}} E_{\text{air}} = \sigma_{\text{int}}. \tag{3.9}$$

Using Kirchhoff's second law under short-circuit conditions, the electric fields in the structure are obtained as [35], [52]

$$\begin{aligned} t_{\text{FEP}} E_{\text{FEP}} + t_{\text{air}} E_{\text{air}} + t_{\text{FEP}} E_{\text{FEP}} = 0 \\ 2t_{\text{FEP}} E_{\text{FEP}} + t_{\text{air}} E_{\text{air}} = 0. \end{aligned} \tag{3.10}$$

From equations (3.9) and (3.10) the remanent charge density can be expressed as

$$\sigma_{\text{int}} = \varepsilon_0 \varepsilon_{\text{FEP}} E_{\text{FEP}} + \varepsilon_0 \varepsilon_{\text{air}} \cdot \frac{2t_{\text{FEP}} E_{\text{FEP}}}{t_{\text{air}}}. \tag{3.11}$$

The electric field in the FEP layers E_{FEP} can be expressed as

$$E_{\text{FEP}} = \frac{\sigma_{\text{int}}}{\varepsilon_0 \varepsilon_{\text{FEP}} + 2\varepsilon_0 \varepsilon_{\text{air}} \frac{t_{\text{FEP}}}{t_{\text{air}}}} = \frac{t_{\text{air}}}{\varepsilon_0 \varepsilon_{\text{FEP}} t_{\text{air}} + 2\varepsilon_0 \varepsilon_{\text{air}} t_{\text{FEP}}} \sigma_{\text{int}}. \tag{3.12}$$

On the metallized side of FEP (external surface), the surface charge density can be calculated as

$$\begin{aligned} Q = \int_A \sigma_0 \mathrm{d}A = \int_A \varepsilon_0 \varepsilon_{\text{FEP}} E_{\text{FEP}} \mathrm{d}A \\ => \sigma_0 = \varepsilon_0 \varepsilon_{\text{FEP}} E_{\text{FEP}}. \end{aligned} \tag{3.13}$$

Thus, the electrode's charge density σ_0 can be expressed in function of σ_{int} and by using equations (3.12) and (3.13) as

$$\sigma_0 = \frac{t_{\text{air}} \varepsilon_{\text{FEP}}}{\varepsilon_{\text{FEP}} t_{\text{air}} + 2\varepsilon_{\text{air}} t_{\text{FEP}}} \sigma_{\text{int}}. \tag{3.14}$$

Hence, it is necessary to chose a boundary condition that solves the continuity between different media with Gauss's law, when a remanent surface charge is defined between them. In COMSOL Multiphysics, the relevant physics interface condition for this case is expressed as [133]

$$n.(D_1 - D_2) = \rho, \tag{3.15}$$

when a volume charge density ρ is available. Otherwise the continuity between different media is fulfilled by the natural boundary condition as [133]

$$n.(D_1 - D_2) = n \cdot [(\varepsilon_0 \nabla V - P)_1 - (\varepsilon_0 \nabla V - P)_2] = 0, \tag{3.16}$$

where P denotes the polarization. The induced charge on the electrodes can be calculated using a terminal, which solves

$$\sigma_0 = \frac{Q}{A} = \frac{1}{A} \cdot \int_A D \cdot \mathrm{d}A, \tag{3.17}$$

where A is the electrode area, Q the electric charge and D is the electric displacement field induced from the remanent charge density σ_{int}. The utilized boundary conditions and the simulated geometry are shown in Figure 3.4.

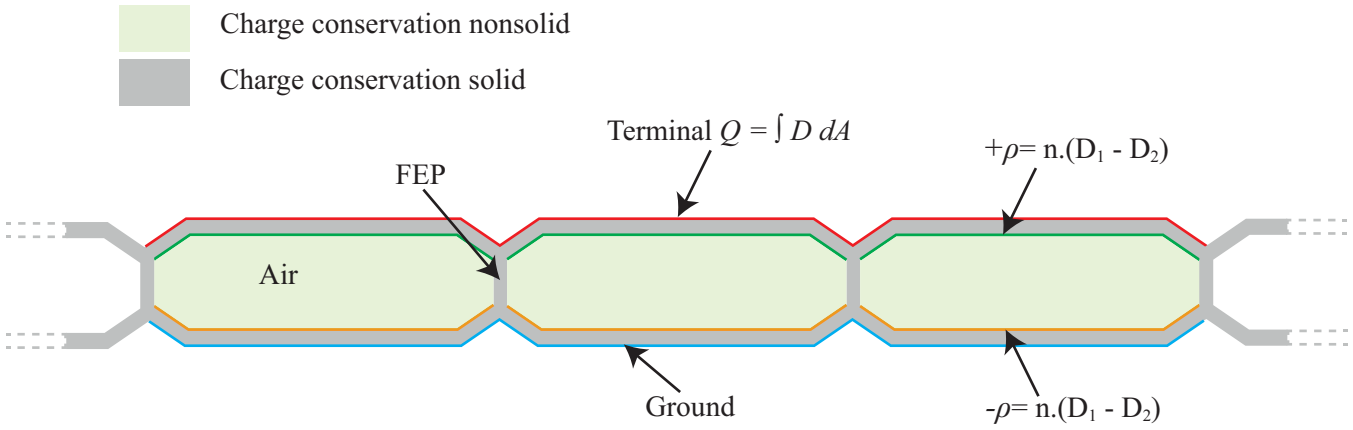

Figure 3.4: Boundary conditions and material definition in COMSOL Multiphysics for simulating the electrostatic property of a ferroelectret using the surface charge density [115].

For a proper approximation of the surface charge density σ_{int}, the induced charge density σ_0 on the electrodes has to be measured. Afterwards, the remanent surface charge density σ_{int} can be approximated using equation (3.14).

A well known measurement method for measuring the surface charge σ_0 is the Sawyer-Tower-Method (ST) [134]. The main idea of the ST circuit is to connect a capacitor in series with the sample to be measured, resulting in a voltage divider. To ensure that the high voltage applied to the circuit is almost completely kept on the sample, the additional capacitor has to exhibit a much larger capacitance than the sample. The amount of displacement charge, however, should be the same due to continuity reasons in a series connection. For the experiment a modified ST circuit is used [135]. Hereby, two additional capacitors are connected in series with the sample featuring a capacitance C_{samp} [Figure 3.5(a)]. The first capacitor C_1 of 3 nF is a HV-capacitor that protects the electrometer in case of electrical breakdown in the sample. The second capacitor C_{m} is a large standard capacitor of 1 µF which builds a voltage divider with C_1 making the voltage across the capacitor

C_m easy to measure. An AC triangular voltage V_in with a frequency of 1 Hz was applied by a high voltage amplifier (Trek, Model 20/20C) controlled by an arbitrary waveform generator, which results in voltages V_1, V_samp and V_out across the capacitor C_1, the sample C_samp and capacitor C_m, respectively as

$$
\begin{aligned}
V_\mathrm{in} &= V_\mathrm{samp} + V_1 + V_\mathrm{out} \qquad (3.18)\\
\text{with } V_\mathrm{samp} &= \frac{C_1 C_\mathrm{m}}{C_1 C_\mathrm{m} + C_\mathrm{samp} C_\mathrm{m} + C_\mathrm{samp} C_1} V_\mathrm{in},\\
V_1 &= \frac{C_\mathrm{samp} C_\mathrm{m}}{C_1 C_\mathrm{m} + C_\mathrm{samp} C_\mathrm{m} + C_\mathrm{samp} C_1} V_\mathrm{in},\\
V_\mathrm{out} &= \frac{C_1 C_\mathrm{samp}}{C_1 C_\mathrm{m} + C_\mathrm{samp} C_1 + C_\mathrm{samp} C_1} V_\mathrm{in}.
\end{aligned}
$$

Since the sample capacitance is in the range between 4 pC and 8 pC, it is valid to assume that $C_\mathrm{m} \gg C_1 \gg C_\mathrm{samp}$ and thus $V_\mathrm{samp} \gg V_1 \gg V_\mathrm{out}$. Therefore, the voltage across the sample V_samp can be considered equal to the input voltage V_in. The hysteresis curves of the ferroelectrets are measured in a charge-voltage mode. In this mode, the charge flowing through the sample during charging is determined from the voltage change across C_m. The measured charge Q can be obtained by the product of standard capacitance and voltage change as

$$Q = C_\mathrm{m} \cdot V_\mathrm{out}. \qquad (3.19)$$

Since the input resistance of the electrometer $R_\mathrm{m} > 10\,\mathrm{G}$ results in a time constant $\tau = R_\mathrm{m} C_\mathrm{m} \gg 1\,\mathrm{s}$, the voltage accross the measurement capacitance is assumed to be without decay during the total measurement time.

The total charge Q in the circuit consists of the charge obtained through the electric field across the sample E_samp and the polarization of the sample P. It should be noted that the polarized sections of the tubular-array ferroelectret correspond to the air voids between two FEP layers resulting in an overall thickness of $2 \times t_\mathrm{FEP}$ and t_air. The polarization can be calculated from the current of the circuit i as

$$
\begin{aligned}
Q(t) &= \int_0^t i \,\mathrm{d}t = C_\mathrm{samp} V_\mathrm{samp}(t) + AP(T) \qquad (3.20)\\
\rightarrow P &= \frac{Q(t) - C_\mathrm{samp} V_\mathrm{samp}}{A} = \frac{C_\mathrm{m} V_\mathrm{out}(t) - C_\mathrm{samp} V_\mathrm{in}(t)}{A}, \qquad (3.21)
\end{aligned}
$$

where A is the metallized surface area of the sample.

The geometric capacity of each tubular-array sample was measured separately with an LCR Meter (HP Model 4332A). The geometric capacitance of all samples vary between 8 pC and 12 pC. The surface of the electrode is approximately $2.25\,\mathrm{cm} \times 2.25\,\mathrm{cm}$.

Before the measurement, the prepared samples are tested regarding their maximum poling voltage to prevent a possible electric breakdown which can damage the measurement setup. Since most samples could withstand a voltage of 3.5 kV, this value was used as the maximum amplitude of the supply voltage.

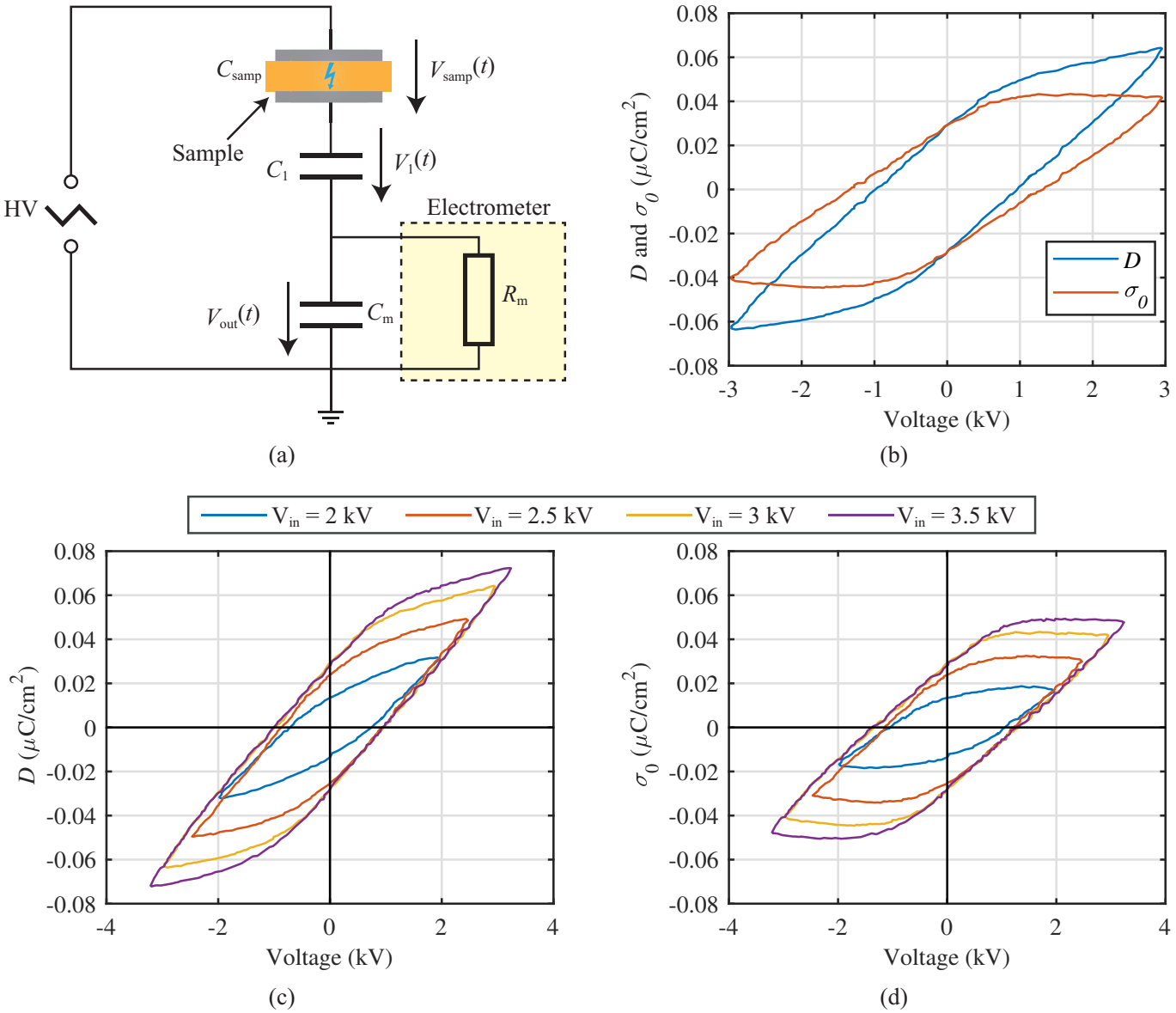

Figure 3.5: Measurement of the surface charge density on the electrodes of the sample: (a) Schematic view of the Sawyer-Tower circuit, (b) measured D and calculated σ_0 as a function of the applied peak voltage of ± 3 kV for a 400 µm thick array fabricated from tubes of 50 µm thick walls, (c) hysteresis loops of D recorded for different maximum voltages for the same specimen and (d) the calculated σ_0 from D.

The measured hysteresis loop of the FEP tubular-arrays exhibits a parallelogram-like shape similar to the polarization hysteresis of open-porous fluoropolymer sandwiches [98]. Therefore, calculating the remanent surface charge density σ_{int} at the FEP/air walls using equation (3.14) is reasonable, yet not accurate.

The loops for the selected tubular-array ferroelectrets have the same slope parameter and the same width equal to the experimental $2\times V_B$ of approximately 2.2 kV and amplitudes proportional to the peak voltage. However, the measured hysteresis curves show a deviation from ideal parallelograms, which can be explained by the differences in the geometry of the air channels, which, in reality, deviates from a rectangular shape

(Figure 3.6). The breakdown voltage V_B as well as the maximum polarization differ from the theoretical values as can be seen in Figure 3.6. It is important to note that the theoretically possible maximum polarization was not achieved.

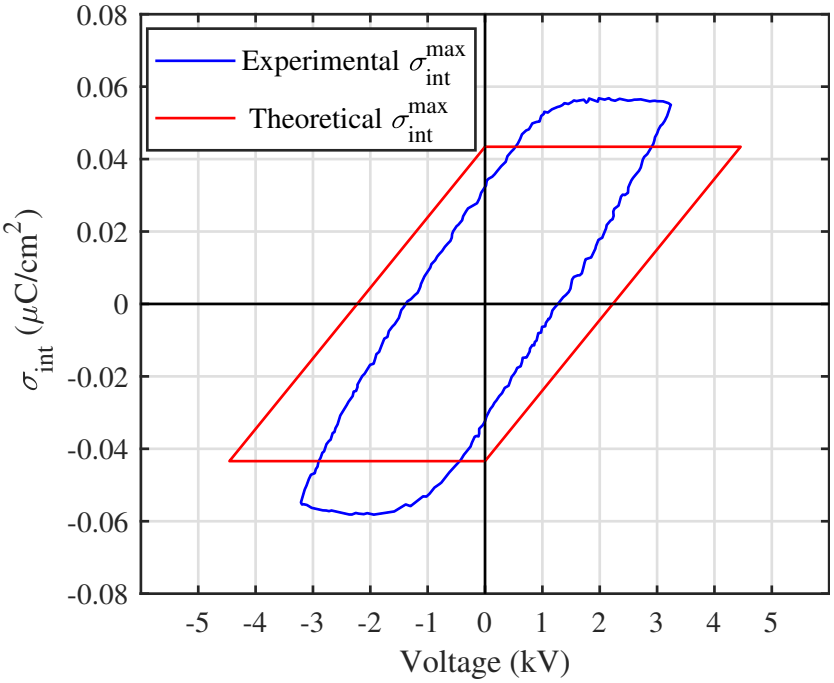

Figure 3.6: Theoretical and experimental hysteresis loops for σ_{int}^{max} for a 400 µm thick array fabricated from tubes of 50 µm thick walls.

Therefore, for the validation of the FEA model, an remanent charge density σ_{int} between 0.03 µC cm^{-2} and 0.04 µC cm^{-2} is selected and the induced surface charge density σ_0 on the electrodes is simulated. The numerical calculations using the aforementioned boundary conditions (Figure 3.4), result in a surface charge density $0.019\,\mu C\,cm^{-2} < \sigma_0 < 0.029\,\mu C\,cm^{-2}$, which is in agreement with the measured values.

The modification of the induced charge on the surface due to mechanical deformation can be determined using the same boundary conditions for the electrical model in combination with the mechanical model.

3.1.3 Modeling of the piezoelectric properties of tubular-array ferroelectrets

In order to simulate the piezoelectric properties of the tubular-array, the ”Electromechanics” interface of COMSOL Multiphysics is chosen. This combines the features of an ”Electrostatics” interface and a ”moving mesh” interface with those of a ”Solid Mechanics” interface. Hereby, the available mechanical model of a previous work can be used with the electrical model.

The measurement of the piezoelectric d_{33} coefficient using the quasistatic-method [136] requires placing a mass on the ferroelectret. A similar scenario is implemented for simulating the piezoelectric response of the ferroelectret, where the tubular-array-structure is placed between two plates. The bottom plate is fixed while the upper plate moves along the thickness direction (y-axis) and applies a force to the ferroelectret. The resulting large deformation of the structure requires the FEP layer to be defined as hyperelastic material. Hereby, the neo-Hookean model is selected and the FEP layers are assumed to be compressible. The material

definition requires defining the Lamé parameters for a parameterization of the elastic moduli for the FEP layer, which can be determined as [137]

$$\lambda = \frac{\nu Y}{(1+\nu)(1-2\nu)}, \tag{3.22}$$

$$\mu = \frac{Y}{2(1+\nu)}, \tag{3.23}$$

where λ is the first Lamé parameter, μ the second, ν Poisson's ratio and Y Young's modulus. The required FEP-layer parameters for the simulated scenario are $Y = 350\,\text{MPa}$, the density $\rho = 2150\,\text{kg}\,\text{m}^{-3}$, $\nu = 0.48$, $\lambda = 2.8378 \cdot 10^9\,\text{N}\,\text{m}^{-2}$ and $\mu = 1.1824 \cdot 10^8\,\text{N}\,\text{m}^{-2}$.

According to COMSOL Multiphysics [133], the large deformation of hyperelastic materials involves the calculation of several stresses: the Cauchy stress σ_{cauch}, which is the force per deformed area in a given direction (not following the body), the first Piola-Kirchhoff stress $P_{\text{p-k}}$, which is an unsymmetrical two-point tensor, the second Piola-Kirchhoff stress $S_{\text{p-k}}$, which is a symmetric tensor for small strains similar to the Cauchy stress tensor (in direction following the body). For a given force F, these stresses can be calculated from each other as [133]

$$S_{\text{p-k}} = F^{-1} P_{\text{p-k}} \tag{3.24}$$

$$\sigma_{\text{cauch}} = J_F^{-1} P_{\text{p-k}} F^{\text{T}} = J_F^{-1} F S_{\text{p-k}} F^{\text{T}} \tag{3.25}$$

$$\text{with } J_F = \det F.$$

The neo-hookean model solves the equation of the strain energy density W_{strain} for compressible materials as [138]

$$W_{\text{strain}} = \frac{1}{2}\mu\,(I_1 - 3) - \mu \ln(J_{\text{el}}) + \frac{1}{2}\lambda\,[\ln(J_{\text{el}})]^2\,, \tag{3.26}$$

where J_{el} is the elastic volume ratio and $I_1\,(C_{\text{el}})$ the first invariant of the elastic right Cauchy-Green deformation tensor.

In order to prevent the upper moving plate from penetrating the ferroelectret in the simulation, the surfaces that need to come into contact are defined as contact pair. The contact pressure method is defined using augmented Lagrangian method for better accuracy. Hereby, the penalty factor is calculated using the in-built preset option for stability.

The air within the tunnels is defined as deforming mesh, since the tunnels are open and, thus, present a domain with free displacement (Figure 3.7). The smoothing method "hyperelastic smoothing" is used to calculate the mesh deformation based on the contraints placed on the boundary. Hereby, the minimum of mesh deformation energy W_{mesh} is solved as [133]

$$W_{\text{mesh}} = \int_\Omega \frac{\beta}{2}(I_1 - 3) + \frac{\kappa}{2}(J_{\text{mesh}} - 1)^2 \text{d}V, \tag{3.27}$$

where β and κ represent the moduli for artificial shear and bulk, respectively, whereas J_{mesh} and I_1 depend on the considered coordinate and can be expressed as [133]

$$J_{\text{mesh}} = \det(\nabla_X x) \tag{3.28}$$
$$I_1 = J_{\text{mesh}}^{-2/3} \operatorname{tr}\left[(\nabla_X x)^{\mathrm{T}} \nabla_X x\right] \tag{3.29}$$
$$J_{\text{mesh}} = \det(\nabla_Y y) \tag{3.30}$$
$$I_1 = J_{\text{mesh}}^{-2/3} \operatorname{tr}\left[(\nabla_Y y)^{\mathrm{T}} \nabla_Y y\right], \tag{3.31}$$
$$\tag{3.32}$$

for x- and y-axis respectively, with X and Y are the reference coordinates and x and y are the spatial coordinates.

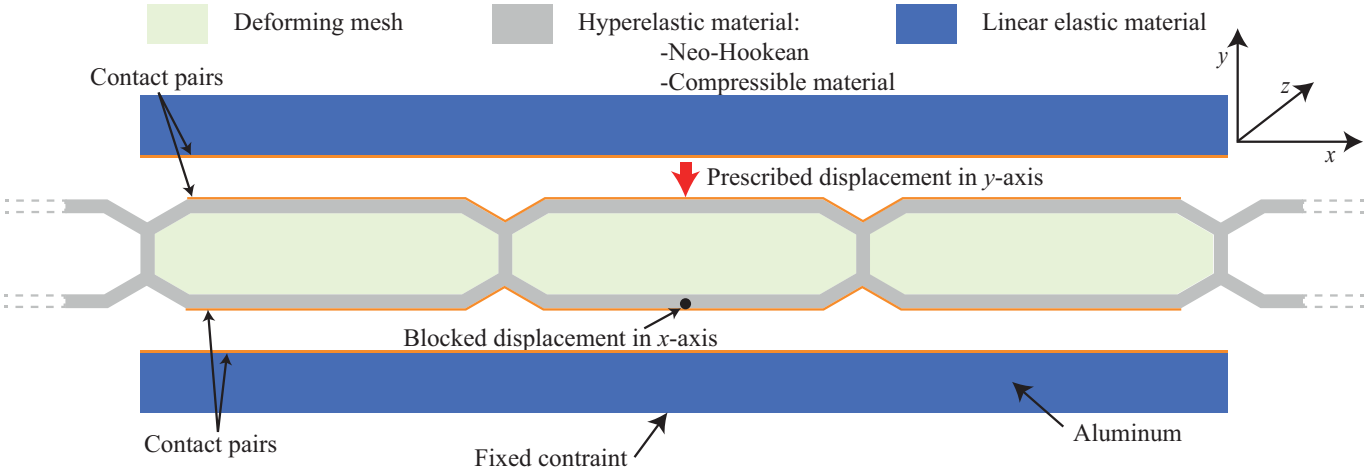

Figure 3.7: Boundary conditions of the simulated scenario in COMSOL Multiphysics to reproduce the measurement setup of the piezoelectric coefficient [115].

For a proper simulation of the contact pairs, the meshing of the contacting boundaries is key. The destination boundary, which in this case is the FEP layer, has to be meshed finer than the source boundary, which in this case is the aluminum plate (Figure 3.8). Furthermore, each corner is a fillet with a radius of 20 µm. After a convergence analysis in order to define suitable meshing, a mapped mesh with a maximum element size of 20 µm and free triangular mesh with a maximum element size of 10 µm are chosen for the ferroelectret and aluminum plate, respectively. The mesh at the corners is refined using an element scaling factor of 0.25.

The change of the surface charge density σ_0 due to the mechanical deformation is solved for each resulting geometry as [133]

$$-\nabla \cdot (\varepsilon_0 \nabla V - P) = \rho, \tag{3.33}$$

where V is the electric potential, P is the polarization, and ρ is the volume charge density. The reference value $\sigma_{0,\text{initial}}$ for the surface charge density is when no force is applied to the ferroelectret. The piezoelectric d_{33} coefficient of the structure after being deformed due to an external force F is calculated as

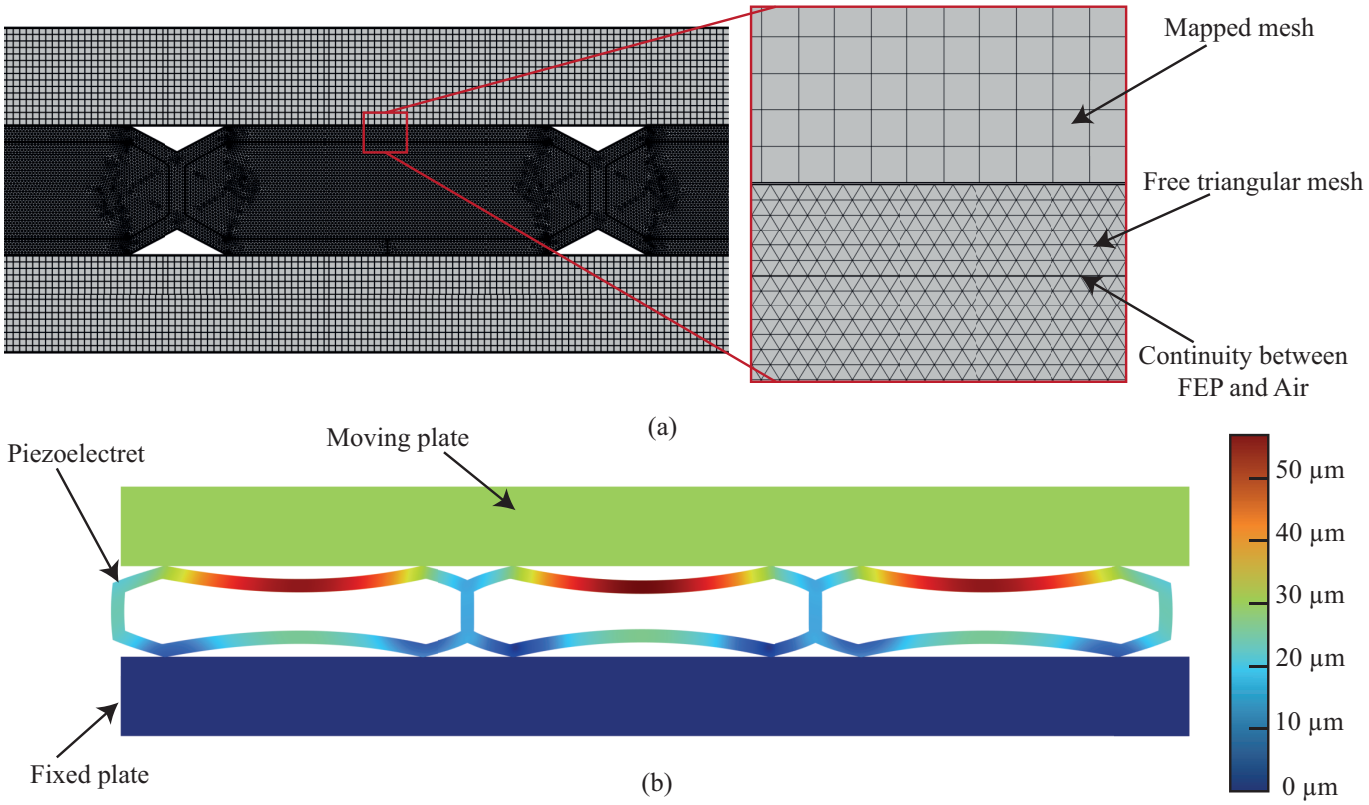

Figure 3.8: FEA simulation of tubular-array ferroelectret: (a) the meshing of different domains and (b) the deformation of the tubular-array due to the displacement of 30 µm of the upper plate in negative y-direction [115].

$$d_{33} = \frac{\sigma_{0,\text{initial}} - \sigma_{0,\text{deformed}}}{F}, \tag{3.34}$$

where $\sigma_{0,\text{deformed}}$ corresponds to the surface charge density of a deformed state of the structure.

The FEA model is validated by comparing the simulation results with measurements of three ferroelectrets exhibiting the same geometry. The ferroelectret is placed between a fixed bottom electrode and a moving upper electrode guided using a linear guide made of PTFE. The whole setup is placed within a metal shield acting as faraday cage to avoid interfering charges in the environment. The measurement is performed in two steps: first, a mass is placed on the sample for 3 min. After removing the mass, the induced charge is measured and integrated over 10 s by means of a triaxial cable and an electrometer (model B2987A, Keysight Technologies, Santa Rosa, California, USA).

The measurements of d_{33} coefficients of all samples are in the same range of the predicted range between $109\,\text{pC}\,\text{N}^{-1}$ and $180\,\text{pC}\,\text{N}^{-1}$ for $\sigma_{\text{int}} = 0.03\,\text{pC}\,\text{N}^{-1}$ and $\sigma_{\text{int}} = 0.05\,\text{pC}\,\text{N}^{-1}$, respectively [Figure 3.9(a)]. The d_{33} piezoelectric coefficient of all samples seems to be relatively stable when increasing the stress, whereas the simulation predicted a slight increase. This can be caused by the manufacturing tolerances, that result in geometries slightly different from the simulated one.

The good agreement of the simulation with the measurement allows the FEA model to be used to optimize the tubular-array ferroelectret for its application as energy harvester. Hereby two main parameters influence

significantly the piezoelectric d_{33} coefficient, which are the thickness of the FEP walls [39] as well as the number of the tubes used [Figures 3.9(c) and (d)]. As the number increases, the tubes hinder each other from transverse stretching when a mechanical stress is applied in thickness direction, due to frictional and elastic forces. This leads to increasing the Young's modulus of the structure and decreasing the piezoelectric d_{33} coefficient. Consequently, a d_{33} energy harvester using single FEP tubes is investigated.

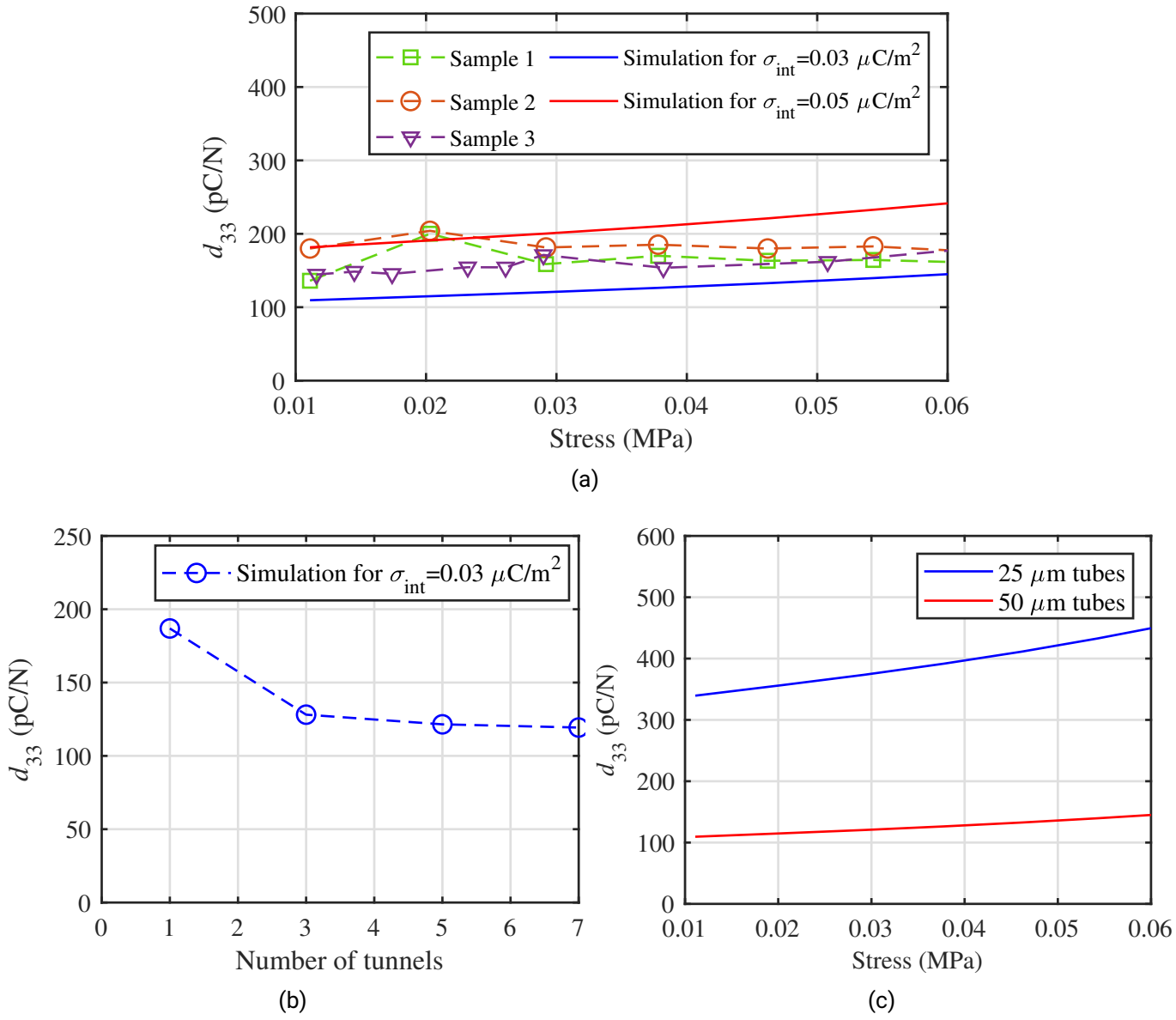

Figure 3.9: (a) Experimental and simulation results for the piezoelectric d_{33} coefficient. The symbols connected with dashed lines correspond to the experimental results, while the solid line represents the simulation, (b) infuence of increasing the number of tunnels on the piezoelectric d_{33} coefficient using the same remanent charge density $\sigma_{\text{int}} = 0.03\,\mu\text{C mm}^{-2}$ and the same mechanical stress of 0.04 MPa, (c) d_{33} coefficient of tubular-array-structure consisting of 3 tubes simulated with $\sigma_{\text{int}} = 0.03\,\mu\text{C mm}^{-2}$ [115].

3.2 Microenergy harvester based on a single FEP tube

Single FEP tubes are deformed using the aforementioned method (Figure 3.2), where a spacer of 0.4 mm is utilized. Two different wall thicknesses of 30 mm long FEP tubes are considered, namely 25 µm and 50 µm. After the deformation, each tube exhibiting a stadium-like shape is metallized on both external flat sides with aluminum and then polarized by direct-contact charging in ambient air at 25 °C. The charging is carried out by contacting the metallized surface area of $20\,\text{mm} \times 1\,\text{mm}$ and applying a voltage up to $\pm 6\,\text{kV}$ using a high-voltage power supply HSN-35 (FUG GmbH).

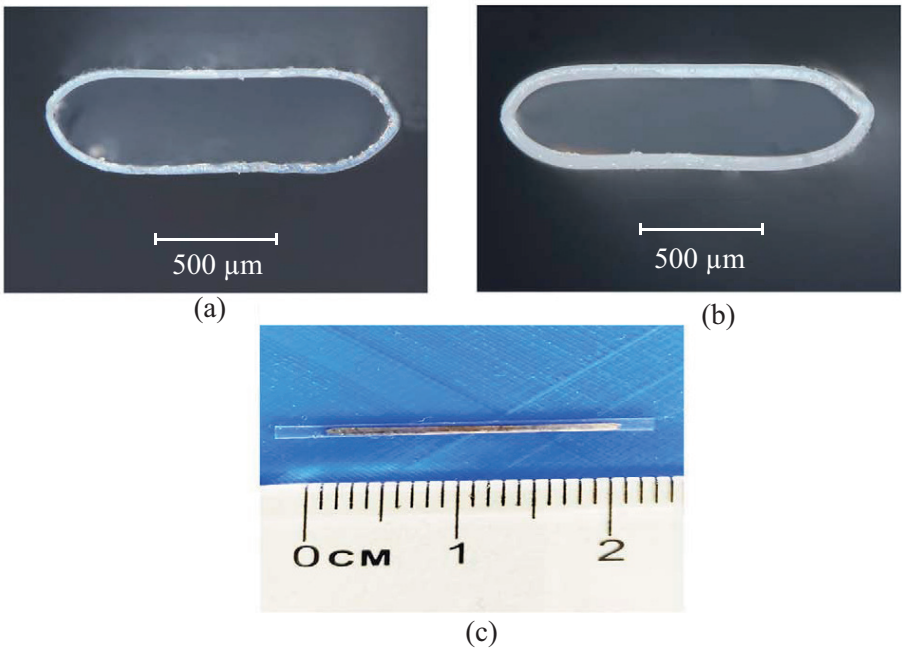

Figure 3.10: Cross-section micrographs of resulting stadium-like structures fabricated at $+250\,°\text{C}$ from FEP tubes of a diameter of 1 mm and with wall thicknesses of (a) 25 µm and (b) 50 µm. (c) Dimensions of actual tube harvester [116].

In view of the application of these tubes as energy harvester, the dynamic piezoelectric d_{33} coefficient is the most relevant parameter, which is generally smaller than the quasi-static d_{33} coefficient due to the viscoelastic property of polymers. For measuring the dynamic d_{33} coefficient, the tube ferroelectret loaded with a seismic mass m_s is mounted on a platform, which is set into vibration with an acceleration a by a shaker (Bruel & Kjaer typ 4809). The seismic mass results in two forces: the static force $F_\text{stat} = m_\text{s} \times g$ and the dynamic force $F_\text{dyn} = m_\text{s} \times a$. The static force acts as pre-stress which defines the initial deformation of the tubes as a working point. This pre-stress may contribute to the sensitivity of the tube and should be investigated. The relevant force for defining the piezoelectric d_{33} coefficient is the dynamic force. Therefore, the dynamic acceleration a is measured with an accelerometer (B&K 4393) in combination with a charge amplifier (B&K 2635). The charge Q generated by the tube is simultaneously measured in short circuit by a second charge amplifier of the same model (Figure 3.11). The output of both charge amplifiers is connected to an audio analyzer (dScope Series III, PrismSound) that converts the analog signals into digital form for further processing.

To investigate the influence of the static force on the dynamic piezoelectric d_{33} coefficient, the dynamic

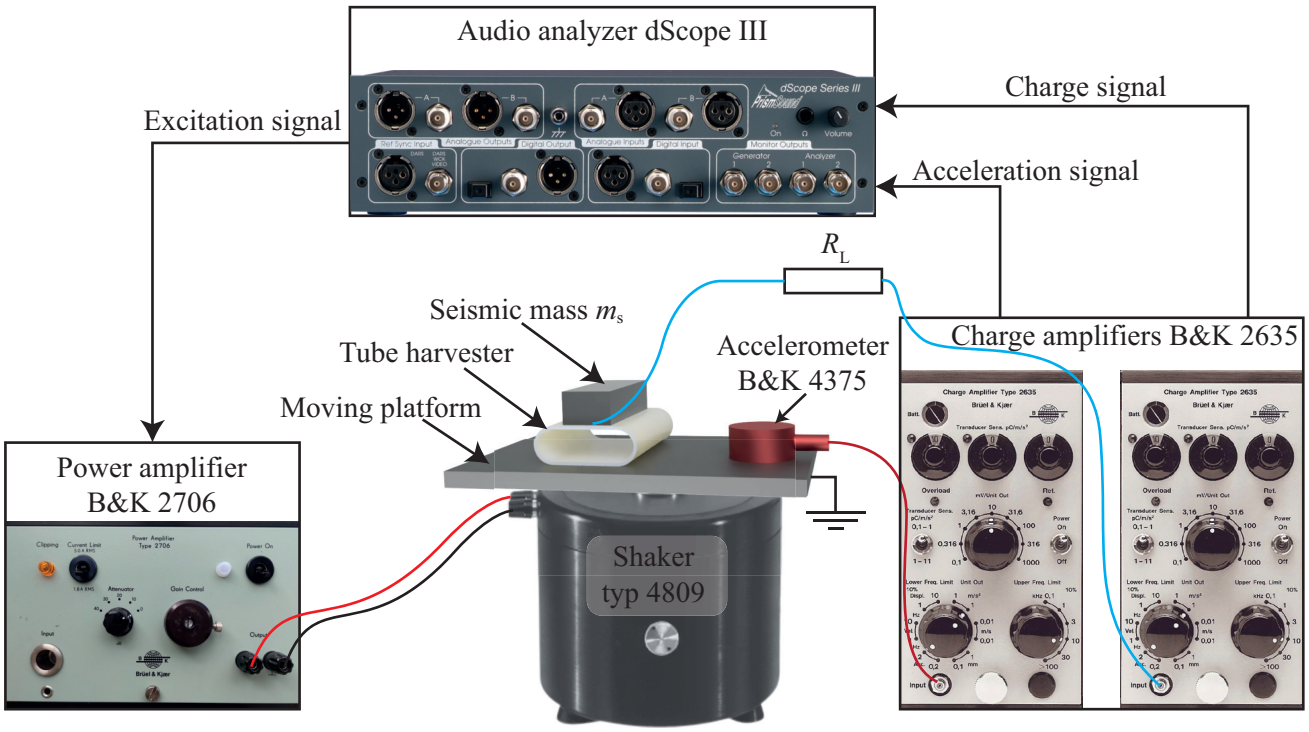

Figure 3.11: Schematic of experimental setup used for evaluating the tube energy harvester [116].

piezoelectric coefficient is measured at a fixed frequency of 20 Hz and determined as

$$d_{33} = \frac{Q}{m_s\, a}. \tag{3.35}$$

The frequency is selected to be significantly lower than the resonance frequency of the harvester. The

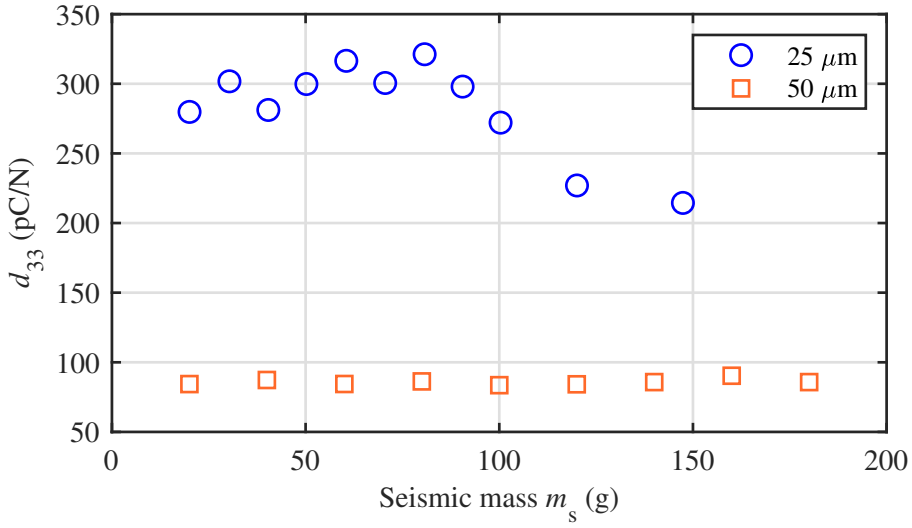

Figure 3.12: Dynamic d_{33} coefficient at 20 Hz versus seismic mass for tubes with different wall thickness as indicated [116].

experimental results for various seismic masses m_s using energy harvesters fabricated from single FEP tubes with 50 µm and 25 µm thick walls are shown in Figure 3.12.

The dynamic d_{33} coefficient of the 50 µm thick tube is constant at about 80 pC N^{-1} for seismic masses between 20 g and 180 g. The thin-walled tube has a noticeably higher piezoelectric response of an average of 290 pC N^{-1}, which is expected based on the FEA model. This large piezoelectric d_{33} coefficient, however, is only stable for a seismic mass under 100 g. An increase of the load results in a remarkable decrease of the piezoelectric d_{33} coefficient. Based on these results, it can be concluded that the initial deformation caused by the static force has a larger influence on the tube with thin walls, and thus a seismic mass of 80 g should not be exceeded for the energy harvester. Nevertheless, the harvester designed using the thick wall tubes can be investigated for larger seismic masses.

3.2.1 Theoretical model of the harvester

The ferroelectret tube can be considered as damped spring. The tube and the seismic mass on the top are excited by the motion of the plattform at the base in thickness direction. Due to the coincidence of the mechanical stress and the electric field, this configuration can be modeled as a d_{33}-energy harvester. Hereby the 1-D configuration allows the linear elastic constitutive piezoelectric relations to be simplified to

$$S_3 = s_{33}^E S_3 + d_{33} E_3, \tag{3.36}$$

$$D_3 = d_{33} T_3 + \varepsilon_{33}^T E_3, \tag{3.37}$$

where D, E, S and T are the electric displacement, electric field, strain, and stress, respectively. ε_{33}^T is the permittivity of the tube consisting of FEP and air at constant electric charge and s_{33}^E the compliance of the structure under short-circuit conditions. In the case of energy harvesting, only equation (3.37) is relevant with

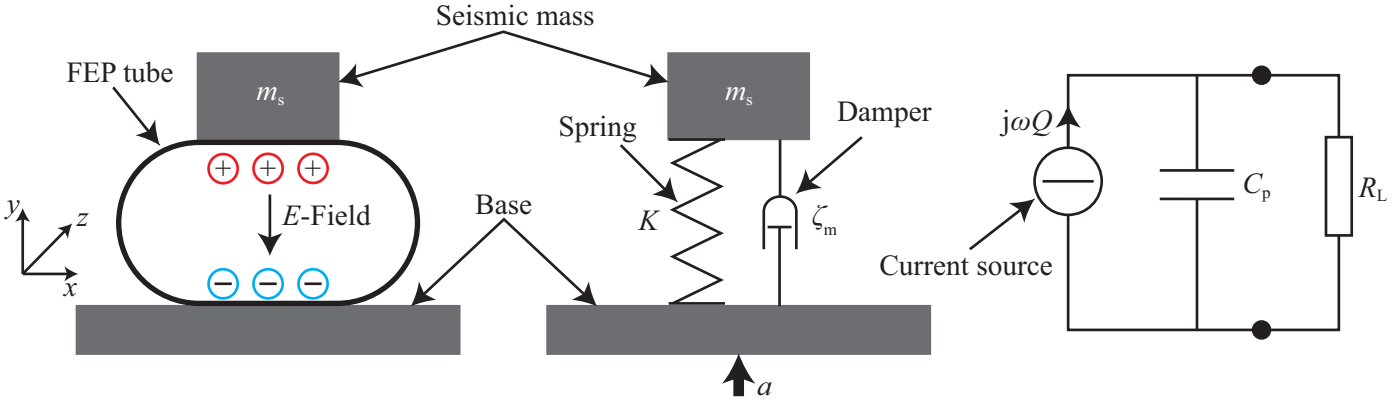

Figure 3.13: Schematic of the 1D harvester model for the FEP Tube.

the external electric field $E_3 = 0$. Assmuning a force equilibrium, the equation of motion of the ferroelectret energy harvester at a harmonic acceleration a is defined as

$$\ddot{y} + 2\zeta\omega_n \dot{y} + \omega_n^2 y = a \tag{3.38}$$

$$y = \frac{a}{\omega_n^2 + 2j\omega\zeta\omega_n - \omega^2}, \tag{3.39}$$

where a is the base acceleration, y is the displacement of the proof mass relative to the base, m_s is seismic mass, ζ is the mechanical damping ratio, and ω_n is the undamped natural frequency. Combining equations (3.39) and (3.37), the generated charge for base acceleration can be determined as

$$D = d_{33} T \rightarrow Q = d_{33}\, \omega_\mathrm{n}^2\, m_\mathrm{s}\, y \tag{3.40}$$

$$Q = d_{33}\, m_\mathrm{s}\, \frac{a}{\omega_\mathrm{n}^2 + 2j\omega\zeta\omega_\mathrm{n} - \omega^2} \tag{3.41}$$

$$Q = \frac{d_{33}\, m_\mathrm{s}\, a}{\frac{\omega^2}{\omega_\mathrm{n}} - 1 - j2\zeta\frac{\omega}{\omega_\mathrm{n}}}. \tag{3.42}$$

This charge flows from the generator into a load impedance, which consists of the parallel connection of the load resistor R_L and the parasitic capacitance C_p of the energy harvester. The charge Q_L through the load resistor can be calculated as

$$Q_\mathrm{L,rms} = \frac{Q}{1 + j\omega R_\mathrm{L} C_\mathrm{p}} = \frac{d_{33}\, m_\mathrm{s}\, a}{\sqrt{\left[\left(\frac{\omega^2}{\omega_\mathrm{n}} - 1\right)^2 + 4\zeta^2\frac{\omega^2}{\omega_\mathrm{n}^2}\right]\left[1 + \left(R_\mathrm{L} C_\mathrm{p}\omega\right)^2\right]}} \tag{3.43}$$

and results in a voltage V_rms across the resistor as

$$V_\mathrm{L,rms} = \frac{R_\mathrm{L}\omega d_{33}\, m_\mathrm{s}\, a}{\sqrt{\left[\left(\frac{\omega^2}{\omega_\mathrm{n}} - 1\right)^2 + 4\zeta^2\frac{\omega^2}{\omega_\mathrm{n}^2}\right]\left[1 + \left(R_\mathrm{L} C_\mathrm{p}\omega\right)^2\right]}}. \tag{3.44}$$

Under the short-circuit condition, for $R_\mathrm{L} << 1/\omega_\mathrm{n} C_\mathrm{p}$ and below ω_n, the energy harvester behaves as an ideal charge source, generating the charge Q. If the parasitic capacitance C_p is negligible and $R_\mathrm{L} >> 1/\omega_\mathrm{n} C_\mathrm{p}$ below ω_n, the energy harvester can be approximated as an ideal voltage source.

The output power P_out of the energy harvester is determined as

$$P_\mathrm{out} = \frac{V_\mathrm{rms}^2}{R_\mathrm{L}},$$

$$P_\mathrm{out} = \frac{R_\mathrm{L}\omega^2 d_{33}^2\, m_\mathrm{s}^2\, a^2}{\left[\left(\frac{\omega^2}{\omega_\mathrm{n}} - 1\right)^2 + 4\zeta^2\frac{\omega^2}{\omega_\mathrm{n}^2}\right]\left[1 + \left(R_\mathrm{L} C_\mathrm{p}\omega\right)^2\right]}. \tag{3.45}$$

In order to compare the output power of the energy harvester with the other energy harvesters in literature, the generated power is normalized to the gravitational acceleration of $g = 9.81\,\mathrm{m\,s^{-1}}$ and is referred to as normalized output power $P_\mathrm{out,N}$. This can be calculated as

$$P_\mathrm{out,N} = \left(\frac{g}{a_\mathrm{rms}}\right)^2 P_\mathrm{out}. \tag{3.46}$$

3.2.2 Performance of the tube energy harvester

The performance of the energy harvester is examined regarding the wall thickness, load resistance, and seismic mass which should be below 80 g.

The output power for different load resistance, is investigated by using a constant seismic mass of $m_s = 60$ g and a tube with 50 µm thick walls. The measurement [Figure 3.14(a)] indicates that the output power increases with increasing frequency below the resonance frequency and reaches its maximum of $P_{\text{out,N}} = 20$ µW at 140 Hz and an optimum load resistance of $R_L = 190$ M.

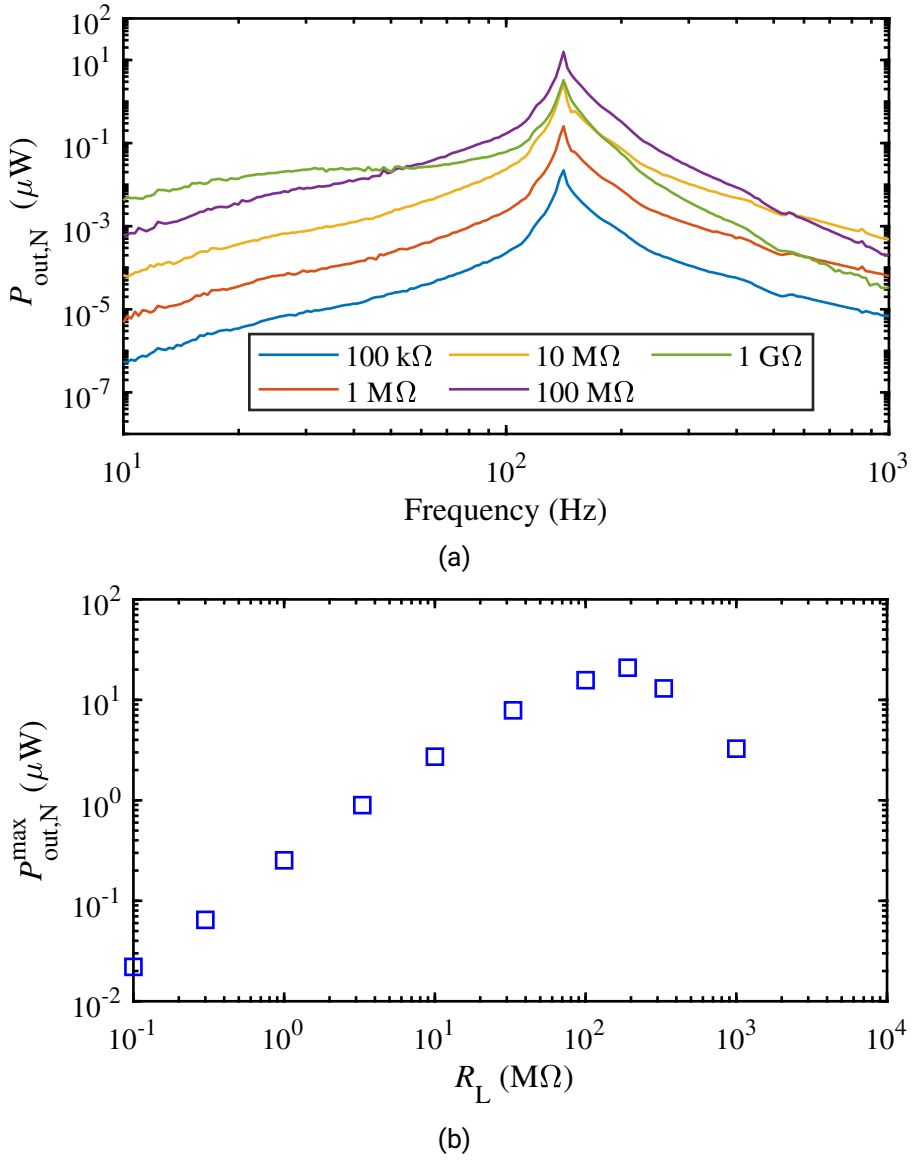

Figure 3.14: (a) Output power $P_{\text{out,N}}$ as a function of vibration frequency f for a single-tube FEP harvester with a wall thickness of 50 µm at various load resistances R_L. b) Peak output power $P^{\text{max}}_{\text{out,N}}$ at the resonance frequency as function of load resistance R_L for the same harvester with the same seismic mass m_s60 g [116].

The measurement of the peak output power $P_{\text{out,N}}^{\text{max}}$ by varying the load resistance R_{L} shows a proportional increase of the output power to an increasing load resistance until an optimal value $R_{\text{L}}^{\text{opt}} = 190\,\text{M}$ is reached [Figure 3.14(b)]. Afterwards, the output power starts to decrease for $R_{\text{L}} > R_{\text{L}}^{\text{opt}}$. This behaviour is expected and can be derived from equation 3.45. Based on the theoretical model, the maximum output power is reached when the electrical cutoff frequency and the resonance frequency of the energy harvester are in agreement. In this case, the normalized peak power $P_{\text{out,N}}^{\text{max}}$ can be expressed as

$$R_{\text{L}}^{\text{opt}} = \frac{1}{\omega_{\text{n}} C_{\text{p}}} \hookrightarrow P_{\text{out,N}}^{\text{max}} = \frac{R_{\text{L}}^{\text{opt}} \omega_{\text{n}} d_{33}^2\, m_{\text{s}}^2\, a^2}{8\zeta^2 C_{\text{p}}}. \tag{3.47}$$

Considering the capacity of the tube harvester being $C_{\text{p}} = 6\,\text{pC}$ between the seismic mass and the moving platform, the theoretical estimation of the load resistance is in very good agreement to the measurement.

The next parameter influencing the output power is the seismic mass m_{s}. Hereby the resonance frequency can be written in function of the the Young's modulus Y, the thickness of the tube t and the seismic mass m_{s} as

$$\omega_{\text{n}} = \sqrt{\frac{YA}{t m_{\text{s}}}} \quad \text{and} \tag{3.48}$$

$$P_{\text{out,N}}^{\text{max}} = \sqrt{\frac{YAm_{\text{s}}^3}{t}}\, \frac{R_{\text{L}}^{\text{opt}} d_{33}^2\, a^2}{8\zeta^2 C_{\text{p}}}. \tag{3.49}$$

According to equation (3.49) the output power of the harvester is proportional to m_{s}^3, which is similar to the electret energy harvester introduced by Pondrom et al. [139].

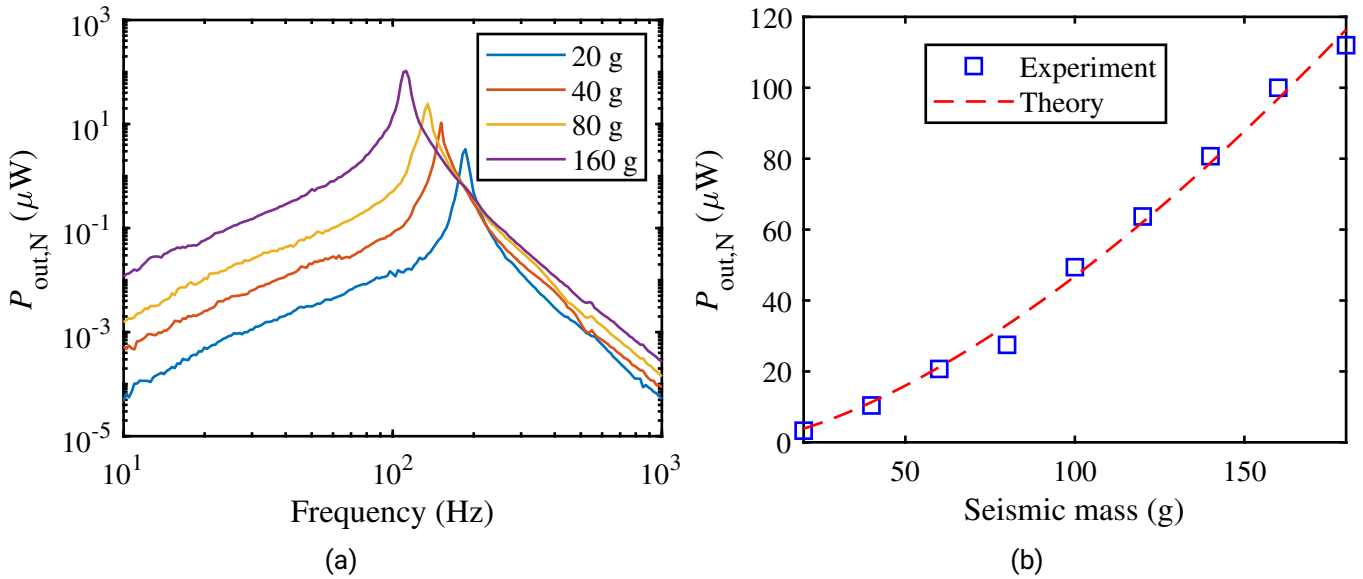

Figure 3.15: Output power $P_{\text{out,N}}$ as a function of vibration frequency for a single-tube FEP harvester at various seismic masses for an optimal load resistance. b) Peak output power $P_{\text{out,N}}^{\text{max}}$ as a function of seismic masses for an optimal load resistance. The symbols correspond to the experimental results, while the dashed line represents the theoretical model [116].

For larger variation of the seismic mass without affecting the d_{33} coefficient, a tube with 50 µm wall thickness is chosen. The experimental results show two effects: first, the output power grows significantly when increasing the seismic mass [Figure 3.15]. The value of $P_{\text{out,N}}^{\text{max}}$ is enhanced from about 3 µW to 100 µW by increasing the seismic mass from 20 g to 160 g. Second, the resonance frequency is shifted towards lower frequencies [Figure 3.15(a)] with increasing seismic mass, which confirms the analytical expectations. The same behaviour is recorded when using a thin-walled tube, without exceeding the seismic mass of 80 g. However, when using a seismic mass of 80 g in combination with the 25 µm thick tube to build the harvester, the normalized output power reaches a $P_{\text{out,N}}^{\text{max}}$ of approximately 300 µW for $R_{\text{L}}^{\text{opt}} = 330\,\text{M}$ (Figure 3.16).

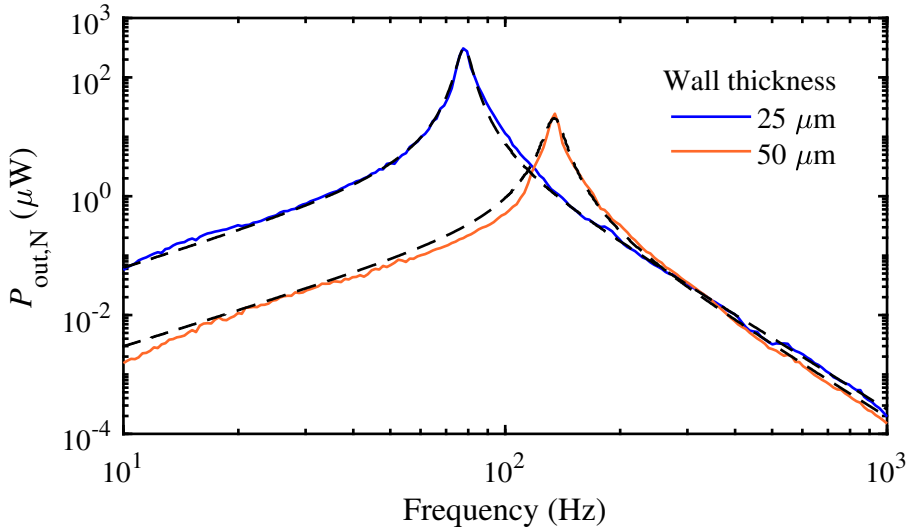

Figure 3.16: Comparison of the output power $P_{\text{out,N}}$ for the energy harvesters based on single FEP tubes for the same seismic mass of 80 g with different wall thicknesses as indicated. The solid lines represent the experimental results while the dashed lines correspond to a fit using equation (3.45) [116].

The peak output power $P_{\text{out,N}}^{\text{max}}$ of the thin-walled device is about one order of magnitude higher than that of the thick-walled sample, which reaches approximately 140 µW for $R_{\text{L}}^{\text{opt}} = 190\,\text{M}$. A further difference between the samples with different tube thicknesses is the resonance frequency of the harvester for the same seismic mass. The resonance frequency is shifted from about 135 Hz for the thick-walled harvester to about 78 Hz for the thin-walled device, which is a clear advantage for harvesting the energy from ambient mechanical vibrations, which are concentrated below 100 Hz [123]. Furthermore, the experimental results are in very good agreement with the theoretical model as can be seen in Figure 3.16. Hereby, the experimentally accessible parameters such as R_{L}, a, m_{s}, d_{33}, ω_{n} and C_{p} are used in equation (3.45). The damping ratio ζ, which largely depends on the mechanical properties and the geometry of the tube is determined by approximating the bandwidth of of the measurement to the theory. The fit parameters are listed in Table 3.1.

Table 3.1: Fitted and measured parameters for thin- and thick-walled tube harvesters

Wall thickness (µm)	R_{L} (MΩ)	C_{p} (pF)	m_{s} (g)	d_{33} (pC N^{-1})	ω_{n} (rad s^{-1})	ζ
25	330	6	80	290	490±1	0.045±0.002
50	190	6	80	80	490±1	0.058±0.005

The normalized power output obtained with the thick-walled energy harvester is in the same range of other

d_{33}-ferroelectret energy harvesters based on stacked PP [41] and IXPP [104]. It is also worth mentioning that the capacitance of the harvester C_p of 6 pF is mainly due to the parasitic capacitance of the measurement setup and is three times larger than the capacitance of the tube when measured alone. According to equation (3.47), by reducing the parasitic capacitance a larger power can be expected. If the thin-walled harvester is considered, a reduction of the parasitic capacitance would lead to a drastic improvement of the power output.

The long-term stability of the tube harvesters depends, however, on the ambient temperature and humidity which influence the charge storage stability and the mechanical load which lead to fatigue. In this case, the utilized material FEP is known to provide a lifetime stable performance at ambient temperature [33], [36], [140], [141]. The mechanical stability on the other hand is limited to small mechanical loads. A large seismic mass causes the collapse of the structure which in turn leads to the degradation of the piezoelectric d_{33} coefficient.

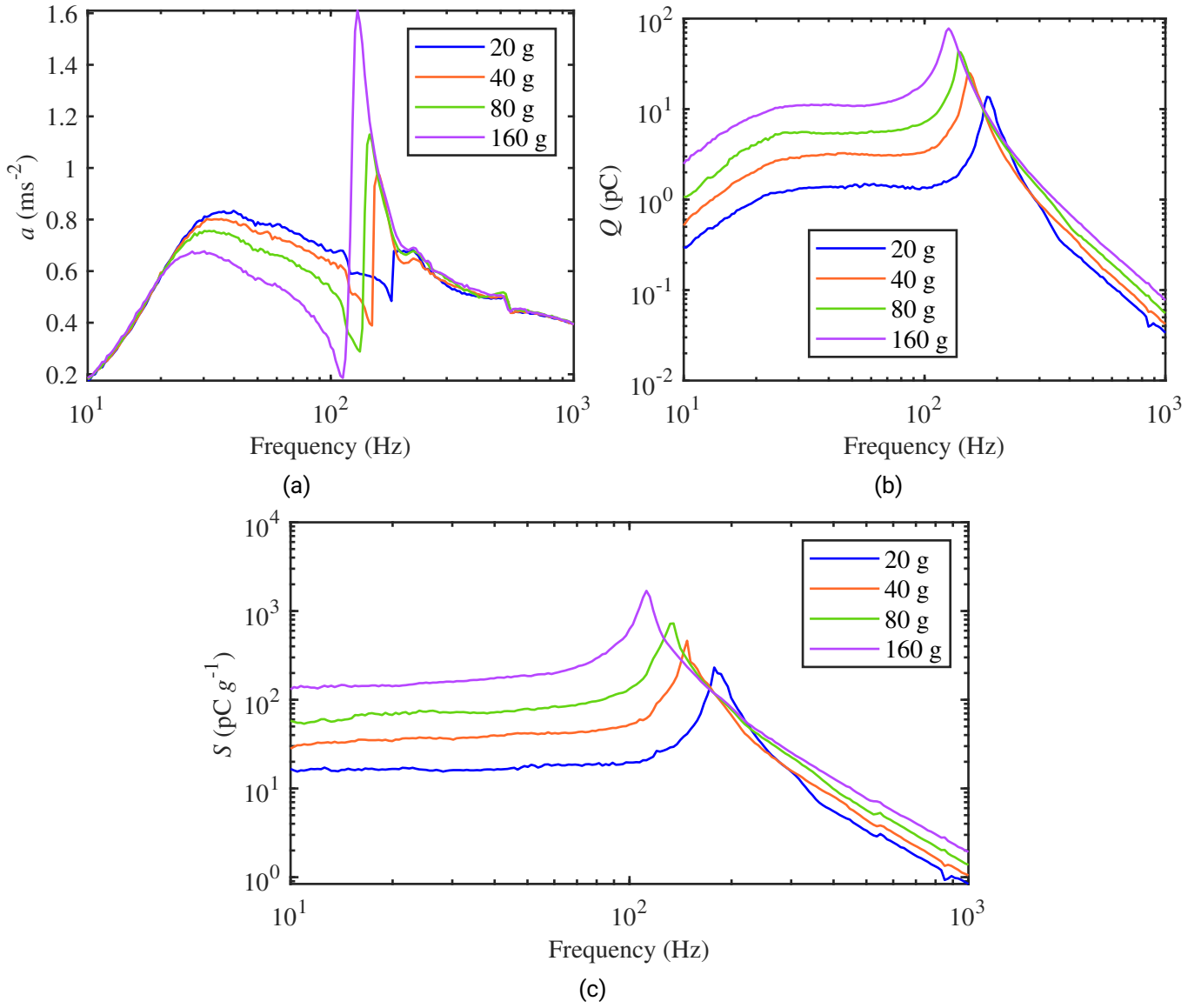

Figure 3.17: (a) Charge Q_rms generated by a 50 µm thick tube transducer in response to (b) base acceleration a. (c) The charge sensitivity S for different seismic masses m_s [116].

The developed tube energy harvester can be used as an accelerometer with sensitivity S, which can be determined as [142]

$$S = \frac{\Delta Q}{\Delta a} \tag{3.50}$$

An accelerometer with a large seismic mass and thin-walled tube would be more sensitive than a thick walled tube, however feature a lower resonance frequency. Since a wide bandwidth is desirable for accelerometers, the thick-walled tube satisfies the compromise between high sensitivity and high resonance frequency more effectively.

The measurement of the sensitivity is performed using seismic masses between 20 g and 160 g at room temperature using the same setup as for the energy harvesting.

All measurements show a stable sensitivity S below the resonance frequency between 16.5 pCg^{-1} and 139 pCg^{-1} corresponding to seismic masses of 20 g and 160 g respectively [Figure 3.17(c)]. The resonance frequency, however decreases from approximately 231 Hz for $m_\mathrm{s} = 20$ g to approximately 112 Hz for $m_\mathrm{s} = 20$ g, which is expected according to equation (3.48).

Unfortunately, these tubes can not be used in a 31-mode energy harvester. A single tube is too small to be clamped and stretched in 1-direction (transverse direction) and an array of tubes is unstable against excessive stress. In fact, the tubes fused together are not all homogeneously bonded and, thus, are detached from each other when stressed in transverse direction.

3.3 Parallel-tunnel FEP ferroelectrets

The parallel-tunnel ferroelectrets introduced by Zhang et al. [47] exhibit a wavy form and are therefore more complicated to characterize regarding their longitudinal and transversal piezoelectric effect. In this section, a way of characterizing them considering the inhomogeneous thickness based on theoretical analysis is introduced. It is worth mentioning that by achieving a large longitudinal and transversal effect with the same structure as well as a high thermal stability, these ferroelectrets can be considered as an outstanding achievement until present date.

3.3.1 Preparation of the parallel-tunnel ferroelectret

The ferroelectrets are made of two 12.5 µm-thick FEP films provided by DuPont (DuPont de Nemours, Wilmington, Delaware, USA). The preparation steps are summarized in Figure 3.18. First, two FEP films are placed on a soft rubber pad, each on one side to form a sandwich. Second, the stack is placed between two 50×50 mm^2 copper templates, which are fabricated by milling parallel grooves on their surfaces. The grooves are 1 mm wide and separated by 0.3 mm. Third, the templates, together with the stacks, are hot pressed at a temperature of 100 °C to deform the FEP film. This step is called patterning (Figure 3.18). The last step is the removal of the softpad followed by fusion-bonding of the already deformed films.

The fusion-bonding is carried out in an oven by exposing the clamped templates with the patterned films in-between to a temperature of 320 °C for 15 min. After cooling down to room temperature, the templates are removed. Afterwards, the samples are metalized on both sides with aluminum electrodes by vacuum

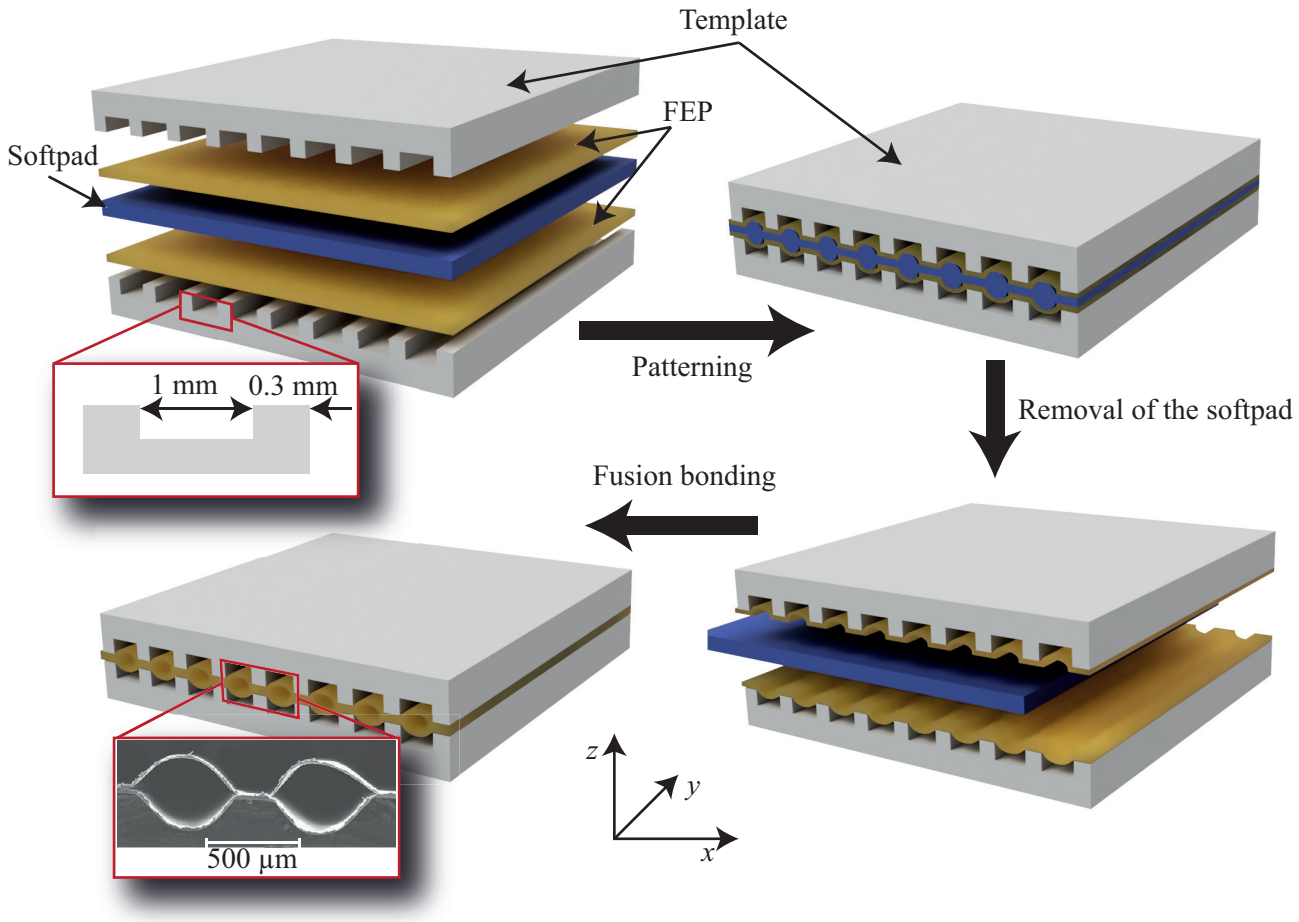

Figure 3.18: Preparation steps of FEP parallel-tunnel samples [46]

evaporation. For polarizing the samples, the contact charging method is utilized by applying a voltage of 3 kV to the sample. This voltage results in the largest polarization possible for such a structure according to the hysteresis loop measured using the ST.

3.3.2 Piezoelectric coefficients of parallel-tunnel FEP films

The parallel-tunnel FEP ferroelectret film consists of numerous soft polarized air-filled tunnels with an elliptical-like shape. Applying a mechanical force in direction of z-axis or x-axis (it can also be described as subscript 3 and 1, respectively) causes a deformation of the shape of the tunnels resulting in charge variation on the electrodes. This effect can be described as the direct piezoelectric 33-mode or 31-mode effect. Therefore, the properties of such structure can be tuned by varying the geometrical parameters of the template as well as the production procedure. In this section, only parallel-tunnel ferroelectrets are utilized featuring 0.5 mm space between two adjacent tunnels, which in turn are 1 mm wide (Figure 3.19).

For measuring the piezoelectric d_{33}, d_{31}, g_{33}, and g_{31}-coefficients, different experimental techniques are used and compared. All investigated samples have open tunnels making their stiffness mainly determined by the geometry of the polymer.

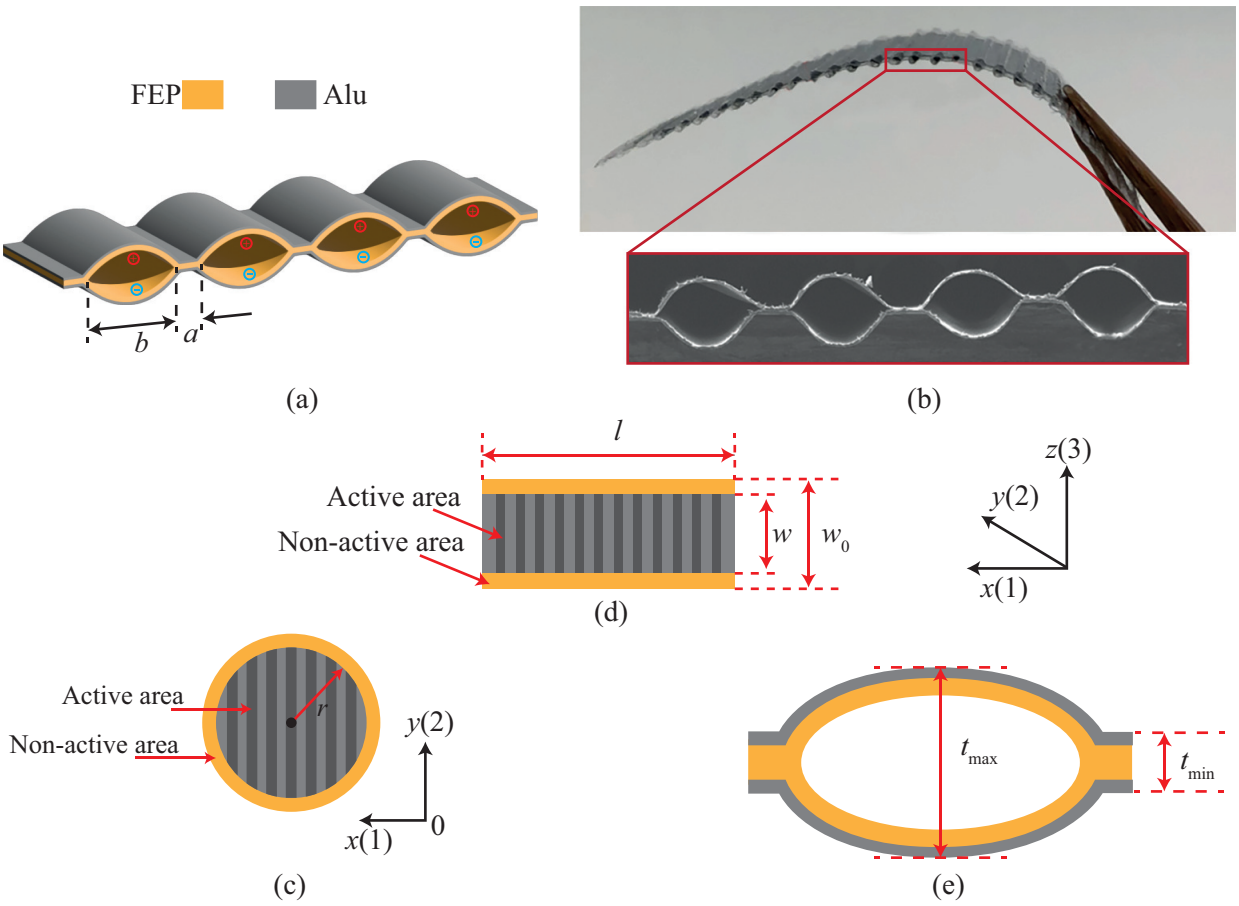

Figure 3.19: (a) Illustration of structure and charges within the tunnels. (b) Photograph of a parallel-tunnel FEP film and an SEM image of the film cross section. (c) Schematic top view of a sample in 33-mode with r the metallized electrode radius of the sample. Stripes mark the tunnel orientation of the sample. (d) Schematic side view of the sample surface in 31-mode, with l, w_0 and w the length, width and effective width of the sample, respectively. The stripes mark the tunnel orientation of the sample. (e) Schematic sample cross-section marked with its maximum thickness t_{max} and its minimum thickness t_{min} [48].

Characterization of the longitudinal piezoelectric d_{33} and g_{33} coefficients using the quasi-static method

For measuring the d_{33}-coefficient, a mechanical stress has to be applied in the direction of polarization while measuring the charge variation on the electrodes. The g_{33}-coefficient is determined by measuring the induced voltage under open-circuit conditions. Hereby, three different methods were utilized: the quasi-static method, the dynamic method and the acoustic method.

The rectangular samples after preparation are cut in a circular shape featuring a diameter of 20 mm. The mechanical stress T_3 is applied in 3-direction through a cylindrical mass of 100 g. Because the mass is placed per hand, some effects such as bending or an angled placement have to be taken into consideration. These problems have been obviated by first placing a cylindrical metal plate with the same diameter as the sample, causing a mechanical pre-load of 0.5 N. The actual measurement is then carried out with an additional mass,

which is first deposited on the sample for an extended period of time (2 min). Then the additional mass is rapidly removed and the generated charge and voltage are measured over 10 s by means of an electrometer (Keithley 64514). Due to the high input impedance of the electrometer for voltage measurements with $Z_{\text{in}} = 100\,\text{T}$, it can be considered as electrical open-circuit condition. The d_{33} and g_{33}-coefficients can be calculated as

$$d_{33} = \frac{D_3}{T_3} = \frac{Q_3/A}{F_3/A} = \frac{Q_3}{F_3} \tag{3.51}$$

$$g_{33} = \frac{E_3}{T_3} = \frac{V_3/t_3}{F_3/A} = \frac{V_3 \cdot C_{\text{eff}}/F_3}{\varepsilon_0 \varepsilon_{\text{eff}}} = \frac{Q_3/F_3}{\varepsilon_0 \varepsilon_{\text{eff}}} = \frac{d_{33}}{\varepsilon_0 \varepsilon_{\text{eff}}}, \tag{3.52}$$

where D_3 and E_3 are the electric displacement and electric field in 3-direction, respectively. ε_0 and ε_{eff} are the permittivity of vacuum and the relative permittivity of the sample, respectively. Q_3 and V_3 are the induced electrode charge under short circuit conditions and voltage output under open circuit conditions. A is the metallized area of the sample on which the mechanical stress is applied and t_3 is the thickness of the sample. Due to the wavy form of the surface, the thickness t_3 can not be assumed to be constant and is, therefore, represented by t_{eff} as an average value, which can be determined by measuring the effective capacitance C_{eff}. The latter is assumed to describe the capacitance of a homogeneous sample with a single relative permittivity ε_{eff} and a uniform thickness t_{eff}.

As can be seen from equations (3.51) and (3.52), the d_{33} can be determined experimentally while g_{33} have to be calculated for a known effective permittivity ε_{eff}. Since the permittivity can not be determined unambiguously in the fabricated FEP films, an upper and lower limit can be chosen by assuming that the capacitance of the sample consists completely of air ($\varepsilon_{\text{eff}}^{\text{min}} = 1$) or FEP ($\varepsilon_{\text{eff}}^{\text{max}} = 2.1$). It should be noted that the force is only applied to the highest points of the wavy form when using the quasi-static method. Since the mass is also used as electrical contact with the sample electrode, it is valid to assume that the area for the mechanical and electrical parts are the same. A uniform stress on the sample can be only applied by the acoustic method.

Due to the wavy form, the sample geometry alternates between a minimum thickness t_{min}, which corresponds to the bonded region of the sample, and a maximum thickness t_{max}, which corresponds to the center of the tunnels. The measurement of t_{max} is carried out by a F-55 thickness gauge, that applies a pressure of 0.36 kPa on the complete upper surface of the sample. The minimum thickness consists of two 12.5 µm thick FEP films, and can therefore be assumed to be 25 µm. The thickness of the aluminum electrode of 100 nm can be neglected.

The quasi-static d_{33}-coefficient obtained experimentally can reach values as high as $4694\,\text{pC}\,\text{N}^{-1}$, exceeding the well known piezoelectric materials PZT with a d_{33}-coefficient of only $650\,\text{pC}\,\text{N}^{-1}$. The g_{33}-coefficient, even when considering the minimum values, can reach several hundred of $\text{V}\,\text{m}\,\text{N}^{-1}$. This confirms the large piezoelectric response of parallel-tunnel FEP samples. All measured results are summarized in Table 3.2.

Longitudinal piezoelectric d_{33} coefficient determined by dynamic method

Similarly to the dynamic measurements discussed in previous section, the samples are placed on top of an electrodynamic shaker (B&K 4809) as the vibrating surface. On top of the samples a cylindrical seismic mass m is fixed with an adhesive tape. The shaker is sinusoidally driven using a function generator (B&K PULSE 3560B) by virtue of a power amplifier (B&K 2713). The generated acceleration a is measured by a vibration

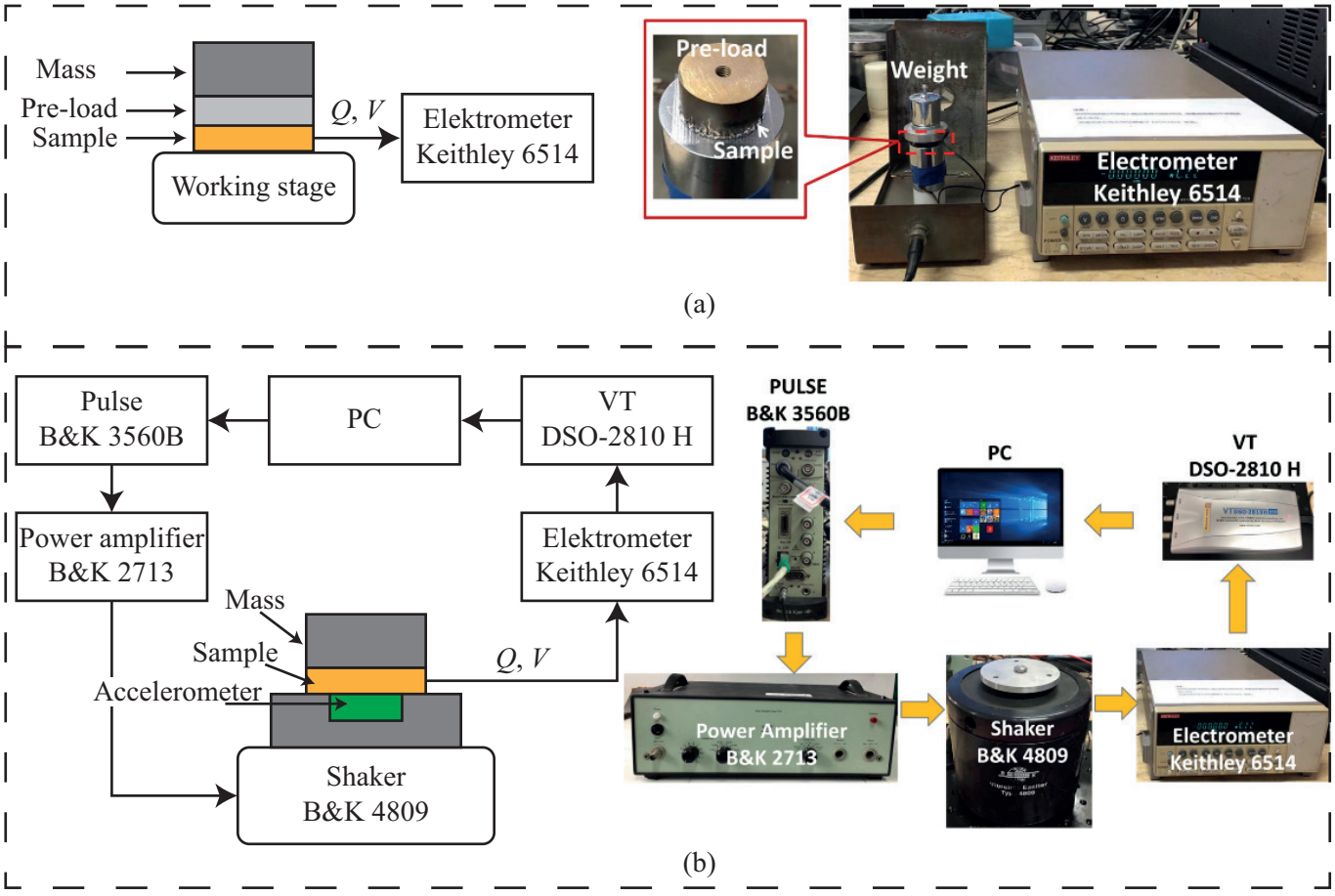

Figure 3.20: (a) Measurement setup for the quasi-static method illustrated as schematic diagram (left) and a picture (right). (b) Setup for dynamic measurement of the d_{33}-coefficients [48].

Table 3.2: Quasi-static d_{33} and g_{33}-coefficients of three different samples. The g_{33}-coefficients are calculated using equation 3.52 by considering the maximum and minimum effective permittivity [48].

Sample	t_{min} (µm)	t_{max} (µm)	F_3 (N)	V_3(V)	Q_3 (pC)	d_{33} (pC/N)	g_{33}^{min} (Vm/N)	g_{33}^{max} (Vm/N)
1	25	426	0.98	19.4	3130	3194	164	360.9
2	25	388	0.98	30.5	4600	4694	241.1	530.4
3	25	460	0.98	12.1	2006	2047	105.1	231.3

meter (VM-6370), which is placed next to the sample. The dynamic force acting on the sample while vibrating is

$$F_3 = m \cdot a. \tag{3.53}$$

The induced charge Q_3 on the electrodes is recorded using a signal collector (MI, VT DSO-2810 H) through an electrometer (Keithley 6514). Knowing the applied dynamic force on the sample and the generated charge, the d_{33} and g_{33}-coefficients can be calculated using equations (3.51) and (3.52), respectively.

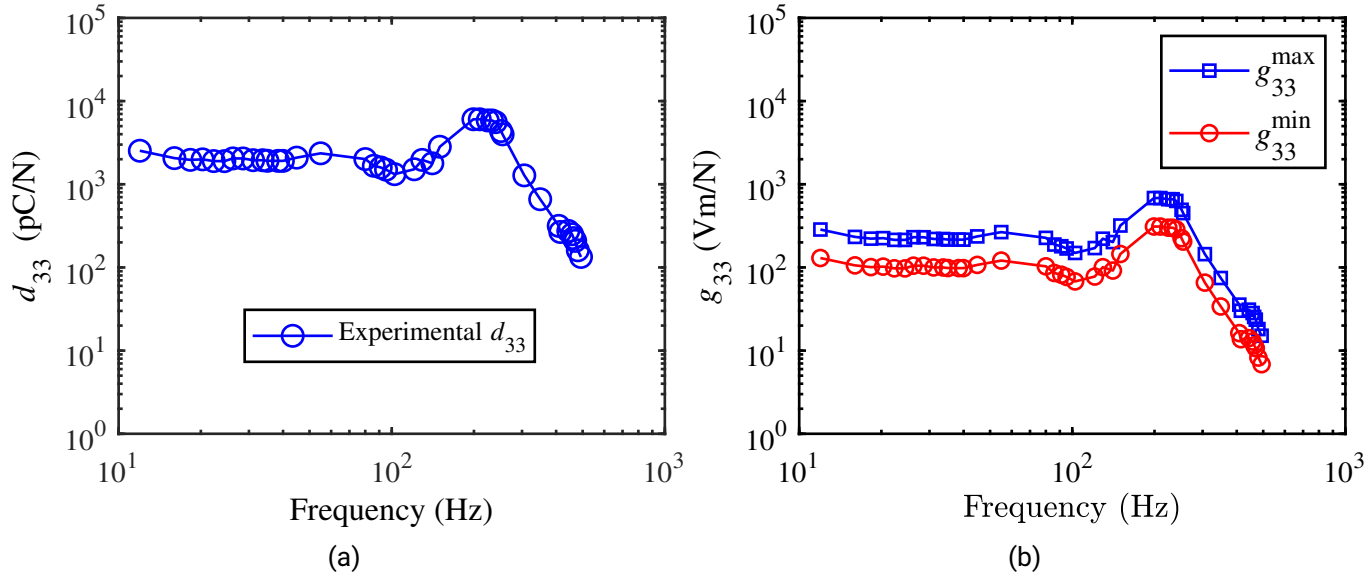

Figure 3.21: (a) Dynamic piezoelectric d_{33}-coefficient of a ferroelectret film with maximum thickness of $t_{max} = 340$ µm using a seismic mass of 25 g and (b) the calculated g_{33}-coefficients for $\varepsilon_{eff}^{max} = 2.1$ and $\varepsilon_{eff}^{min} = 1$ [48].

The measurement is performed in the frequency range from 10 to 1000 Hz using a seismic mass $m = 25$ g. The frequency response shows a relatively constant dynamic d_{33}-coefficient of approximately 2100 pC N^{-1} in the frequency range below 80 Hz. Afterwards, the d_{33}-coefficient decreases slightly in the frequency range between 80 and 100 Hz and increases again to reach approximately 6000 pC N^{-1} at the resonance frequency of approximately 200 Hz. The decrease of the d_{33}-coefficient with increasing frequency is a known effect of ferroelectrets, as reported in previous research using other films [143]–[145], and is due to the frequency dependence of the Young's modulus. The dynamic g_{33}-coefficient is relatively constant between 100 pC N^{-1} as minimum value and 280 pC N^{-1} as a maximum value for a vibration frequency under 80 Hz and between 310 pC N^{-1} and 683 pC N^{-1} at the resonance frequency.

Longitudinal piezoelectric d_{33} coefficient by acoustic method

The advantage of the acoustic method is that the wavy form of the ferroelectrets does not influence the measurement. Hereby, the d_{33}-coefficient is averaged over the complete sample area, due to the even distribution of the acoustic sound pressure. The sound pressure p at the location of the ferroelectret microphone is measured by a calibrated quarter-inch microphone (KW4420) (Figure 3.22). The sensitivity S_p of a microphone is defined as the ratio of the generated open-circuit voltage V and the sound pressure p acting on its diaphragm [146]. Knowing the sensitivity S_p, the d_{33}-coefficient can be calculated as [147], [148]

$$d_{33} = \frac{S_p \cdot C_{eff}}{A}, \tag{3.54}$$

$$\text{with } S_p = \frac{V}{p}, \tag{3.55}$$

where C_{eff} is the effective capacitance of the sample and A the active area.

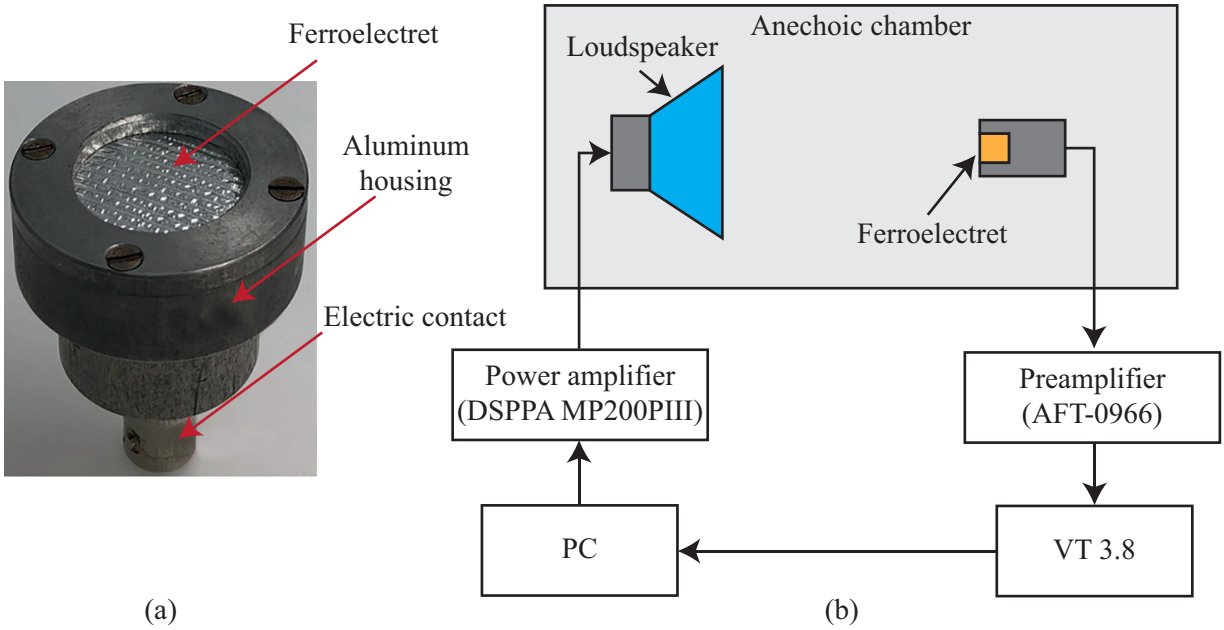

Figure 3.22: (a) Photograph of an FEP film microphone. (b) Schematics of the test system for measuring piezoelectric d_{33}-coefficient by the acoustic method [48].

The measured samples are cut into circles with 22 mm diameter and pasted on a brass back electrode with a double-sided adhesive conductive tape. The electrical shielding for the acoustic measurements is provided by an aluminum housing [Figure 3.22 (a)]. As a sound source, a computer controlled active dynamic loudspeaker is utilized and placed at a distance of 30 cm from the ferroelectret. For the measurement to be carried out under free field conditions, the whole setup is placed in an anechoic chamber. The sample is exposed to an uniform sound pressure in the frequency range from 300 Hz to 870 Hz allowing the determination of a proper average value of the d_{33}-coefficient, regardless of individual irregularities of the surface.

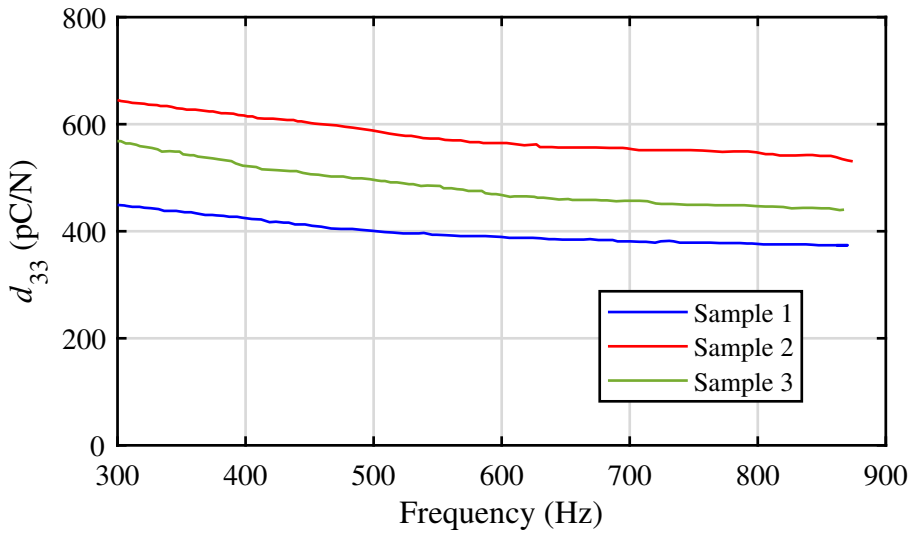

Figure 3.23: Frequency response of piezoelectric d_{33}-coefficients for similarly manufactured parallel-tunnel FEP film samples by acoustic method [48].

It should be noted that the free-field sound pressure p_{ff} at frequencies below 1 kHz is similar to the sound pressure p in front of the microphone. This means that the free-field sensitivity S_{ff} can be assumed to be equal to the pressure sensitivity S_{p}.

The d_{33}-coefficient measured for three different samples fall between 400 pC N^{-1} and 700 pC N^{-1} at the starting frequency 300 Hz. By increasing the frequency all samples exhibit the same behavior with a slight decrease over the measured frequency range. This can be explained by the fact that the sensitivity is inversely proportional to the Young's modulus Y [83], which in turn increases slightly with an increasing frequency. The increase of the Young's modulus was found for several polymers such as FEP, PTFE and PP in the frequency range between 10^2Hz and 10^6Hz [147], [149], [150]. The d_{33}-coefficients measured by the acoustic method are about 30% of the d_{33}-coefficients obtained by the dynamic method most probably due to the different stressing types.

During the dynamic measurement, the rigid seismic mass, which is glued to the sample, applies the stress mainly to the maximum thickness of the sample in addition to the static pre-stress. The effective area A on which the force is applied is smaller than the stressed area with the acoustic method due to the solid connection between the protruding parts of the tunnels. This results in larger mechanical stress and in addition to the focused force on the active parts of the film. When the ferroelectret with the seismic mass are set into vibration, the sample is distorted everywhere resulting in an adequate charge. This charge quantity depends on the local deformation and the local piezoelectric coefficient. Since the local properties are unknown, only an average stress by averaging the force over the total area of the sample can be considered.

During the acoustic measurement the acoustic pressure is applied uniformly to the complete sample. Hereby, because of the wavy geometry of the sample, the local deformations differ from each other, leading as well to local piezoelectric coefficients. Adding the geometrical inhomogeneity of the sample to the local properties leads to the fact, that the acoustic method as well allows only the measurement of an averaged piezoelectric response.

Stress dependence of d_{33} coefficient

Ferroelectrets show generally a nonlinear stress-strain behavior. However, when a small range of stress-strain is considered, the materials can be assumed to be linear around a working point. Therefore, the characterization of the stress dependence of the d_{33}-coefficient of the parallel-tunnel provides a better understanding of the linearity of such ferroelectrets. This study is caried out for all different measurement methods.

The quasi-static measurement shows a similar behavior of all three samples. By increasing the applied stress, the d_{33}-coefficient increases for stresses under 0.7 kPa and more slowly afterwards (Figure 3.24).

The first and third sample show a similar increase of the d_{33}-coefficient of almost 20 % when the stress is increased from 0.15 kPa to 3.1 kPa. The second sample is the most sensitive and shows more load dependence than the other samples. Between a mechanical stress of 0.15 kPa and 0.15 kPa, the d_{33}-coefficient almost doubled from 2479 pC N^{-1} to 4639 pC N^{-1}. The difference of the sensitivity of the samples is mainly due to the manufacturing tolerances resulting in nonuniform shapes of the tunnels. The load dependence on the other hand can be explained by the non-linearity of the stress-strain behavior of the film. Furthermore, a buckling effect due to non-homogeneity of the surface can not be excluded. In this case the inner surfaces of some tunnels come closer to each other resulting in inhomogenious charge distribution in the tunnels. This in turn could explain the different d_{33}-coefficients of different samples especially for small loads.

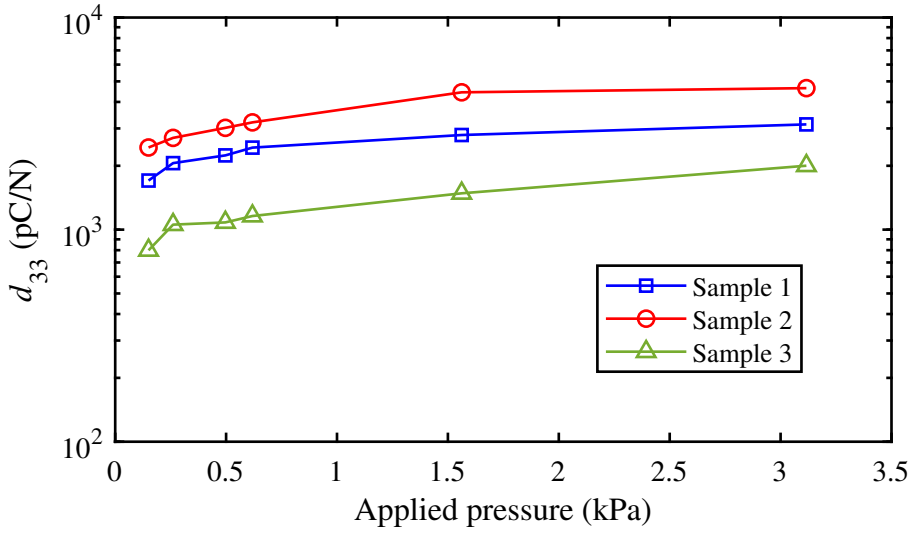

Figure 3.24: Load dependence of the quasi-static piezoelectric d_{33}-coefficients for parallel-tunnel FEP film samples as a function of applied pressure [48].

The static pre-load of the ferroelectret influences the initial deformation of the voids, which also influences the overall load dependencies and as a result the sensitivity of the film. Hereby, the working point of the ferroelectret is defined by the initial deformation given by the pre-load. In order to investigate this effect, the dynamic d_{33}-coefficient is measured for pre-loads ranging from 6.3 kPa to 21 kPa at a fixed frequency of 2 Hz.

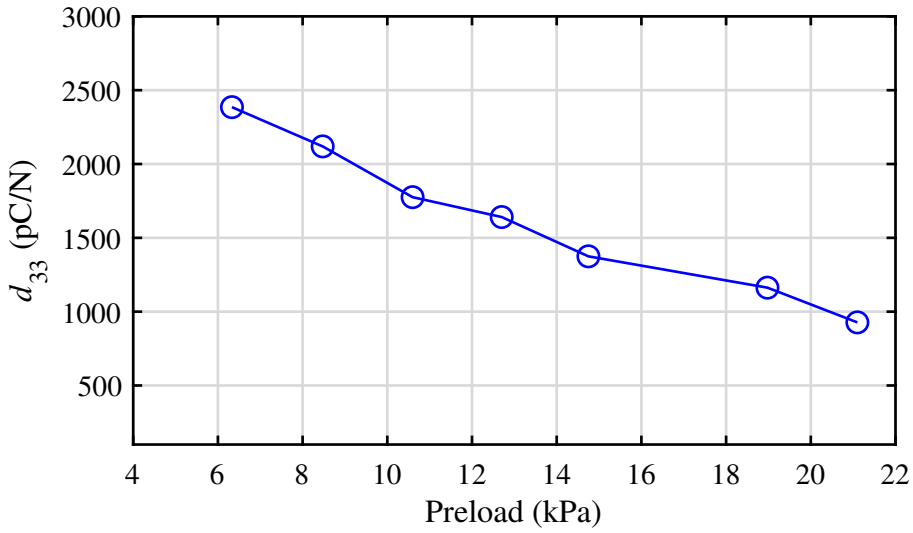

Figure 3.25: Stress dependence of the dynamic piezoelectric d_{33}-coefficient of a parallel-tunnel FEP film sample at 2 Hz [48].

A relatively strong decay of the piezoelectric d_{33}-coefficient with increasing pre-load is observed starting from approximately 2400 pC N^{-1} down to 940 pC N^{-1} at pre-loads of 6.3 kPa and 21 kPa, respectively. This is attributed to a compression of the cellular sample and the protrusions (e.g. buckling) at increasing stresses. In fact, the dynamic measurement includes two phases of deformation, which are the stress and the release. By increasing the initial deformation, the ferroelectrets become less declined to deformation under stress and

deforms more when released. This leads to smaller d_{33}-coefficients when increasing the pre-load.

Pre-strain dependence of d_{33} coefficient

For applications such as an accelerometer, the assembling of the ferroelectret with other mechanical components results in its stretching, which may affect the piezoelectric coefficients. In order to investigate the effect of stretching on the dynamic piezoelectric d_{33}-coefficient, a rectangular sample was used. Both ends of the sample were fixed on a vernier caliper for a defined strain (Figure 3.26). The ferroelectret is then placed between a vibrating electrode and a fixed electrode, which applies a pre-load of 6.4 kPa. Since one claw was fixed and the other claw can move, the elongation of the sample is adjusted by changing the total length of the sample. The length of the sample of 30 mm is considered as the initial state.

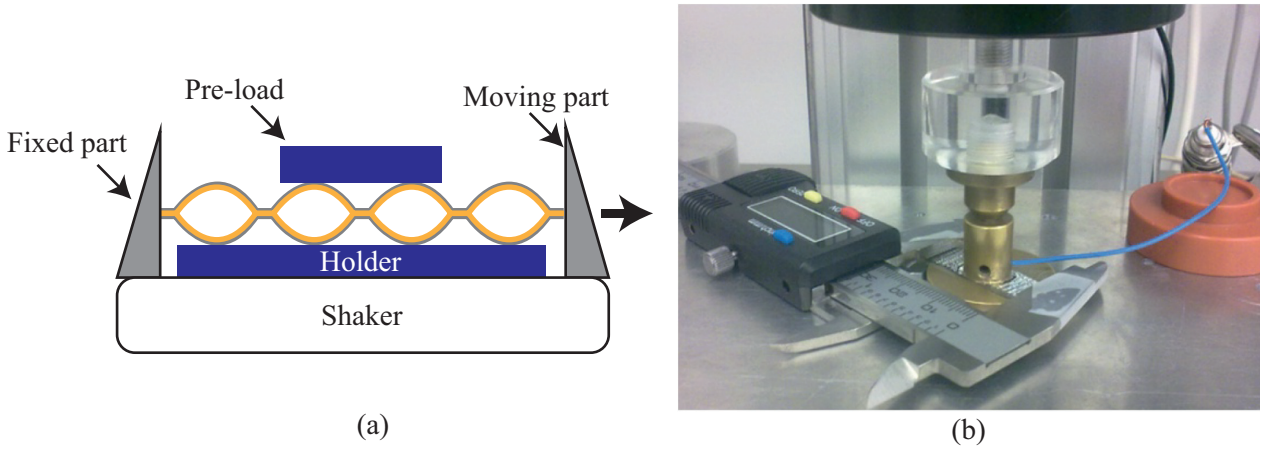

Figure 3.26: (a) Schematic representation of the setup for measuring the dependence of dynamic piezoelectric d_{33}-coefficient on stretching ratio, and (b) a photograph of the experimental setup [48].

As expected, for all measured frequencies between 2 Hz and 100 Hz, a change of the piezoelectric d_{33}-coefficient due to the increasing stretch ratio was observed (Figure 3.27). The maximum d_{33}-coefficient of 2848 pC N^{-1} is reached at a frequency of 20 Hz and a stretching ratio of approximately 2.1 %. If the same vibration frequency of 20 Hz is considered, the minimum d_{33}-coefficient of 2098 pC N^{-1} is reached at a stretching ratio of approximately 3.1 %.

Since the influence of the pre-strain on the longitudinal piezoelectric effect is relatively high, this should be considered when using these films as sensors in d_{33}-mode. Nevertheless, large piezoelectric-coefficients are maintained even with large pre-strain.

Since these films are made to be used in energy harvesting application, investigating their stability regarding the piezoelectric coefficients is mandatory. Therefore, three different stability tests are required: the thermal stability, humidity sustainability and fatigue resistance. These tests are valid for both the longitidunal and transversal effects.

Thermal stability

An important feature of sensors and energy harvesters is a temperature independent behaviour. In cases where the temperature would vary, it is essential that the films still exhibit the same performance. Although

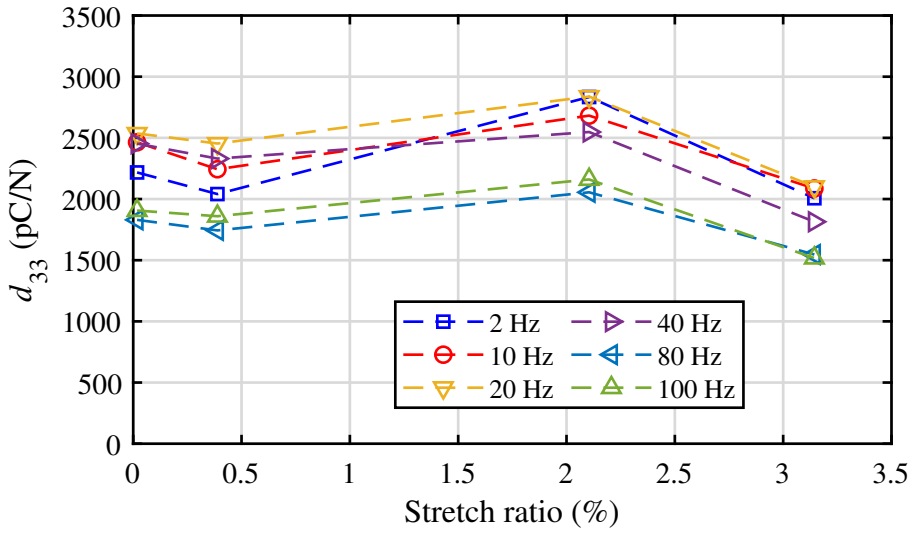

Figure 3.27: Influence of the stretching ratio on the dynamic piezoelectric d_{33}-coefficients of parallel-tunnel FEP samples [48].

FEP is known for its thermal stability as an electret material, at the time of this thesis, the thermal stability of parallel-tunnel FEP ferroelectret is still poorly characterized.

In order to eliminate the influence of the temperature during charging, all samples were polarized at room temperature. For investigating the isothermal decay of the quasi-static piezoelectric d_{33}-coefficient, three different sample groups are used. The piezoelectric d_{33}-coefficient of each sample is measured directly after the charging process. The initial d_{33}-coefficients of each sample are summarized in Table 3.3

Table 3.3: Initial Piezoelectric d_{33}-coefficients of FEP parallel-tunnel ferroelectret samples charged at different temperatures [48].

Group	Storage Temperature	Initial piezoelectric d_{33}-coefficient
1	25 °C	2337 pC N^{-1}
2	90 °C after pre-aging at 100 °C	2529 pC N^{-1}
	90 °C	3012 pC N^{-1}
3	120 °C	3601 pC N^{-1}

The first group of samples was stored at room temperature of 25 °C, the second group of samples was stored at 90 °C and the third group of samples was stored at 120 °C. The second group is then divided into two subgroups: the first subgroup was annealed at 90 °C directly after charging, and the second subgroup was first pre-aged at 100 °C for 30 min before annealing at 90 °C.

For a proper comparison of the decay of each group of samples, only the normalized piezoelectric d_{33}-coefficient is considered.

As one could expect, the samples of the first group show no notable decay of the piezoelectric d_{33}-coefficient over the measurement period of 21 h. A more interesting result is recorded for the second group which consists

of pre-aged and not pre-aged samples (Figure 3.28a). The measurement shows a similar speed of decay, however with different magnitude. The pre-aged samples retain approximately 80% after 20 h of the initial value, while the samples without pre-aging retain only 67% of the initial value. The samples annealed at 120 °C retained only 38% of the initial value after the same period of time.

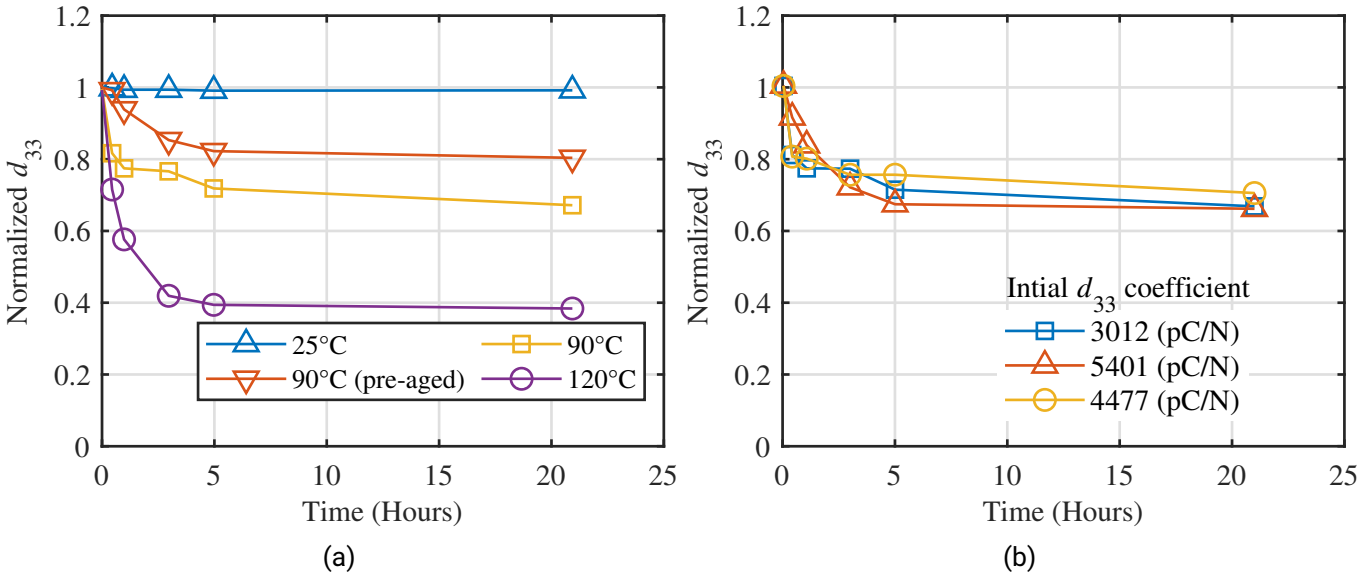

Figure 3.28: (a) Isothermal decays of quasi-static piezoelectric d_{33}-coefficients at various temperatures of different thermally treated samples. The tested sample marked 'pre-aged' was annealed at 100 °C for 30 min prior to the experiment. (b) Normalized isothermal decay of the d_{33}-coefficient of three different ferroelectrets at 90 °C (without pre-aging treatment) [48].

Since the initial values of the d_{33}-coefficient differ from each other, it is valid to suspect that a larger initial value is more likely to expect a larger drop. In order to exclude this assumption and explain the different isothermal decay, three similarly treated samples with different initial d_{33}-coefficients are chosen and stored at 90 °C. When the normalized values are considered, the measurements show a very similar decay of the initial d_{33}-coefficient (Figure 3.28b). Therefore, the observed decay at different temperatures is definitely not caused by the initial d_{33}-coefficients but rather by the storage temperatures and the prior treatment of the samples before the measurement. Such behaviour is also known for other ferroelectret materials such as FEP/PTFE [30], polyethylene-naphthalate (PEN) [151], cellular polyethylene (PE) [152] and PP [153]. Based on previous work using FEP [31], it is also expected that at 120 °C a faster decay of the piezoelectric activity can be recorded. However, since all samples are polarized at room temperature, the parallel tunnel ferroelectrets still feature a superior temprerature stability as well as a superior piezoelectric d_{33}-coefficient than all aforementioned materials.

To examine the thermal stability of the trapped charges in the ferroelectret, a short circuit TSDC is used. This technique is explained in section 2.4.2. The sample for this measurement is two-side metallized circular ferroelectret with 10 mm radius. The heating of the sample is carried out using a programmable oven with a heating rate of 3 °C min^{-1} from 25 °C to 300 °C. While heating, the generated discharge current is recorded using an electrometer (Keithley 6514).

Considering the polarization of the sample and how the terminals of the electrometer are connected, a postive TSD current indicates a transport of postive charges upwards or negative charges downwards within the

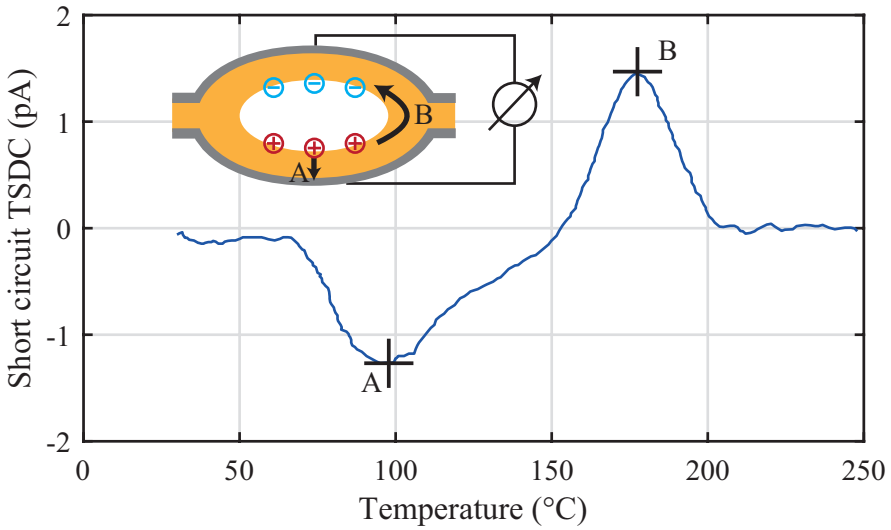

Figure 3.29: Short circuit TSD current spectrum without pre-aging treatment. The utilized sample had a circular shape with an electrode diameter of 20 mm. The two current peaks are marked A and B. The inset image shows the initial charge distribution after poling. Arrow A indicates the main transport pathways of detrapped positive charges at 100 °C and arrow B the pathway of detrapped negative charges at 180 °C.The quasi-static d_{33}-coefficients of the tested sample are 2326 pC N^{-1} and 7 pC N^{-1} before and after the TSDC measurement, respectively [48].

samples. A transport of charges in the opposite direction results in a negative TSD current. However, this only indicates a charge transport without exact information of which charge carriers are transported.

Two major current peaks are apparent in the measurement shown in Figure 3.29. The first peak, denoted ”A”, starts at approximately 70 °C and reaches a saturation between 90 and 100 °C. The sign of the peak is negative, which indicates a dominant transport of positive charges through the FEP layer. This corresponds to experimental results reported earlier regarding the activation temperature of energetic traps of postive charges in Teflon-A [154]. Due to the electrodes on both sides of the film, it should be mentioned that the positive charges recombine with part of the induced negative charges in the electrode. At a temperature of 150 °C a positive TSD current starts to increase and reaches a maximum at approximately 180 °C, denoted ”B”. This current is generated by the motion of detrapped negative charges [155]. This confirms earlier investigations of the stability of positive and negative charges in Teflon. However, the ferroelectret film is as stable as the least stable charges in the tunnel. For the piezoelectric behaviour, it is necessary for the ferroelectret to be carrying both polarity of the charges in the cavities. This explains the drop of the piezoelectric d_{33}-coefficient differently at 90 °C and 120 °C.

Humidity sustainability

The storage of electrets in humid environment results in forming of water-molecule clusters on its surface, due to the absorption of water molecules [156]. The accumulation of clusters results in percolation lattice that increases in time. For an increasing concentration of absorbed water, the separate clusters start to connect, leading to a connected cluster. Because of the larger conductivity of water in comparison to the polymer, a neutralization of the electret charges occurs, causing a fast discharge of the electrets.

For the humidity test, two different group of samples are used. A test group is stored in a closed glass container exhibiting 98% humidity and a control group is stored in lab environment with an average humidity of 60%. The decay of the piezoelectric activity of the parallel-tunnel ferroelectrets is determined by measuring the d_{33}-coefficients periodically.

Over the measurement period of 14 days, the samples of the control group show a stable piezoelectric coefficient. On the other hand the piezoelectric coefficients of the samples stored under high humidity drop to 80% after only three days. Afterwards the d_{33}-coefficient drops more slowly and remain stable at 75% of the initial value.

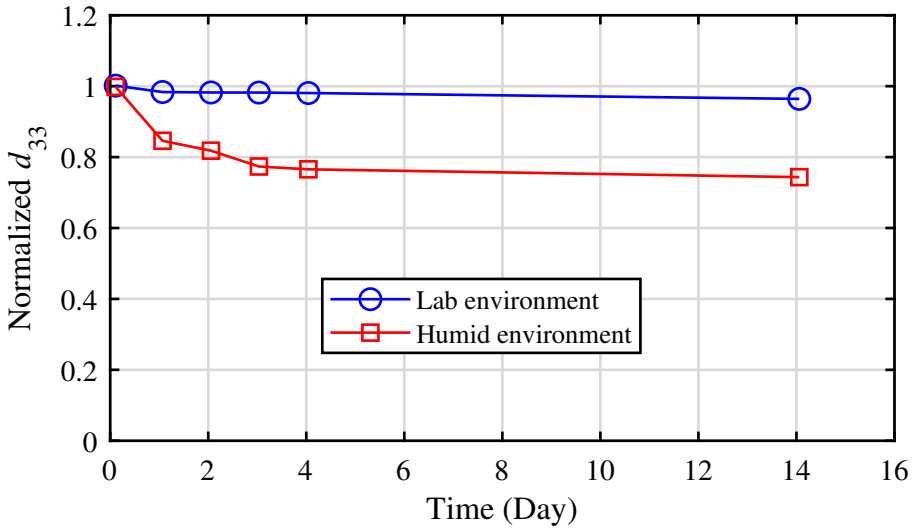

Figure 3.30: Humidity sustainability of the ferroelectrets with open tunnels [48].

Despite the tunnels being open, the parallel-tunnel ferroelectrets exhibit an acceptable stability in a humid environment. However, for their use as sensors in humid environment, waterproofing of the ferroelectret through protective layers should be considered [157], [158].

One more important property of these films considering their application in energy harvesting, is the transverse piezoelectric effect. In the following, the piezoelectric d_{31} and g_{31}-coefficients are examined.

Transverse piezoelectric d_{31}- and g_{31}-coefficients

The quasi-static transverse piezoelectric g_{31}-coefficient of the parallel-tunnel FEP ferroelectrets is determined using rectangular samples with an electrode length l and width w of 30 mm and 10 mm, respectively [Figure 3.19(d)]. w_0 is the total width of the sample, which is a larger than w to avoid any contact between the electrodes of both sides of the ferroelectret. The samples are tested utilizing a tensile tester (KJ-1065 A) that stretches them in x-direction by a static force F_1. The generated voltage V_3 between the electrodes in 3-direction is recorded with an electrometer (Keithley 6514). Since the applied force F_1 acts on the whole sample and not only the active area, the effective force F_1' can be expressed as

$$F_1' = F_1 \frac{w}{w_0}. \tag{3.56}$$

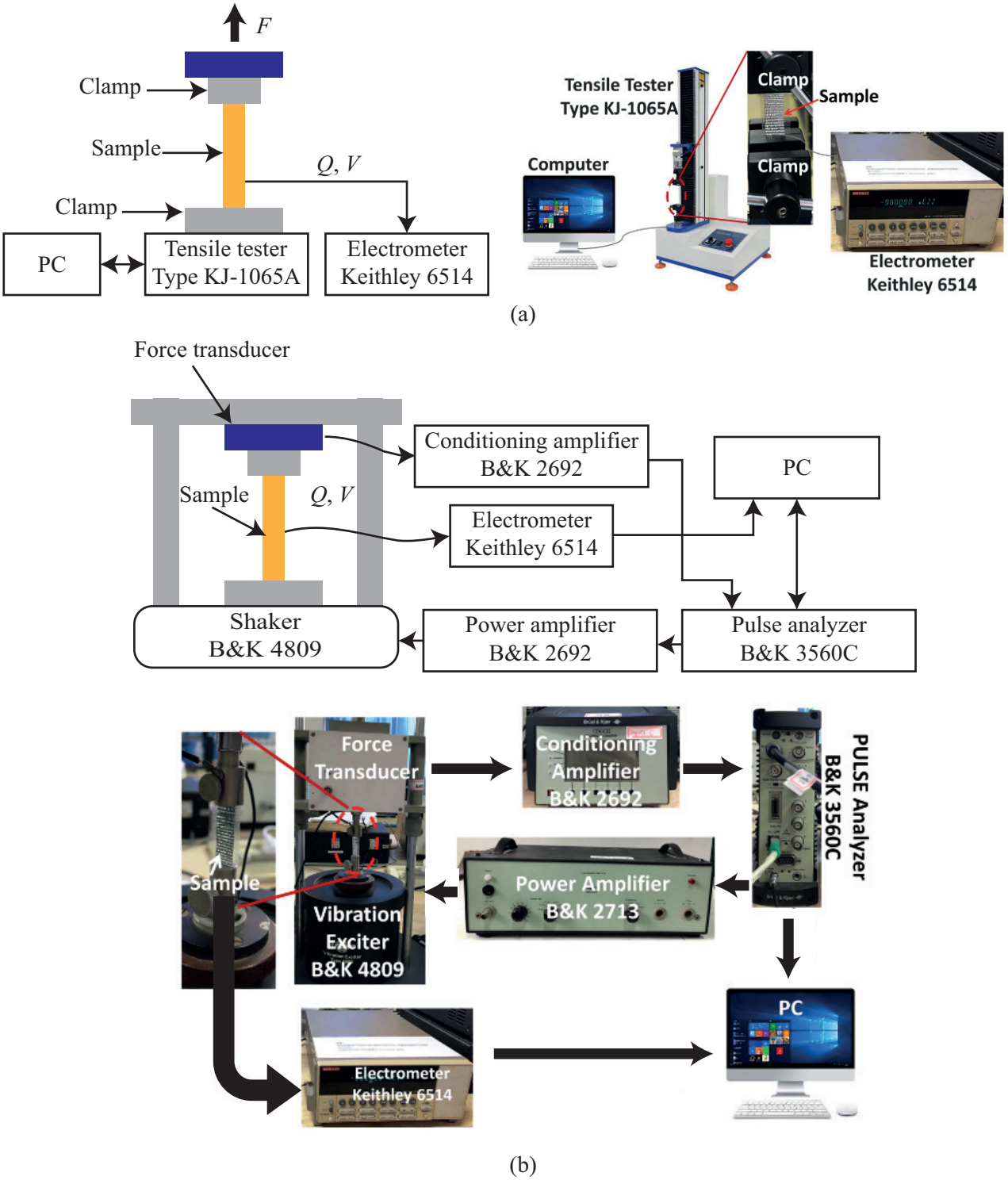

Figure 3.31: Measurement setup for determining piezoelectric g_{31}-coefficient in parallel-tunnel FEP ferroelectret films. (a) Setup for quasi-static measurements: schematic diagram (left) and photograph (right). (b) Setup for dynamic measurement: schematic diagram (top) and photograph (bottom) [48].

The g_{31}-coefficient and the d_{31}-coefficient have to be expressed as

$$g_{31} = \frac{E_3}{T_1} = \frac{V_3}{F_1'} w, \tag{3.57}$$

$$\begin{aligned} d_{31} = \frac{D_3}{T_1} &= \frac{\frac{Q_3}{w\ l}}{\frac{F_1'}{w\ t_{\text{eff}}}} = \frac{C_{\text{eff}} \cdot V_3}{F_1'} \frac{t_{\text{eff}}}{l} \\ &= \frac{\varepsilon_0 \varepsilon_{\text{eff}} \frac{w \cdot l}{t_{\text{eff}}} \cdot V_3}{F_1'} \cdot \frac{t_{\text{eff}}}{l} = \frac{V_3}{F_1'} w \varepsilon_0 \varepsilon_{\text{eff}} = g_{31} \varepsilon_0 \varepsilon_{\text{eff}}, \end{aligned} \tag{3.58}$$

where T_1 denotes the applied stress in x-direction and the other physical quantities were discussed previously.

Accoring to equation(3.57), the transverse piezoelectric voltage coefficient g_{31} is thickness independent and can be unambiguously determined experimentally. The transverse piezoelectric charge coefficient d_{31}, however, has a maximum and a minimum depending on the value used for ε_{eff} as discussed for determining the g_{33}-coefficient. The maximum and minimum values can be calculated as

$$\begin{aligned} d_{31,\text{min}} &= g_{31} \varepsilon_0 \varepsilon_{\text{air}} \\ d_{31,\text{max}} &= g_{31} \varepsilon_0 \varepsilon_{\text{FEP}}. \end{aligned} \tag{3.59}$$

The measurements of the quasi-static g_{31}-coefficients are conducted using the setup shown in Figure 3.31(a). The experimental results of the quasi-static g_{31}-coefficient show values up to $4.24\,\text{V m N}^{-1}$ reached by sample 4, which corresponds to d_{31}^{min} and d_{31}^{max} of $37.5\,\text{pC N}^{-1}$ and $82.6\,\text{pC N}^{-1}$, respectively. The measurement of similarly manufactured samples are summarized in Table 3.4. As a reference, the ferroelectrets are compared

Table 3.4: Results of quasi-static g_{31}-coefficients determined experimentally and upper and lower limits of the d_{31}-coefficients for three parallel-tunnel FEP film samples [48].

Sample	l (mm)	W (mm)	F_1' (N)	Q_3 (pC)	V_3(V)	g_{31} (Vm/N)	d_{31}^{min} (pC/N)	d_{31}^{max} (pC/N)
4	30	10	0.0125	250	5.3	4.24	37.5	82.6
5	30	10	0.0286	331	5.6	1.96	17.3	38.2
6	30	10	0.0313	370	6.6	2.11	18.7	41.1

with a commercial PVDF sample, whose measurement is conducted using the same measurement setup, results in d_{31} and g_{31}-coefficients of $16\,\text{pC N}^{-1}$ and $0.18\,\text{V m N}^{-1}$, respectively, which are considerably smaller than those of the parallel tunnel structure.

For measuring the dynamic piezoelectric g_{31}-coefficient, the ends of the sample pointing in x-direction are clamped for force application. A force transducer is utilized to measure the sinusoidal stretching force generated by the shaker (B&K 4809) driven by a PULSE Analyzer and amplified by a power amplifier (B&K 2713). The signal of the force sensor is recorded using a Conditioning Amplifier (B&K 2692) and a PULSE Analyzer (B&K 3560 C). The dynamic open-circuit voltage V_3 is recorded by the same PULSE analyzer through an electrometer (Keithley 6514) (Figure 3.31). The measurements are performed in the frequency range from 10 to 100 Hz with a dynamic force of 0.0125 N.

The experimental values of g_{31}-coefficients and based on it the d_{31}-coefficients show a decreasing trend for increasing frequencies, from $1.2\,\text{V m N}^{-1}$ at 10 Hz down to $0.78\,\text{V m N}^{-1}$ at 100 Hz [Figure 3.32(a)]. The

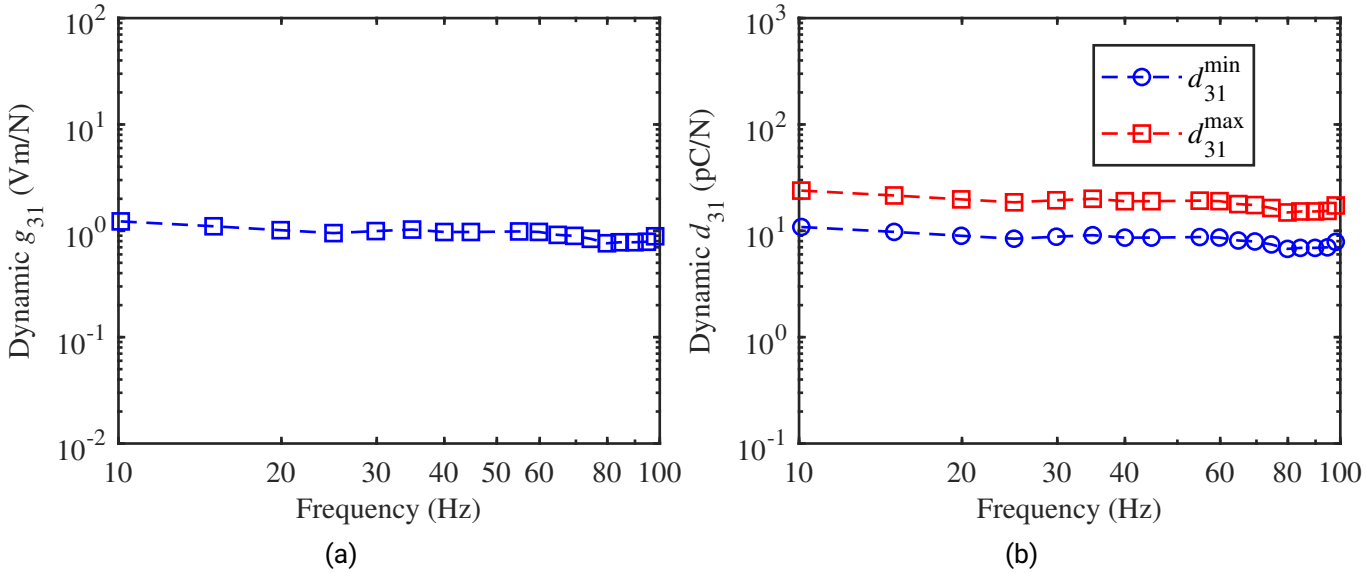

Figure 3.32: (a) Frequency response of the piezoelectric g_{31}-coefficient of sample 4. The maximum thickness of the test sample is 431 µm. (b) maximum and minimum values of the dynamic d_{31}-coefficient calculated equation (3.59) [48].

dynamic g_{31}-coefficient at 100 Hz is only about 20% of the quasi-static value. This drop with increasing frequency is expected due to the viscoelastic property of the film, i.e. to the increase of the stiffness with frequency [149]. The upper and lower limits of the calculated d_{31}-coefficients for $\varepsilon_{\min} = 1$ and $\varepsilon_{\max} = 2.2$ are approximately 11 pC N^{-1} and 24 pC N^{-1}, respectively, at 10 Hz [Figure 3.32(b)]. By increasing the frequency up to 100 Hz, these values decrease to a maximum value of approximately 17 pC N^{-1} and minimum value of approximately 8 pC N^{-1}. Note that the maximum values can not be really reached, since $\varepsilon_{\max} = 2.2$ corresponds to collapsed air tunnels, that can not contribute to the piezoelectric effect, resulting in piezoelectric coefficients equal to zero.

Since this decrease is caused mainly by the viscoelastic property of FEP, it is mandatory to investigate the stability of the piezoelectric coefficients of the parallel-tunnel ferroelectret upon mechanical fatigue. Since in actual applications, repeated reversible mechanical pressure or tension is applied to the ferroelectret films.

To evaluate the sustainability of parallel-tunnel ferroelectrets against stress, a periodic dynamic force at a fixed frequency was applied to the samples for about 1.6 million cycles. The quasi-static d_{33} and g_{31}-coefficients are then measured at selected number of cycles. Each coefficient is investigated under one type of force application: the d_{33}-coefficient is investigated by applying a force of 240 N at a frequency of 110 Hz in thickness direction, whereas the g_{31}-coefficient is investigated by stretching the sample with a force of 30 mN at a frequency of 100 Hz. Both the longitidunal and transversal piezoelectric coefficients are stable. The g_{31}-coefficient, however, is pre-stress dependent which results in different stability of the samples. This pre-stress can not be measured as it depends on the homogeneity of the structure itself and the manufacturing tolerance.

In conclusion, the parallel tunnel ferroelectrets exhibit outstanding piezoelectric d_{33} and d_{31}-coefficients, which are key parameters in energy harvesting as mentioned before. However, because of the wavy form of the structure, a d_{33} harvester configuration is unstable and not reproducible. In fact, the seismic mass does not follow the acceleration and starts to wiggle when set into vibration. Nevertheless, due to the high transverse coefficient of these ferooelectrets, it was possible to develop energy harvesters as presented by Zhang et

al. [46]. However, the performance of such harvester depends on its orientation with respect to gravity in addition to its low robustness. Therefore, more rugged energy harvester solutions have to be introduced.

3.4 Simple air-spaced cantilever design

The most common design of d_{31}-based energy harvester is the use of a cantilever, with piezoelectric layers on one side (unimorph) or both sides (bimorph) of the beam. The piezoelectric layer is generally flexible such as PVDF or composite of polymer with PZT fibers. Such materials exhibit a Young's modulus in the range of GPa and influence therefore the overall stiffness of the cantilever. Furthermore, an excessive strain of such materials leads to their destruction, which should be taken into account. A unique property of the parallel-tunnel ferroelectrets in comparison with other piezoelectric polymers apart from the large piezoelectric d_{31}-coefficient, is their outstanding flexibility. The Young's modulus is approximately 1 MPa [46]. This offers the opportunity to further stretching the film without worrying about influencing the stiffness of the cantilever structure. A way to generate a large strain of the piezoelectric polymer using a cantilever design is to place the film at a large distance from the neutral axis, which is the approach in this work.

The energy harvester using the parallel-tunnel ferroelectret consists basically of a cantilever and at a certain distance h the ferroelectret film. The dynamic stretching is achieved via the displacement of the tip mass by subjecting the cantilever base to an acceleration a (see Figure. 3.33). The orientation of the tunnels is perpendicular to the cantilever direction. Since the piezoelectric d_{31}-coefficient depends on the thickness of the ferroelectret film, it is more appropriate to use the thickness-independent piezoelectric g_{31}-coefficient for modeling the output power of the such harvester.

3.4.1 Theoretical model of the cantilever based energy harvester

When the cantilever base is subjected to an acceleration a in z-direction, the tip mass is deflected by inertia into the negative z-direction from its position of equilibrium and forms an angle φ with the cantilever's plane [see Figure 3.33(b)]. The deflection z of the free end of a cantilever depends on the seismic mass and thus is the result of a point force F concentrated at its free end pointing into the negative z-direction. The obtained deflection z is given by [159]

$$z = \frac{F L_{\mathrm{C}}^3}{3 Y I}, \tag{3.60}$$

where L_{C} is the length of the cantilever, Y its Young's modulus and I the moment of inertia of the beam. It should be mentioned that the force F is also pointing in the same direction as the inertia induced deflection z. For small z deflections, the displacement of the tip of the cantilever in the x-direction can be neglected. The transverse contraction of the beam and the ferroelectret film is also neglected. The angle φ can be expressed as [160]

$$\varphi = \frac{3}{2} \frac{z}{L_{\mathrm{C}}}. \tag{3.61}$$

The change of the length of the ferroelectret film is then geometrically determined by the intercept theorem, still neglecting the displacement of the cantilever tip in x-direction, as suggested by Beléndez [160]. Under these assumptions one obtains

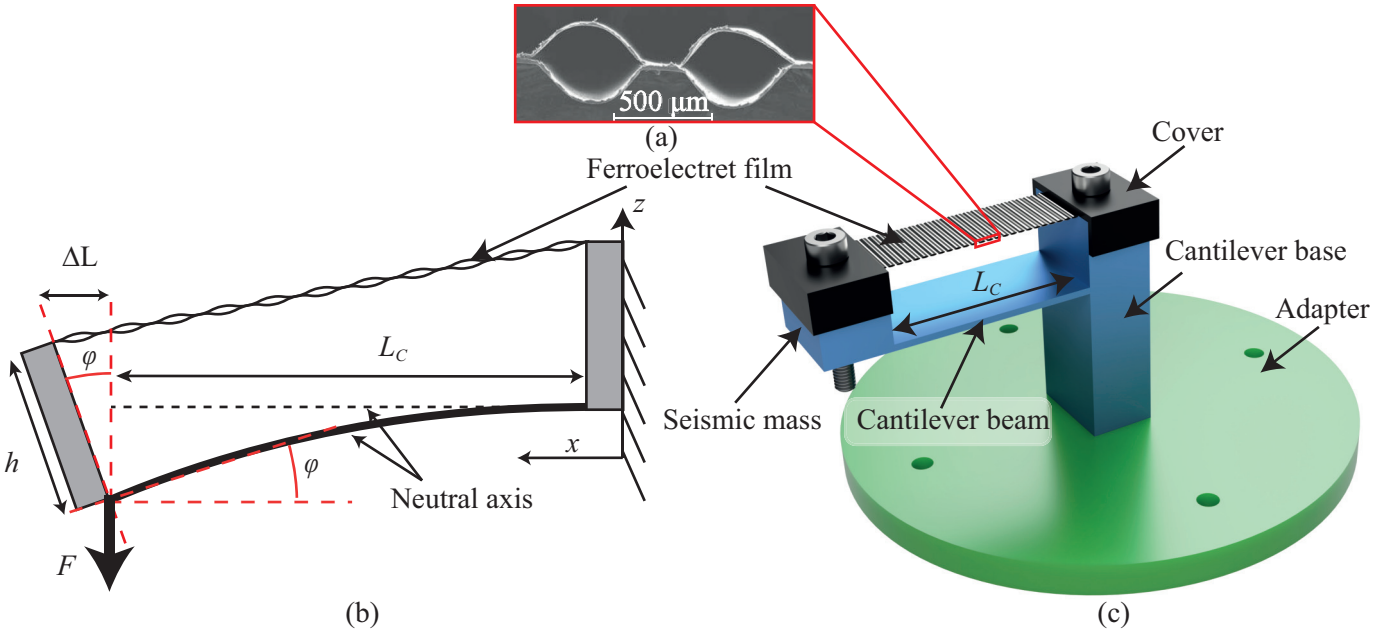

Figure 3.33: (a) Cross section of a parallel-tunnel FEP ferroelectret film. (b) 3D representation of the air-spaced cantilever energy harvester.(c) Cantilever beam loaded with an external load F in negative z-direction at the free end. This illustrates the cantilever beam under exaggerated bending condition. The black dashed line represents the non-deflected state while the thick black line is the deflected neutral axis of the cantilever beam [49], [50].

$$\Delta L = h\varphi = \frac{3hz}{2L_{\mathrm{C}}}. \tag{3.62}$$

Hence, only for small deflections the stretching of the film is proportional to its distance h from the neutral axis of the cantilever beam. Since the z axis is defined as the direction of acceleration and the x axis is the perpendicular axis, the equation of motion for the cantilever's tip in z-direction can be written as

$$\ddot{z} + 2\zeta\omega_0\dot{z} + \omega_0^2 z = -a. \tag{3.63}$$

Assuming a sinusoidal steady-state motion, the displacement z can be expressed as

$$z = \frac{-a}{\omega_0^2 - \omega^2 + 2j\zeta\omega_0\omega}, \tag{3.64}$$

where ω is the exciting angular frequency of the cantilever base, $\omega_0 = \sqrt{k_{\mathrm{C}}/m}$ the resonance frequency of the undamped harmonic oscillator of the beam which depends on the cantilever stiffness k_{C} and the damping constant ζ of the beam. In this approach, the influence of the spring constant k_{f} and the damping constant of the ferroelectret on the resulting cantilever properties are neglected. Substituting z in equation (3.62), the film's elongation ΔL can then be expressed as

$$\Delta L = \frac{3h}{2L_{\mathrm{C}}} \cdot \frac{-a}{\omega_0^2 - \omega^2 + 2j\zeta\omega_0\omega}\,. \tag{3.65}$$

Using the direct piezoelectric voltage coefficient $g_{31} = (V_{\mathrm{OC}}/F_1) \cdot w_{\mathrm{F}}$ linking the generated open circuit voltage V_{OC} to the applied force F_1 on the ferroelectret film in x-direction (which differs from the force F in z-direction) and utilizing the mechanical force constant k_{f} of the ferroelectret film, the voltage V_{OC} generated in open circuit can be written as

$$\begin{aligned} V_{\mathrm{OC}} &= \frac{g_{31}}{w_{\mathrm{F}}} F_1 = \frac{g_{31}}{w_{\mathrm{F}}} k_{\mathrm{f}} \cdot \Delta L \\ &= \frac{g_{31}}{w_{\mathrm{F}}} k_{\mathrm{f}} \cdot \frac{3h}{2L_{\mathrm{C}}} \cdot \frac{-a}{\omega_0^2 - \omega^2 + 2j\zeta\omega_0\omega}, \end{aligned} \tag{3.66}$$

where w_{F} is the ferroelectret film width. The rms-value of the voltage V_{L} across a load resistance R_{L} connected between the electrodes of the ferroelectret film can be written by means of a voltage divider as

$$V_{\mathrm{L,rms}} = V_{\mathrm{oc,rms}} \frac{R_{\mathrm{L}} C\omega}{\sqrt{1 + (R_{\mathrm{L}} C\omega)^2}} = \frac{g_{31}}{w_{\mathrm{F}}} k_{\mathrm{f}} \cdot \frac{3h}{2L_{\mathrm{C}}} \frac{\frac{a}{\omega_0^2}}{\sqrt{\left(1 - \left(\frac{\omega}{\omega_0^2}\right)^2\right)^2 + 4\zeta^2 \left(\frac{\omega}{\omega_0}\right)^2}} \cdot \frac{R_{\mathrm{L}} C\omega}{\sqrt{1 + (R_{\mathrm{L}} C\omega)^2}}, \tag{3.67}$$

where C is the static capacitance of the ferroelectret film. Since this equation is only valid for small displacements, the change of film capacitance is much smaller than its static value. Thus, the capacitance can be assumed to be constant. Increasing the acceleration a of the cantilever base results in further stretching of the ferroelectret film, and, thus, results in a higher output power, i.e.

$$P_{\mathrm{out}} = \frac{V_{\mathrm{L,rms}}^2}{R_{\mathrm{L}}} = \left(g_{31} \frac{3hk_{\mathrm{f}}}{2L_{\mathrm{C}} w_{\mathrm{F}}}\right)^2 \frac{a^2 R_{\mathrm{L}} C^2 \frac{\omega^2}{\omega_0^4}}{\left[\left(1 - \left(\frac{\omega}{\omega_0}\right)^2\right)^2 + 4\zeta^2 \left(\frac{\omega}{\omega_0}\right)^2\right] \left[(1 + R_{\mathrm{L}} C\omega)^2\right]}. \tag{3.68}$$

The maximal power at the resonance frequency, for the optimal load resistance $R_{\mathrm{L}}^{\mathrm{opt}} = 1/C\omega_0$, amounts to

$$P_{\mathrm{out}}^{\mathrm{max}} = \left(g_{31} \frac{3\,h\,k_{\mathrm{F}}}{2\,L_{\mathrm{C}}\,w_{\mathrm{F}}}\right)^2 \frac{C}{8\xi^2\omega_0^3} a^2 = \frac{9}{32} \frac{h^2}{L_{\mathrm{C}}^2 \xi^2 \omega_0^3} \frac{k_{\mathrm{F}}^2}{w_{\mathrm{F}}^2} g_{31}^2\, C\, a^2. \tag{3.69}$$

According to equation (3.69), the maximum power output with the optimal load exhibits the same dependence on the resonance frequency as a ferroelectret energy harvester based on the d_{33}-coefficient. Apart from the properties of the cantilever beam and from the ferroelectret film, the parameter with the major influence on the generated power is the distance h between the film and the neutral axis of the beam. However, increasing the distance h or using a large acceleration a, leads to a larger ΔL, which is restrained due to increasing restoring force of the ferroelectret film described by k_{F}. This leads to an increase of the stiffness of the film-cantilever system and an increase of the resonance frequency. For the presented cantilever geometry, the measurement of the resonance frequency of the cantilever structure with and without ferroelectret film, shows a difference of approximately 2 Hz.

3.4.2 Validation of the theoretical model

The parallel-tunnel ferroelectret film used in this study has the dimensions of $10 \times 40\,\mathrm{mm}^2$. It exhibits static and dynamic piezoelectric g_{31}-coefficients of $1.9\,\mathrm{V\,m\,N^{-1}}$ and $0.8\,\mathrm{V\,m\,N^{-1}}$, respectively. The energy-harvesting

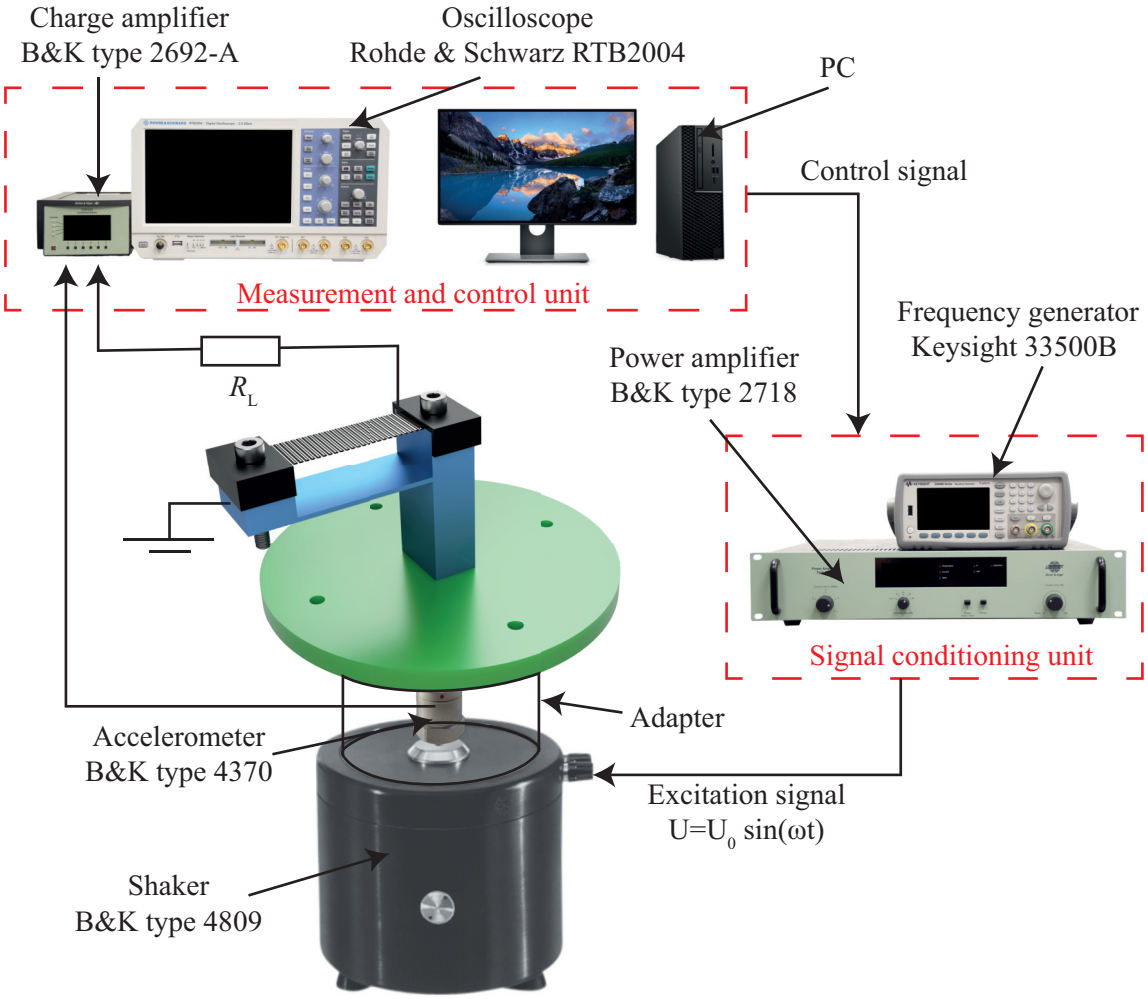

Figure 3.34: Schematics of experimental setup used for energy harvesting evaluation [50].

device is an air-spaced cantilever arrangement that is mostly made by additive manufacturing technique known as fused deposition modeling (FDM). The used cantilever material hereby is polylactide acid (PLA) with 15% infill and a gyroid fill pattern. The cantilever beam of dimension $10 \times 30\,\mathrm{mm}^2$ is responsible for the stiffness of the mechanical resonant system. The ferroelectret film is incorporated into the structure by clamping it between the cantilever base and the seismic mass [Figure 3.33(c)]. The metal electrodes are connected to an external electrical network consisting of the load resistor R_L in addition to a charge amplifier (B&K Nexus TYPE 2692-A) and a digital oscilloscope (Rohde & Schwartz RTB 2004) (see Figure 3.34). The device is tested by exposing it to vibrations with an acceleration a generated by a shaker (Brüel&Kjaer type 4809) driven by a function generator (Keysight 33500B Series) and a power amplifier (B&K 2718). The generated power is determined as a function of frequency by terminating the ferroelectret with a load resistor $R_\mathrm{L} = \frac{1}{\omega_0\, C}$. The film capacitance is measured with an impedance meter (LCR Databridge 451).

The power generated is measured through the optimal resistance $R_\mathrm{L}^\mathrm{opt}$, whereas the normalized power is

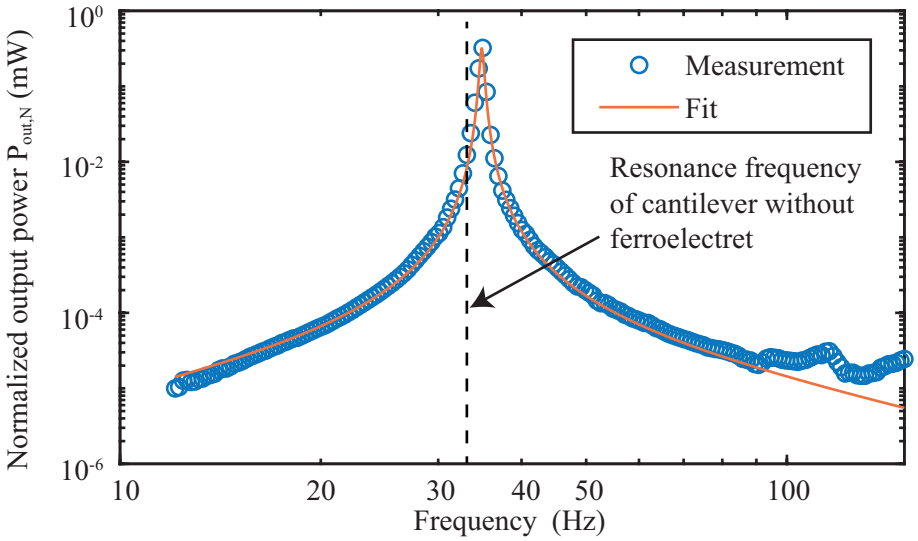

Figure 3.35: Normalized power of a cantilever-based ferroelectret energy harvester with a distance h of 1 cm between the ferroelectret film and the cantilever neutral axis and a seismic mass of 4.5 g. The theoretical curve is calculated from equation (3.68) and (3.46) using parameters of Table 3.5. The actual acceleration at the resonance frequency amounts to 0.1 g, whereas the normalized power is calculated using equation (3.46). Also shown (dashed line) is the resonance frequency of the cantilever without the ferroelectret [49].

calculated using equation (3.46). The fit of experimental results according to equation (3.68) is used to determine the variables ξ while other parameters listed in Table 3.5 are treated as experimentally verified for the fitting procedure. The parameters used for the calculations of the generated power via equation (3.68) are summarized in Table 3.5.

Table 3.5: Parameters for the calculations of Figure 3.35.

Parameters	Fit values	Source
g_{31} (Vm/N)	0.8	Measurement
C (pF)	40	Measurement
h (mm)	10	Measurement
L_C (mm)	30	Measurement
w_F (mm)	10	Measurement
R_L (MΩ)	113	Measurement
k_F (N/m)	∼500	Calculated from [23]
f_0 (Hz)	34.7	Measurement
ξ	0.0084±0.0001	Fit

The measurement of the normalized power $P_{out,N}$, generated by a ferroelectret energy harvester into a load resistance R_L (Figure 3.35), agrees well with the fit result obtained from equation (3.46). At frequencies well below resonance, $P_{out,N}$ increases proportionally to ω^2 and at frequencies above resonance it decreases proportionally to $1/\omega^4$. Referred to the seismic mass of 4.5 g and to the applied acceleration of $0.1\,g$, a maximum normalized power of 320 µW at resonance is achieved.

Further validation of the theoretical dependencies of the model requires the investigation of the influence of the seismic mass on the frequency response as well as the maximum power generated. This is achieved by adding various masses to the tip of the cantilever, which are fixed by the screw, and measuring the corresponding frequency responses. The tip mass without additional mass amounts to 4.5 g whereas the maximum mass equals 12.1 g. The measurement shows that the resonance frequency of the energy harvester decreases proportionally to $1/\sqrt{m_s}$ as expected from the model (Figure 3.36). The normalized power at resonance frequency is proportional to $m_s^{3/2}$ (Figure 3.36). This relation between $P_{\text{out,N}}$ and m_s follows from equation (3.68) using the relation $\omega_0^2 = k_C/m_s$, where k_C is the spring constant of the complete energy harvester.

All measurements are conducted at the same acceleration for a better comparison of the results. One major

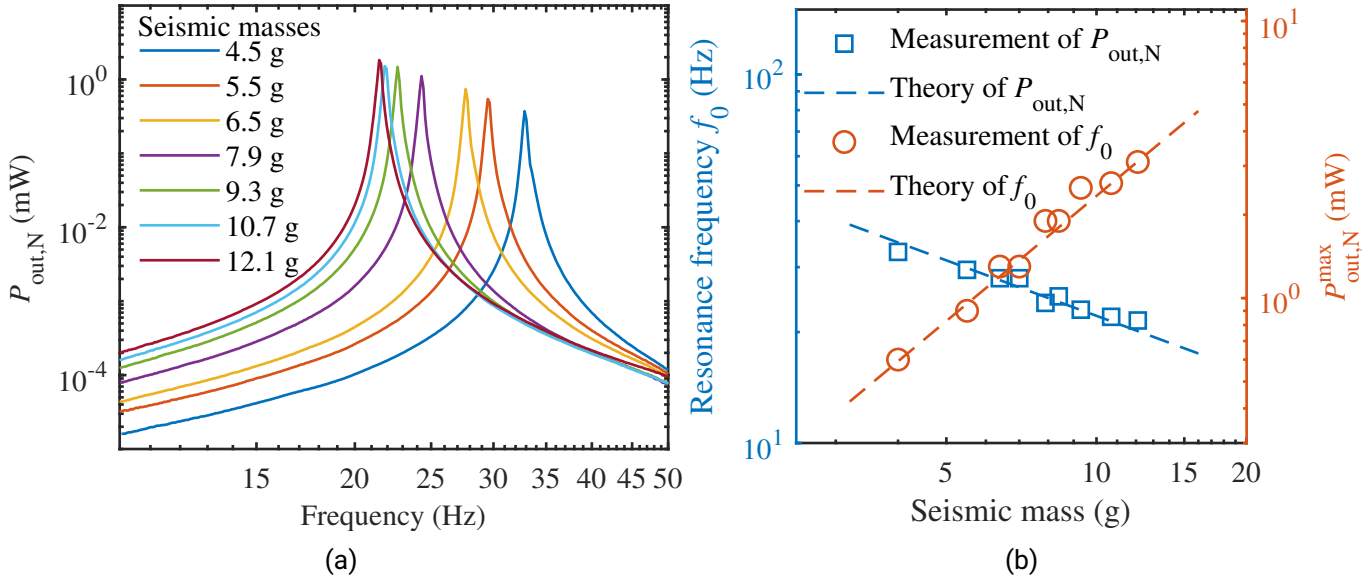

Figure 3.36: (a) Measured frequency responses of the normalized power of an energy harvester with various seismic masses including the tip mass. (b) Normalized power at resonance and resonance frequency as a function of seismic mass. The theoretical curves are fitted, using the expected slopes [49].

difference to the conventional cantilever based energy harvesters, where the piezoelectric film is directly placed on the cantilever, is that the film in the air-spaced configuration does not follow the deformation of the cantilever. When the film is directly applied to the surface of the cantilever beam, the bending direction of the beam leads to its stretching or compressing. In the air-spaced cantilever design, on the other hand, the film is stretched in one direction and released in the other one. This results in an increased dependency of the air-spaced configuration on the acceleration. To investigate that effect, the cantilever is subjected to various acceleration amplitudes ranging from 0.005 g to 0.5 g (rms) and the generated power at resonance is measured for each acceleration amplitude. Hereby, one seismic mass of 4.5 g (tip mass) is used in all cases. Below an acceleration of 0.06 g, the generated power is proportional to a^2, as expected from equations (3.68) and (3.69). Referred to an rms value of 1 g, the results correspond to a normalized power of approximately 0.8 mW [Figure 3.37(b)]. For $a > 0.06\,g$, the generated power increases less than proportionally to a^2, reaching a normalized value $P_{\text{out,N}} = 80\,\mu\text{W}$ for $a = 0.5\,g$. This decrease can be explained by the mechanical behavior of the ferroelectret film in the two stages of deformation developed during upward and downward cycles. When the cantilever is bent upward [Figure 3.37(c)] for large amplitude vibrations, the film as such is bent instead

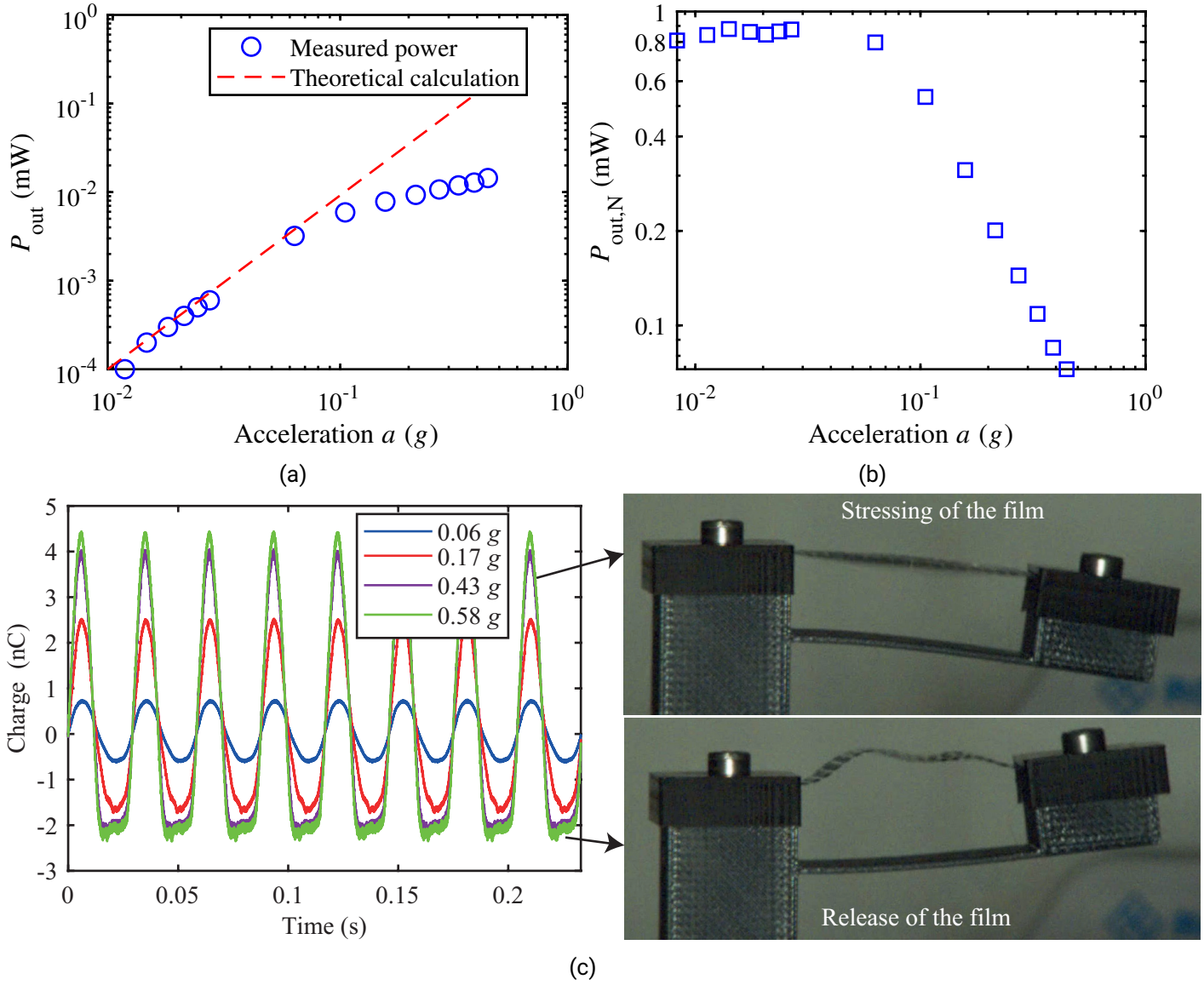

Figure 3.37: (a) Power generated by a cantilever-based ferroelectret energy harvester at resonance as a function of the input acceleration for a seismic mass of 4.5 g. (b) Normalized power as a function of input acceleration. (c) Temporal waveform of the generated power for various input accelerations with a photograph of a cantilever-based ferroelectret energy harvester at resonance for $a = 0.58\,g$ [49].

of being compressed and the power thus starts to saturate, as evident from Figure 3.37(c). On the other hand, when the cantilever is bent downwards the film is excessively stretched for large amplitude vibrations. In such a case, the stiffness of the ferroelectret film increases and results in a smaller deformation or equivalently to a smaller g_{31}-coefficient.

With the current design, the air-spaced energy harvester shows a strong dependence on the acceleration. For accelerations above $0.06\,g$, the generated power increases more slowly than expected theoretically, due to an asymmetrical stretching of the film. Since an excessive stretch of the film would considerably influence

the output power of the harvester, it should be taken into consideration, that increasing the distance h may not follow the theoretical prediction. Furthermore, in the current design, the influence of the pre-strain of the ferroelectret while assembling the harvester devise is neglected. In order to address these effects, the cantilever design is improved to allow the examination of the influence of each individual parameter as well as minimizing the the dependence of the output power on the acceleration.

3.5 Advanced air-spaced cantilever design

Two major modifications of the first version of the cantilever design are performed (Figure 3.38): first, the fixation of the ferroelectret between the base and the seismic mass is carried out using removable clamps instead of the covers. The clamps ensure a reproducible replacement of the cantilever structure without varying the initial pre-stress of the film. Second, the clamp on the base side is movable using a µm screw, to allow an accurate modification of the pre-strain.

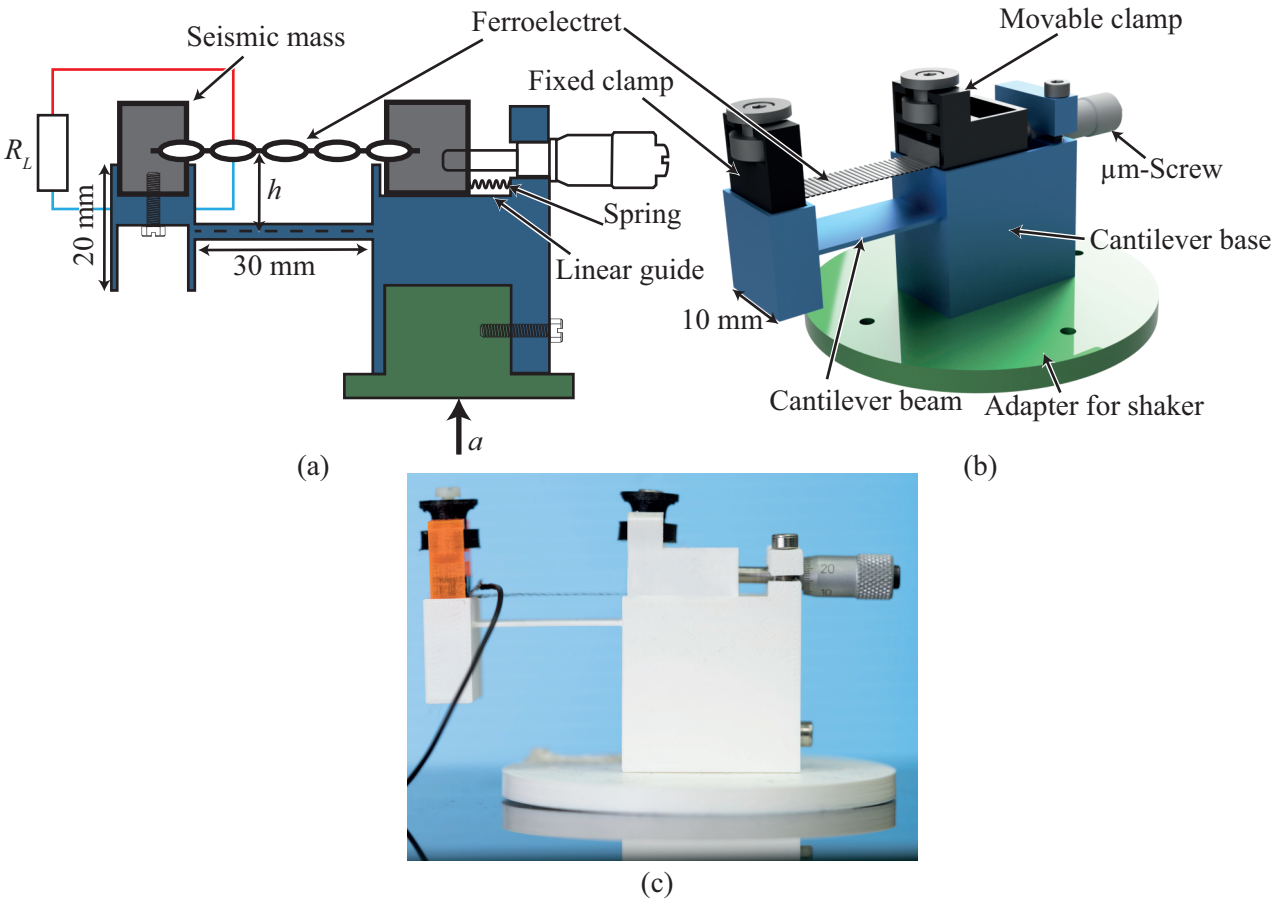

Figure 3.38: (b) Schematic representation of the advanced air-spaced design in idle state. (c) 3D representation of the advanced air-spaced ferroelectret energy harvester. The clamps are used to ensure a reproducible replacement of the cantilever structure without varying the initial pre-stress of the film. (d) Photograph of the advanced air-spaced cantilever energy harvester [50].

The smallest experimental distance h_0 was achieved by placing the ferroelectret film at a distance of 1 mm

above the neutral axis of the cantilever beam. Afterwards, the distance h is varied up to 20 mm. The seismic mass is designed as a hollow structure to minimize its weight. Furthermore, all parts including screws are made of plastic. Since the characteristics of different ferroelectret films are likely to differ slightly, only a single film was used for all measurements. Thereby, the change in the generated power during the experiments is exclusively caused by only one experimental parameter, namely the different distance h. Therefore, all measurements have been conducted using the same acceleration and seismic mass. This suppresses the influence of unknown factors, such as film slipping from the clamp that may be triggered by large accelerations particularly for larger h. For changing the distance h, the cantilever structure is modified accordingly. In order to avoid different mechanical pre-stress of the film, each time the harvester is assembled for a new distance h, the ferroelectret film length is fixed between the two 3D-printed clamps by a spacer block with a fixed length allowing for an undisturbed dismantlement and installation.

3.5.1 Influence of film distance h on the output power

It follows from equation (3.68), that if the generated power is $P_{\mathrm{h_0}}$ for the smallest experimentally achievable distance h_0 (in our case $h_0 = 1\,\mathrm{mm}$), the power P_{h} corresponding to a distance of h is increasing quadratically as

$$P_h = \left(\frac{h}{h_0}\right)^2 P_{\mathrm{h_0}}. \tag{3.70}$$

All measurements were performed at the same acceleration $a = 0.1 \times g$, the same pre-stress and seismic mass

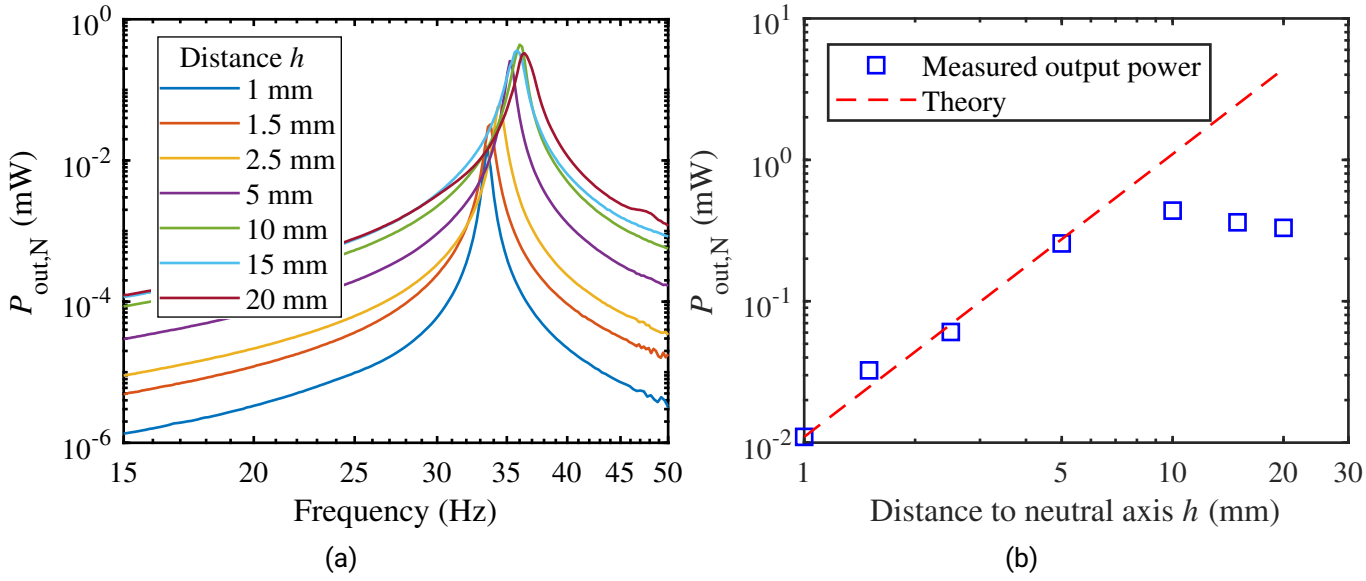

Figure 3.39: (a) Frequency responses of the normalized power of energy harvesters with various distances h between the ferroelectret film and the cantilever beam for a seismic mass $m_{\mathrm{s}} = 3.5\,\mathrm{g}$. (b) the normalized power at resonance frequency as a function of distance h. The theoretical curve (red dashed) for $P_{\mathrm{out,N}}$ is calculated using equation 3.70 [50].

$m_{\mathrm{s}} = 3.5\,\mathrm{g}$, for a proper test of the power generated for different values of h. The measurements indicate that the normalized output power increases from 16 µW to 438 µW for $h = 1\,\mathrm{mm}$ to $h = 10\,\mathrm{mm}$ and decreases for

larger distances h as can be seen in Figure 3.39(a). In all cases the resonance frequency shifts toward higher frequencies, indicating an increasing influence of the film stiffness k_f on the cantilever stiffness k_C.

Note that in the present analysis, k_C and k_f are assumed to be independent of each other, which is only valid for small angles φ and small values of h resulting in small film displacements ΔL. For larger angles φ and larger h values, k_f starts to influence ω_0 toward higher frequencies. According to the above presented theory, the film length variation ΔL is assumed to be proportional to h (see equation 3.62).

Increasing h enhances the stiffness of the film-cantilever system. In fact, when the air-tunnels are subjected to more stress in x-direction, the stiffness of the solid FEP layers enclosing the air tunnels becomes more and more dominant compared to the air-filled regions. This means that the ferroelectret stiffness k_f is no longer negligible compared to the beam stiffness k_C. This leads to an effectively larger k_C in the above theory which then results in a shift to higher resonance frequencies [Figure 3.39(a)] and at larger distances h to even smaller normalized power [Figure 3.39(a)].

The *first reason* for the decrease of the power is related to the fact that the voltage generating tunnels of the ferroelectret become more and more rigid with increasing h, leading to a smaller voltage output (smaller g_{31}) and thus to a decrease of the power generation. This effect is noticeable for the present device, starting from a film distance of $h = 5\,\mathrm{mm}$ [Figure 3.39(b)]. The *second reason* for the flattening of the generated output signal at larger h-values is mainly due to the asymmetry of the ferroelectret stretching, when the beam is bent in positive or negative z-direction, as mentioned before. The reason for such asymmetry is the different mechanical stress the ferroelectret film is exposed to, when the beam moves down (stretching) and up (loosening).

3.5.2 Influence of pre-stress on output power and device stability

In order to avoid such asymmetry and to achieve a symmetric deformation compared to the initial state of the ferroelectret film during operation, a relocation of the operating point of the device by pre-stressing the ferroelectret film is investigated. Two distances h between the neutral axis of the cantilever beam and the ferroelectret film were considered, namely, 1 mm and 5 mm, respectively, the latter being close to the film distance with maximum normalized power output [Figure 3.39(b)]. The pre-stressing of the film has to be carried out using the setup shown in Figure 3.38. The clamp at the end of the cantilever beam [see Figures 3.38(b) and (c)] is fixed and represents the seismic mass m_s.

On the side of the cantilever base, a movable clamp is used that can slide in a reproducible way in a guide structure. This structure is controllable in the negative x-direction by a micrometer screw. By such sliding the produced strain results in a pre-stress of the ferroelectret film. The term pre-stress is used since the performed straining leads to a slight bending of the beam, which even after mechanical relaxation results in a remaining pre-stress on the ferroelectret. If under such conditions the cantilever is set into vibrations, the individual tunnels will be stretched when the cantilever is bent downward and the stress is partially released when bent upward. The difference to a stress-free bending of a displaced ferroelectret is that under upward bending the film still stays under stress which is not the case without pre-stress. Advantageous for the pre-stress is that the same deformation occurs in both bending directions leading to an equal energy gain in both directions of acceleration. The disadvantage, however, is that an excessive pre-stress of the sample leads to a decrease in the g_{31}-coefficient, and, therefore, to a decrease in the generated power [see equation (3.68)]. The optimum pre-stress is difficult to predict and has to be determined experimentally. In order to find the optimum pre-stress for our energy harvester, measurements under different pre-stress conditions were conducted using the same seismic mass of $m_\mathrm{s} = 3.5\,\mathrm{g}$ and a fixed acceleration $a = 0.1 \times g$.

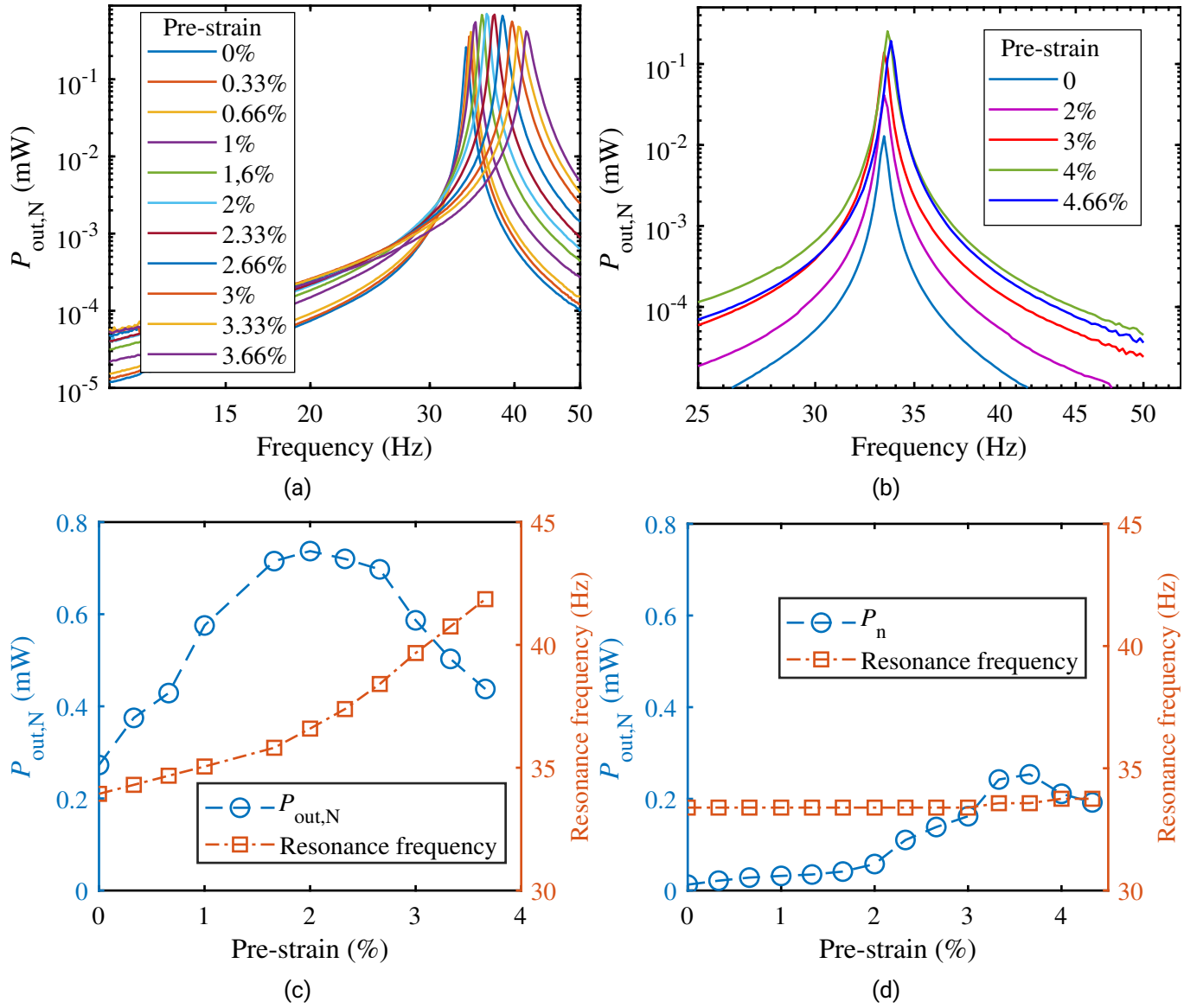

Figure 3.40: (a), (b) Frequency responses of the normalized power of energy harvesters with various pre-stresses of the ferroelectret film introduced by pre-straining the ferroelectret films to the indicated values by using distances $h = 5\,\text{mm}$ and $1\,\text{mm}$, respectively. (c), (d) Normalized power at the resonance frequency and the resonance frequency for each pre-stress by using a distance $h = 5\,\text{mm}$ and $1\,\text{mm}$ from the neutral axis of the beam, respectively. The ordinates of (c) and (d) are scaled in the same way to allow a direct comparison of the two measurements. All measurements were performed at the same acceleration $a = 0.1 \times g$ and using the same seismic mass $m_s = 3.5\,\text{g}$ [50].

For $h = 5\,\text{mm}$ a 2% strained sample leads to a twice as large peak power of $737\,\mu\text{W}$ compared to the unstrained structure. For $h = 1\,\text{mm}$ the output power is relatively more enhanced from approximately $13\,\mu\text{W}$ up to $253\,\mu\text{W}$ by straining the ferroelectret to 3.66%, however, still below the value reached for $h = 5\,\text{mm}$ [Figures 3.40(a) and (b)]. Unfortunately, one can uniquely specify the pre-strain applied to the samples, but not the pre-stress. The physically important property is, however, the pre-stress which cannot be determined

quantitatively. Nevertheless, the parameter stress or pre-stress will be mostly used in the following discussions.

Considering the nonlinear behaviour of the stress-strain curve of the used ferroelectret as described before [46], a reallocation of the working point also influences the stiffness of the ferroelectret film and consequently the g_{31} coefficient. Since the dynamic displacement ΔL increases with distance h, the stiffness enhancement of the film-cantilever system for larger h is more noticeable [Figures 3.40(c) and (d)].

Despite the fact that the dynamic deformation of the film while vibrating is much larger for larger h [see equation 3.62], it can be noted that the maximum power output of the pre-stressed film for $h = 1\,\text{mm}$ corresponds approximately to the output power of the cantilever structure without pre-stress using a distance of $h = 5\,\text{mm}$ [Figures 3.40(c) and (d)]. The comparability of the two maximum power outputs indicates that the limit is determined neither by the distance h of the ferroelectret film nor by the pre-stress but rather by a common source which has to be looked for in the ferroelectret film itself. Since for both cases (increasing of distance or strain) the power output drops below its maximal value, the reason for the decrease must be assumed to be in the film itself. It is most likely originating from the deformation of the tunnels after reaching saturation, where any further deformation starts to strongly decrease the piezoelectric g_{31} voltage coefficient. Under positive or negative loads the thickness of the tunnels decreases to a value, where the induced strain mainly acts on the already strongly elongated FEP framework, instead of compressing the tunnels any further. The consequence thereof is a strongly reducing additional strain, leading to a reduction of the power generation.

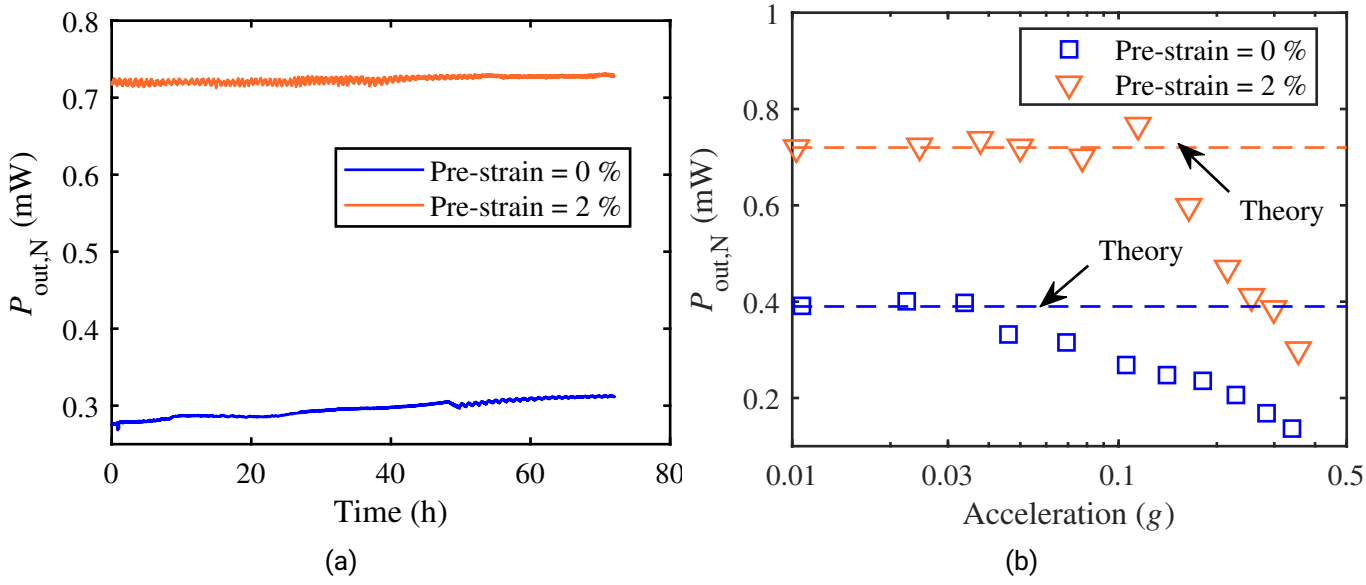

Figure 3.41: (a) Long-term stability of the normalized output power at resonance frequency for two different initial strains. The cantilever used in this experiment features a distance of $h = 5\,\text{mm}$. The measurements are conducted using the same acceleration $a = 0.1 \times g$ and seismic mass of $m_s = 3.5\,\text{g}$. (b) Normalized output power at resonance frequency for increasing acceleration [50].

A further interesting benefit of utilizing a pre-stress is the improved temporal stability of the output power as can be seen from Figure 3.41(a). For this experiment, the power output of the energy harvester was determined for an acceleration of $a = 0.1 \times g$ and a seismic mass of $m_s = 3.5\,\text{g}$. Approximately 9 million cycles were applied, which correspond to approximately 70 hours of operation at a frequency of 35 Hz, which

is a reasonable stress test. Pre-stressing of the film results in a stable output power of 720 µW over the measurement duration, whereas the absence of pre-stress leads to a steady increase of the output power.

Another advantage of the pre-stressed ferroelectrets compared to the stress-free ones is the enhancement of the power stability as a function of acceleration as shown in Figure 3.41(b). When no pre-stress is used, the measurements indicate a decay of the normalized power as soon as an acceleration of $a = 0.04 \times g$ is reached. This limit can be enhanced up to $a = 0.1 \times g$, when a pre-strain of 2% is applied to the ferroelectret film. In addition, the output power is enhanced from 270 µW to 737 µW.

3.5.3 Viscoelastic property

Considering the viscoelastic and plastic properties of solid FEP films used to manufacture parallel-tunnel ferroelectrets, one can expect that under pre-stress the ferroelectret film behaves accordingly. In order to examine such effects a fixed pre-strain was applied to the ferroelectret and its impact on three aspects was investigated. The *first aspect* is the constancy of the pre-stress for a given pre-strain. It was measured using a universal testing machine (Inspekt table 5 kN, Hegewald & Peschke). Hereby, the pre-strain is increased in steps of 0.33% up to 4% while simultaneously measuring the force (as indication for a varying stress) that results from keeping the applied strain constant [Figure 3.42(a)]. For each pre-strain the position is maintained for 60 min while measuring the force developing while preserving the reached position [Figure 3.42(a)]. To avoid overshooting, a small velocity of 0.1 mm s^{-1} was used to move from one strain to another.

The measurement shows different creep behaviour of the ferroelectret film depending on the pre-strain. By using 0.33% pre-strain to stretch the ferroelectret film, a negligible decay of the resultant initial stress is reached after 60 min. On the other hand, when using a pre-strain of 2%, which corresponds to the optimal strain regarding the output power, a decay of approximately 4% of the initial pre-stress is measured after 60 min. A drop of 10% of the initial pre-stress has been recorded for an even higher pre-strain of 3.7%.

The *second aspect* was to find out whether the mechanical relaxation has an effect on the generated power at the resonance frequency of 35 Hz. Therefore the constancy of the power was examined, when the harvester is not used continuously. Two measurements were conducted for each pre-strain. The first measurement is directly carried out after the adjustment of the pre-strain and the second measurement is conducted 24 h later. The pre-strain is increased by the aforementioned steps in order to compare the mechanical and electrical properties under almost the same conditions. The resulting output powers show almost the same values [see Figure 3.42(b)] with a small increase in power for 2% pre-strain.

The *third aspect* is the hysteresis of the output power for ascending and descending pre-stress [Figure 3.42(c)]. The pre-stress is increased by increasing the strain in steps of 0.33% until a strain of 3.66% is reached and decreased by reducing the pre-strain with the same step size down to 0%. For each pre-strain, the frequency response of the harvester is measured and the achieved amplitude at the resonance frequency is noted. Therefore, each pre-strain is maintained during the measurement time of approximatly 30 min. For an ascending pre-strain, the highest reached amplitude is 737 µW at 2% pre-strain, whereas, a descending pre-strain shows a different amplitude and different optimal pre-strain, namely 1029 µW and 1.66% respectively. Starting from a pre-strain of 2.66% the hysteresis becomes thinner (if the pre-strain increases) and the achieved amplitudes for both ascending and descending pre-stress become more similar.

The increase of the output power for ascending pre-strain can be explained by the fact that the stiffness of the film has decreased due to the excessive stretching. The decrease of the stiffness k_{f} can be explained by the viscoelasticity of the FEP films used to manufacture the ferroelectret. This means a larger deformation of the air-filled tunnels can be reached for the same force, resulting in a larger piezoelectric voltage constant

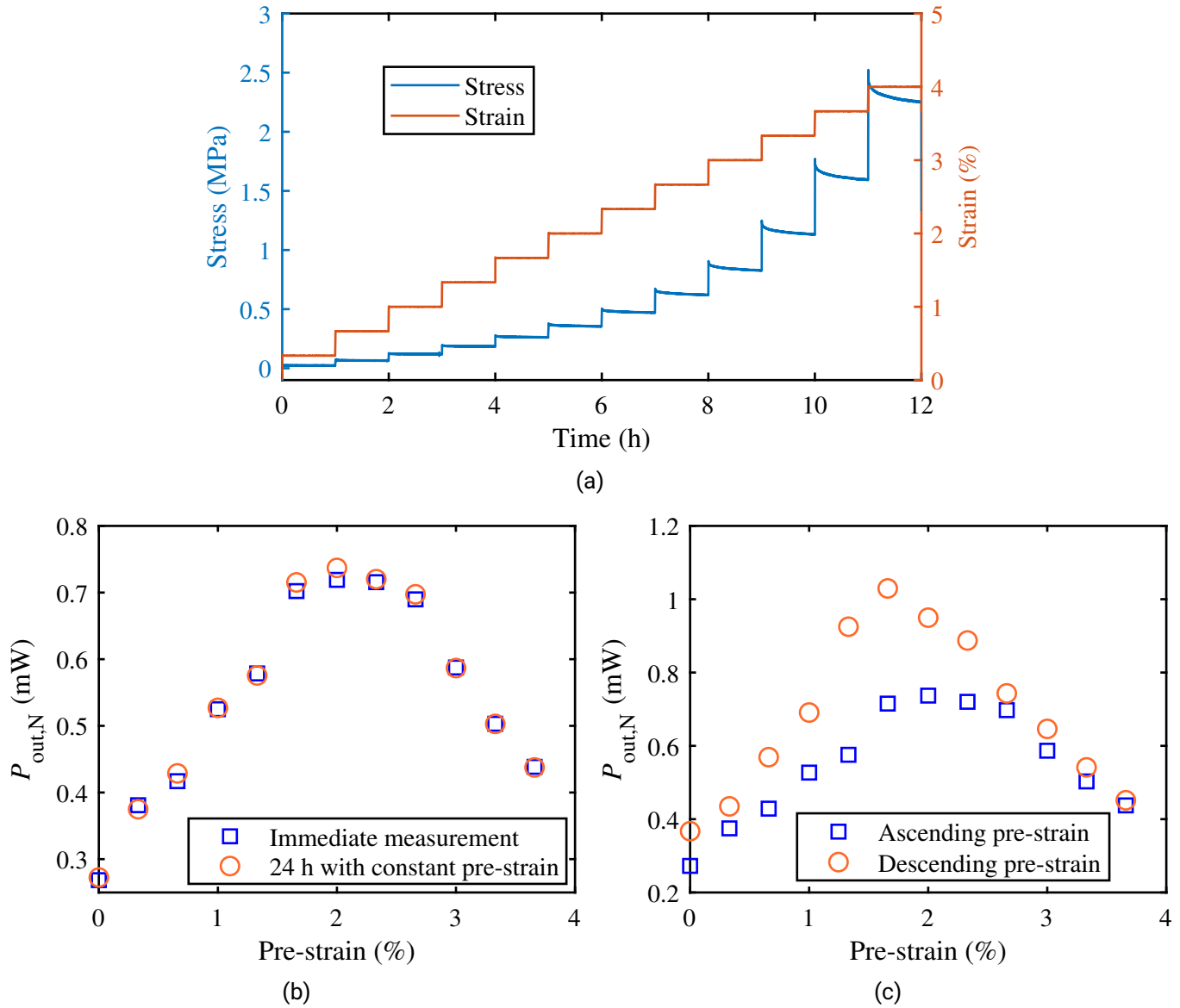

Figure 3.42: (a) Stress-strain relation of the ferroelectret film, while holding each strain value for 60 min. (b) Normalized power at the resonance frequency. The first measurement is conducted directly after the adjustment of the pre-strain and the second measurement 24 h afterwards, while keeping the film under the same pre-strain. (c) Hysteresis of the normalized output power at resonance frequency for ascending and descending pre-strain [50].

g_{31}. This hysteresis can also be used to improve the performance of the energy harvester without adjustment of the geometry. Before the energy harvester starts to operate, the ferroelectret film can be stretched and then relaxed until the new optimal working point is reached. When the energy harvester is set into vibration, a maximum power of 1029 µW can be reached. Note that all hysteresis measurements are reproducible for pre-strains not exceeding 4%. An excessive pre-strain results in a plastic deformation of the samples and therefore in local destruction of the film leading to an unpredictable behavior.

3.6 Summary of ferroelectret energy harvesting

Ferroelectret based energy harvesters based on the longitidunal as well as the transversal piezoelectric response are demonstrated.

Table 3.6: Normalized power generated by various kinds of ferroelectret energy harvesters including the one presented in the present work. Normalizing the power takes into account that the generated power is proportional to a^2.

Type of harvester	Normalized power (µW)	Resonance frequency (Hz)	Size of active area (cm^2)
Ferroelectret g_{33} IXPP (m_s = 33.7 g) [104]	120	800	3.14
Ferroelectret g_{31} (m_s = 2 g) [47]	230	30	3
Ferroelectret g_{31} advanced design (m_s = 0.3 g) [46]	109	58	0.4
Ferroelectret simple air-spaced cantilever g_{31} (m_s = 4.5 g) [49]	320	35	3
FEP-Tube g_{33} harvester (m_s = 80 g) [116]	300	78	0.2
Ferroelectret advanced air-spaced cantilever g_{31} (m_s = 3.5 g) [50]	1000	35	3

The tube energy harvester is more compact and can be easily fabricated from commercially available FEP tubes with a wall thickness of 25 µm and 50 µm. The output power generated by the tube harvester can reach up to 300 W at frequencies around 100 Hz when using 25 µm-thick tube and a seismic mass of 80 g. The theoretical model describes very well the frequency response of the harvester and can be used to customize the harvester for its application as harvester or as accelerometer. Such tubes can also be arranged next to each other to build an array of such harvester to improve the output power.

Energy harvesting with ferroelectrets in conjunction with a cantilever arrangement can as well be easily manufactured using additive manufacturing technique and provides a modular assembly which ensures reproducibility. In fact the output power reached by the air-spaced cantilever exceeds that of previously described ferroelectret nanogenerators and is far above the conventional piezoelectret energy harvesters based on the longitudinal piezoeffect. Its more robust design is a great advantage and should help the present harvester to become accepted for application in spite of its relatively large structure. The harvester generates a normalized output power of more than 1 mW at a resonance frequency of about 35 Hz for a seismic mass of 3.5 g and an acceleration of $0.1 \times g$. It was experimentally verified that the power generated at the resonance frequency can be stabilized over the measurement duration of 70 h as well as for different accelerations up to $0.1 \times g$ by using mechanical pre-stress. The influence of varying the distance between the neutral axis of the cantilever beam and the ferroelectret film shows an excellent agreement with theory up to a distance of $h = 10$ mm. Thus, the presented energy harvester proves to be particularly suitable for low acceleration amplitudes up to $0.1 \times g$.

As can seen in Table 3.6, the normalized power exceeds that of previously described ferroelectret nanogenerators and is far above the conventional piezoelectret energy harvesters based on the longitudinal piezoeffect. Its more robust design is, however, a great advantage and should help the present harvester to become accepted for application despite its relatively large seismic mass. Depending on the specific requirements for a given application such as robustness, high normalized power, small mass, miniature size, or suitable resonance frequency, one finds in Table 3.6 a useful selection of appropriate energy harvesting devices to choose from.

4 Ferroelectrets for sensor applications

The following chapter was published in [161]–[165].

In this chapter new ferroelectrets are introduced. The focus hereby lies on finding new ferroelectret materials and arrangements to improve the sensibility, mechanical stability and broaden the application possibilities.

4.1 Multimaterial ferroelectrets alternating FEP/Spacer/FEP

Ferroelectrets as discussed in previous sections, can be made artificially by using polymer materials with electret properties and arranging them in a way to build artificial air-voids. An alternative manufacturing method, which is much easier than the ones discussed earlier, is the use of bulk films in combination with a well structured spacer, to build the artificial voids. A similar approach was investigated by using a porous ePTFE film with nominal porosity of 91% as a spacer that separates two FEP films [98] resulting in stochastically distributed air-voids. The analytical description of the piezoelectric d_{33}-coefficient of such an arrangement was carried out by assuming that cellular films consist of plane parallel solid and gaseous layers charged at their interfaces [22], [166]. A further model was introduced by Zhukov et al. describing similar arrangement of plane parallel solid and gaseous layers, which are horizontally separated by non active areas. The model was used to describe the tubular-array ferroelectrets, where the non active areas correspond to the bonding areas of the tubes [131]. Based on the two models, the structure of a ferroelectret arrangement as shown in Figure 4.1 can be analyzed by dividing the structure into two elements: Element I consists of parallel layers by alternating dielectric/spacer/dielectric and Element II by alternating dielectric/air tunnel/dielectric.

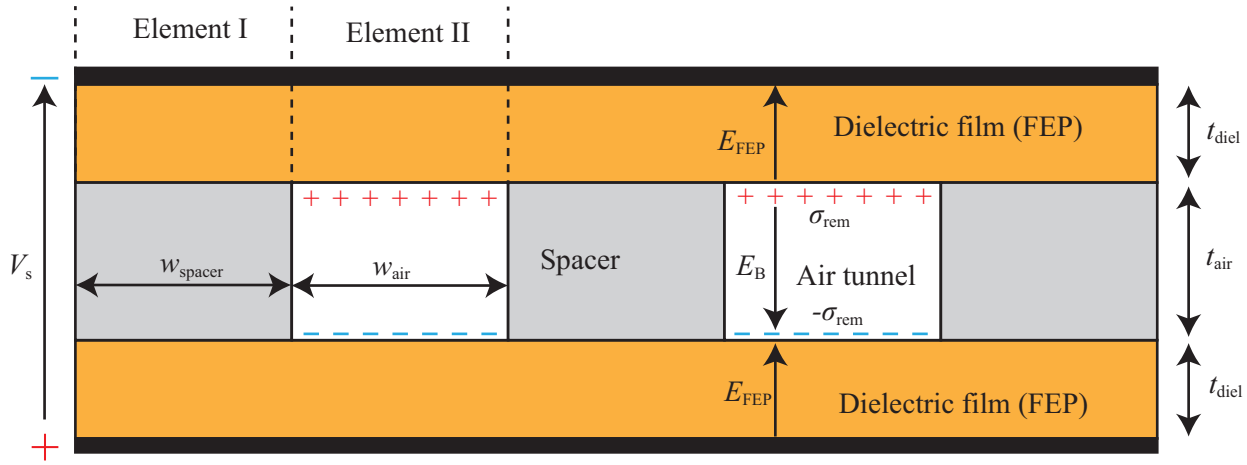

Figure 4.1: Schematic cross-section of a generalized structure of a ferroelectret [161].

Such structures with air voids show maximum remanent charges (polarization) $\sigma_{\text{int}}^{\text{max}}$ as discussed in section 3.1. For the sake of clarity, the polarization and the d_{33}-coefficient of such geometry will be briefly discussed. The maximum polarization can be expressed as [131], [161]

$$\sigma_{\text{int}}^{\text{max}} = \frac{w_{\text{air}}}{w_{\text{air}} + w_{\text{spacer}}} \left(\varepsilon_{\text{air}} \varepsilon_0 + \varepsilon_{\text{diel}} \varepsilon_0 \frac{t_{\text{air}}}{2t_{\text{diel}}} \right) E_{\text{B}}, \tag{4.1}$$

where E_{B} represents the electric breakdown field, ε_{air} the dielectric constant of air and t_{air} the thickness of the air gap and between two FEP films with a thickness t_{diel} and dielectric constant $\varepsilon_{\text{diel}}$. The width of the tunnel and spacer are represented by w_{air} and w_{spacer}, respectively. The Elements I and II have the same length and thickness to make the area and volume directly proportional to its respective width. The ratio $\alpha = w_{\text{air}}/(w_{\text{air}} + w_{\text{spacer}})$ is taken into account, since the induced charge under mechanical stress is only generated in Element II and is averaged over the entire electrode area of the sample. The contribution of Element I to the total charge is negligible [36], [147], and, thus, only contributes to total Young's modulus Y_{total} by acting as a restoring force to maintain the air gap. The maximum d_{33}-coefficient for the structure shown in Figure 4.1 can be expressed as in equation (3.3). However, for more clarity in this section, equation (3.3) is rewritten in function of the variables shown in Figure 4.1 as [35], [131]

$$d_{33}^{\text{max}} = \alpha \cdot \frac{\varepsilon_{\text{diel}} \varepsilon_{\text{air}} \sigma_{\text{int}}^{\text{max}}}{Y_{\text{total}}} \cdot \frac{1 + \left(\frac{t_{\text{air}}}{2t_{\text{diel}}} \right)}{\left[\varepsilon_{\text{air}} + \varepsilon_{\text{diel}} \left(\frac{t_{\text{air}}}{2t_{\text{diel}}} \right) \right]^2}. \tag{4.2}$$

According to equation (4.2), by optimizing both key parameters: the polarization at the air/polymer interface and Young's modulus Y_{total}, the final magnitude of the piezoelectric response can be enhanced. Several strategies to optimize them have been discussed in several recent reviews [40], [167].

Here, a different strategy is utilized to increase the overall piezoelectric response by using a 3D-printed ultra-soft thermoplastic polyurethane (TPU) [168] as spacer material in order to reduce the Young's modulus of the device. The dielectric films are chosen to be made of FEP to keep the polarization characteristics of the air tunnels similar to previous work [28], [30]–[36], [39], [98], [147], [169]–[171]. In addition to the influence of electrical and mechanical parameters on the d_{33}-coefficient, the influence of the geometry is additionally investigated. Furthermore, issues related to the influence of the spacer material on the optimal charging conditions, the stability of the piezoelectric coefficients over time and their dependence on mechanical stress and frequency are experimentally examined.

4.1.1 Preparation of the ferroelectrets

The ferroelectrets are assembled using two 25 µm-thick FEP films (FEP-A, Sheldahl Ltd., Northfield, MN, USA) sandwiching a grid of foamed thermoplastic polyurethane (VARIOSHORE TPU NATURAL, colorFabb B.V., DK Belfeld, The Netherlands) as shown in Figure 4.2.

The TPU spacer geometry is designed in Autodesk Fusion 360 (Autodesk, Inc) and digitally sliced using an open source software (Slic3r). The slicer converts the object model into a stack of flat layers and describes them as linear movements of the 3D-printer extruder (Prusa Mk3s, Prusa3d DE). The printing parameters are listed in Table 4.1. The used print bed is a double sided polyethylenimine (PEI) coated spring steel sheet.

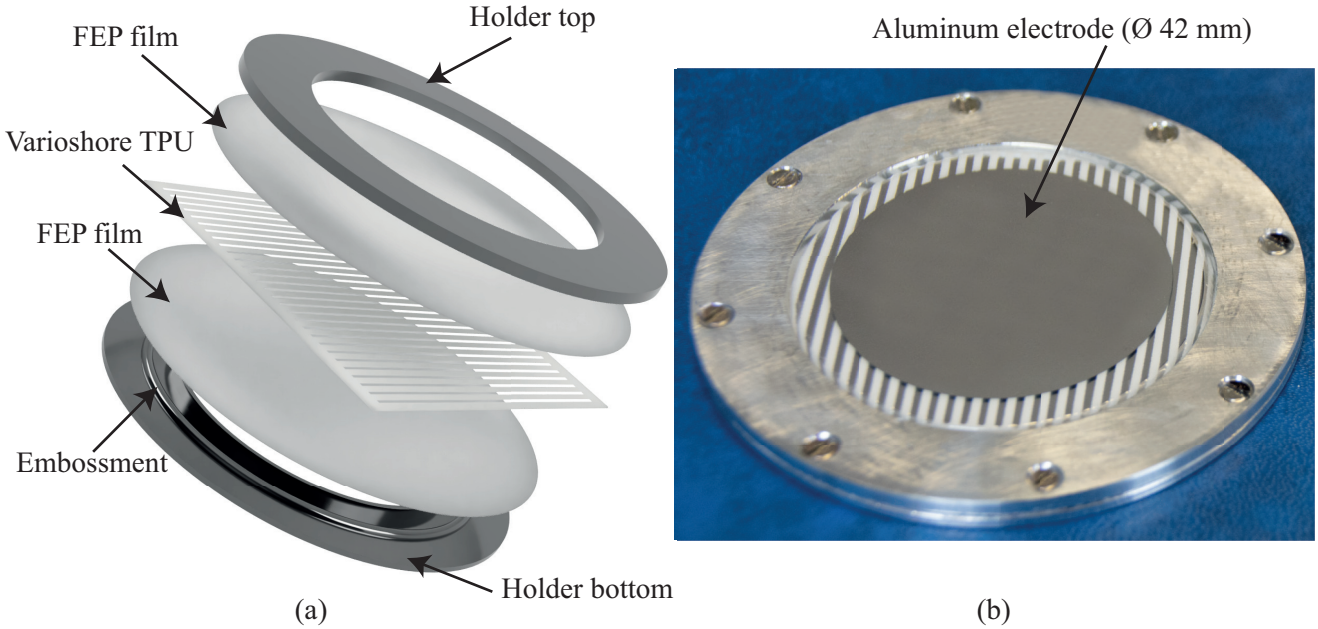

Figure 4.2: (a) Sandwich structure consisting of a 3D-printed Varioshore TPU frame with FEP layers on the top and bottom. All three layers are clamped together using an aluminum holder with tensioning embossments. (b) Photograph of the FEP/TPU-air/FEP device equipped with aluminum electrodes [161].

All printed TPU spacers have the same thickness of $270 \pm 5\,\mu m$ and the same dimension of $50 \times 50\,mm^2$ (Figure 4.2). The width of the TPU stripe w_{TPU} amounts to 1 mm, whereas the air tunnel w_{air} is investigated for two values: 1 and 3 mm.

The FEP films together with the TPU spacer are clamped in an aluminum holder with an inner diameter of 45 mm, which serves as support for electrical and mechanical testing. The bottom part of the holder has a ring-shaped embossment that matches a groove on the top part of the holder (not shown in Figure 4.2) to maintain an equilateral pre-stress on the sandwich. To prevent any excess air in the sandwich, small holes created in the non-metallized outer periphery of each air tunnel, that allow the air channels to maintain a normal air pressure after assembly or stressing. The total thickness of the prepared sandwiches is $320 \pm 5\,\mu m$. Depending on the performed experiment, one or both sides of the sample are metallized with 100 nm thick circular aluminum electrodes by thermal vapor deposition on the rear side of the bottom FEP layer or top and rear sides of the FEP layers. The electrodes have a diameter of 42 mm.

The samples are polarized by a corona triode in air under ambient conditions (atmospheric pressure and a relative humidity of 50%) utilizing a DC corona voltage of $V_C = -10\,kV$ and a DC grid voltage V_G between 0 and $-4\,kV$ depending on the investigated surface potentials. The samples are either charged at temperatures of 25 °C or 120 °C. The poling experiment is carried out with one-sided metallized sandwiches with the non-metallized surface facing the corona grid. Three signals are recorded simultaneously during poling: the DC charging current I_C, the surface potential V_S, the photomultiplier current I_{PM}. The charging current is measured by means of an electrometer (Keithley 600B) and the surface potential V_S, by the Kelvin technique (see Section 2.4.1). A photomultiplier (Hamamatsu, model R6094) is used to monitor the light emission during poling initiated by Paschen breakdown in the air tunnels [79]. The quasi-static and the dynamic d_{33}-coefficients are determined as described above.

Table 4.1: Printing parameters for the Varioshore TPU grid.

Parameter	Value
Extruder temperature	220 °C
Temperature of the heatbed	30 µm
Layer height	250 µm
Number of layers	1
Fan	disabled
Extrusion multiplier	0.7
Filament diameter	1.75 mm
Extrusion width	0.42 mm
Nozzle diameter	0.4 mm
Printing velocity	20 mm s^{-1}

4.1.2 Charging of elastomer-spaced fluoropolymer ferroelectret

The first parameter investigated is the optimal poling voltage of the devise. According to equation (3.4) describing two solid blocking layers (in this case FEP) separated by an air gap [95], the breakdown voltage depends on the thickness of the FEP layers, the air gaps, and breakdown field strength E_B. E_B can be taken from the well-known Paschen law for air [87]. However, since in a number of cases the experimentally determined value for this parameter significantly differs from the values predicted by Paschen's law [95], it seems advisable to determine this parameter specifically for the here utilized sandwiches. The breakdown voltage V_B is measured and E_B is determined by means of equation (3.4). Furthermore, the maximum residual polarization, σ_{int}^{max} can be determined using equation (4.1) taking into account the ratio of the polarized to the total sample area. Instead of measuring the hysteresis using the ST as discussed in section 3.1.2, a technique utilizing the light emission at breakdown is used [79], [85], [172].

With the corona triode setup discussed in section 2.3.2, three signals are measured simultaneously: the poling current I_C, the surface charge V_s and the photomultiplier current I_{PM}. Their temporal evolution is shown in Figure 4.3. The samples measured in this experiment are one-side metallized sandwiches. The poling process starts at $t = 0$ s, which corresponds to the moment of switching on the corona and grid voltages. The grid voltage V_G amounts to -3 kV. As soon as the corona voltage is applied, light is emitted from the plasma discharge at the tip of the corona needle and amounts to $I_{PM} \approx 1.5$ µA which remains constant during the complete charging process [Figure 4.3(c)]. This light emission is, however, not related to the air-breakdown, leading to polarization of the sample. The actual onset of the breakdown-induced polarization is seen by the increase in the light intensity starting at $t = t_1$. At this moment, the surface potential reaches the breakdown voltage $V_B = -1.9$ kV. The change in the slopes of the surface potential [Figure 4.3(b)] and the charging current [Figure 4.3(a)] indicate the onset of the poling process. The build-up of the polarization is terminated after approximately 35 s. At this time, the poling current I_C and the light intensity I_{PM} both approach their initial values, while the surface potential saturates at a value close to the applied grid potential V_G.

Based on the experimentally determined $V_B = \pm 1.9$ kV and the experimental value of $t_{FEP} = 25$ µm, $t_{air} = 270$ µm, $\varepsilon_{FEP} = 2.1$, and $\varepsilon_{air} = 1$, the breackdown electric field E_B can be calculated using equation (3.4) and amounts to $E_B = 65$ kV cm^{-1}. Interestingly, this value is very close to the value predicted by Paschen's law of 66.1 kV cm^{-1}. Assuming that the maximum possible polarization is reached at $V_s = 2 \times V_B$ as known in

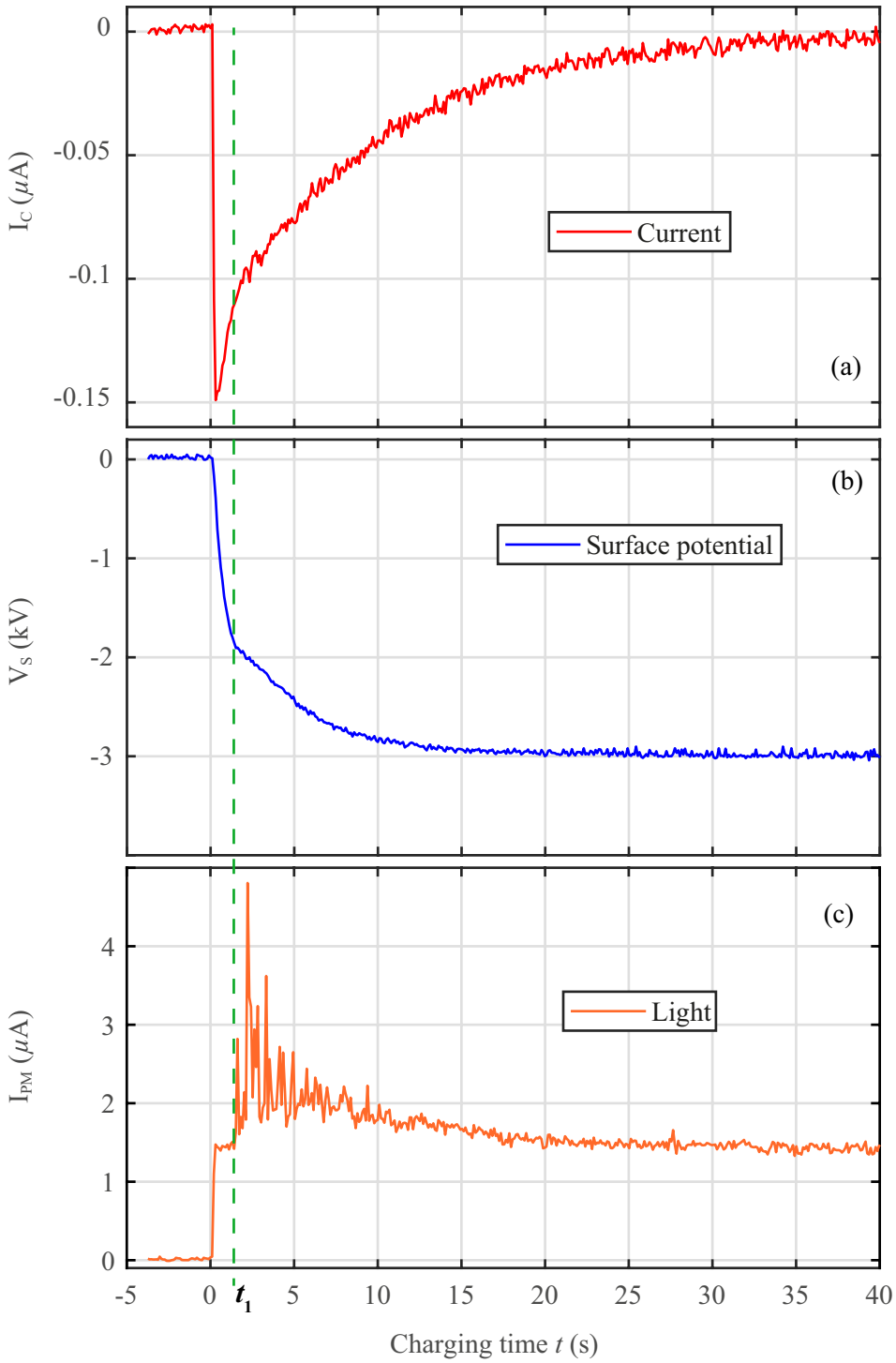

Figure 4.3: Temporal dependencies of (a) charging current I_C, (b) surface potential V_S, and (c) photomultiplier current I_{PM} for poling of a virgin sandwich of alternating FEP/TPU/FEP and FEP/air/FEP elements with a width ratio of 1 at $V_G = -3$ kV. The corona voltage is switched on at time $t = 0$ s. Time t_1 indicates the onset of breakdown-induced light emission and polarization of the sample [161].

literature for similar structures [98], utilizing a poling voltage of $V_G = 4\,\text{kV}$ is sufficient to obtain the maximal possible polarization.

4.1.3 Temporal and thermal stability of the d_{33}-coefficient

An important property of ferroelectrets generally is the temporal stability of the piezoelectricity under ambient conditions. Therefore, a batch of five similarly prepared samples at room temperature (25 °C) are polarized at $2 \times V_B$, and their piezoelectric d_{33}-coefficients are measured periodically over six months under ambient conditions using the same static stress of 1.2 kPa (see Figure 4.4). The immediate measurement after charging shows a large initial piezoelectric response of approximately $d_{33} = 2430\,\text{pC}$. This value decreases over the next 180 days and only an average of 60% of the initial d_{33}-coefficient remains. The temporal loss of the piezoelectricity can be attributed to the relatively poor charge storage stability of the positive charge in FEP [140]. Since during poling an equal amount of positive and negative charge is generated and trapped at the FEP/air interfaces of the air-filled tunnels, the temporal stability of the positive charge will dominate the overall discharge process. The instability of the positive charges explains the order of magnitude of the observed loss of approximately 40% for the d_{33}-coefficient. It is known from literature that a small fraction of the positive charge can also be deeply trapped [140]. The experiments of charge storage properties of TPU indicate a high electrical conductivity, since all attempts to charge individual TPU films by corona triode were unsuccessful. Therefore, it is allowed to assume that the FEP/TPU/FEP element are piezoelectrically inactive due to the quick discharge of possible poling-induced charges on the FEP layers in these elements. It is, however, also known from the literature that a positive charge in FEP can be stabilized by poling FEP films [140] and also fluoropolymer-based ferroelectrets at elevated temperatures [30], [33], [36], [48]. The physics behind this stabilization is explained by the existence of a large amount of shallow hole traps and a relatively small amount of deep hole traps [140]. Poling at elevated temperatures allows the shallow traps

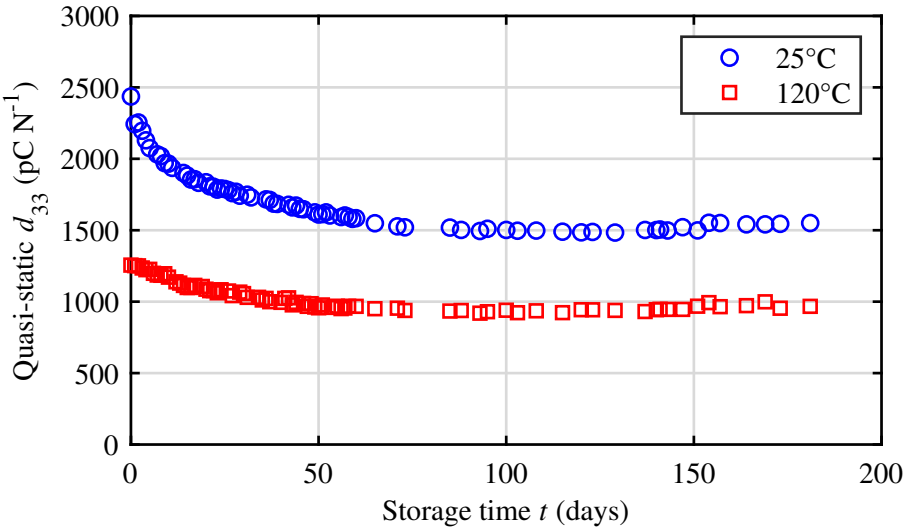

Figure 4.4: Isothermal decay of an averaged piezoelectric d_{33}-coefficient for five similar alternating FEP/TPU/FEP and FEP/air/FEP samples, all with a width ratio of 1, polarized at 25 and 120 °C, respectively, and measured at room temperature by using a static load of 1.2 kPa [161].

to empty spontaneously and for the charge to transit the sample quickly. This transit is accompanied by a gradual filling of the deep traps which prevail at the end of poling. In order to determine how this approach is

applicable to the systems studied in this research, a batch of manufactured devices is polarized at 120 °C, and the isothermal decay of the d_{33}-coefficients is investigated. The corresponding experimental results for the averaged piezoelectric d_{33}-coefficient for five samples are shown in Figure 4.4. The strongly reduced decay observed for the 120 °C poled structure can be explained by the improved stability of the positively charged FEP when charged at an elevated temperature [140]. The still observed decay for the high-temperature poled samples is not clearly understood, but it may be related to charging of the residual air gaps near the FEP/TPU/FEP interfaces, the physics of which has yet to be explored in detail in future research.

The thermal charge stability of the samples is investigated by polarizing them at different temperatures and measuring the TSDC in open-circuit as described in literature [140], [155], [173]. This method allows a more thorough understanding of the reasons for the increase in thermal stability of the sandwich charged at 25 °C and 120 °C. the charging is performed using a grid potential of -4 kV and a poling time of five minutes, resulting in a surface potential of $V_s = -3.9$ kV and -3 kV at temperatures of 25 °C and 120 °C, respectively. The charging temperature was limited at 120 °C to avoid thermal degradation and deformation of the TPU spacers. Additionally, the TSDC measurement is stopped at a maximum temperature of 150 °C, which is the maximum temperature before destroying the samples. This experiment is carried out using a gold-plated metal electrode, which is placed at a distance of 4 mm above the non-metallized surface of the corona-poled sample, and the discharge currents are monitored by a Keithley electrometer (model 610C) utilizing a constant heating rate of 3 K min^{-1}.

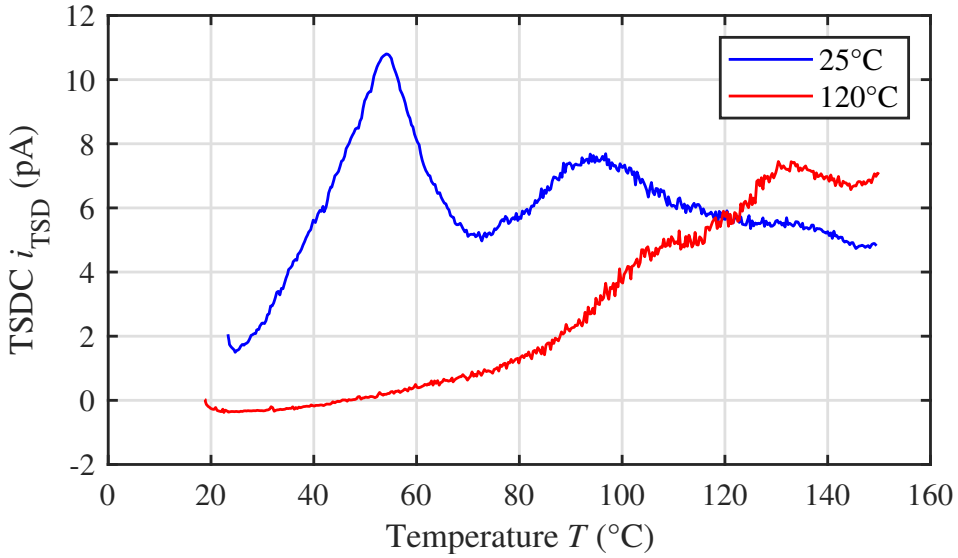

Figure 4.5: Open-circuit TSDC spectra measured for alternating FEP/TPU/FEP and FEP/air/FEP devices with a width ratio of 1 charged in a corona triode utilizing $V_C = -10$ kV and $V_G = -4$ kV and two different temperatures as indicated [161].

The TSDC measurement shows three peaks at 50, 95 and 130 °C, that can be well distinguished in the samples polarized at 25 °C, while only two overlapping peaks presumably at 95 °C and 130 °C remained in the sample poled at 120 °C. The first peak at 50 °C completely disappeared for the sample poled at 120 °C, the second peak at 95 °C decreased significantly, and the peak at 130 °C increased.

For the assignment of the polarity of the trapped charge carriers to the respective detrapping peaks of the TSDC spectra, it is known from the literature that holes release shallow traps mainly at 50 °C and deep traps at temperatures distributed in the range from 90 °C to 200 °C [154], [155], while electron detrapping occurs

between 120 °C and 150 °C as well as between 170 °C and 220 °C [141], [173]. The observed discharge currents can then be explained as follows: For the poling at room temperature, holes filled preferentially shallow traps indicated by the pronounced TSDC peak at 50 °C. The other two peaks are correlated to deeper hole traps (at 95 °C) and to electrons traps (at 130 °C). For the charging at 120 °C, the shallow traps at 50 °C are no longer trapping holes, since charges are released immediately after capture. Thereafter, the deeper hole traps filled gradually, dependent on their trap density. Contrary to the negative trap density, the trap density for deep holes is limited in FEP [140]. As a result, the total amount of captured charge would be less in a device polarized at an elevated temperature and the surface potential would also be less than that possible by the grid potential of the corona poling setup. In practice, the final surface potential for the sample polarized at 120 °C is $V_S = -3$ kV for a grid voltage of -4 kV. The consequence is that the sample polarized at 120 °C possesses a smaller piezoelectric response, whereas its stability over time and temperature is significantly improved. The sample charged at 120 °C exhibited approximately half the value of the initial piezoelectric d_{33}-coefficient compared to the device polarized at 25 °C, but only loses approximately 20% of its initial value after 180 days of storage under laboratory conditions. The reason for the 20% decay remains unknown.

4.1.4 Mechanical properties and dependence of the d_{33}-coefficient on pressure, frequency, and acceleration

The effective mechanical modulus of the alternating FEP/TPU/FEP–FEP/air/FEP sandwich is mainly determined by the mechanical properties of the TPU layer. According to equation (4.2), the Young's modulus of of the whole devise plays a decisive role for the achievable piezoelectric d_{33}-coefficient. It is known that FEP has a Young's modulus Y_{FEP} of approximately 520 MPa [174], which is 50 times larger than the modulus of TPU elastomers Y_{TPU} [168], [175]. However, the 3D-printing parameters have a very large influence on the mechanical parameters of the TPU layers, since the foaming process depends on it. Therefore, in order to predict the mechanical properties of the alternating FEP/TPU/FEP sandwiches, it is necessary to determine the mechanical properties of the printed TPU independently.

First TPU films are 3D-printed as full materials with a thickness of 270 ± 5 µm utilizing the parameters from Table 4.1. Several films are annealed at 120 °C for 30 min to examine the influence of the thermal treatment during corona poling on the mechanical properties of the TPU elastomer. Afterwards, quasi-static stress–strain dependencies are measured at room temperature for nonannealed and annealed films for strain levels $\varepsilon_{\text{mech}}$ up to 0.1. Stress–strain curves under compression are measured at room temperature by a universal testing machine (Inspekt table 5, Hegewald & Peschke). Thus, the specimens are compressed between two parallel plates at a rate of 0.1 N s^{-1}, and the resultant force is recorded by a force sensor (S2M/100N, HBM) allowing for the determination of the Young's modulus in thickness direction.

It turned out that printed TPU films treated at the two temperatures exhibited very similar mechanical properties (Figure 4.6). When comparing the Young's moduli $Y_{\text{TPU}} = \partial\sigma_{\text{mech}}/\partial\varepsilon_{\text{mech}}$ for non-annealed and annealed films at different stress levels, it can be observed that for 3D-printed foamed TPU, the Young's moduli at low stress (< 0.1 kPa) are constant at approximately 7.5 kPa for both films, which is a factor 1000 times smaller than the published values for solid TPU [168], [175]. Such low values indicate an open porous, air-filled structure of the printed TPU, and the constant Young's moduli for stress up to 0.1 kPa indicates that the TPU follows Hooke's law. At higher stress levels, the stiffness of both films increases to approximately 50 kPa, which suggests a densification of the open porous TPU polymer. From this experiment, it is valid to assume that the stiffness of the alternating FEP/TPU/FEP–FEP/air/FEP sandwiches is mainly determined by the intrinsic mechanical properties of the TPU elastomer for open air tunnels and is practically independent of the thermal pretreatment of the TPU up to 120 °C.

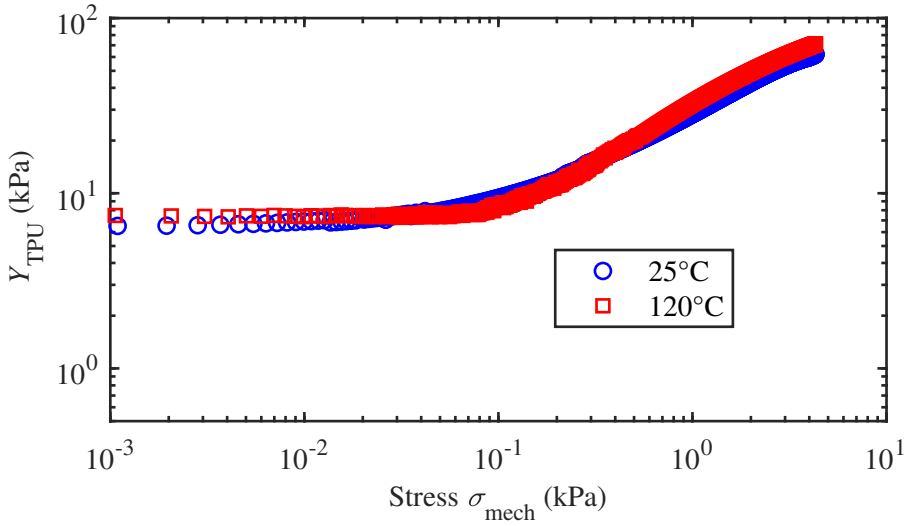

Figure 4.6: Y_{TPU} versus compression stress for non-annealed (25 °C) and annealed (120 °C) 270 µm-thick printed TPU films [161].

Since the two elements of the alternating FEP/TPU/FEP–FEP/air/FEP sandwich are clearly separated into electrical and mechanical properties, one can use the classic Voigt and Reuss approaches to model the Young's moduli of the complete sandwich as shown in Figure 4.1 [176], [177]. Therefore, Elements I and II of the manufactured sandwich can be considered as two parallel elements. Element I consisted of a three-layer structure of FEP/TPU/FEP with the width w_{TPU}, and Element II consisted of a three-layer structure FEP/air/FEP with the width w_{air}, where the lengths and thicknesses of those elements are the same as mentioned previously. For such parallel arrangements, the Voigt model can be used to calculate the total Young's modulus of the combination of Elements I and II as

$$Y_{total} = f\ Y_{E1} + (1 - f)Y_{E2}, \tag{4.3}$$

where f denotes the volume fraction of Element I and Y_{E1} and Y_{E2} are the Young's moduli of Elements I and II, respectively. Since, as already mentioned above, the TPU stripes and air tunnels are of the same total length and height, f can be reduced to the width of the TPU stripes and air tunnels w_{TPU} and w_{air}, respectively, and can be written as

$$f = \frac{w_{TPU}}{w_{TPU} + w_{air}} \text{ and } 1 - f = \frac{w_{air}}{w_{TPU} + w_{air}}. \tag{4.4}$$

Furthermore, the Reuss model is adopted to calculate the Young's moduli of the elements E1 and E2. It yields under the assumption of constant stress throughout each element

$$Y_{E1} = \frac{2\ t_{FEP} + t_{TPU}}{\frac{2\ t_{FEP}}{Y_{FEP}} + \frac{t_{TPU}}{Y_{TPU}}} \text{ and } Y_{E2} = \frac{2\ t_{FEP} + t_{air}}{\frac{2\ t_{FEP}}{Y_{FEP}} + \frac{t_{air}}{Y_{air}}}, \tag{4.5}$$

where Y_{air} is the Young's modulus of air, which for non-sealed air tunnels can be assumed to be equal to zero. It can also be assumed that $Y_{\text{FEP}} \gg Y_{\text{TPU}}$. With these two simplifications combined with equations (4.3) and (4.5), the overall Young's modulus can be calculated as

$$Y_{\text{total}} = \frac{w_{\text{TPU}}}{w_{\text{TPU}} + w_{\text{air}}} \times \frac{2\, t_{\text{FEP}} + t_{\text{TPU}}}{t_{\text{TPU}}}\, Y_{\text{TPU}}. \tag{4.6}$$

Combining equation (4.1) describing the electrical property of the sandwich with equation (4.6) describing the d_{33}-coefficient, equation (4.2) can be rewritten as

$$d_{33}^{\text{max}} = \frac{w_{\text{air}}}{w_{\text{TPU}}} \times \frac{\varepsilon_0 \varepsilon_{\text{FEP}} E_{\text{B}}}{Y_{\text{TPU}} \left(\frac{2\, t_{\text{FEP}}}{t_{\text{TPU}}} + \varepsilon_{\text{FEP}} \right)}. \tag{4.7}$$

At this point it should be emphasized that equation (4.7) can be used as a guide for the further optimization of elastomer-spaced piezoelectrets. It can easily be seen that one possibility is to diminish the denominator $\left(\frac{2t_{\text{FEP}}}{t_{\text{TPU}}} + \varepsilon_{\text{FEP}} \right)$, which under the premise of using FEP as blocking layers, most effectively can be conducted by decreasing the thickness of the FEP film or increasing the thickness of the TPU spacer. The limit of such a reduction would be reached for $\frac{2t_{\text{FEP}}}{t_{\text{TPU}}} \approx 0$, which results in a gain of approximately 20% compared to the present geometry. The other possibility, which is more effective, is the variation of $\frac{w_{\text{air}}}{w_{\text{TPU}}}$ ratio. For example changing the ratio from 1 to 3 will triple the d_{33}-coefficient, according to equation (4.7). Experimentally, the ratio of 3 is easy to be implemented by cutting off every second TPU channel in the already printed grid with the ratio of 1. The corresponding theoretical results are shown in Figure 4.7 as dashed lines, while the measured d_{33}-coefficients at various loads are also depicted in Figure 4.7 by symbols for devices polarized at 25 °C. The stress dependence of Y_{TPU} is thereby taken from Figure 4.6, and the above derived breakdown field strength $E_{\text{B}} = 66.1\,\text{kV cm}^{-1}$ is utilized. Since the measurements of the d_{33}-coefficients are carried out at rather low stress values, it is necessary to take into account the initial tension of the samples in the radial direction introduced by the clamping in the sample holder. The influence of such radial tension on the d_{33}-coefficients is measured for tensioned and non-tensioned specimens (Figure 4.7). It can be seen that the release of the initial tension had an especially large effect on the piezoelectric response of the sandwich with the ratio $\frac{w_{\text{air}}}{w_{\text{TPU}}} = 3$. This can be explained by the fact that the radial tension induced by stretching the sandwich through the embossment and groove of the sample holder compressed mainly the TPU spacer of the sandwich to a point where the induced pre-stress exceeded 0.1 kPa and the Young's modulus started to increase. After removing the initial pre-stress by loosening the screws (see Figure 4.2), the sample revealed the values of the d_{33}-coefficients, which are in excellent agreement with the theoretical estimation.

In general, it can be stated that the here presented model provided reliable prediction of the piezoelectric response of elastomer-spaced piezoelectrets at different stress levels. The observed decrease of the d_{33}-coefficients under larger loads can be explained by the increase in Young's modulus depicted in Figure 4.6 and has been reported for other ferroelectrets as well [28], [31], [32], [36], [131], [169]. It should also be noted that the quasi-static d_{33}-coefficients at low stresses of approximately 8000 pC N^{-1} and 22 000 pC N^{-1} obtained for samples with the $\frac{w_{\text{air}}}{w_{\text{TPU}}}$ ratios of 1 and 3, respectively, seemed to significantly exceed those for the already published ferroelectrets and compared to the values reported for the unipolar electret microphones when considered as ferroelectrets [117], [178].

In addition to the quasi-static piezoelectric d_{33}-coefficients, the dynamic d_{33}-coefficients are also measured. Hereby, the frequency response of the of the ferroelectrets is measured for various seismic masses m_{s} and

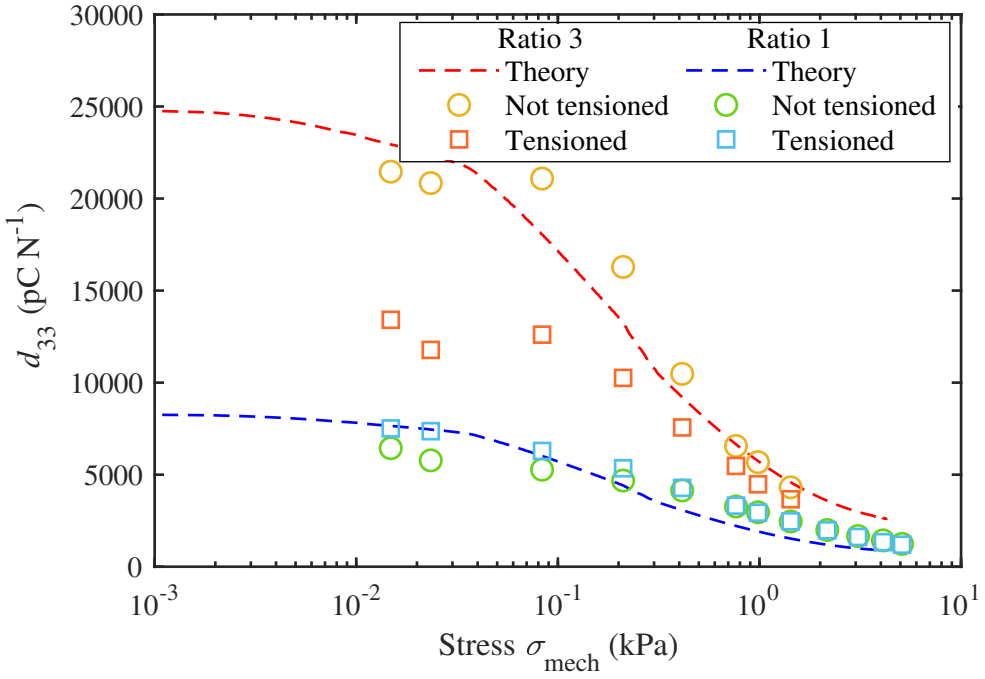

Figure 4.7: Quasi-static piezoelectric d_{33}-coefficients versus stress for the alternating FEP/TPU/FEP-FEP/air/FEP sandwiches with different $w_{\mathrm{air}}/w_{\mathrm{TPU}}$ ratios as indicated. The symbols represent the experimental results, while the dashed lines correspond to theoretical calculation utilizing equation 4.7 [161].

a constant acceleration of 3 m s^{-2} for samples with a different width ratio $\frac{w_{\mathrm{air}}}{w_{\mathrm{TPU}}}$. It can be observed that the dynamic d_{33}-coefficients for both specimens displayed remarkable dispersion over the measured frequency window, especially for low m_{s}. Increasing m_{s} attenuated the piezoelectric response, which at the frequency of 10 Hz gradually decreased from approximately 7500 pC N^{-1} to 3000 pC N^{-1} for the sample with the width ratio of 3 [Figure 4.8(b)]. As in the case of quasi-static d_{33}-coefficients, the observed decrease in the dynamic coefficients for increasing m_{s} can be explained by an increase in the elastic modulus [178]. The obtained values for the dynamic d_{33}-coefficients are considerably smaller than their static counterparts. However, this seems to be a common property of ferroelectrets, where the dynamic piezoelectric coefficients can reach only 30–50% of the static ones, mainly caused by the difference between static and dynamic Young's moduli [149], [178].

The dynamic d_{33}-coefficient is also investigated as function of acceleration applied to the device loaded by different seismic masses, while maintaining a constant frequency of 30 Hz. Corresponding experimental results for the same set of m_{s} values as before (see (Figure 4.8) are shown in Figure 4.9 for the sample with the width ratio of 1. It can be realized that the piezoelectric response exhibited a good and linear performance for accelerations up to 7.5 m s^{-2}, which is much improved compared to that of recently reported performances for ferroelectrets used for cantilever-based energy harvesting discussed in section 3.3 [49], [50]. In general, the dynamic d_{33}-coefficient obtained for the FEP/TPU/FEP–FEP/air/FEP sandwiches significantly exceeded the typical values for classical bulk polymer ferroelectrics, such as PVDF, and even exceeded the best PZT ceramics [179]. Such results are promising for applications in highly sensitive sensors.

The main advantage of such an arrangement is completely separating the mechanical and electrical properties from each other. The TPU stripes are responsible for the mechanical properties, whereas the air-filled regions

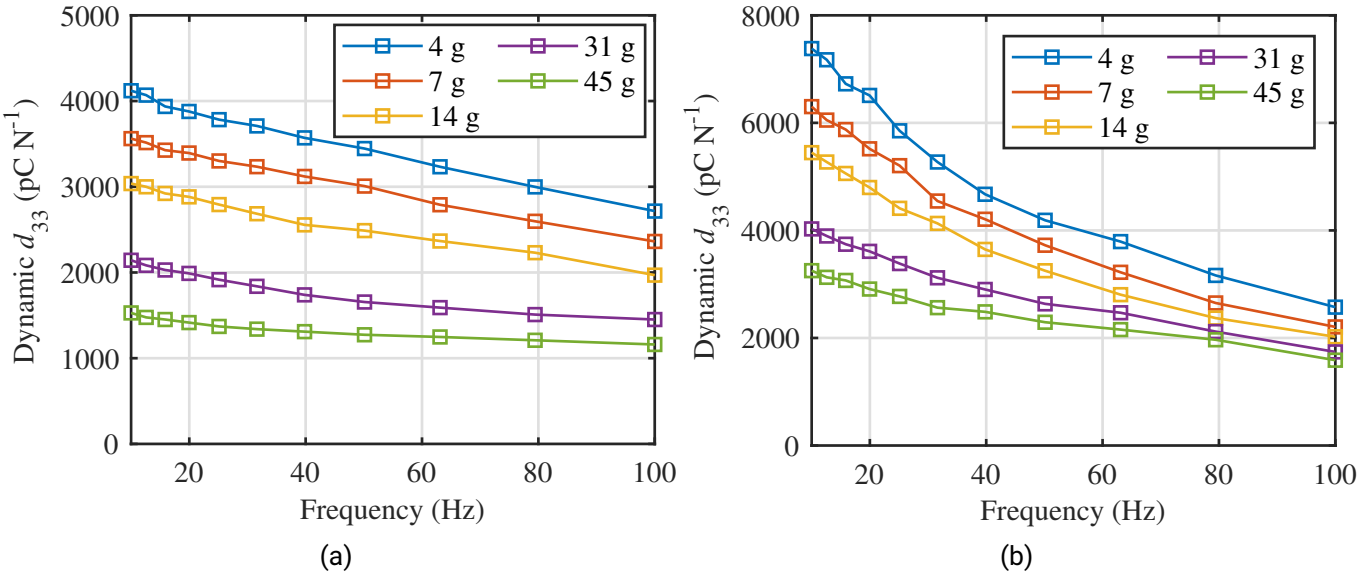

Figure 4.8: Dynamic piezoelectric d_{33}-coefficients versus frequency for different seismic masses m_s, as indicated, and a constant acceleration of 3 m s^{-2}: (a) sample with the $\frac{w_{air}}{w_{TPU}}$ ratio of 1; (b) sample with the $\frac{w_{air}}{w_{TPU}}$ ratio of 3. Both samples are charged to the maximum remanent polarization at 25 °C [161].

in combination with the dielectric material FEP are responsible for the charge storage property after corona poling in an electric field exceeding the Paschen breakdown of air. The proposed design results in the formation of thermally stable, macroscopic electric dipoles in the FEP/air/FEP tunnels due the electric stability of FEP, and as a restoring force using foamed TPU with an extremely low Young's modulus under compressive load. The outstanding piezoelectric response is partly due to the large amount of trapped charges in FEP. However, FEP is a harmful substance when disposed of and, thus, poses a threat to the environment and human health. In this regard, more and more attention is be paid to the development of piezoelectrets composed from biodegradable polymers, such as polylactic acid (PLA), for example.

4.2 Eco-friendly ferroelectrets based on PLA

In view of piles of plastic polluting the environment, it is urgent necessary to develop new sustainable and biodegradable functional ferroelectrets that can be used as mechanical sensors. The growing demand for small sensors for collecting information from various locations at such as entire cities, agricultural infrastructures, manufacturing plants, public energy/water supply networks up to monitoring individual vital functions even inside the human body, makes the development of eco-friendly sensors essential.

An increasing research effort has been devoted to develop sensors and electronics, including energy harvesters, based on biodegradable polymers [180]–[183]. Well-known candidates are natural cotton fibers, cellulose, or synthetic polymers such as poly(glycerol sebacate) (PGS) and PLA. PLA, exists in three forms $_{L}$-PLA (PLLA), $_{D}$-PLA (PDLA), and racemic mixture of $_{D,L}$-PLA (PDLLA) [184]. Only recently, Curry et al. [183] introduced a piezoelectric, biodegradable force sensor made of PLLA. In the same year, Gong et al. [182] presented a piezoelectric PLLA-based nanogenerator for electronic skin applications. However, the piezoelectricity of solid PLLA with only 5 - 15 pC N^{-1} is considered very low and is based on the crystalline moiety of the material,

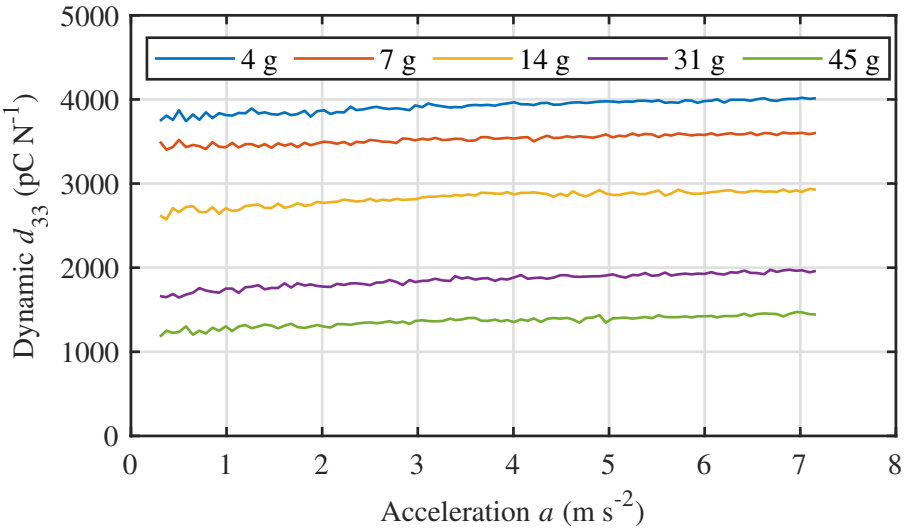

Figure 4.9: Dynamic d_{33}-coefficient as a function of acceleration measured at 30 Hz and different seismic masses m_s, as indicated for the FEP/TPU/FEP–FEP/air/FEP sandwiches with the width ratio of 1 and charged to the maximum remanent polarization at 25 °C [161].

i.e a material property that can not be increased significantly [185]. Recent studies examined custom-made PLA as biodegradable electret material [186]–[190] and reported rather low electret stability [189]. The piezoelectricity of PLA in the crystalline state is determined by the internal rotation of the polar group CO-O [185].

PLA is presently one of the fastest developing biodegradable and bioabsorbable polymer materials. It is derived from renewable plant sources, such as corn or potato starch, tapioca roots or sugar cane [191] and is a cheap mass product commercially available in the form of granulate, filament for FDM 3D-printing, thin film, and cellular foam. Much is known about biodegradable polymers, but the ability to store charges, has hardly been addressed so far. The ability to retain a charge for a long time is one of the requirements for films used to fabricate ferroelectrets.

Note that the large piezoelectric effect discovered here is the result of a unique combination of space-charge electret and mechanical properties of PLA-based ferroelectrets and is not related to the inherent low crystalline piezoelectricity of solid PLA, which therefore can be completely neglected in this work.

In the following the suitability of commercially available PLA as ferroelectret material is investigated. Hereby three forms are of interest: cellular films, bulk films, and Filaments.

4.2.1 Ferroelectrets based on cellular PLA films

Ferroelectrets with cellular polymers are the most known and have been intensively reported in literature such as PP [22]–[24], PE [192], PETP [90], PEI and PEEK(PEEK) [193], COP [194] and COC [195], and fluorocarbon polymers [29], [39]. In this work, knowing the potential of PLA to store charges, a modified PLA resin (Bio-plus 301H) with a density of 1240 kg m^{-3} and a melting point ranging from 165 °C to 175 °C is used as raw material. The resin is physically foamed with carbon dioxide (CO_2) in the melt by utilizing an industrial foaming production line, resulting in PLA foam sheets with a thickness of 1.3 mm and an area density of 0.134 kg m^{-2}, corresponding to a nominal porosity of 92%. In order to fabricate the ferroelectrets, the

microstructure of the PLA foams is modified through pressing them at elevated temperatures [Figure 4.10(a)]. Hereby, the PLA foam sheets are clamped between two metal plates and pressed for 4 min at 50 °C at a pressure of 2 MPa using a Platen vulcanizing press machine. The desired thickness of film is defined by using four pieces of brass sheets with specified thicknesses placed around the samples [Figure 4.10(a)]. Thereafter, the PLA film is cooled down to room temperature while maintaining the mechanical pressure to stabilize the micro-structure.

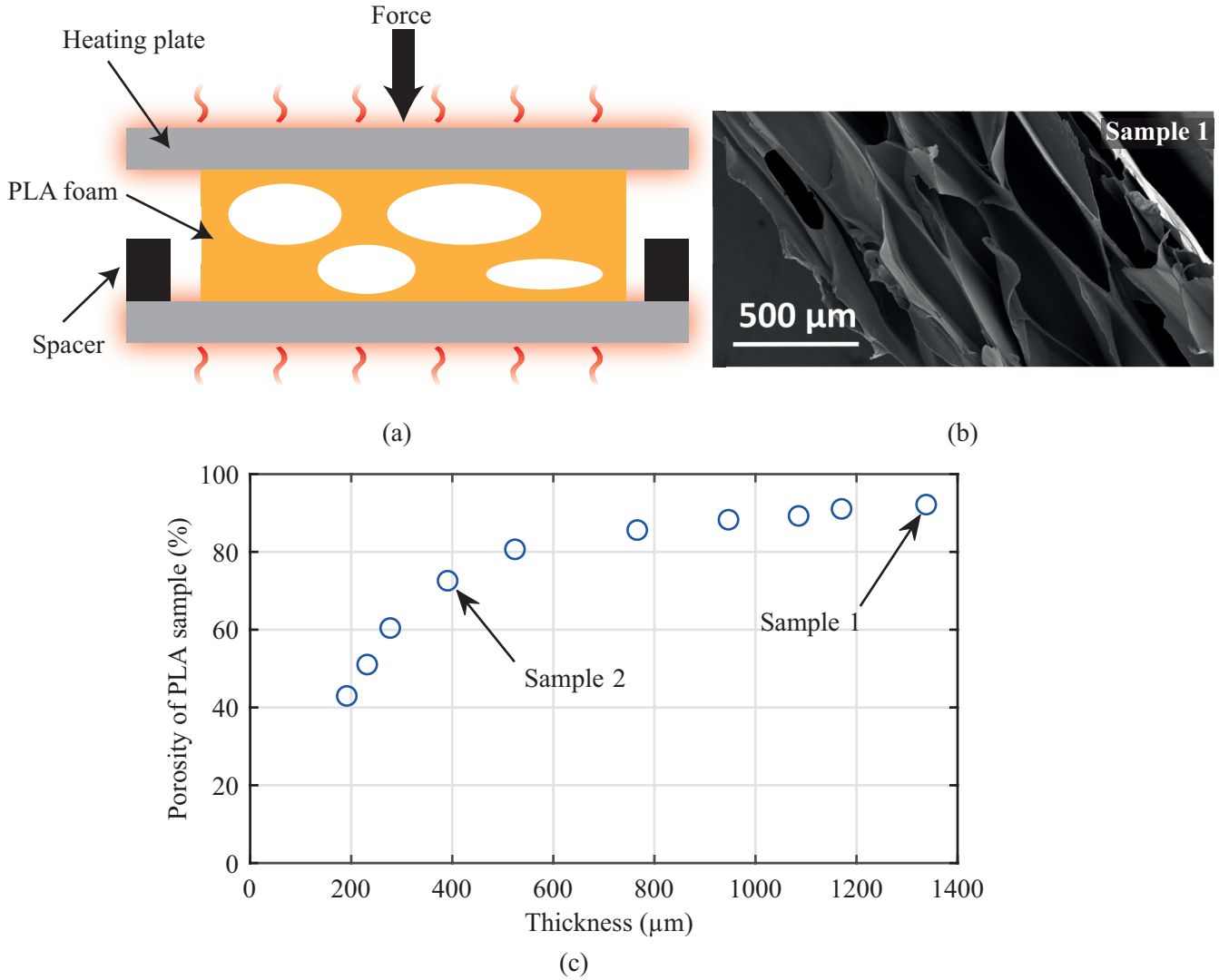

Figure 4.10: Schematic diagram of the preparation process of PLA ferroelectrets: (a) hot pressing treatment, (b) SEM image of the cross-sections of an original PLA foam (Sample 1), (c) porosity of PLA foam samples after hot pressing to a defined thickness [163].

The porosity the PLA foam films after treatment is determined based on their volume and weight. For a better correlation between thickness and porosity as can be seen in Figure 4.10(c), all measured samples are cut to the same shape and surface. The original PLA foam sheet (Sample 1) feature a thickness of 1.3 mm and a porosity of 92%. The porosity of the pressed films decreased as low as 40% for a thickness of 200 µm. The shape of the pores also undergoes alterations during the hot-pressing process. For example, the original PLA

film contains a large number of elliptical voids, the height of which is about 150 µm with a wall thickness of several micrometers. Upon pressing this film to a thickness of about 360 µm, the elliptical cavities flatten. The average thickness of the air voids decreases to about 30 µm. Such a modification of the porous shape influences not only the charging efficiency of the cellular structure as reported in literature [37] but also reduce the Young's modulus, in particular in thickness direction, leading to a significant increase in the piezoelectric d_{33}-coefficient of the film [98], [166].

the PLA film is polarized at room temperature using corona charging setup by mounting the non-metallized film on a metal plate. The corona tip voltage and charging time are -25 kV and 5 min, respectively. Note that in this case the grid is not used to control the voltage applied to the sample, since V_G is limited to 4 kV in the setup. Thereby, enough voltage is applied to the corona tip to ensure the maximum polarization. After charging, both sides of the samples are metallized with 100 nm-thick aluminum electrodes by thermal vapor deposition. Such samples are used to study their piezoelectric characteristics.

In order to determine the quasi-static and dynamic d_{33}-coefficients, circular samples with an electrode diameter of 20 mm are used. The quasi-static piezoelectric d_{33}-coefficients are determined by application of a mass $m = 100$ g to the sample and recording the induced charge Q for 10 s with an electrometer (Keithley, Model 6514).

The first step is to determine the optimal thickness of cellular PLA films corresponding to the maximal reachable d_{33}-coefficient. The PLA transducers are charged one day before measurement, and each experimental d_{33}-coefficient shown in Figure 4.11 is the result of averaging 10 measurements performed on the same sample with a pitch of 1 min. All the PLA ferroelectrets obtained exhibited a strong piezoelectric response with a maximum value of 600 pC N^{-1} observed for the 360 µm-thick sample. This maximum value significantly surpasses typical values of d_{33}-coefficients known for other cellular polymers with a thickness exceeding 100 µm. Again, note that the well-known piezoelectric polymer PVDF has a d_{33}-coefficient of only 25 pC N^{-1}.

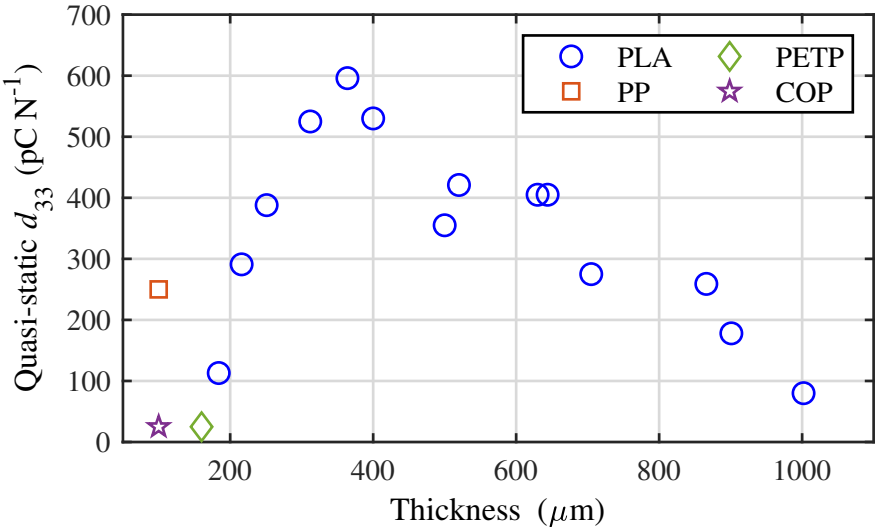

Figure 4.11: Comparison of the static piezoelectric d_{33}-coefficients of PLA films of different thickness developed in this work and previously reported cellular ferroelectrets [22]–[24], [90], [192]–[194]. All PLA samples are measured at room temperature [163].

The peaked dependence of the d_{33}-coefficient on thickness in cellular polymers is a known phenomena and has been reported in several works [98], [193]. This fact can be explained by the the variation of the elastic

modulus for different thicknesses, which results from a compromise of void wall thickness, void size and void shape [19], [90], [98], [166], [196]. Since the goal of this investigation is only to demonstrate the feasibility of using PLA in cellular form as ferroelectret material. Additional studies of the mechanical and charging properties to explain the observed peak for particular PLA structures is beyond the scope of this thesis. Instead, the dynamic longitudinal and transverse piezoelectric characteristics of cellular PLA samples, as well as their temporal stability, are investigated. Hereby, the same measurement setups discussed in section 3.2 are used.

The dynamic longitudinal piezoelectric d_{33}-coefficient is determined by placing a seismic mass m_s onto the sample. The experimental results obtained for various m_s ranging from 20 g to 160 g for a 360 µm-thick sample show a remarkable and flat frequency responses under the resonance region located between 100 Hz and 200 Hz. For the same specimen the dynamic d_{33}-coefficients at a fixed frequency of 20 Hz are measured for different seismic masses m_s. It can be observed that an increase in the dynamic mechanical load to approximately 1 kPa, coressponding to a seismic mass of 160 g, only slightly weakens the piezoelectric d_{33} response, which over the measurement range gradually decreases from about 250 pC N^{-1} to 185 pC N^{-1}. It should be noted that the obtained values for the dynamic d_{33}-coefficients are considerably smaller than the static ones shown in Figure 4.11.

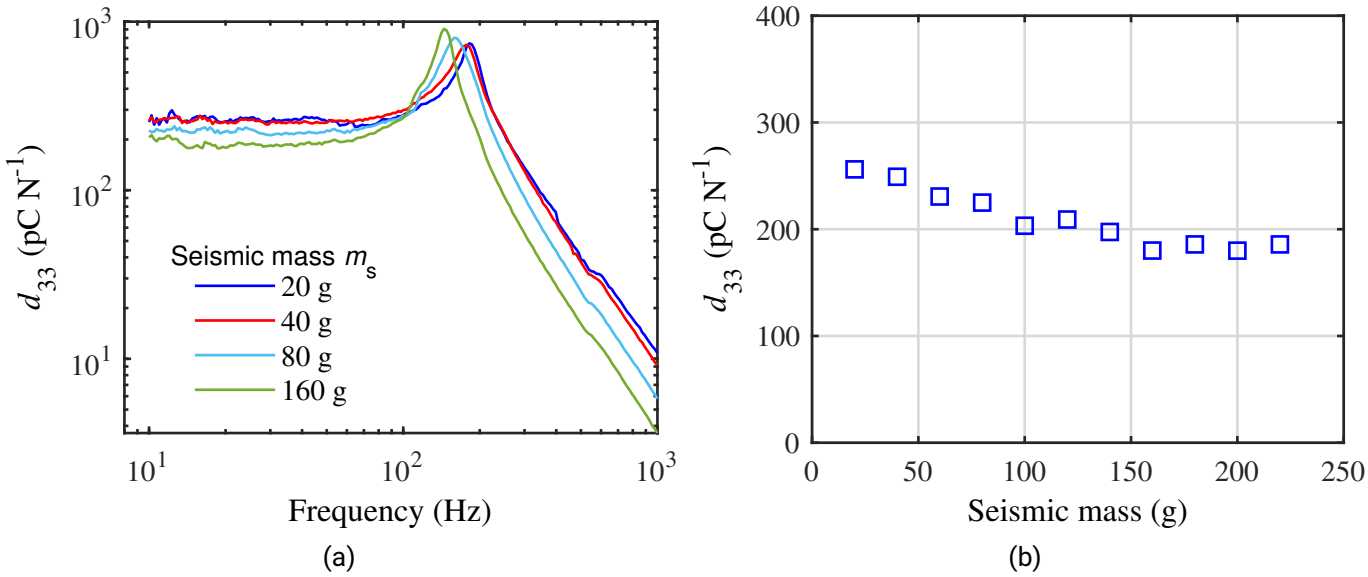

Figure 4.12: (a) Dynamic piezoelectric d_{33}-coefficients for the 360 µm-thick PLA film versus frequency for different seismic masses as indicated. (b) d_{33}-coefficient at a fixed frequency of 20 Hz versus seismic mass [163].

However, it seems to be a common property of ferroelectrets, where the dynamic piezoelectric coefficients reach only half of the static ones, mainly due to the difference between the static and dynamic elastic moduli [197]. The experiments show that, regardless of the thickness of the samples, all the cellular PLA samples exhibit flat low-frequency dynamic piezoelectric responses with amplitudes about one half of their quasi-static d_{33}-coefficients (see Table 4.2).

A further interesting property of the cellular PLA ferroelectrets is the transverse piezoelectric activity. It is known for other cellular films such as PP, that the transverse piezoelectric d_{31}-coefficient is very small. Nervertheless, for the sake of a complete investigation, the cellular PLA ferroelectrets are exmained regarding the dynamic d_{31}-coefficient. Samples with thickness t are therefore cut into stripes with an electrode length l and width w of 30 mm and 10 mm, respectively. A tensile tester (KJ-1065A) is utilized to stretch the sample in

Table 4.2: Piezoelectric coefficients for selected PLA foams.

Thickness	Static d_{33}	Dynamic d_{33} (at 20 Hz)	Static d_{31}	Dynamic d_{31} (at 20 Hz)
250 µm	388 pC N^{-1}	181 pC N^{-1}	22 pC N^{-1}	4.8 pC N^{-1}
360 µm	596 pC N^{-1}	277 pC N^{-1}	44 pC N^{-1}	6.1 pC N^{-1}
400 µm	530 pC N^{-1}	252 pC N^{-1}	25 pC N^{-1}	3.2 pC N^{-1}
520 µm	420 pC N^{-1}	210 pC N^{-1}	28 pC N^{-1}	3.8 pC N^{-1}
630 µm	405 pC N^{-1}	179 pC N^{-1}	39 pC N^{-1}	5.7 pC N^{-1}

the length direction with a static force F. The resulting charge Q is recorded with an electrometer (Keithley, Model 6514). In this approach, the d_{31}-coefficient is determined as

$$d_{31} = \frac{Q}{F}\frac{t}{l}. \tag{4.8}$$

Therefore, striped cellular PLA samples are clamped in a holder at both ends to investigate the dynamic transverse piezoelectric properties. A shaker (B&K 4809) driven by a PULSE Analyzer (B&K 3560C) and amplified by a power amplifier (B&K 2713) is used to stress the sample. The stretching force is measured by means of a built-in force sensor (B&K 8200). The force signal is amplified via a conditioning amplifier (B&K 2692) and then recorded through the PULSE Analyzer. The charge generated by this process is also recorded by the same PULSE Analyzer (see Figure 3.31).

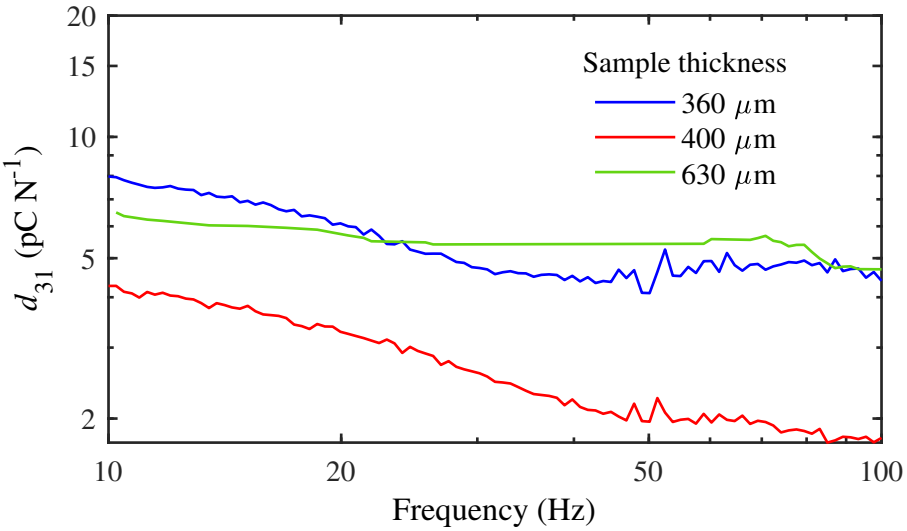

Figure 4.13: Dynamic piezoelectric d_{31}-coefficient as a function of frequency for cellular PLA ferroelectrets of various thicknesses, as indicated. The measurements are performed utilizing a dynamic force of 0.2 N [163].

The experimental d_{31} coefficients for the selected PLA ferroelectrets are listed in Table 4.2, while the frequency responses thereof are shown in Figure 4.13. The results show that the transverse quasi-static piezoelectric coefficients of PLA foams significantly exceed the d_{31} response of cellular PP by more than a factor of 10. However, as in the case of the longitudinal response, the obtained values for the dynamic d_{31}-coefficients are much smaller than those for the static ones and only amount to about 20% thereof.

One further investigation is the temporal stability of the piezoelectric effect of cellular PLA. Since the measurement of the d_{33}-coefficient is more simple than measuring the d_{31} coefficient, the temporal decay of the quasi-static piezoelectric d_{33}-coefficient is measured over 150 days. Two cellular PLA ferroelectrets are selected exhibiting different thicknesses of 200 and 310 µm. All measurement are conducted at room temperature and ambient atmosphere.

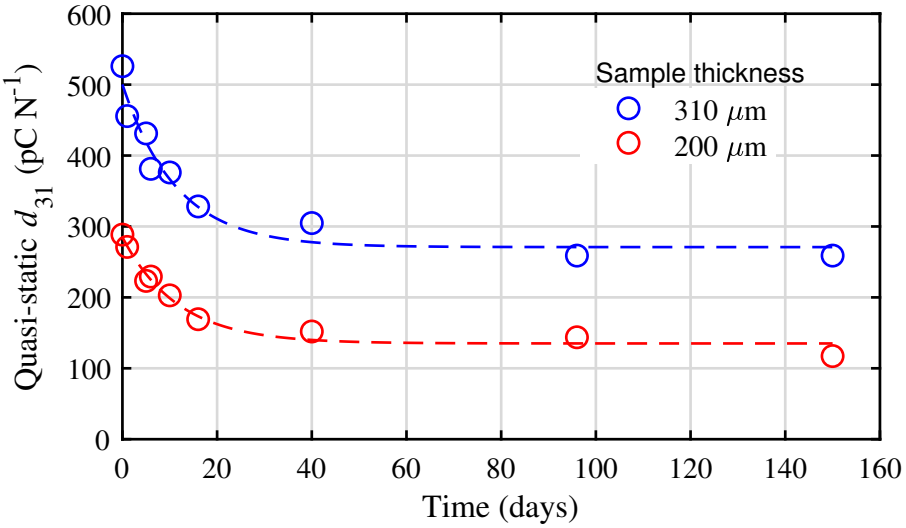

Figure 4.14: Temporal decay of the quasi-static d_{33}-coefficient at room temperature and in ambient atmosphere for two cellular PLA ferroelectrets of different thickness as indicated. The samples are polarized under the same conditions, with a corona tip voltage of -25 kV for 5 min [163].

For both samples, their piezoelectric coefficients indicate a fast decay in the first few days after charging. However, after approximately 20 days of storage under ambient conditions, the coefficients stabilize and remain virtually unchanged over the next 130 days. Quantitatively, the d_{33}-coefficient decreases to about 50% of the initial value during the first 20 days for all investigated PLA ferroelectret samples, regardless of their thickness. Note that the residual d_{33}-coefficient after 150 days of storage is still very high and, depending on the thickness of the samples, amounts from 100 pC N^{-1} to 300 pC N^{-1}. Unfortunately, almost all cellular ferroelectrets demonstrate a partial degradation of their piezoelectric characteristics in course of time [178], [198]. As previously reported for other systems, the use of additional processing treatments, including charging and pre-aging at elevated temperatures, may help to improve the long-term piezoelectric stability of PLA ferroelectrets. It is known for ferroelectrets in general, that their resistance to fatigue and aging is mainly determined by two factors: their mechanical stability and their charge storage stability. In the present case, a temporary decrease in piezoelectricity can be associated, first of all, to the instability of the remanent charge, and not to the mechanical degradation of the cellular structure. It is known as well that charging polymers above the glass transition temperature should stabilize the charges, as the deep energetic traps and thus more stable traps, will be adressed. In cellular ferroelectrets, it is believed that the storage of charges occurs at the polymer/air interfaces of the voids as discussed earlier. However, for better understanding of the charge storage capability of PLA, it is more appropriate to investigate bulk films.

4.2.2 Ferroelectrets based on bulk PLA films

The investigation of bulk PLA is more straightforward as no further steps such as hot pressing are needed. However, in this case charges are not trapped at the interface of the voids as in the cellular films, but in the bulk i.e. film interface. Hereby, another type of investigation can be caried out, which is the temporal surface potential stability of one-side metallized bulk PLA films. The metallization is carried out by thermal vapor deposition of 100 nm-thick aluminum. For poling, the same corona charging setup is used, where a DC corona voltage of $V_C = \pm 10\,\text{kV}$ and DC grid voltage of $V_G = \pm 1.5\,\text{kV}$ are utilized for three minutes at 25 °C and 80 °C, respectively. The temperature of 80 °C is chosen to be above the glass transition temperature of 60 °C without causing waviness or deformation of the films. After corona poling the resulting surface potential is measured by an electrostatic voltmeter from Monroe Electronics (model N244). All measurements were performed at ambient temperature of $24\,°\text{C} \pm 2\,°\text{C}$ and atmospheric pressure. The relative humidity of the ambient air in the lab fluctuated slightly around 50%. The temporal decay of the obtained surface potentials is recorded over six months, which significantly exceeds the observation period of previous studies of only 50 days [199]. The experimental results of positively and negatively corona charged PLA films are summarized in Figure. 4.15.

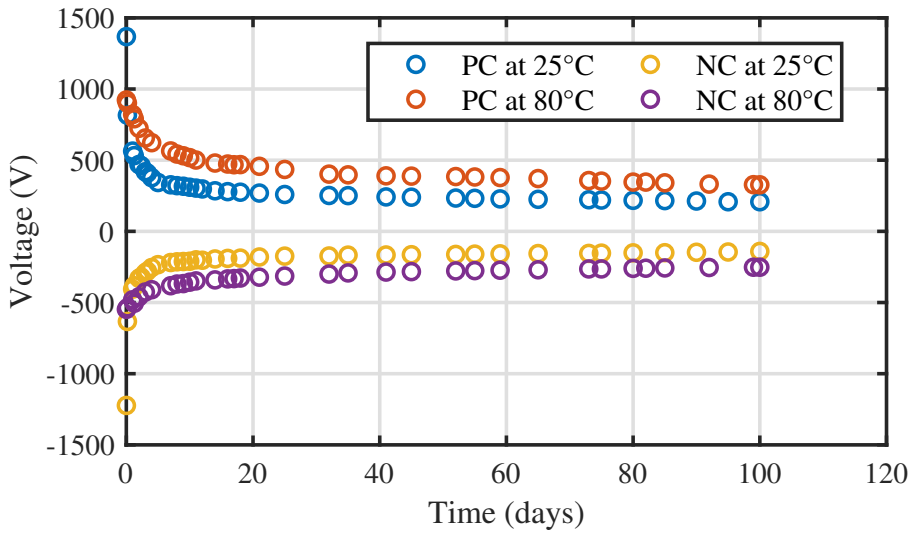

Figure 4.15: Isothermal decay of surface potential for samples polarized at 25 °C and 80 °C, and measured at room temperature. The abbreviations ”PC” and ”NC” indicate positively charged and negatively charged with a voltage magnitude of 1.5 kV [165].

Thereby films polarized at room temperature show a rapid drop in surface potential during the first 30 days to about 1/3 of the initial surface potential. Afterwards, the surface potential decreases slowly and attains about 10% of the initial value at the end. In contrast, samples charged at an elevated temperature of 80 °C show much smaller initial surface potentials of 925 V and −875 V, and retain about 30% of the initial potential after 180 days of storage under laboratory conditions. The results show that PLA films polarized at elevated temperatures have superior electret properties and are more suitable for long term use. A more detailed investigation of the physical reasons for charge stabilization at elevated charging temperatures is presently being conducted and is beyond the scope of this thesis. Nevertheless, similar behavior for ferroelectrets based on FEP has been reported previously [22], [29], [33], [140].

Since the surface potential seems to be stable enough, the PLA film can be used to build a ferroelectret. One possibility for manufacturing sensitive ferroelectrets is the multilayer structure (sandwich structure with TPU

spacer) as mentioned before, however, replacing the FEP films by PLA. It is expected to reach high values due to the low Young's modulus of the foamed TPU elastomer used as a spacer between the two PLA films.

The ferroelectrets are fabricated utilizing two 20 µm-thick PLA films (Macropack GmbH & Co. KG, Germany), sandwiching a grid of foamed TPU (VARIOSHORE TPU NATURAL, colorFabb B.V., DK Belfeld, The Netherlands), as previously described and shown in Figure 4.2 [161]. The width of the air tunnel is equal to the width of the TPU stripe and amounts to 1 mm. The total thickness of the prepared sandwiches is approximately 310 µm. The charging process is carried out using the corona triode.

The d_{33} coefficients obtained from ferroelectrets depend to a large extend on the obtainable surface potential as can be conculed from equation 4.7. The ferroelectret is considered fully charged when the poling voltage exceeds twice the value of V_B [95]. This leads to an optimal poling voltage of approximately ±4 kV when the following values are utilized in equation (3.4): $d_{air} = 270\,\mu m$, $d_{PLA} = 20\,\mu m$, $\varepsilon_{PLA} = 3.5$, $\varepsilon_{air} = 1$ and $E_B = 66.1\,kV\,cm^{-1}$.

A total of 20 samples are prepared and polarized. Ten of them are polarized at room temperature (25 °C), where five are positively charged and five negatively charged. The other ten samples are charged at 80 °C, of which again each five are polarized with a negative or positive polarity.

The quasi-static piezoelectric d_{33}-coefficient is determined by applying a defined mass m to the device in short-circuit prior to the measurement. Afterwards the mass is removed and the generated charge Q is recorded for 10 s by an electrometer (Keithley model 6517). The d_{33}-coefficient is then calculated as

$$d_{33} = \frac{Q}{m \cdot g}, \tag{4.9}$$

where g denotes the gravitational acceleration.

The piezoelectric d_{33}-coefficients are measured periodically for six months under ambient conditions using a static stress of 1.2 kPa. The results show that the samples polarized in the negative and positive corona discharge have similar initial d_{33}-coefficient as well as temporal decay. At the same time, the temperature, at which the poling of samples is performed, has a significant effect on both the initial value of the d_{33}-coefficient and on its temporal decrease. For example, the initial d_{33}-coefficient immediately after charging in negative corona discharge reached approximately 2800 pC N^{-1} and 1700 pC N^{-1} for temperatures of 25 °C and 80 °C, respectively (Figure 4.16).

Considering that for such ferroelectrets the piezoelectric d_{33}-coefficient depends mainly on the areal charge density of trapped charges at PLA/air channels interfaces σ_{int}, the Young's modulus of the entire transducer Y and the structure factor α according to equation (4.1), one can expect that the temporal stability of the d_{33}-coefficient is determined by both the stability of the interfacial charges and the mechanical properties. At present, it is assumed that the initial drop in d_{33}-coefficient is due to the rapid discharge of PLA films, as shown in Figure 4.16. Interestingly, after 180 days of storage, the d_{33}-coefficients for samples charged at 25 °C are still larger compared to the samples charged at 80 °C. At first glance, this seems to contradict the results shown in Figure 4.15. However, the conditions for surface potential discharge are different for single films and three-layer sandwiches. In the first case, the charged surface of the PLA film contacts the ambient air directly, whereas in the second case it interacts with the air confined inside the channels. Therefore, the rate of discharge in both cases may be different, for example, due to the difference in humidity of the air. Important to note that after storage for half a year, the PLA-(TPU/air)-PLA transducers still show high piezoelectric properties, which are significantly superior to conventional piezoceramics (d_{33} ~500 pC N^{-1}) and piezopolymers (d_{33} ~30 pC N^{-1}).

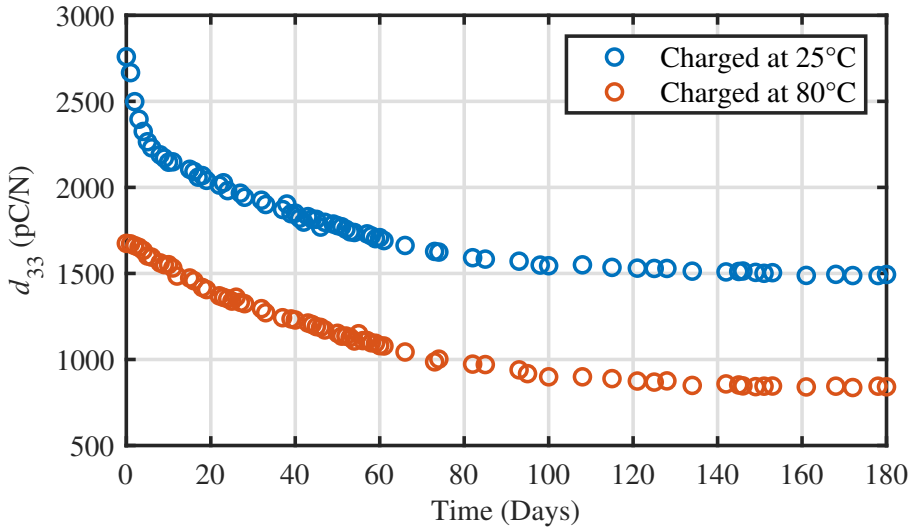

Figure 4.16: Isothermal decay of the longitidunal piezoelectric d_{33}-coefficient, polarized using 4 kV at 25 °C and 80 °C, respectively and measured at room temperature. All Measurements of d_{33}-coefficients are performed at a static load of 1.2 kPa [165].

The auspicious surface potential stability as well as the relatively large piezoelectric activity, the PLA/TPU/PLA sandwich structures is suitable to be used as an eco-friendly force sensor for force myography to detect slightest muscle deformations on the forearm caused by finger movements. This application is discussed in section 5.1.

4.2.3 3D-printed ferroelectrets using PLA filaments

3D-printing of ferroelectrets has been investigated with well known electret materials such as PP [200], [201], acrylonitrile butadiene styrene (ABS) [202] and PDMS [203]. Some groups tested the possibility of completely 3D-printing ferroelectrets by utilizing the infill geometry as artificial air voids of the ferroelectret. However, fully printing ferroelectrets remains a challenging task due to the relatively large minimum printable layer thickness and possible defects in the layers, which represent shortcomings that prevent the structure from being charged. An alternative way, that also has been tested, is to print two independent films, where one layer exhibits well defined pores and the other one is an unstructured plane-parallel film. The two layers were subsequently thermal-bonded together in order to form the ferroelectret [200], [204]. The further treatment of the printed films with heat deforms, however, the printed polymer and results in partly distorted structures.

PLA is also one of the most popular materials for 3D-printing using fused deposition modeling. Here, a novel approach is used to build a 3D-printed ferroelectret using PLA filament. The ferroelectret is examined regarding the charge stability of the printed PLA, its mechanical properties that result from both the geometry and the printing process and its piezoelectric response. The main focus hereby is providing a sensitive and versatile material for various mechanical sensor applications.

Preparation of the ferroelectret transducer

All geometries investigated here are designed in Autodesk Fusion 360 (Autodesk, Inc) and sliced using an open source software (Slic3r). The slicing software divides the 3D-model into layers and defines the printing

path for the 3D-printer (Prusa Mk3s, Prusa3d DE).

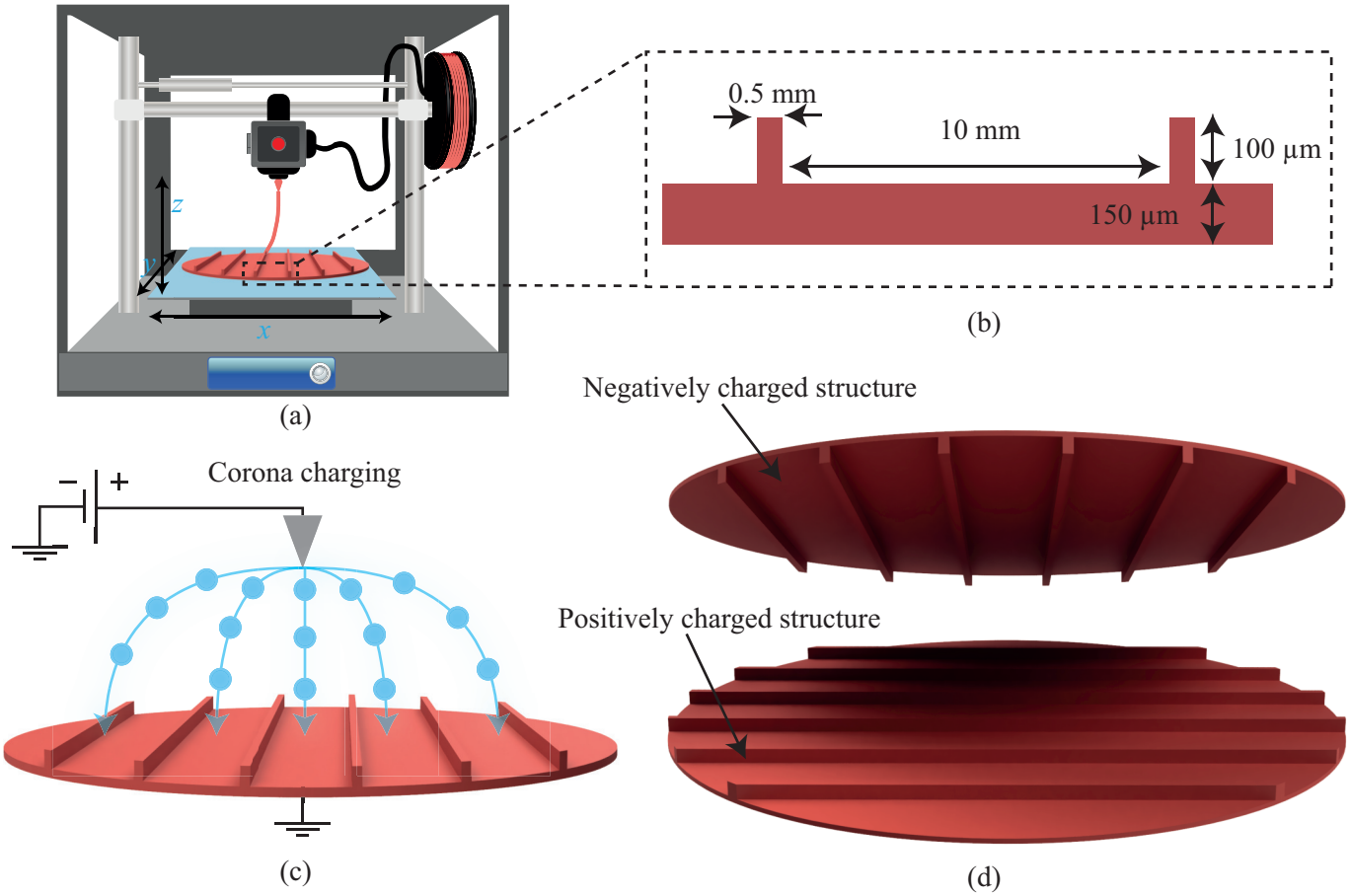

Figure 4.17: Preparation steps of the ferroelectret: (a) and (b) 3D-printing of the structures and the chosen geometry, (c) charging of one part of the PLA ferroelectret and (d) assembly of two charged parts to build the ferroelectret [162].

The initial layer thickness is 0.1 mm to maximize bed adhesion, while using a layer thickness of 0.05 mm for all following layers. The print speed is 20 mm s^{-1} with a nozzle diameter of 0.4 mm that extrudes fused PLA-filament (REDLINE FILAMENT GmbH). For a smooth bottom layer that is directly printed on the bed, a spring steel sheet with smooth double-sided PEI is used. The printing parameters are summarized in Table 4.3.

The printed component is then provided with an evaporated aluminum electrode on the smooth side to allow for an electrical contact for the charging process. For a reproducible evaporation of the electrode on all samples, a shadow mask that features a 42 mm hole is used. This corresponds to the electrode diameter and the active part of the ferroelectrets.

Normally, for charging a ferroelectret, an electric field is applied between both sides of the ferroelectret generating large electric fields in its air-filled voids. The generated positive and negative charges are separated by the applied electrostatic field and move towards the polymer walls, where they are quasipermanently trapped. In this case the charging process is carried out differently, since the ferroelectrets are built using two independent parts. The two parts are charged with opposite polarization using corona charging. These

Table 4.3: Printing parameters for PLA. All samples were printed using filament from the same spool and using the same 3D-printer.

Parameter	Value
Extruder temperature	215 °C
Heatbed temperature	60 °C
layer height	0.05 mm
Filament diameter	1.75 mm
Nozzle diameter	0.4 mm
Printspeed	35 mm s^{-1}

parts can be considered as electrets charged with different polarities. Afterwards, the two charged parts are glued together such that the ridges in the two parts are at 90° angles [Figure 4.17(d)], to form an artificial ferroelectret (Figure 4.17). The 90° angle prevents the ridges from slipping when subjected to an external force.

Each part of the ferroelectret consists of a 150 µm-thick base with 100 µm-thick ridges on the top. Between each two ridges, a distance of 10 mm is chosen, which in turn represents the width of the charged area. The ridges feature a width of 0.5 mm to minimize the contact surface between the two parts, and as a result the overall stiffness of the structure.

Characterization of ferroelectrets using printed PLA

In view of its practical interest as sensor material, a long term measurement of the surface potential after charging is conducted. The samples are polarized in a corona triode under ambient conditions utilizing a DC

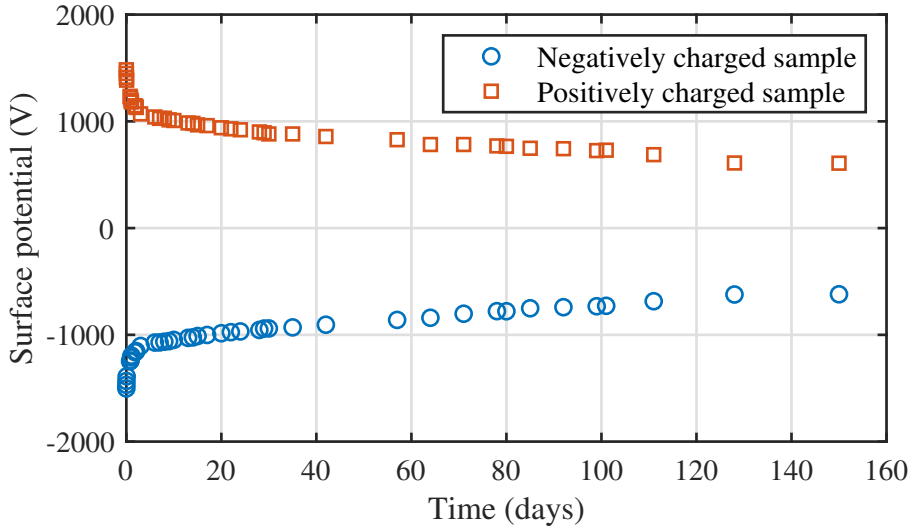

Figure 4.18: Surface potential decay of the positively and negatively corona charged samples in function of time. Charging and decay measurement are both performed at room temperature [162].

corona voltage of $V_C = 9\,\text{kV}$ (power supply HCN 350-20000, fug Elektronik GmbH) for the positively charged sample and $V_C = -9\,\text{kV}$ for the negatively charged one. The grid voltage V_G is fixed at 1.5 kV or $-1.5\,\text{kV}$ depending on the desired polarization, to control the surface electret potentials. The poling experiments are carried out at room temperature with the non-metalized surface, which is the surface with the ridges, facing the grid and needle of the corona triode. The total poling time is sufficiently long for the poling process to be completed. After charging, the surface potential is measured with an electrostatic voltmeter (model 244, Monroe Electronics Inc.).

The experimental results (Figure 4.18) show a similar behavior of both samples with different polarities. The fastest surface potential decay is recorded during the first days after charging. Within three days, the surface potential decreases to 70% of the initial value measured directly upon charging. After 30 days the surface potential decreases more slowly to reach approximately 42% of the initial value after 150 days. Since a similar behavior is recorded for cellular PLA [45] and bulk PLA [205], [206], we can assume that printed PLA is very similar to bulk PLA.

The mechanical properties were determined at room temperature using a universal testing machine (Inspekt table 5 kN, Hegewald& Peschke). During the measurement, the specimen is compressed between two parallel plates with a rate of $0.1\,\text{N}\,\text{s}^{-1}$. The resulting force is measured by the 100 N-force sensor as described before.

The mechanical properties of the ferroelectret were examined regarding the creep behavior of the sensor while maintaining the stress and the Young's modulus. Hereby, the stress is increased in steps of 0.5 N while simultaneously measuring the force (as indication for a varying stress) used to move from one strain to another [Figure 4.19(a)]. When the target force is reached, the stress is maintained for 60 s while measuring the strain developing for preserving the reached force.

When the stress is increased from zero to 1 kPa the ferroelectret is deformed by a strain of approximately 7.5% [Figure 4.19(c)]. Up to this point, the stress and strain show a relatively linear behavior [Figure 4.19(b)]. The Young's modulus Y for a strain up to 7% is approximately 0.7 MPa.

By increasing the stress above 1 kPa, the deformation of the ferroelectret decreases at each step until 2 kPa is reached. Subsequently, each step of 0.5 kPa results in an equal strain of 0.7%. In this part, however, the Young's modulus increases up to 0.55 kPa. Furthermore, a relatively small creep of 0.05% is recorded at each step after 60 s. When the stress is increased to 3.6 kPa und then decreased to zero, a hysteresis behavior is observed. In addition, the ferroelectret does not return to its original state once the stress is removed and a strain of approximately 1.2% remains.

The piezoelectric response of the ferroelectret is measured using the same setup as shown in Figure 4.19(a) to measure the force F while measuring the resulting charge difference Q using an electrometer (6517A, Keithley Instruments). Since the surface of the electrode corresponds to the surface of the plate used to apply the stress, the piezoelectric d_{33} coefficient can be calculated as $d_{33} = Q/F$.

When the force is increased from zero to 0.5 N a piezoelectric response of approximately $d_{33} = 750\,\text{pC}\,\text{N}^{-1}$ is recorded (Figure 4.20). This response, however, decreases with each force step to attain the minimum value of approximately $220\,\text{pC}\,\text{N}^{-1}$ starting from 4.5 N. This value seems to be invariable for larger applied forces. The decrease of the piezoelectric coefficient is expected as a consequence of the mechanical properties of the ferroelectret, which shows a nonlinear behavior. For a large applied force, the ferroelectret becomes stiffer, and, thus, less inclined to deformation resulting in a reduced charge. It should be noted that the d_{33}-coefficients discussed here are relative coefficients for a given pre-stress. For some applications, such as a piezoelectric accelerometer, a pre-stressing of the piezoelectric material through a seismic mass is necessary. In this case the piezoelectric d_{33}-coefficient changes according to the pre-stress. Hence it is important to investigate the relative piezoelectric response when a pre-stress is applied or the force is increased in steps.

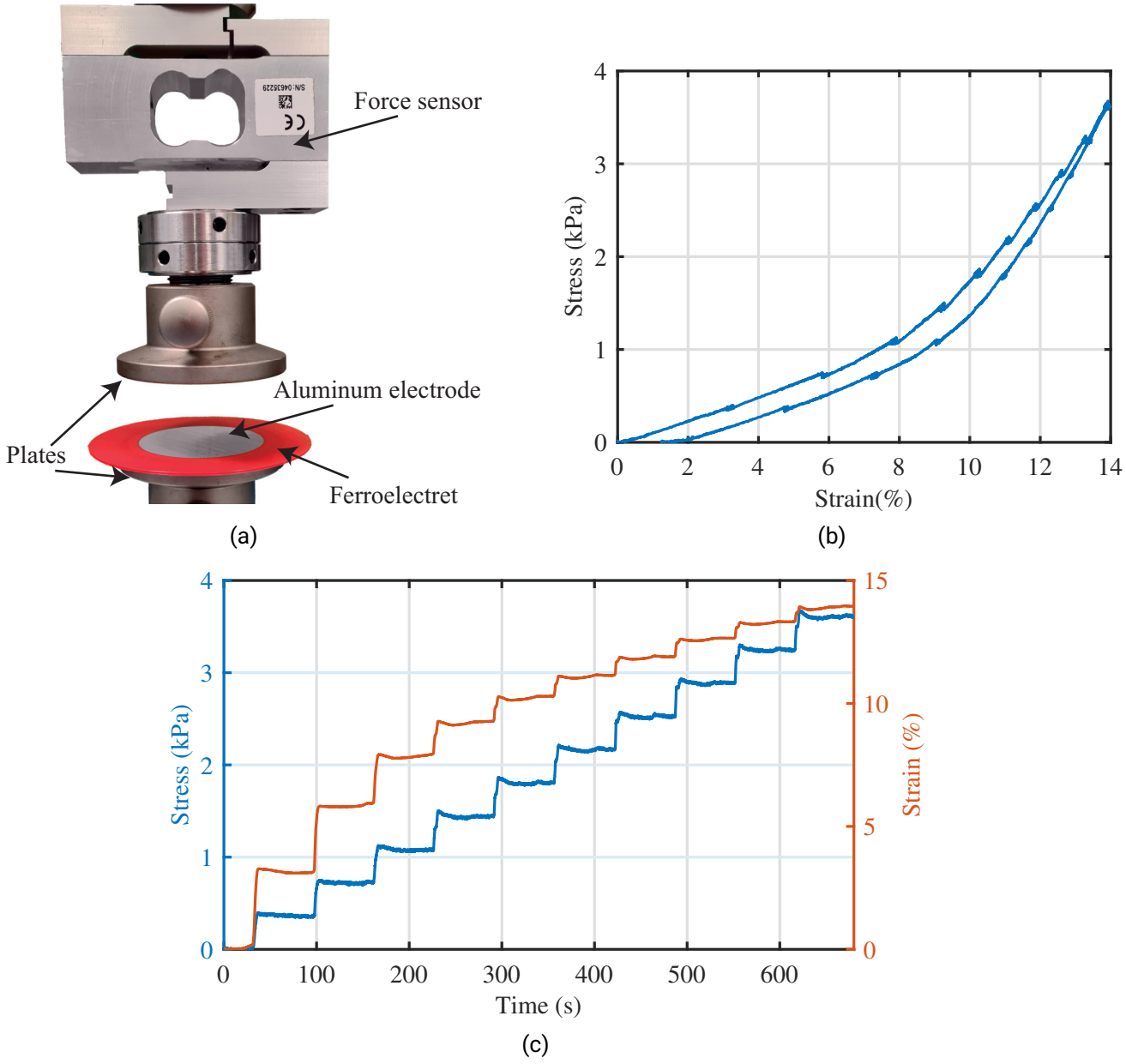

Figure 4.19: (a) Measurement setup to measure the force, (b) stress-strain curve of the ferroelectret, (c) stress-strain relation of the ferroelectret film, while holding each strain value for 60 s [162].

In addition to the good electret property of PLA, the possibilities of designing more complex structures using 3D-printing techniques is a new field with a great potential to be investigated. In fact, ferroelectrets can be printed using multimaterial printer. The base material, where the charges are trapped can be printed using any known electret material, whereas the ridges (Figure 4.17) can be printed using a soft material such as varioshore TPU, as discussed in section 4.1. In fact 3D-printing of the spacer can be conducted on bulk PLA films as well, by placing a PLA film on the printing bed of 3D-printer.

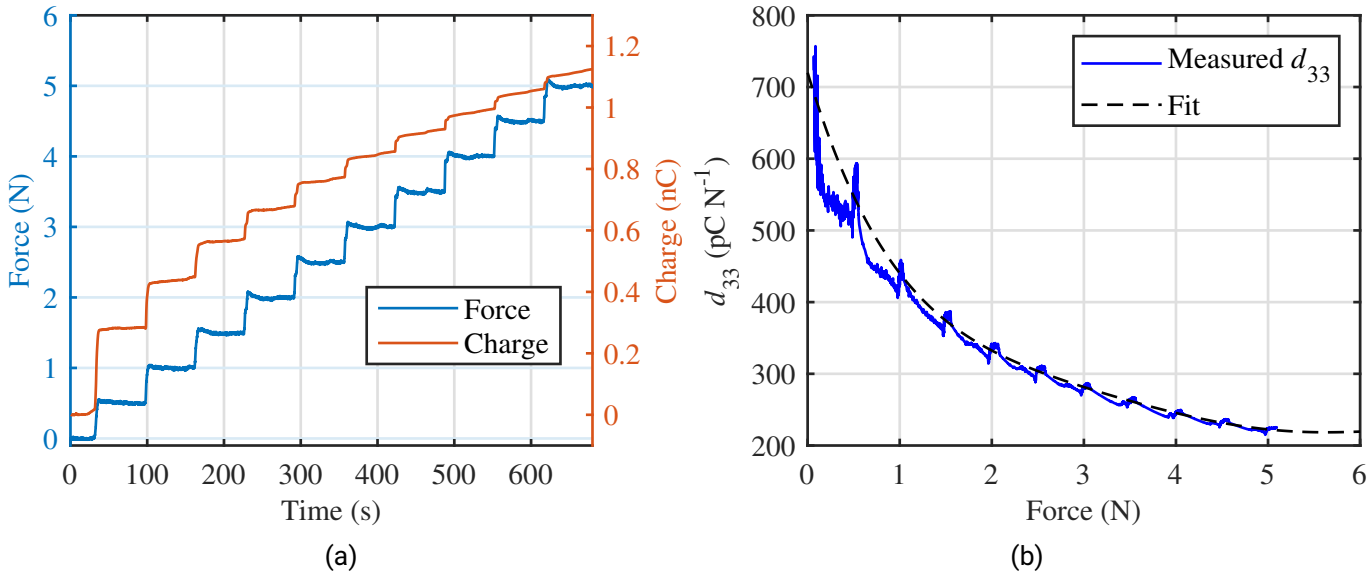

Figure 4.20: Measurement of the charge difference for an increased force in steps of 0.5 N. (a) In blue is the applied force whereas in orange is the measured charges difference. (b) The piezoelectric response is calculated by dividing the charge by the force [162].

4.3 Summary of ferroelectrets for sensor applications

The proposed sandwich design by combining bulk materials with 3D-printed soft spacer elements guarantees a high longitudinal piezoelectric response. A practical advantage of such structures is the linearity of the piezoelectric response for accelerations of up to $0.7 \times g$. This distinguishes the present structure from other ferroelectrets such as the discussed parallel-tunnel structure, where a saturation of the piezoelectric activity is reached at much smaller accelerations. The obtained experimental and theoretical results constitute an excellent basis for further optimization of sandwiched ferroelectrets. Especially interesting would be to optimize the geometrical effects and the electromechanical properties such as the extreme softness of the elastomer by air inclusion.

The PLA based ferroelectrets can be potentially used in a variety of biological applications, such as biosensors embedded in tissue, micro-energy harvesters and artificial muscles. In addition, the developed PLA transducers retain most of the advantages of conventional polymer ferroelectrets, such as flexibility and good processability, and at the same time are environmentally friendly and biodegradable. Another important challenge is the ability to 3D-print multilayer structures in a one-stage printing process, which would greatly simplify the manufacturing process and variability of such devices resulting in an improved overall electromechanical performance. Here, small but successful steps will pave the way to new ferroelectret structures with further possibilities to make them biodegradable or at least more ecofriendly.

5 Transducer applications

The following chapter was published in [164], [165], [207].

In this chapter, the potential of the newly developed ferroelectrets including the new manufacturing routes is demonstrated through examples of applications. For instance, the high sensitivity is demonstrated in measuring the slightest muscle deformation on the forearm due to finger movement, the new manufacturing route using 3D-printing is demonstarted by 3D-printing a highly sensitive insole. Furthermore, the potential of combining 3D-printing parts with bulk materials is demonstrated by building an ultrasonic transducer.

5.1 Gesture recognition using Support Vector Machine

The Human Machine Interface (HMI) refers to a dashboard that allows users to communicate with machines, computer programs or systems. From a technical perspective, the term HMI describes any input instrument that is used to communicate with a machine. Whether it is the use of a prosthesis, the control of a robot by teleoperation or writing an e-mail on a computer. Therefore, numerous possibilities for operation have been investigated and commercialized, such as keyboards, camera systems, acceleration sensors or even brain-computer interfaces. A more intuitive control possibility is the use of hand gestures since almost every communication is handled or accompanied by hand motions. In the state of research, many possibilities for recognizing hand gestures have been investigated such as camera systems [208] and recording the muscle movements, also known as myography. The advantage of the latter method compared to the camera approach is the independency of light conditions and, more importantly no fixed environment requirement. Moreover, such systems can be applied to the forearm [209]–[211], making them wearable and flexible for everyday use such as controlling a prosthetic arm [212].

The main methods for such applications are electromyography (EMG) and force myography (FMG). EMG is an electrophysiological method in neurological diagnostics, in which electrical muscle activity is measured in resting and contracted muscles. This requires, however, a good placement of electrodes for a meaningful signal recording, followed with high-level and complex signal processing. The signals recorded by EMG are usually unstable due to muscle fatigue in long-term employments. In addition, the electromagnetic interference and conductivity variation of the skin, e.g., through sweating, has to be taken into account. In contrast to the EMG based method, the FMG based method relies on volumetric changes that occur when contracting the muscles against a mechanical default state of the sensor. Hence, the deformation results in a radially directed force distribution which can be measured using the piezoresistive effect which is increasingly gaining in importance and has been investigated intensively in the last 20 years [213].

Thereby the most utilized FMG sensors are flexible piezoresistive polymers [214]–[216]. A force applied to such a sensor results in a proportional change in resistivity. On the other hand, the creep behaviour of such sensors causes a low measurement accuracy and low repeatability.

An alternative possibility for FMG based sensors is the use of flexible piezoelectric polymers, which generate charge upon mechanical excitation. The direct conversion of mechanical deformation into electric signal offers a more precise measurement with less electronic components and power consumption. This can be achieved using ferroelectrets introduced in Chapter 4. In order to demonstrate the potential of the eco-friendly ferroelectrets discussed in section 4.2.2, they will be used as sensors for FMG on the human forearm.

5.1.1 Design of the FMG-system

In order to apply the PLA/TPU/PLA ferroelectrets to the forearm, four sensor holders connected with elastic cord are used, on each a polarized ferroelectret sensor is glued [Figures 5.1(a) and (c)]. Hereby, the ferroelectrets are cut into squares with dimension $40\,\text{mm} \times 25\,\text{mm}$ and are located between the forearm and holder as indicated in Figures 5.1(b) and (c). For guaranteeing cohesion of the layers and protect the sensors from external influences such as sweat, a silicone layer (Ecoflex 0035) is used to embed each sensor with its holder. The adhesion of the silicon to the skin allows the sensors to maintain their positions on the forearm.

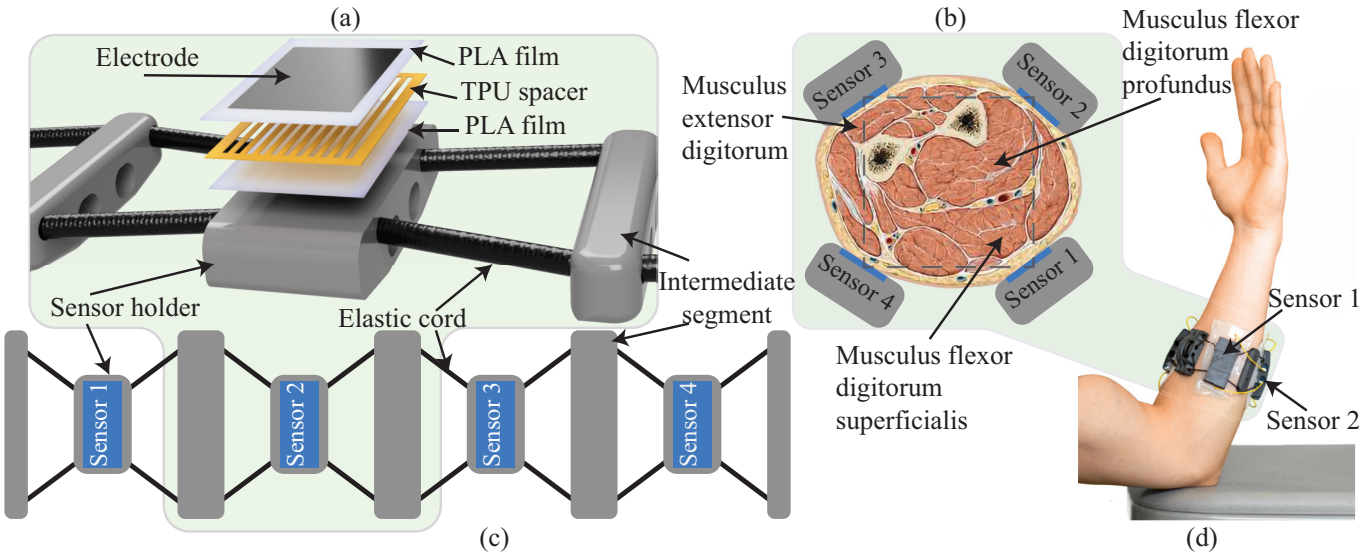

Figure 5.1: Measurement setup for force myography: (a) the ferroelectret sensor as a sandwich structure consisting of PLA-TPU/air-PLA layers placed on the sensor holder of the (c) bracelet structure. The sensor holder as well as the intermediate segments are 3D-printed using PLA. The sensors are then placed on the forearm equidistantly (d) to measure the deformation of the flexor and extensor muscles as indictated in the forearm cross section (b) [165].

The transmission of a gesture or finger movement is made possible through the contraction of the responsible muscles, which results in a measurable deformation of the forearm. In order to utilize the deformation properly, the sensors are positioned on the responsible muscles for finger movements [(Figure. 5.1(b)]. Since the arm diameters varies significantly from one person to another, we designed the holder as presented by Schätzle et al. [217] that maintain the sensors at their intended positions [Figures 5.1(c) and (d)].

Since the protection layer made of silicone also influences the overall stiffness of the device, the d_{33}-coefficients of all sensors at various loads after embedding them into the rubber silicone layer are measured. Note that the silicone layer was added ten days after the charging process and the measurement is carried out two days later. The mechanical stress is applied using an universal testing machine (Inspekt table 5, Hegewald&Peschke).

Each specimen is compressed between two parallel plates with a velocity of $0.1\,\mathrm{N\,s^{-1}}$, while measuring the resulting force by a force sensor (S2M/100N, HBK). The measurement setup is similar the one shown in Figure 4.19. The resulting charge on the electrodes is recorded simultaneously using an electrometer. Afterwards, the d_{33}-coefficient is calculated as previously described.

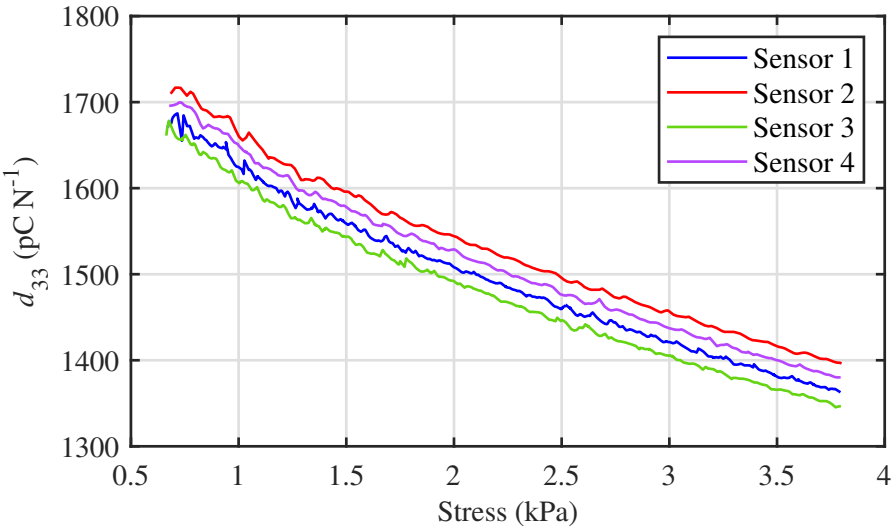

Figure 5.2: Quasi-static piezoelectric d_{33}-coefficients versus stress. The four sensors were measured under the same environmental conditions [165].

The experiments show a decreasing d_{33}-coefficient when increasing the stress. When considering the applied stress of 1.2 kPa used to measure the temporal stability of the d_{33}-coefficient, we conclude that the rubber silicone layer also influences the overall stiffness of the ferroelectret making them less sensitive. Nevertheless, the piezoelectric coefficient varies between 1710 and $1350\,\mathrm{pC\,N^{-1}}$ for an applied stress of 0.6 kPa and 4 kPa, respectively, and is adequate for FMG applications.

For measuring the charge Q generated on the electrodes of each sensor the electrometer used for the characterization can not be used anymore, since all 4 sensors have to be measured simultaneously. Therefore, a charge amplifier circuit with 4 measuring channels is developed.

The circuit consists of two stages (Figure 5.3): the input signal conditioning stage and the analog-digital converter (ADC) stage. The signal conditioning stage converts the induced charges at the sensor electrodes into voltage using the operational amplifier op_1 and capacitor C_2. Its output is amplified by the noninverting amplifier represented by op_2 and resistors R_7 and R_8. Since the circuit operates in single supply configuration, an offset of $V_{\mathrm{offset}} = 1.25\,\mathrm{V}$ is used to condition the sensor signal (AC signal) to the input range of the ADC (0 V to 2.5 V). The offset voltage is provided by buffering and attenuating the voltage reference V_{REF} from the ADC using the operational amplifiers op_3 and op_4 and resistors R_1 and R_2, that build a voltage divider. The output voltage $V_{\mathrm{out},1}$ of the charge amplifier can be expressed as

$$V_{\mathrm{out},1} = V_{\mathrm{offset}} - \frac{Q}{C_2} = V_{\mathrm{offset}} - \frac{d_{33}}{C_2} F, \tag{5.1}$$

where F denotes the force applied to the ferroelectret upon muscle deformation. The output voltage $V_{\mathrm{out},2}$ after the non-inverting amplifier is

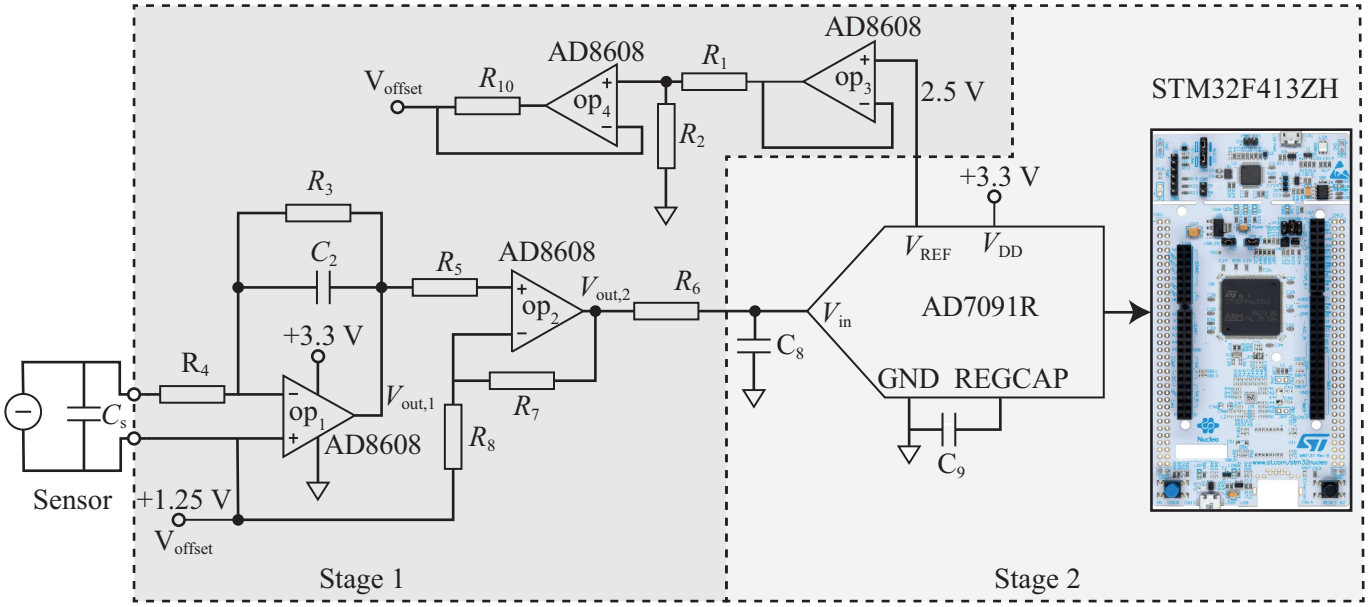

Figure 5.3: Evaluation electronics of the ferroelectret sensors. Shown here is the electronics of only one sensor. However, the circuit consists of 4 sensors, each with the same evaluation electronics.

$$V_{\text{out,2}} = V_{\text{offset}} + \left(1 + \frac{R_7}{R_8}\right) \frac{d_{33}}{C_2} F. \tag{5.2}$$

The R_3 in the charge amplifier circuit has to be chosen as small as possible as it defines the lower corner frequency f_{L} as

$$f_{\text{L}} = \frac{1}{2\pi R_3 C_2}. \tag{5.3}$$

Based on experimental values of the sensors when applied to the forearm, a maximum charge $Q = 1000\,\text{pC}$ is recorded. This requires the capacitor C_2 to not exceed 1 nF which corresponds to $V_{\text{out,1}} = 1\,\text{V}$. Since the input voltage of the ADC should be between 0.1 and 2.4 V (100 mV headroom to maintain linearity), the ratio R_7/R_8 in equation (5.2) should not exceed 0.15. The resistor R_3 for this application is chosen to be 100 MΩ resulting in a lower corner frequency of 1.6 Hz. This defines the lowest frequency input range and has been determined experimentally. Otherwise, the mechanical creep caused by the sensors and holders can affect the measurement significantly.

The resistor R_4 in series at the input of op_1 is for improving the stability and limiting the input currents which can be caused by accidental discharge of the sensors leading to large input voltages. Hereby, R_4 also defines the higher corner frequency f_{H} as

$$f_{\text{H}} = \frac{1}{2\pi R_4 C_{\text{s}}}, \tag{5.4}$$

where C_{s} is the capacity of the ferroelectret. Since the capacity of the ferroelectret sensors C_{s} is around 10 pF and the frequency of the human movement is not in the range of MHz, R_4 is chosen to be $R_4 = 100\,\text{k}$.

All operational amplifiers used in this cuircuit are one quad AD8608 due its low bias current of maximum 1 pA, low noise, and low offset voltage. The ADC is AD7091R with resolution of 12-bit, which offers an internal reference voltage V_{ref}, that can be used as described previously, and allows a sampling rate of 1 MSa/s for a serial clock (SCLK) of 50 MHz. Due to the relative low frequency of the signals in this case, an STM32F413ZH was used to extract the ADC-values via SPI with an SCLK of 20 MHz.

5.1.2 FMG experiment

The suitability of the FMG application for gesture recognition is tested with three probands (P1, P2, P3) and five different gestures. These gestures are the flexions of the individual fingers, starting from an open hand, being the reference state. The movement of one finger compared with the reference state is one measurement. After carrying out a movement, the position of each finger is maintained for 5 s. Since the relevant information of the gesture is recorded during execution, the period of holding the gesture is used to guarantee a separation of the signals for further processing. This measurement is repeated 30 times for each proband.

Each gesture results in different signals of the four sensors. Gesture 1 is moving the little finger (Figure. 5.4). This results in a relatively uniformly distributed force on all the sensors with a small amplitude. Moving the ring finger (Gesture 2) stimulates the sensor 1, placed on a flexor, and sensor 3, placed on an extensor, significantly more than the other two sensors. Almost the same amplitude of stimulation of sensor 1 is recorded when moving the middle finger (Gesture 3), yet shows a deformation in the opposite direction than the middle finger. Moving the index finger (Gesture 4) and the thumb (Gesture 5) results in a smaller deformation of the muscles, and, thus, generates a smaller pressure on the sensors. The shape and amplitude of all sensor-signals change in accordance with the movement, making them gesture-specific. This allows one to distinguish them by using machine learning methods.

Support Vector Machine

In machine learning, support-vector machines (also known as support-vector networks [218]) are supervised learning models with associated learning algorithms that analyze data for classification and regression analysis. We use Support Vector Machine (SVM) as a supervised learning method for hand gesture recognition [219]. Thereby, a trained algorithm with optimized parameters is called a model. The main idea of SVM is to create lines or hyperplanes for separating feature groups of a data set into different classes. This decision boundary is determined in a way that the distance between the support vectors, which define the closest points of the distinct classes [220], is maximum (Maximal Margin Classifier).

SVM allows both linear and non-linear separation of data. Non-linear decision boundaries are created by using the kernel trick method [221]. In this case, the data is efficiently transformed into a higher dimension, so that more complex decision boundaries can be formed [221]. Furthermore, SVM offers adjustable hyperparameters, that influence the model performance, and, thus, the separation of the different classes. Here, the GridSearch method enables hyperparameter tuning to determine optimal values for a model [222]. This evaluates all combinations of given values of the hyperparameters and determines the parameter set with the best accuracy. The classification accuracy (CA) is used as a metric. In the context of gesture recognition, this specifies the ratio of correctly predicted gestures to the total number of gestures.

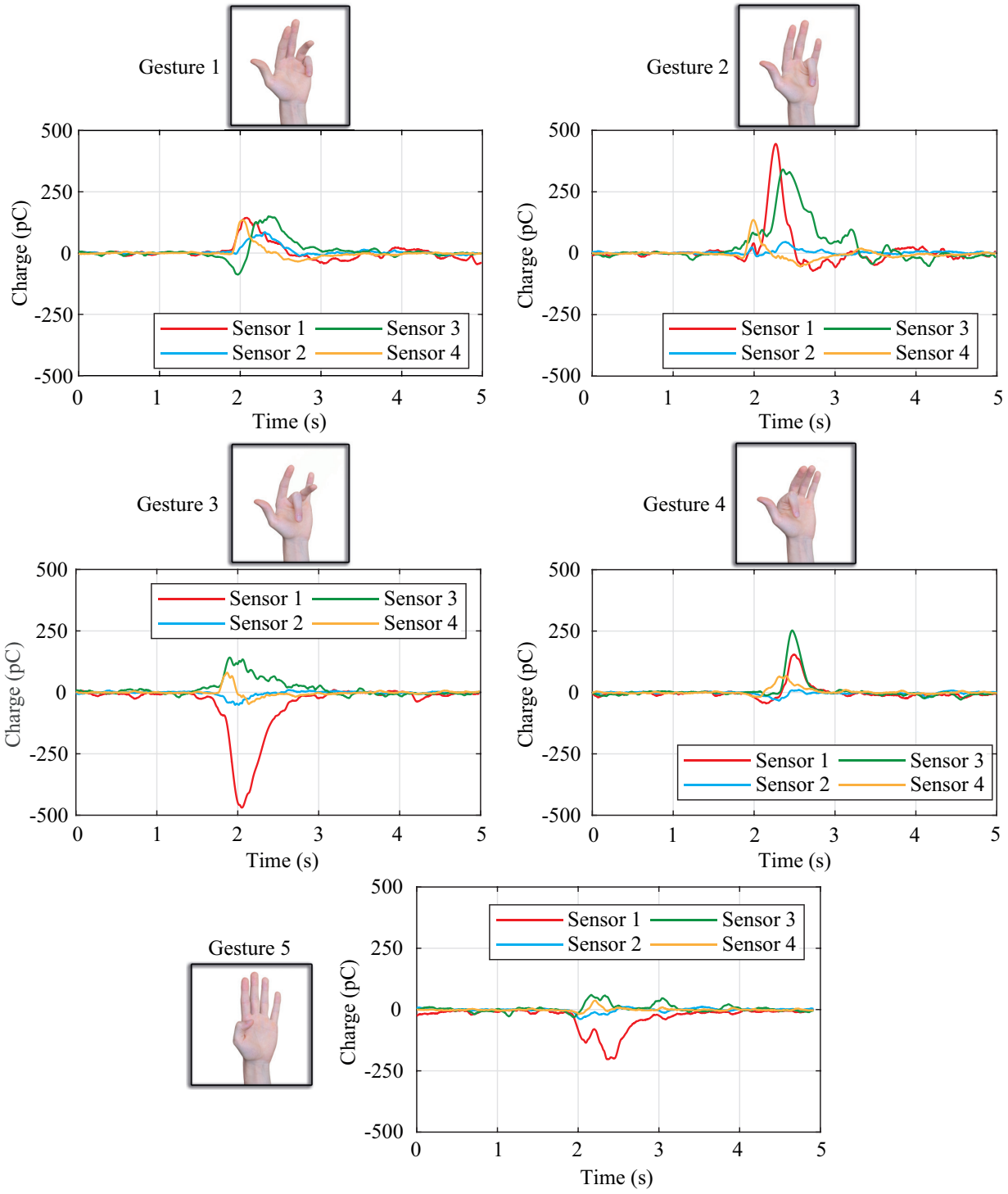

Figure 5.4: The five gestures examined for gesture recognition. All movements are executed starting from an open hand as the initial state. The gestures represent the inflections of the individual fingers [165].

Table 5.1: Features for classification.

Number	Feature	Formula
1	Minimum	$MIN = Min(x_1, x_2, \ldots, x_N)$
2	Maximum	$MAX = Max(x_1, x_2, \ldots, x_N)$
3	Max-min	$MM = Max(x_1, x_2, \ldots, x_N) - Min(x_1, x_2, \ldots, x_N)$
4	Standard deviation	$SD = \sqrt{\frac{1}{N-1}\sum_{i=1}^{N}(x_i - M)^2}$
5	Mean	$M = \frac{1}{N}\sum_{i=1}^{N} x_i$
6	Mean absolute value	$MAV = \frac{1}{N}\sum_{i=1}^{N} \lvert x_i \rvert$
7	Log detector	$LOG = e^{\frac{1}{N}\sum_{i=1}^{N} log(\lvert x_i \rvert)}$
8	Mean frequency	$MNF = \frac{\sum_{i=1}^{N} f_i p_i}{\sum_{i=1}^{N} p_i}$
9	Mean power	$MNP = \frac{1}{N}\sum_{i=1}^{N} p_i$
10	Peak frequency	$PKF = max(p_1, p_2, p_3, \ldots, p_N)$
11	Zero crossing	$ZC = \sum_{i=1}^{N-1} f(\Delta_i)$, $f(\Delta_i) = \begin{cases} 1, x_i x_{i+1} < 0 \text{ and } \Delta_i > th, \\ 0, \text{otherwise}, \end{cases}$
12	Slope sign change	$SSC = \sum_{i=2}^{N-1} f(\Delta_i)$, $f(\Delta_i) = \begin{cases} 1, & \Delta_i \geq th, \\ 0, & \text{otherwise}, \end{cases}$ $\Delta_i = (x_i - x_{i+1})(x_i - x_{i-1})$. In this workt $th = 0$.
13	Average amplitude change	$AAC = \frac{1}{N-1}\sum_{i=1}^{N-1} \lvert x_{i+1} - x_i \rvert$
14	Willison amplitude	$WAMP = \sum_{i=1}^{N-1} f(\Delta_i)$, $f(\Delta_i) = \begin{cases} 1, & x_i \geq th, \\ 0, & \text{otherwise}, \end{cases}$ $\Delta_i = \lvert x_{i+1} - x_i \rvert$. In this work $th = 1$.
15	Skewness	$Sk = \frac{N}{(N-1)(N-2)\sigma^3}\sum_{i=1}^{N}(x_i - \mu)^3$
16	Kurtosis	$Kr = \frac{N(N+1)}{(N-1)(N-2)(N-3)}\sum_{i=1}^{N}(x_i - \mu)^4 - 3\frac{(N-1)^2}{(N-2)(N-3)}$

Data pre-processing and feature extraction

The gesture recognition is based on the following structure: pre-processing of the data, segmentation of the data, feature extraction and classification.

The pre-processing includes filtering the main frequency followed by smoothening the signal using the peak envelope function of MATLAB 2021b. Then, the data is scaled before it serves as input to the model. This

prevents data with variables of higher magnitude from being weighted more during training [222]. For this purpose, we use Z-Normalization which results in data with a mean value of 0 and a standard deviation of 1.

The subsequent segmentation serves to delimit the gesture in the data set. Here, a sliding window-based segmentation with a window width of 100 data points (equivalent to 218 ms) and an overlap of 50 data points is applied. In each window the mean absolute value (MAV) of all four sensors is calculated and summed up. The time t_F with maximum sum corresponds to the halfway of the gesture change with an average gesture duration of 1 s. The relevant range, $t_F \pm 1\,\mathrm{s}$ is chosen to retain the entire information of the gesture signal.

For this remaining signal, features need to be extracted for classifying the distinct gestures. We use common features from gesture recognition in time and frequency domain [219], [223] that do not correlate with each other. This results in 16 features (Table 5.1). In order to identify the optimal combination of features, models with all feature combinations (65535 combinations) are considered. The classification is then performed on all models for each proband. Each model is tuned utilizing the GridSearchCV function [224] and a k-fold cross-validation with $k = 10$ to determine the optimal hyperparameter-set. The split for the training and test data is 1/3 and 2/3. In addition to the individual models, a general model is implemented including the data of all three probands by the same method.

Classification results

The CAs of the individual models based on the training and test data of each proband are 97.5 % for P1, 96 % for P2 and 89.5 % for P3. Here, P3 is noticeable with its lower CA compared to P1 and P2. This is primarily due to the execution of Gesture 1 and 5 by P3. These were executed too fast in most cases, resulting in higher output signals with larger scattering compared to the ones of P1 and P2. In fact, this was also reported by P3 as feedback. The larger scattering of P3 affects the hyperparameters. For P1 and P2 a linear kernel and a C of 1, which controls the number of possible misclassifications, results from the hyperparameter tuning. In the case of P3, the hyperparamter tuning leads to a radial basis function (rbf) kernel and a C of ten. Thus, a non-linear separation with higher possible misclassifications is done for P3. As a result, Gesture 1 and 5 of P3 are classified correctly only by 60 % and 75 %, respectively. This is far below the classification accuracies of P1 with 100 % for both of these gestures as well as of P2 with 95 % and 90 % for these gestures.

The general model based on the data of all three probands is significantly influenced by the data of P3. Furthermore, including the data of all three probands results in a larger scatter in the feature clusters due to variations in gesture execution. These two aspects complicate classification using a linear decision boundary and little misclassifications, so that the hyperparameter tuning also results in an rbf kernel with a C of ten. Besides Gesture 0, which represents the initial state, all gestures are classified with an accuracy of more than 72 % by the general model using the features MIN, MM, M, MAV, PKF, AAC, $WAMP$ and SK. However, an overall CA of 89.5 % shows a well-performing model.

In conclusion, the eco-friendly ferroelectret sensors using the sandwich arrangement by alternating PLA-TPU/air-PLA layers show two outstanding properties in addition to the eco-friendliness: an auspicious surface potential stability and large longitudinal piezoelectric d_{33}-coefficients. The high sensitivity of these sensors makes them suitable to be used as force sensors for FMG, showing a prominent performance to detect slightest muscle deformations caused by finger movements.

Despite the small number of test persons, the potential for generalization of the model has been confirmed. The flexion of each finger can be correctly classified at 99.5% for a single person, whereas the general model trained by three probands can correctly classify 89.5% of the gestures. The resulting scatter in the data of the

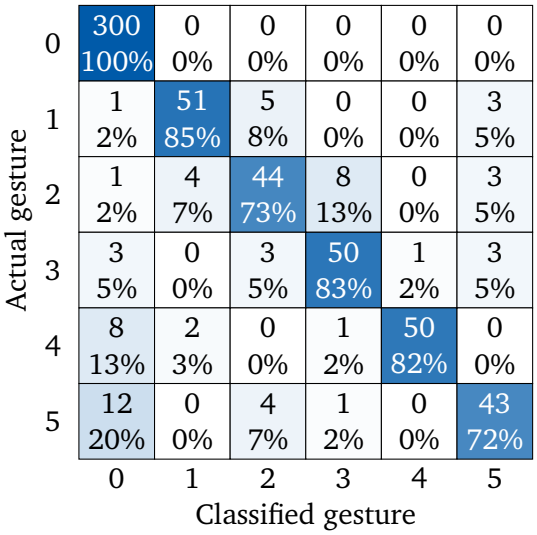

Figure 5.5: The confusion matrix of the general model shows that all gestures are classified with a classification accuracy of 89.5 % [165].

general model due to different gesture executions of individual could be improved. It is worth mentioning that the utilized algorithms are simple and commonly applied.

5.2 Piezoelectric insole using ferroelectrets

Healthcare solutions to improve the quality of daily life and to enable early diagnosis of diseases are rapidly gaining in importance. Some neurodegenerative diseases such as Alzheimer's and Huntington's disease have symptoms that involve deficits in gait and balance [225]. Therefore, wearable insoles for gait analysis have become a very active research topic. Various techniques have been proposed including different force measurement principles such as capacitive [226], resistive [227] and piezoelectric insoles [228]. In this context, piezoelectric insoles feature additional advantages compared to the other principles due to their simple structure, high sensitivity and their unique ability to be self-sufficient [229].

The available commercial insoles are mainly based on resistive sensors and/or inertial measurement unit (IMU). Generally, the first insoles were mainly used in laboratory environment for gait analysis such as PoDoSmart, which sells a package containing 6 smart insole with foot sizes ranging from 36 to 47 EU at a price of approximately 2000$ [230]. Currently, smart insoles for everyday use are increasingly being commercialized such as the the wireless sensor insole system "OpenGo" by Moticon GmbH. According to the price list presented by the company in September 1st, 2021, a pair of this insole costs 1845$. Further resistive commercial insoles for simple activity recognition are also available such loadsol (novel GmbH) as NURVV Run Smart Insoles (NURVV Run) or the Pedar system smart insole (novel GmbH). All these sensors exhibit the same disadvantages: high cost (several hundred to thousand euro), low dynamic and low accuracy due to creep. As mentioned before, a better solution would be the use of piezoelectric sensors as presented by Dai et al. [231], that used PVDF as piezoelectric layer. PVDF is a flexible piezoelectric material, however, with very low sensitivity when compared to ferroelectrets as discussed in this work.

Here the potential of ferroelectrets in combination with the new manufacturing route of 3D-printing is demonstrated. The investigated insole consists of an active layer sandwiched between two cover-layers. The

active layer is printed using PP and exhibits eight cavities that can be treated to act as independent piezoelectric sensors. The insole is tested regarding the piezoelectric response of each sensor and its applicability in gait analysis. The main focus hereby is providing a very sensitive, low-cost and self-sufficient insole for gait analysis, and, thus, also health monitoring.

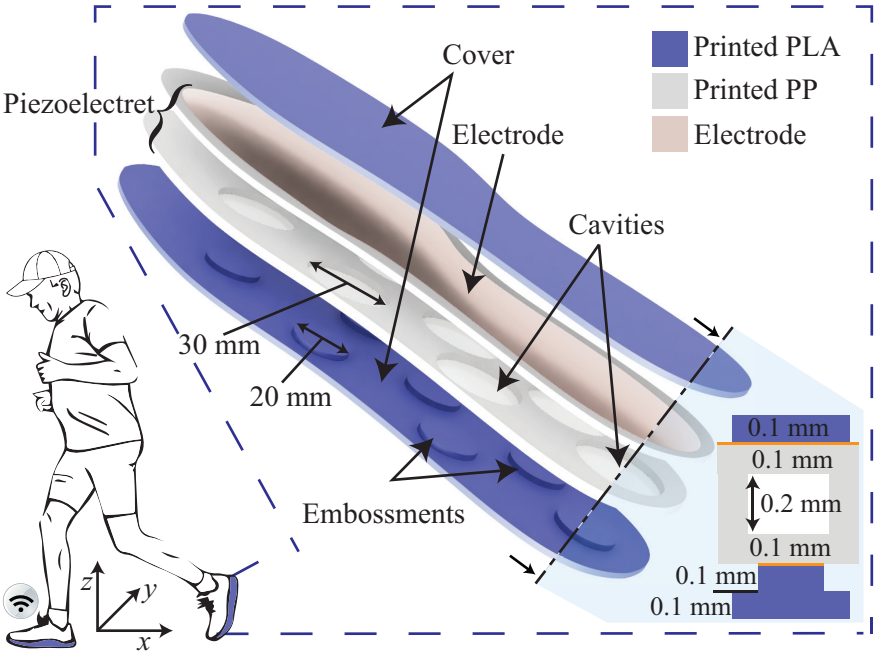

Figure 5.6: Schematic representation of the smart insole embedded in a person shoes. The exploded-view of the insole displays two grey layers consisting of printed PP, that form together the piezoelectret. The two outer blue layers consist of PLA and present the cover of the piezoelectret [207].

5.2.1 Preparation of the insole

The piezoelectret, which is the active part of the insole, is printed using polypropylene (PP) and exhibits eight well defined circular cavities, each with 30 mm diameter. Due to the large diameter of the cavities, bridging them results in undefined sagging of the printed lines, thus hindering the charging process. Therefore, the piezoelectret is assembled from two independently printed parts. The first part is 0.3 mm thick, with cavities of 0.2 mm and the second part is an unstructured plane-parallel film (Figure 5.6). The two parts are subsequently thermal-bonded and together form the piezoelectret structure. The insole geometry is designed in Autodesk Fusion 360 (Autodesk, Inc) and prepared for 3D printing using the same software as previously described. Each printed layer is 0.1 mm thick, using a printing speed of 5 mm s^{-1}. The nozzle diameter is 0.4 mm that extrudes fused PP filament (Formfutura BV) on a spring steel sheet with smooth double-sided PEI as the printing bed. The assembled insole is then provided with a large-area electrode on the outer side of the flat PP film and eight electrodes on the outer side of the structured PP film (Figure 5.6). The eight electrodes feature a diameter of 20 mm and are placed on top of the eight cavities.

The polarization of the structure is carried out under ambient conditions by applying a DC voltage of -7 kV (power supply HCN 350-20000, fug Elektronik GmbH) on each sensor, resulting in large quasi-permanently trapped charges [Figure 5.7(a)]. The charged insole is then placed between two 3D-printed PLA layers as a cover. The printing parameters of PP filament are listed in Table 5.2 and the printing parameters for PLA

are listed in Table 4.3. The bottom layer of the cover features eight embossments in order to maximize the

Table 5.2: Printing Parameters for PP filament. All samples are printed using the same printer.

Parameter	**Value**
Extruder temperature	220 °C
Heatbed temperature	100 °C
layer height	0.1 mm
Filament diameter	1.75 mm
Nozzle diameter	0.4 mm
Printspeed	5 mm s^{-1}

force on the active area while walking. Each embossment features a diameter of 20 mm, which corresponds to the electrodes diameter (Figure 5.6) and a thickness of 0.1 mm. The thickness of the embossments limits the maximum possible deformation under an external load. This also serves as a safeguard as well since the weight of individual persons can vary significantly. The top layer of the cover, on the other hand, is flat to ensure the comfort of the person walking.

5.2.2 Characterization of the insole and measurement circuit

The piezoelectric response is characterized by measuring the d_{33} coefficient of each sensor using the quasi-static method. First a mass of 200 g and 20 mm diameter is applied to the sensor for an extended period of time (3 min). After removing the mass, the previously induced charge is measured by means of an electrometer (6517A, Keithley Instruments) and integrated over 10 s. The measured piezoelectric d_{33} coefficient of all sensors is approximately 2000 pC N^{-1}. This value, however is only valid for small loads up to approximately 10 N. A larger deformation than 0.1 mm is restrained by the contact of the large surface of the cover with the rigid surface of the piezoelectret [Figure 5.7(a)]. Note that a discharge of the films has not been observed in the case of contact. An increase of the load still deforms the entire structure since the polymers compress, although with a much smaller amplitude compared to the initial deformation of the air cavities.

In view of its practical interest as sensor for gait analysis, a measurement circuit is designed, that measures the individual voltages of the sensors when a force is applied (Figure 5.7). The output voltage of each sensor is measured through the voltage divider R_1 and R_2 [Figure 5.7(b)]. The capacitor C_1 is a coupling capacitor that acts as DC blocking component and C_2 is used to bypass the ac signals appearing on the supply line. For the single supply configuration an artificial zero-signal reference voltage is fixed between the supply rails using the voltage divider consisting of two resistors R_3. The same resistor R_3 is used to establish the bias at the midpoint of the supply voltage. The output voltages of all eight operational amplifiers are converted to digital signals through an analog-digital-converter (MCP3008), which transmits the sensors data to the microcontroller ESP32 through the serial peripheral interface (SPI). The ESP32 in turn sends the measured data to a computer as a data receiver using the communication protocol user datagram protocol (UDP). The MPU6050 is an accelerometer and gyroscope which is used to track and validate the walking steps.

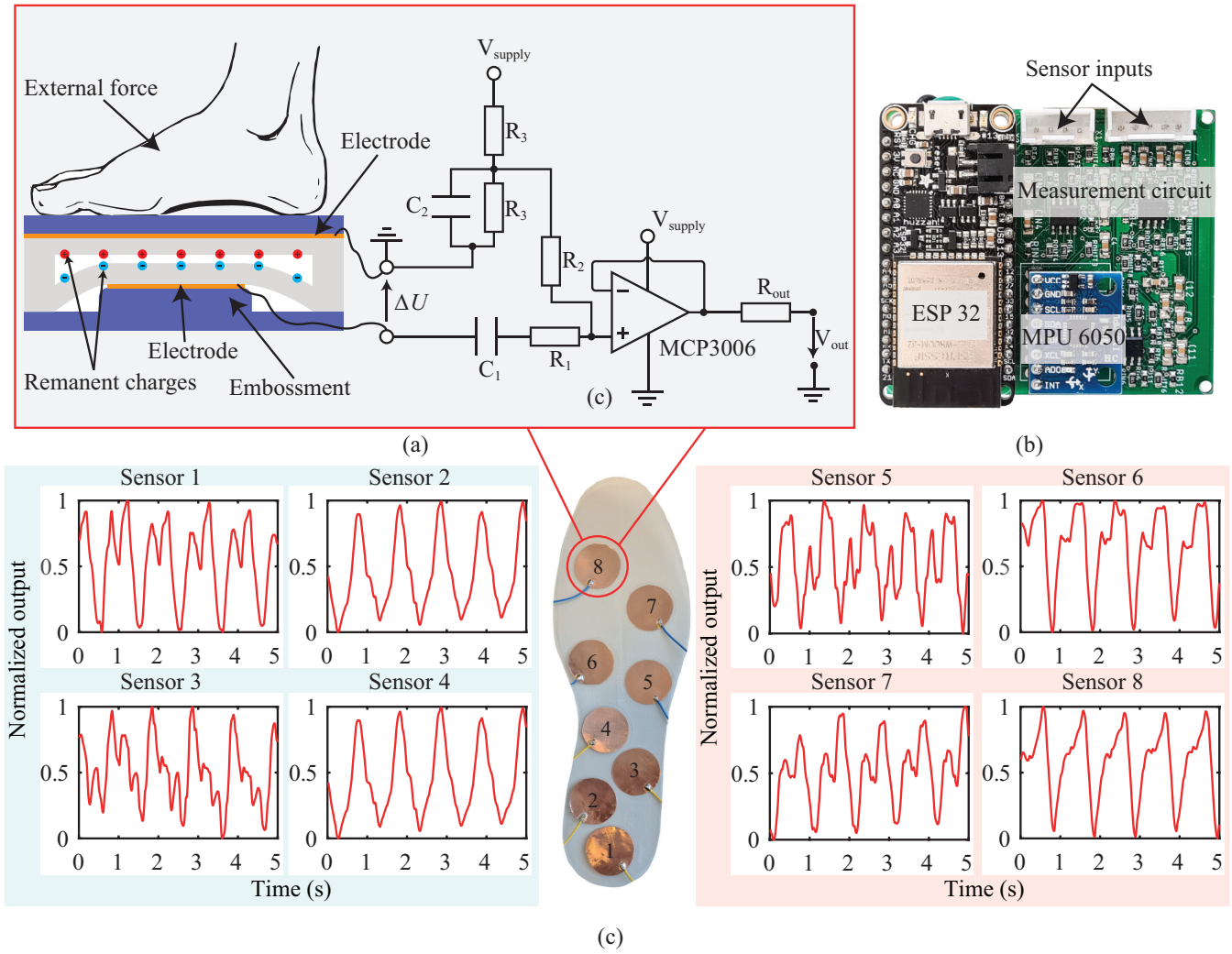

Figure 5.7: Scheme of the gait analysis: (a) Illustration of a deformed cavity when an external force is applied to the insole with the measurement circuit of one sensor using single supply operational amplifier design. (b) Photograph of the used hardware consisting of the measurement circuit of all eight sensors, an accelerometer (MPU 6050) and a microcontroller (ESP32 Feather Board). (c) Normalized output voltages of the eight sensors of the insole corresponding to the signal generated by a walking 60 kg male of foot size 40. The heel part includes the sensors from one to four and their signals are shown on a blue background. The forefoot area include the sensors from five to eight and their signals are shown on a red background [207].

5.2.3 Experimental results of the gait analysis

The measurement results correspond to a walking 60 kg male of foot size EU 40 [Figure 5.7(c)]. An enumeration of the sensor locations is given to compare the sensors of the insole, which helps allocating the measurement results to their corresponding measured sensor. The sensors placed on the heel part of the foot are enumerated from 1 to 4 and the ones placed on the forefoot from 5 to 8.

One stride can be divided into two major phases, i.e. stance phase and swing phase [232]. The transition from swing phase to stance phase (heel-strike) corresponds to stressing the sensors whereas the opposite

transistion (toe-off) marks the release. The stressing results in negative voltage output of all sensors whereas the release results in a positive output voltage. The polarity of the output voltage depends on the utilized charging polarity of the sensors. The maximum strike of one sensor corresponds to approximately 150 V which is converted to 3.3 V on the measurement board. However, since the focus of this work lies solely on detecting the movement as proof of concept, only the normalized output signals are considered (Figure 5.8). The shapes

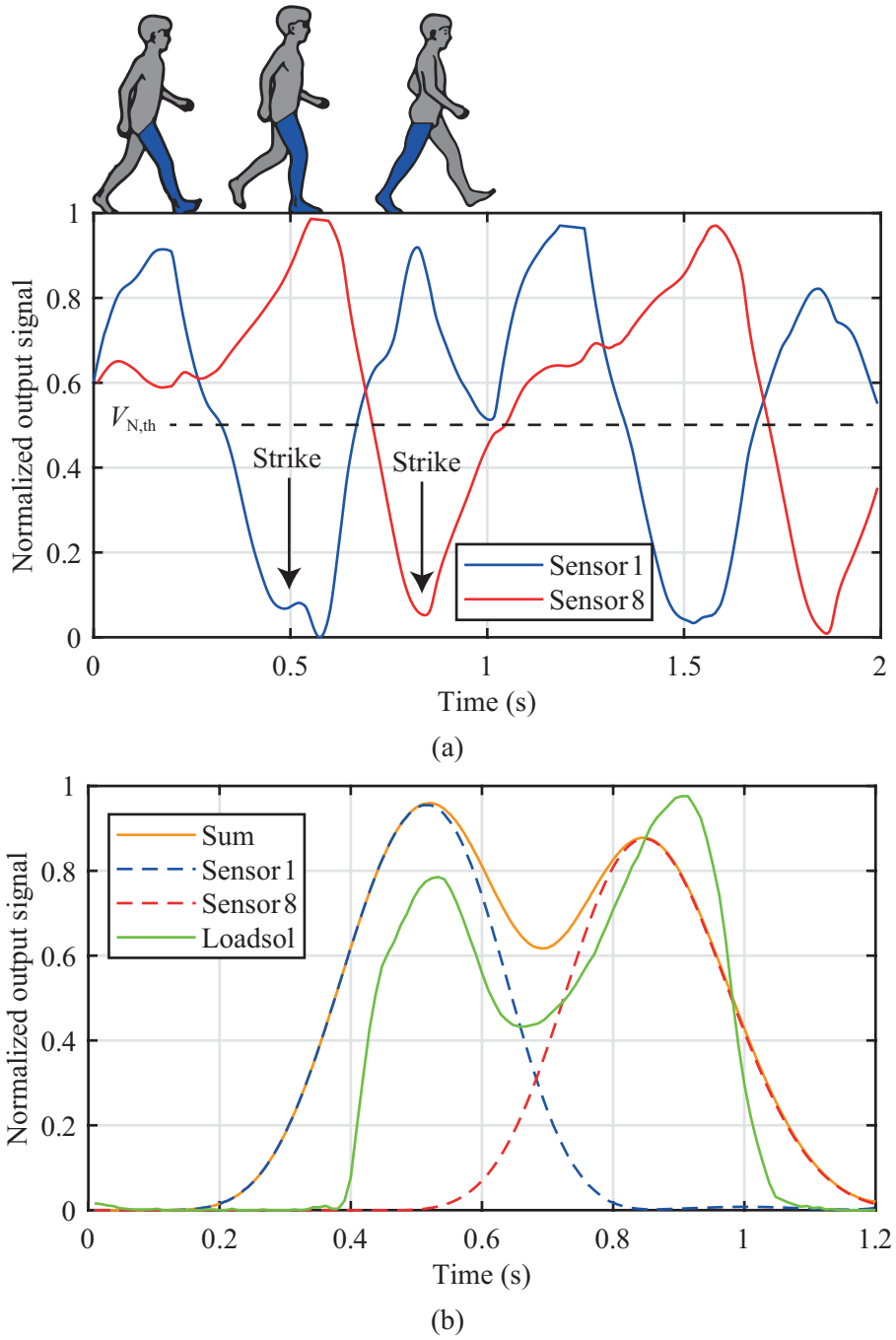

Figure 5.8: Output of (a) Sensor 1 and Sensor 8 of the ferroelectret insole considering one and a half gait cycles and (b) Filtered signals of both sensors of the ferroelectret insole along their summation in addition to the signals generated by the loadsol for the same step.

of the sensor signals differ from each other due to the different load types while walking (Figure 5.7). In the present case, Sensor 1 shows first an increasing voltage followed by the main strike [Figure 5.8(a)]. The increasing voltage matches the contact of the edge of the heel with the ground resulting in a small inclination of the insole. The inclination acts as stressing the sensor in the positive z-direction leading to a positive output voltage [Figure 5.8(a)]. Afterwards, the heel stresses the sensor in the negative z-direction and causes the main strike presented by the negative voltage peak. Further movement forward first releases Sensor 1 and then inclines the insole one more time. This results in an overlap of the two deformation stages which can be seen at the signal shape.

Sensor 4 is placed under the arch of the foot resulting in smaller deflections and larger release signals. The amplitude of the strikes of this sensor depends on the arch of foot. A flatfoot would result in larger strikes. The last sensor to be stressed when moving forward is Sensor 8. The strike of Sensor 1 can also be seen in the signal of Sensor 8 due to the bending of the insole structure.

For comparing the performance of the ferroelectret insole with the commercially available insoles at least for the task of gait recognition, a loadsol (Novel GmbH) is used. Since the loadsol features only two sensors, one at the heel and one at the forefoot, which correspond to Sensor 1 and Sensor 8 of the ferroelectret insole, only these two sensors are considered. The normalized output signals of Sensors 1 and Sensor 8 are first filtered by removing the values above a threshold of $V_{\text{N, th}} = 0.5$ so that only the strikes are considered. Afterwards the signals are smoothed and inverted to make the strikes resemble the output of the loadsol [Figure 5.8(b)]. The direct comparison of both insoles shows very similar behaviour, showing the suitability of the ferroelectret insole for such application. However, using a threshold value to filter the strikes from each other can be insufficient when applied to different persons with different gait cycles. In order to exploit the full potential of the insole, it is more appropriate to use an artificial intelligence (AI) algorithm. Here two types AI can be utilized: machine learning (ML) or its subset deep learning (DL). The term ML refers to learning techniques for pattern recognition such as SVM (discussed in section 5.1.2), which require a manual extraction of features from segments of sensors data [233]. Since the use of this insole is intended in the long term for medical applications, it is complicated to manually extracting appropriate features. Therefore, deep learning as tool that automatically extracts features, is more precise and an efficient alternative for this application [234].

5.2.4 Deep learning and classification results

Deep learning is a form of machine learning inspired by the human brain neurons and is known as artificial neural network (ANN) [235]. A Neural Network (NN) is a system of interconnected entities known as neurons, each of which is assigned a weight [236]. A neuron consists of an input vector X with a length N, a neuron with weights W, an activation function $F_{\text{activation}}$ and the output value Y. The output value can be calculated as [237]

$$Y = F_{\text{activation}} \left(W_0 + \sum_{1}^{N} X_{\text{i}} \times W_{\text{i}} \right), \tag{5.5}$$

where W_0 is a an offset that can be added to the activation function.

The activation function $F_{\text{activation}}$ can be a binary step, sigmoid step, hyperbolic tangent, a rectified linear unit function (ReLU) etc. ReLU is the most utilized non-linear activation function [237], [239], [240] and is also

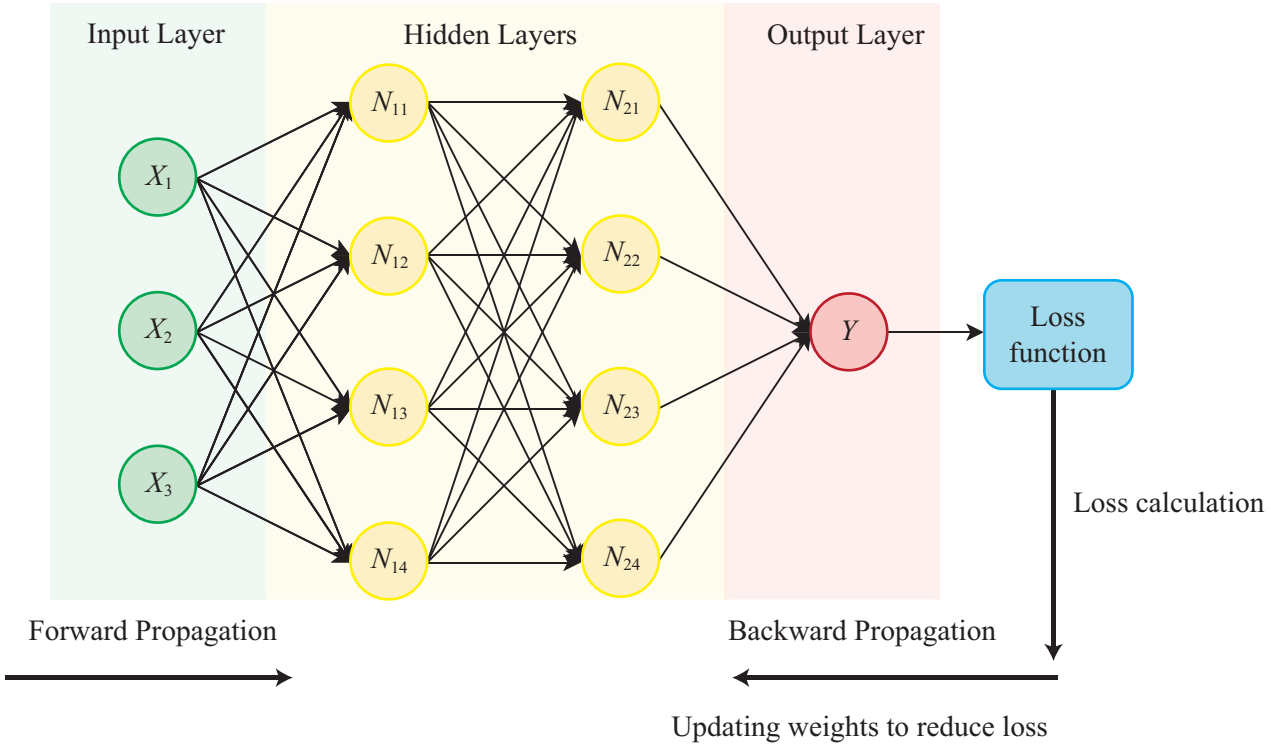

Figure 5.9: Illustration of Neural Network mechanism: Forward and Backward propagation [238]

used in this work. This principle imitates in a simplified way the function of a neuron in the human brain. The activation function corresponds to the minimum activation potential that a neuron needs to transmit a signal.

The simultaneous use or connection of multiple neurons creates a feed forward neural network (FFNN). In a simplified way the FFNN architecture has three essential layers (Figure 5.9): an input layer, an output layer, and the layers in between are called the hidden layers [236], [241]. The NN calculates and stores the weights from the input layer X to the output layer throughout the hidden layer. This is referred to as "forward propagation" (Figure 5.9). The reverse is termed as Backward Propagation. Hereby, the input data flows through the network to reach the output, where the loss function calculates the total error of the model. Subsequently, the backward propagation process calculates the gradient of the loss function with reference to each weight. This procedure is repeated until the desired results are reached [242].

As proof of concept for using deep learning in combination with the ferroelectret insole, five common daily human activities are collected for classification purpose: (1) Slow walking, (2) Normal walking, (3) Jogging, (4) Running and (5) Standing. A suitable NN for processing time-series are the recurrent neural network (RNN) and long short-term memory (LSTM) [238]. For training the algorithm, activities are recorded over 12 min at different time periods, to ensure a more generalized data collection. It should be noted that the data of all sensors fed to the algorithm is filtered and segmented. The labeling of the data, as required for supervised learning, is ordered alphabetically as : ['Jogging', 'Normal Walk', 'Running', 'Slow Walk', 'Standing']. The data splitting is implemented using the method $train\_test\_split()$ method by the Sckit-learn python library with a ratio of 70:15:15 for train, validation and test data [243]. The model is trained with the Adam optimizer [244] and the categorical cross-entropy as loss function [245]. The learning model is implemented on the Jupyter Notebook using python as programming language and the open source, machine learning library TensorFlow introduced by Google Brain Team [246]. The model evaluation is performed over two

external test sets that are unknown to the trained model.

For better understanding the architecture of the model, some hyperparameters have to be explained. The hyperparameters are the number of variables that define the model and have to be chosen properly:

- Number of hidden layers between the input and output. Here, it should be taken into account that each layer consists of a number of units (neurons), which is a further variable.
- Regularization: This presents techniques to prevent overfitting. In this work two techniques are considered: Dropout and Ridge regularization. Dropout removes randomly some of the neurons from the hidden layer to reduce the model and prevent the neurons from co-adapting [247]. The Ridge regularization add a penalty term to the cost or loss function.
- Loss function: also known as error function calculates the difference or error between the output of the learning model and the expected output [235]. For multi-class classification problems such as human activity recognition, the categorical cross-entropy is utilized [240].
- Number of epochs and batch size: The number of epochs defines how many times the training set is shown to the learning model. The batch size defines the number of sub samples fed to the learning model in one epoch. As example, assuming that the model training set consists of 1600 samples and the batch size is defined at 32. This means that in each epoch the model is fed with 1600/32= 50 batches.

The model architecture with the corresponding hyperparameters used in this work is summarized in Table 5.3.

Table 5.3: Hyperparameters tuning on the third proposed model architecture.

Architecture	**Hyperparameters adjustments**
First LSTM Layer	8 units with Ridge regularization(0.0001)
Dropout	0.1
Second LSTM Layer	8 units with Ridge regularization(0.0001)
Dropout	0.1
Flatten() + Dense layer	8 units activation function (ReLU)
Epochs and batch size	5 epochs and 32 batches
Fitting type	Good Fit
Accuracy/Loss on test-set	95.5 % / 0.1290

The model shows a classification accuracy of 95.5%. Only 10 samples from the 'Jogging' activity were confused with 'Running' and 11 samples from 'Normal Walk' were confused with the 'Slow Walk' (Figure 5.10).

The outstanding results confirm the suitability of using NN for activity recognition. It should be noted that all measurements are conducted by the same person as proof of concept. For a proper generalization of the model, more probands are needed.

Here two main contributions to human activity recognition, and consequently to health monitoring, are provided. First, 3D-printing the insole with well-defined artificial cavities broadens the possibilities of piezoelectric insole design. Designing more complex structures using 3D-printing techniques is a field with great potential, allowing custom insole with adjustable local sensitivities. The readout circuit suggested is simple and consists of low-cost discrete components, which is an additional advantage of using ferroelectrets. Second, the classification of the output signals of the sensors with automatically extracted features after minor

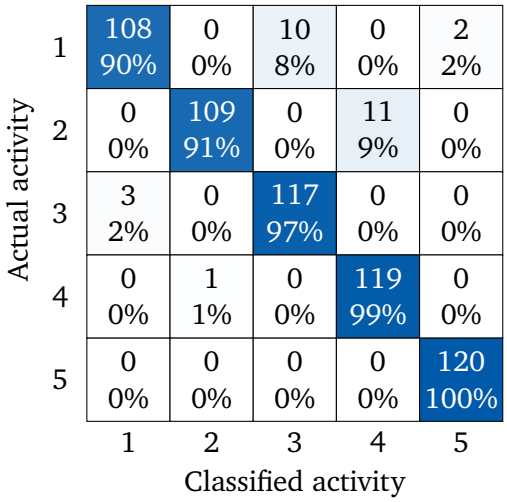

Figure 5.10: The confusion matrix of the trained model shows that all activities are classified with a classification accuracy of 95.5 %.

filtering and segmentation shows the potential of recognition possibilities of several activities and, where applicable, and early diagnosis of diseases.

5.3 Additively manufactured ferroelectret ultrasonic transducer

Electroacoustic transducers transform acoustic energy into electrical energy (acoustic receivers) or vice versa from electrical energy into acoustic energy (acoustic transmitters). For the transduction a mechanical oscillation system is generally required, which consists either of a membrane (possibly with additional coupling elements) or of the transducer material itself (as piezoelectric transducers). Thus, the conversion process for the transducers is performed in two steps: an electrical-mechanical and mechanical-acoustic (or vice versa).

The mechanical-electrical conversion can be carried out with different principles and can be distinguished between reversible converters that can work both as receivers and transmitters, and non-reversible converters that can only be operated in one direction such as plasma speaker or carbon microphone. The reversible transducers are classified on the basis of their fundamental mechanical-electrical conversion principles and are divided into 5 groups: Electrostatic, Piezoelectric, Magnetostrictive, Electromagnetic and Electrodynamic transducers.

The presented transducer in this section belongs to the category of electrostatic transducers. Electrostatic transducers are capacitors consisting of a light, vibrating electrode (membrane) and a rigid counter electrode (backplate) separated by a distance d. When a driving AC-voltage V_{AC} is applied to the electrodes, a force F_{el} between them is generated that can be expressed as

$$F_{\mathrm{el}} = \frac{1}{2}\frac{A}{d^2}\varepsilon_0\varepsilon\left(V_{\mathrm{AC}}\sin(\omega t)\right)^2 = \frac{\varepsilon_0\varepsilon A}{4d^2}V_{\mathrm{AC}}^2(1-\cos(2\omega t)), \tag{5.6}$$

where A is the electrodes surface. This quadratic proportionality between force and driving voltage leads to oscillations with a frequency of 2ω when a driving voltage with frequency ω is applied to the transducer. For

such transducers to operate linearly around a working point, they must be biased by an external DC-voltage V_{DC} in addition to the driving AC-voltage V_{AC} that is responsible for the vibration of the membrane. In this case the force between the two electrodes consist of three parts: a DC-force, an AC-force proportional to the driving voltage and a small distortion term as

$$F_{\mathrm{el,biased}} = \frac{A}{2d^2}\varepsilon_0\varepsilon\left(V_{\mathrm{DC}}^2 + 2V_{\mathrm{AC}}V_{\mathrm{DC}} + V_{\mathrm{AC}}^2\right). \tag{5.7}$$

For the linear part to be dominant, V_{DC} must be large compared to V_{AC}.

The required bias-voltage of several hundred volts represents the main disadvantage of capacitive transducers compared to piezoelectric transducers, which require only an AC-signal. However, for air-coupled ultrasonic applications, the capacitive ones are superior due to their broad bandwidth in air. An additional advantage is the possibility to tune the resonance frequency of capacitive ultrasonic transducers through the geometry of the grooves of the backplate and the material of the membrane and its tensile stress [248], [249].

Due to the permanent polarization of ferroelectrets, a ferroelectret ultrasonic transducer benefits from the advantage of the capacitive transducers without the need of DC-biasing. The possibility of 3D-printing ferroelectrets offers further advantages such as design freedom and low cost.

As discussed in previous sections, fully printed ferroelectrets remain a challenging task due to the possible layer defects, which are severe obstacles preventing the structure from being charged. Additionally, the minimum printable layer thicknesses of several 100 µm remains relatively thick compared to the reachable thickness of bulk materials. However, for building an ultrasonic transducer, the backplate needs to be relatively stiff, which makes the disadvantage of the minimal printable layer thickness irrelevant. This presents an alternative way of using 3D-printing for ferroelectrets, by combining a commercial bulk PLA film of 20 µm thickness and a printed PLA backplate to build an ultrasonic transducer. The backplate, being much thicker and stiffer than the bulk film, results in the film being the movable component under the influence of the electrostatic forces.

5.3.1 Preparation of the ferroelectret transducer

The design of the backplate geometry and its preparation for 3D-printing are similar to the previous strucutres using PLA. The printing steps are carried out as follows: the initial layer thickness is 0.1 mm to maximize bed adhesion, while all subsequent layers feature a height of 0.05 mm. The printing speed is 20 mm s^{-1} and the nozzle diameter is 0.4 mm, which defines the width of one extruded layer of PLA-filament (REDLINE FILAMENT GmbH). The smooth side of the printed backplate is then provided with an evaporated aluminum electrode for the electrical contact. The bulk PLA film is then attached to the printed backplate with a holder, also 3D-printed using PLA (Figure 5.11). For a symmetrical evaporation of the electrode on both sides of the ferroelectret, we used a mask that features a 42 mm hole, which corresponds to the electrode diameter and the active part of the ferroelectret.

The electrical charging is performed with contact-charging by applying a DC voltage at room temperature. During charging, an electric field is applied to the metallized surfaces of ferroelectret generating large electric fields in the air-filled voids. Considering the different thicknesses of the film and printed backplate, the polarization σ_{int} can be calculated as [164]

$$\sigma_{\mathrm{int}} = \begin{cases} 0 & V \leq V_{\mathrm{B}} \\ \dfrac{V - E_a^B\left(\frac{t_{p1}\varepsilon_a}{\varepsilon_a\varepsilon_{p1}} + t_a + \frac{t_{p2}\varepsilon_a}{\varepsilon_a\varepsilon_{p2}}\right)}{\frac{t_{p2}}{\varepsilon_0\varepsilon_{p2}} + \frac{t_{p1}}{\varepsilon_0\varepsilon_{p1}}} & V > V_B \end{cases}, \tag{5.8}$$

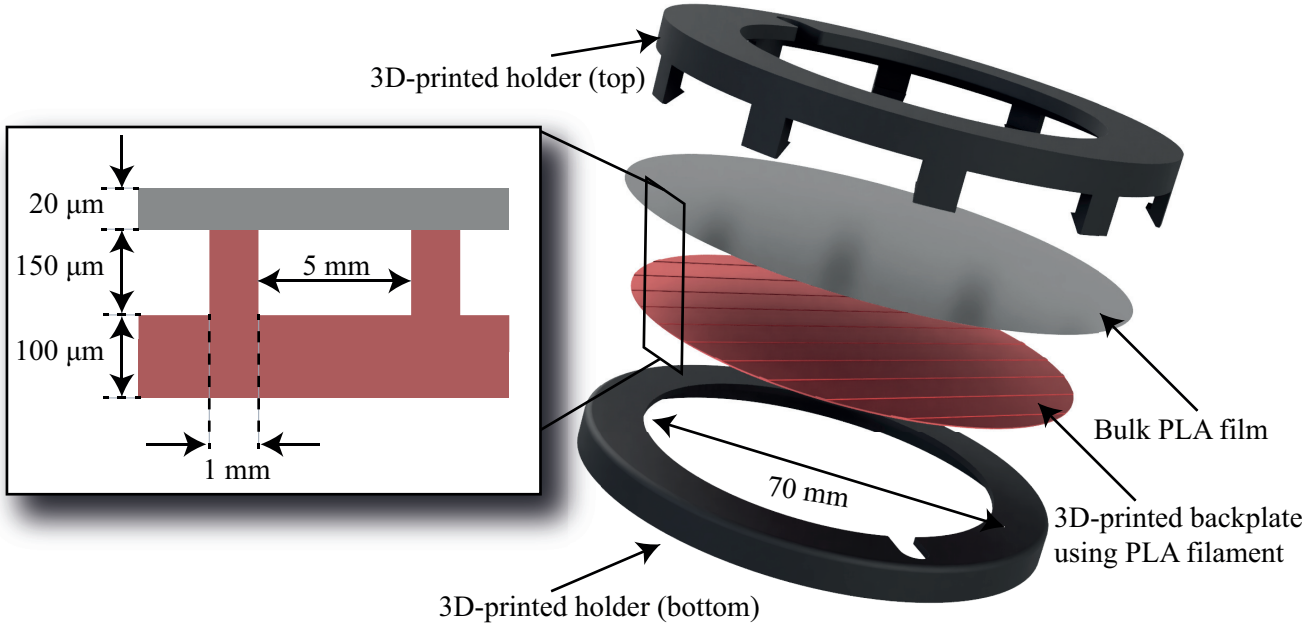

Figure 5.11: Exploded 3D model of the ferroelectret transducer's structure. The red colored plate is the 3D-printed part that feature well defined grooves, where the negative surface charges are trapped. In grey is the bulk PLA film with trapped positive surface charges. The bulk film is stretched on the printed plate and clamped with the printed holder (in black) [164].

where V is the poling voltage, $E_{\mathrm{a}}^{\mathrm{B}}$ is the electric field, t_{p1}, t_{p2} and t_{a} are the thicknesses of the first polymer layer, the second polymer layer and of the air gap, respectively, with relative dielectric permittivities ε_{p1}, ε_{p2} and ε_a. This theoretical model is based on a previously published model for symmetrical sandwich structures [79], [98] and generalized to describe asymmetric structures. The derivation of the equations is similar to the derivation discussed in section 3.1.2.

The charging process starts as soon as the applied voltage reaches the breakdown voltage V_{B}, which initiates Paschen breackdown. This corresponds to a remanent charge of $\sigma_{\mathrm{int}} = 0$ and is correlated with the breakdown electric field $E_{\mathrm{a}}^{\mathrm{B}}$ by [164]

$$V_{\mathrm{B}} = E_a^B \left(\frac{t_{p1}\varepsilon_a}{\varepsilon_a \varepsilon_{p1}} + t_a + \frac{t_{p2}\varepsilon_a}{\varepsilon_a \varepsilon_{p2}} \right). \tag{5.9}$$

The maximum possible remanent polarization $\sigma_{\mathrm{int}}^{\mathrm{max}}$ of the structure is attained when the applied voltage on the sandwich geometry is equal to double the value of the breakdown voltage V_{B}.

The theoretical breakdown voltage V_{B} amounts to 1.28 kV, which is in agreement with the measured value using ST of approximately 1.34 kV. The maximum polarization reached amounts to approximately $\sigma_{\mathrm{int}}^{\mathrm{max}} = 2.3 \times 10^{-4}\,\mathrm{C\,m^{-2}}$. The parameters used to calculate the polarization and breakdown voltage are listed in Table 5.4.

Table 5.4: Parameters to calculate the breakdown voltage and polarization

Parameter	Value
t_{p1}	20 µm
t_a	100 µm
t_{p2}	150 µm
E_a^B	86 kV cm^{-1}
ε_a	1
ε_1	3.4
ε_2	3.4

5.3.2 Operation principle of the transducer

The trapped charges at the polymer walls on both sides of the air gap result in a surface potential difference. This acts as a biasing voltage of the transducer as well as mechanical pre-stress due to the electrostatic force between the two polymers. The PLA bulk film being only 20 µm thick is the less stiff component of the ferroelectret consisting of this latter and a 150 µm printed backplate. Thus, the bulk PLA film represents the vibrating component which is pulled to the grooves as a result of the driving voltage.

While vibrating, the thickness of the PLA film can be assumed to be constant because of the small displacement. Taking into account that the electrostatic force F_{el} is uniformly distributed over the movable film, it is valid to assume that the bending stiffness of the pre-stressed PLA film (out-of-plane stress) dominates the dynamic behavior. Consequently, it is more appropriate to consider the movable film as a plate [250]. Hence, each channel can be considered as a beam with fixed outer edges. In this case, the bending stiffness of the film k_{film} depends on the Young's modulus Y, the area moment of inertia I and more importantly the gap between the grooves l. When the gap l between two walls is enlarged, the bending stiffness becomes smaller and vice versa. Additionally, the closed air volume between the film diaphragm and the grooves on the resonance frequency presents an additional stiffness k_{air} that can be approximated as [251]

$$\begin{aligned} k_{\text{total}} &= k_{\text{film}} + k_{\text{air}}, \\ \text{with } k_{\text{air}} &= \frac{\gamma \rho_0 A_{\text{g}}}{t_{\text{g}}}, \end{aligned} \tag{5.10}$$

where ρ_0 is the atmospheric pressure, γ is the adiabatic index of air, t_{g} is the thickness of the groove and A_{g} its area. Thus, by modifying the geometry of the grooves, the resonance frequency will be changed consequently. The ability of 3D-printing the backplate offers therefore further design freedom. In this work, only a tunnel structure resonating at 66 kHz is investigated with the geometry shown in Figure 5.11.

5.3.3 Characterization of the transducer

The acoustic properties of the transducer have been measured in an anechoic chamber whose walls are covered with mineral wool cones (Grunzweig + Hartmann AG, Ludwigshafen am Rhein, Germany). These cones are

1000 mm long and feature a base area of $240\,\text{mm} \times 240\,\text{mm}$, resulting in a cut-off frequency of 70 Hz and a reflection coefficient below 0.01.

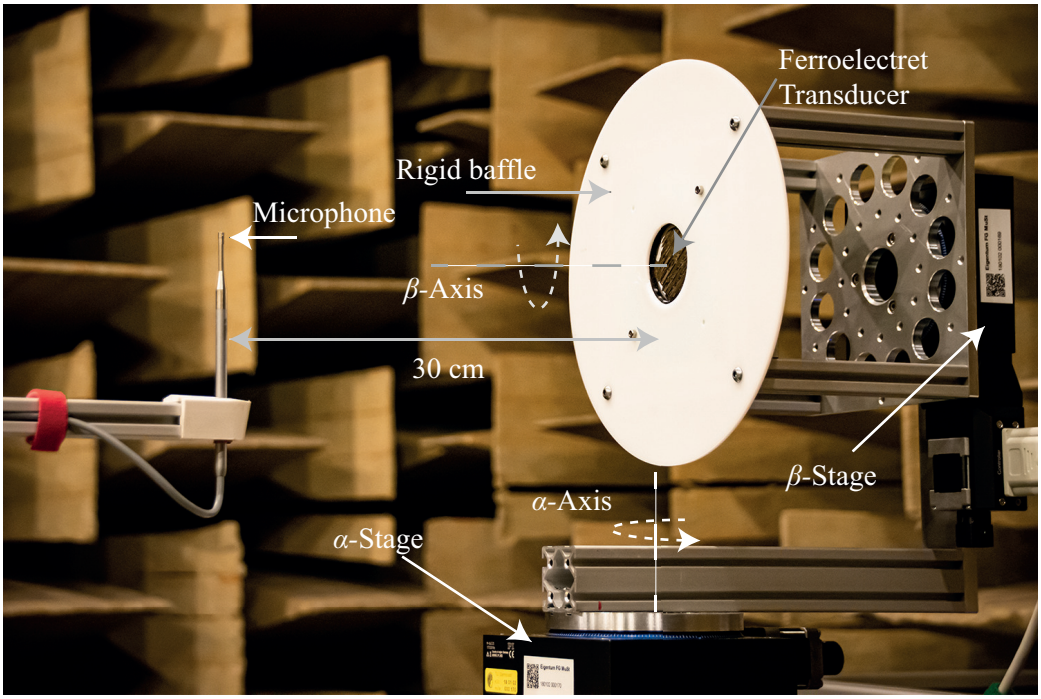

Figure 5.12: Measurement setup consisting of two rotational stages that rotate along the β and α-axes. In this work only the α-axes is used. The microphone is mounted on a linear stage and placed at 30 cm from the ferroelectret transducer, which is mounted in a rigid baffle made from acrylic glass [164].

The measurement system consists of three movable axes, with two of them being rotational (M-061.2S and M-062.2S, Physik Instrumente, Karlsruhe, Germany) and one being a linear axis. The rotation of the axis allows the sender to rotate in plane to the receiver (microphone) with an accuracy of $\pm 0.0011°$ and $\pm 0.00051°$ for the β-axis α-axis, respectively. On the linear axis (LEFZ 1, Isel Automation, Eichenzell, Germany), a calibrated measurement microphone (Type 4138, Bruel & Kjaer, Naerum, Denmark) is mounted. This allows to measure the sound pressure in a defined distance with an accuracy of ± 0.2 mm. The output of the microphone is analyzed by a data acquisition system (NI PXI-5922, National Instruments, Austin, TX, USA) with 500 kSa.

The ferroelectret transducer is mounted in a rigid baffle, which in turn is mounted on the measurement setup (Figure 5.12). The microphone is placed at a distance of 30 cm and characterized using three different driving voltages with rms-values varying between $35.5\,V$ and $70.7\,V$. The frequency responses of all driving voltages show a high bandwidth of 45 kHz and the same resonance frequency of approximately 66 kHz [Figure 5.13(a)]. The sound pressure levels reached at the resonance frequency are 100.3 dB, 103.9 dB and 106.5 dB for driving voltages of $35.5\,V$, $53\,V$ and $70.7\,V$, respectively.

At low frequencies between 1 kHz and 7 kHz the sound pressure levels do not follow the increased driving voltage resulting in larger electrostatic forces. The sound pressure at 2 kHz when using $70.7\,V$ is lower than the generated sound pressure with $53\,V$. By increasing the frequency the sound pressure generated by $70.7\,V$ increases and becomes larger than the sound pressure generated by $53\,V$. The same effect is not to be seen when the driving voltage is increased from $35.5\,V$ to $53\,V$. Thus, this unexpected behavior at low frequencies is assumed to be a measurement error due to the small output voltage of the microphone.

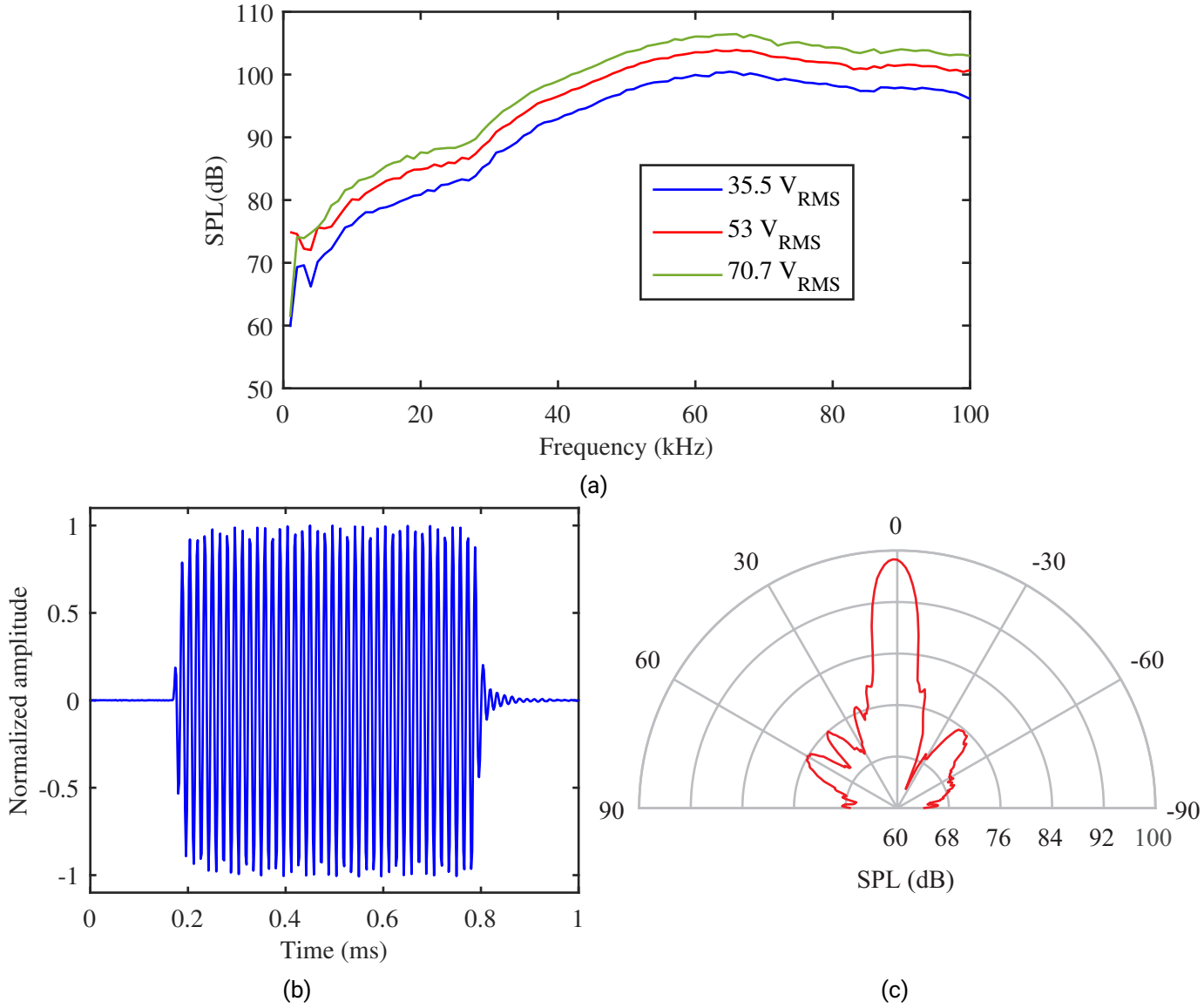

Figure 5.13: (a) Frequency response of the ferroelectret transducer by using driving voltages from $35\,V$ to $70.7\,V$, (b) long-pulse excitation of the Ferroelectret transducer. The sound pressure measured with a microphone is normalized since the same shape is recorded for all driving voltages and (c) directivity pattern of the ferroelectret transducer. The half power beam width is approximately $\pm 4°$ [164].

Furthermore, the directivity pattern is measured for a driving voltage of $35.5\,V$ [Figure 5.13(c)]. It shows a relatively narrow directivity around $0°$ with a half bandwidth of $8°$. The narrow directivity is, however, to be expected due to the large vibrating surface of 42 mm.

In order to characterize the build-up and decay phenomena of the sound pressure when the AC voltage is applied or switched off, a burst signal with 40 cycles is used [Figure 5.13(c)]. The measured sound pressure level is normalized since the dynamic behavior of the transducer is independent from the magnitude of the applied voltage. The maximum displacement of the vibrating plate is reached three cycles after applying

the AC voltage, whereas the steady state is reached approximately six cycles after switching off the driving voltage. Hence, this transducer provides the opportunity of generating short pulses and therefore offers the possibility of detecting close objects.

In this prototype we used PLA to build the transducer to make it ecor-friendly and demonstrate the potential of the newly proven material as electret material. In addition to the good electret property, the possibilities of designing more complex structures of the backplate using 3D-printing techniques are a new field with a great potential to be investigated. The backplate geometry is the main component of the transducer that defines the resonance frequency and acts as an active part of the ferroelectret. However, it should be noted that the mechanical property of the PLA film does not belong to the best suited for such application. A better alternative material as diaphragm would be biaxially-oriented polyethylene terephthalate (BoPET), which is made from stretched polyethylene terephthalate (PET). Even though some experiments have been conducted in this regard, further improvements are beyond the scope of this work and will be conducted in future research.

6 Conclusion and future work

In this work the developement of new ferroelectret materials and their applications were investigated. In the first stage, the aim was to develop new hollow-structure films based on polymers with excellent electret properties, which is FEP. The void structure were achieved either by thermally fusing FEP films so that certain air gaps, such as parallel tunnels, are formed between them, or by fusing round-section FEP tubes together so that they form a band or membrane. The voids in these films were then charged in a suitable way to make them piezoelectric. Experimental studies of the mechanical, electrical, and piezoelectric properties of the obtained ferroelectric materials as well as their modelling by FEM and analytical theoretical approaches were presented. These ferroelectrets were used to build energy harvesters using the longitudinal and transverse piezoelectric effect and reached an output power of 300 µW and over 1000 µW, respectively. It is worth mentioning that the output power of 1000 µW exceeds that of previously described ferroelectret nanogenerators and is far above that of the conventional piezoelectret energy harvesters based on the longitudinal piezoeffect. It was shown that incorporating the ferroelectret films in 3D-printing structures provides a modular assembly which ensures reproducibility and high efficiency.

In the second stage, new ferroelectret materials were investigated, that are more favorable for sensor applications. Here, further strategies for using 3D-printing for manufacturing ferroelectrets were introduced. The first structure is the three-layer-sandwich-method by using a 3D-printed grid of periodically spaced foamed TPU spacers and air channels between two thin FEP films. After corona charging, the air-filled sections acted as electroactive elements, while the ultra-soft TPU sections determined the mechanical stiffness. Due to the ultra-soft TPU sections, very high quasi-static and dynamic d_{33} coefficients of 22.000 $\mathrm{pC\,N^{-1}}$ and 7500 $\mathrm{pC\,N^{-1}}$, respectively, were achieved. Based on the same principle, and taking into account the environmental challenges, eco-friendlier ferroelectrets using PLA were investgiated. It turned out that PLA, which is biodegradable polymer derived from renewable plant sources such as corn or potato starch, feature a promising charge stability when charged properly. To demonstrate the potential of these materials, several applications have been introduced.

Electronic-skin or e-skin is a pseudonym for a device that mimics sensing properties of the human skin for various external influences such as pressure, temperature along with other influences. In general, collecting personal and environmental data is rapidly gaining importance for improving the quality of daily life, enabling early diagnose of harmful environmental conditions or diseases [252]–[254]. Application areas of e-skin can be seen in skin attached devices such as robotics or prosthetics, being integrated in clothing, or mounted directly on skin. In this context, conventional electronics can not be deployed because of their rigidity. Thus, flexible electronic sensors, which are more adhered to moving and rough surfaces have been intensively studied. Therefore the focus of research has shifted towards lightweight, flexibility, and stretchability, all critical matters when extreme conditions such as lateral tension, compression, and twisting movements at joints or skin segments are addressed. Since e-skin incorporates all possible sensor principles, many transduction mechanisms have already been considered, especially capacitive [256], [257], piezoresistive [258], [259], triboelectric [260], [261], and piezoelectric [262], [263] ones. However, for a better reproduction of the dynamic and static pressure sensitivity of the human skin, a combination of multiple transduction mechanisms

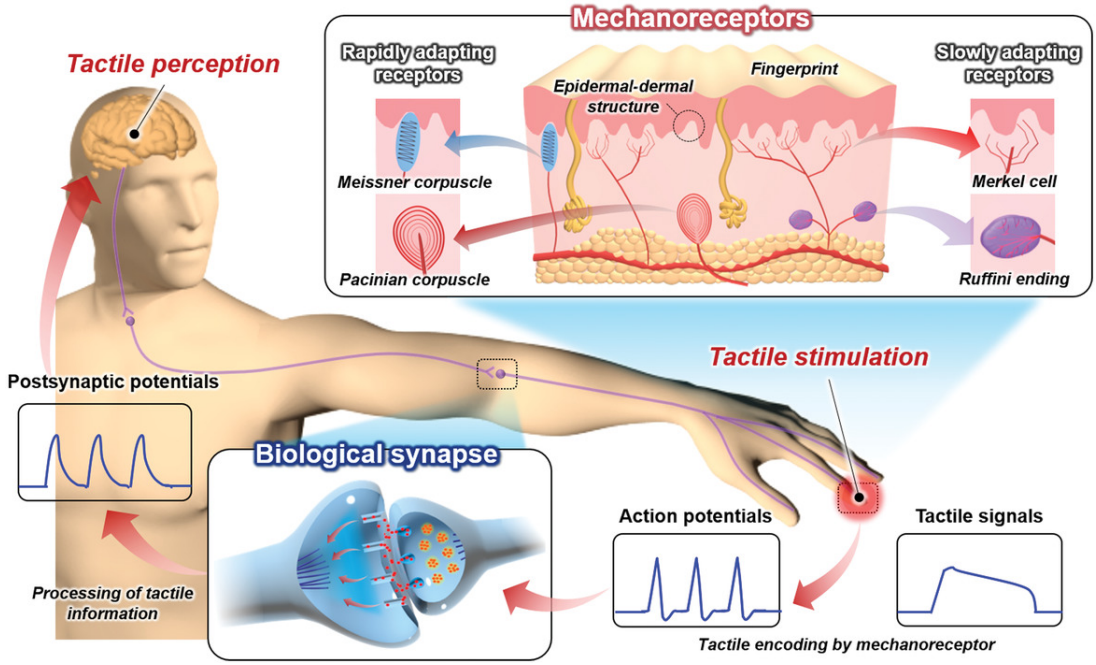

Figure 6.1: Human tactile perception system [255]

is required. Ferroelectrets exhibit piezoelectric behavior, yet they can also be considered as charged capacitors. Therefore, under static stress the measurement of the capacity of the ferroelectrets provides information about the static deformation, whereas the charge measurement provides information about the dynamic deformation. Thus two features of the human skin (Figure 6.1) can be reproduced: The rapid adaptation of Meissner corpuscles and hair-follicle receptors as well as the Pacinian corpuscles [264] are represented by the piezoelectric effect of the ferroelectret films. The slow adaptation rate to detect static stimuli represented by the tactile disks, Runi endings, and Merkel's disks is reproduced by measuring the capacity. An additional advantage of ferroelectret e-skin is the possibility to be self-powered.

Thereby two strategies can be investigated: The first approach is a battery-less system by using the output signal of the piezoelectric part as a power source. In literature, self-powered systems are suggested using a full-bridge rectifier and large capacitor to obtain a DC voltage from the AC voltage generated by the energy harvester [Figure 6.2(a)]. However, because of the small amount of mechanical energy that can be harvested from movements, such an approach dissipates the total amount of converted energy during the AC-DC rectification. A better approach is using SSHI. The SSHI method [Figure 6.2(b)] is based on a resonant loop that changes the polarity of the capacitor charge, which flips the capacitor voltage instantly. The energy harvester current charges the internal capacitor continuously instead of first discharging it. However, such a method requires a large output signal from the ferroelectrets and, thus, a very high sensitivity to the smallest vibrations. The second approach is using a battery that can be switched on when needed using a wake-up circuit. This can be achieved by using the output signal of the ferroelectrets as a trigger to activate the circuit.

Due to the outstanding sensitivity of the ferroelectrets demonstrated in this work, they can be inserted as very sensitive sensors in active leg prostheses and orthoses. In fact, the most growing problem regarding the aging society, is that elderly become weaker and physically limited in daily life activities. A solution thereof are active assistance systems that can provide support such as stand-up aid that provides support when the patient's own strength is insufficient or standing up becomes too much of a burden. Hereby, EMG and FMG

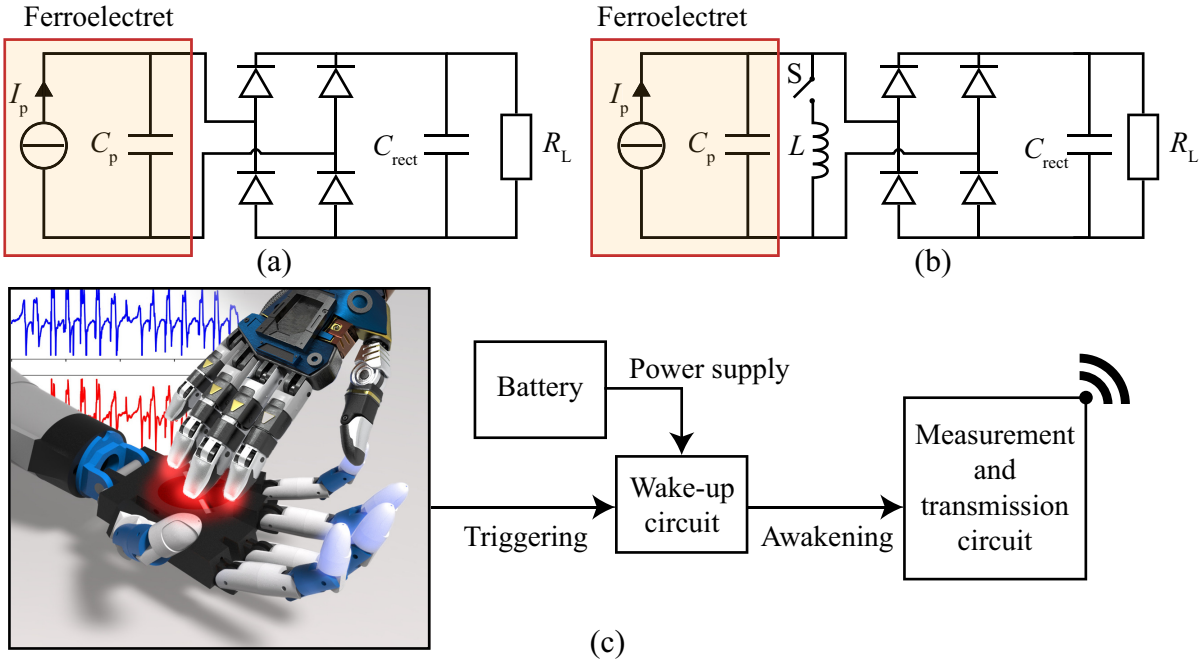

Figure 6.2: Self powering schemes: (a) Circuit schematic of the direct energy transfer rectifier, (b) typical Parallel-synchronized switch harvesting on inductor (SSHI) (P-SSHI) circuit, (c) schematic diagrams showing the wake-up circuit's working principle.

sensor fusion can be used in combination with machine learning to detect the movement intention and provide assistance accordingly.

Ferroelectrets, as demonstrated in this work, can be manufactured using the biodegradable polymer PLA. Even though the charge stability is promising, this property is not yet well understood. Therefore, investigating the influence of a customized fabrication process on electret properties is mandatory. An additional option, that is worth examining is improving of the stability of stored charges in PLA-based films by adding filler materials. Being biodegradable and at the same time biocompatible, PLA-based ferroelectrets have prospective applications in the field of sustainable devices and active medical implants. It is known that the degradation process of PLA is favored by temperature, and enzymatic activity inside the human body [265]. For such applications, it is mandatory to investigate the ferroelectrets in terms of their functionality during the degradation process in a biological environment.

Bibliography

[1] Research and markets, *Sensor Market Report: Trends, Forecast and Competitive Analysis*. 2020.

[2] Markets and markets, *Wearable Technology Market: Wearable Technology Market by Product (Wristwear, Headwear, Footwear, Fashion & Jewelry, Bodywear), Type (Smart Textile, Non-Textile), Application (Consumer Electronics, Healthcare, Enterprise & Industrial), and Geography - Global Forecast to 2026*. 2021.

[3] G. Chen, Y. Li, M. Bick, and J. Chen, "Smart textiles for electricity generation", *Chemical Reviews*, vol. 120, no. 8, pp. 3668–3720, 2020.

[4] Y. Zou, J. Xu, Y. Fang, X. Zhao, Y. Zhou, and J. Chen, "A hand-driven portable triboelectric nanogenerator using whirligig spinning dynamics", *Nano Energy*, vol. 83, p. 105 845, 2021.

[5] Y. Zou, A. Libanori, J. Xu, A. Nashalian, and J. Chen, "Triboelectric nanogenerator enabled smart shoes for wearable electricity generation", *Research*, vol. 2020, 2020.

[6] C. Yan, Y. Gao, S. Zhao, *et al.*, "A linear-to-rotary hybrid nanogenerator for high-performance wearable biomechanical energy harvesting", *Nano Energy*, vol. 67, p. 104 235, 2020.

[7] S. Jo, M. Kim, M. Kim, and Y. Kim, "Flexible thermoelectric generator for human body heat energy harvesting", *Electronics letters*, vol. 48, no. 16, pp. 1015–1017, 2012.

[8] A. Nozariasbmarz, R. A. Kishore, B. Poudel, *et al.*, "High power density body heat energy harvesting", *ACS applied materials & interfaces*, vol. 11, no. 43, pp. 40 107–40 113, 2019.

[9] H. R. Yun, D. J. Lee, J. R. Youn, and Y. S. Song, "Ferrohydrodynamic energy harvesting based on air droplet movement", *Nano Energy*, vol. 11, pp. 171–178, 2015.

[10] S. R. Anton and H. A. Sodano, "A review of power harvesting using piezoelectric materials (2003–2006)", *Smart Materials and Structures*, vol. 16, no. 3, R1–R21, 2007.

[11] A. Erturk and D. J. Inman, *Piezoelectric energy harvesting*. John Wiley & Sons, 2011.

[12] D. Briand, E. Yeatman, S. Roundy, *et al.*, *Micro energy harvesting*. Wiley Online Library, 2015.

[13] S. Priya and D. J. Inman, *Energy harvesting technologies*. Springer, 2009, vol. 21.

[14] T. J. Kazmierski and S. Beeby, "Energy harvesting systems", *Principles, Modeling and Applications; Springer Science+ Business Media LLC: New York, NY, USA*, 2011.

[15] A. Jain, P. KJ, A. K. Sharma, A. Jain, and R. PN, "Dielectric and piezoelectric properties of pvdf/pzt composites: A review", *Polymer Engineering & Science*, vol. 55, no. 7, pp. 1589–1616, 2015.

[16] K. S. Ramadan, D. Sameoto, and S. Evoy, "A review of piezoelectric polymers as functional materials for electromechanical transducers", *Smart Materials and Structures*, vol. 23, no. 3, p. 033 001, 2014.

[17] S. Sukumaran, S. Chatbouri, D. Rouxel, E. Tisserand, F. Thiebaud, and T. Ben Zineb, "Recent advances in flexible pvdf based piezoelectric polymer devices for energy harvesting applications", *Journal of Intelligent Material Systems and Structures*, vol. 32, no. 7, pp. 746–780, 2021.

[18] S. Bauer, R. Gerhard, and G. M. Sessler, “Ferroelectrets: Soft electroactive foams for transducers”, 2004.

[19] M. Wegener, W. Wirges, R. Gerhard-Multhaupt, *et al.*, “Controlled inflation of voids in cellular polymer ferroelectrets: Optimizing electromechanical transducer properties”, *Applied Physics Letters*, vol. 84, no. 3, pp. 392–394, 2004.

[20] W. Wirges, M. Wegener, O. Voronina, L. Zirkel, and R. Gerhard-Multhaupt, “Optimized preparation of elastically soft, highly piezoelectric, cellular ferroelectrets from nonvoided poly (ethylene terephthalate) films”, *Advanced Functional Materials*, vol. 17, no. 2, pp. 324–329, 2007.

[21] J. Lekkala and M. Paajanen, “Emfi-new electret material for sensors and actuators”, in *10th International Symposium on Electrets (ISE 10). Proceedings (Cat. No. 99 CH36256)*, IEEE, 1999, pp. 743–746.

[22] G. Sessler and J. Hillenbrand, “Electromechanical response of cellular electret films”, in *10th International Symposium on Electrets (ISE 10). Proceedings (Cat. No. 99 CH36256)*, IEEE, 1999, pp. 261–264.

[23] M. Paajanen, J. Lekkala, and K. Kirjavainen, “Electromechanical film (emfi)—a new multipurpose electret material”, *Sensors and Actuators A: Physical*, vol. 84, no. 1-2, pp. 95–102, 2000.

[24] G. S. Neugschwandtner, R. Schwödiauer, S. Bauer-Gogonea, S. Bauer, M. Paajanen, and J. Lekkala, “Piezo-and pyroelectricity of a polymer-foam space-charge electret”, *Journal Applied Physics*, vol. 89, no. 8, pp. 4503–4511, 2001.

[25] N. Wu, X. Cheng, Q. Zhong, *et al.*, “Cellular polypropylene piezoelectret for human body energy harvesting and health monitoring”, *Advanced Functional Materials*, vol. 25, no. 30, pp. 4788–4794, 2015.

[26] A. Mellinger, M. Wegener, W. Wirges, and R. Gerhard-Multhaupt, “Thermally stable dynamic piezoelectricity in sandwich films of porous and nonporous amorphous fluoropolymer”, *Applied Physics Letters*, vol. 79, no. 12, pp. 1852–1854, 2001.

[27] Altafim, Basso, Lima, Aquino, Neto, and Gerhard-Multhaupt, “Piezoelectrets from thermo-formed bubble structures of fluoropolymer-electret films”, *IEEE Transactions on Dielectrics and Electrical Insulation*, vol. 13, no. 5, pp. 979–985, 2006.

[28] Z. Hu and H. von Seggern, “Breakdown-induced polarization buildup in porous fluoropolymer sandwiches: A thermally stable piezoelectret”, *Journal of Applied Physics*, vol. 99, no. 2, p. 024 102, 2006.

[29] X. Zhang, J. Hillenbrand, and G. M. Sessler, “Thermally stable fluorocarbon ferroelectrets with high piezoelectric coefficient”, *Applied Physics A*, vol. 84, no. 1, pp. 139–142, 2006.

[30] X. Zhang, J. Hillenbrand, and G. Sessler, “Ferroelectrets with improved thermal stability made from fused fluorocarbon layers”, *Journal of Applied Physics*, vol. 101, no. 5, p. 054 114, 2007.

[31] J. Huang, X. Zhang, Z. Xia, and X. Wang, “Piezoelectrets from laminated sandwiches of porous polytetrafluoroethylene films and nonporous fluoroethylenepropylene films”, *Journal of Applied Physics*, vol. 103, no. 8, p. 084 111, 2008.

[32] R. A. P. Altafim, X. Qiu, W. Wirges, *et al.*, “Template-based fluoroethylenepropylene piezoelectrets with tubular channels for transducer applications”, *Journal of Applied Physics*, vol. 106, no. 1, p. 014 106, 2009.

[33] H. von Seggern, S. Zhukov, and S. N. Fedosov, “Poling dynamics and thermal stability of fep/eptfe/fep sandwiches”, *IEEE Transactions on Dielectrics and Electrical Insulation*, vol. 17, no. 4, pp. 1056–1065, 2010.

[34] Z. Sun, X. Zhang, Z. Xia, *et al.*, "Polarization and piezoelectricity in polymer films with artificial void structure", *Applied Physics A*, vol. 105, no. 1, pp. 197–205, 2011.

[35] H. von Seggern, S. Zhukov, and S. Fedosov, "Importance of geometry and breakdown field on the piezoelectric d 33 coefficient of corona charged ferroelectret sandwiches", *IEEE Transactions on Dielectrics and Electrical Insulation*, vol. 18, no. 1, pp. 49–56, 2011.

[36] X. Zhang, J. Hillenbrand, G. Sessler, S. Haberzettl, and K. Lou, "Fluoroethylenepropylene ferroelectrets with patterned microstructure and high, thermally stable piezoelectricity", *Applied Physics A*, vol. 107, no. 3, pp. 621–629, 2012.

[37] B.-X. Xu, H. von Seggern, S. Zhukov, and D. Gross, "Continuum modeling of charging process and piezoelectricity of ferroelectrets", *Journal of Applied Physics*, vol. 114, no. 9, p. 094 103, 2013.

[38] N. Nepal, R. A. P. Altafim, and A. Mellinger, "Space charge deposition in tubular channel ferroelectrets: A combined fluorescence imaging/limm study with finite element analysis", *Journal of Applied Physics*, vol. 121, no. 24, p. 244 103, 2017.

[39] S. Zhukov, D. Eder-Goy, C. Biethan, S. Fedosov, B.-X. Xu, and H. von Seggern, "Tubular fluoropolymer arrays with high piezoelectric response", *Smart Materials and Structures*, vol. 27, no. 1, p. 015 010, 2017.

[40] Y. Zhang, C. R. Bowen, S. K. Ghosh, *et al.*, "Ferroelectret materials and devices for energy harvesting applications", *Nano Energy*, vol. 57, pp. 118–140, 2019.

[41] P. Pondrom, J. Hillenbrand, G. Sessler, J. Bös, and T. Melz, "Vibration-based energy harvesting with stacked piezoelectrets", *Applied physics letters*, vol. 104, no. 17, p. 172 901, 2014.

[42] B. Wang, J. Zhong, Q. Zhong, *et al.*, "Sandwiched composite fluorocarbon film for flexible electret generator", *Advanced Electronic Materials*, vol. 2, no. 4, p. 1 500 408, 2016.

[43] Z. Luo, D. Zhu, and S. Beeby, "An electromechanical model of ferroelectret for energy harvesting", *Smart Materials and Structures*, vol. 25, no. 4, p. 045 010, 2016.

[44] W. Li, N. Wu, J. Zhong, *et al.*, "Theoretical study of cellular piezoelectret generators", *Advanced Functional Materials*, vol. 26, no. 12, pp. 1964–1974, 2016.

[45] S. Zhukov, X. Ma, H. von Seggern, *et al.*, "Biodegradable cellular polylactic acid ferroelectrets with strong longitudinal and transverse piezoelectricity", *Applied Physics Letters*, vol. 117, no. 11, p. 112 901, 2020.

[46] X. Zhang, P. Pondrom, G. M. Sessler, and X. Ma, "Ferroelectret nanogenerator with large transverse piezoelectric activity", *Nano energy*, vol. 50, pp. 52–61, 2018.

[47] X. Zhang, P. Pondrom, L. Wu, and G. M. Sessler, "Vibration-based energy harvesting with piezoelectrets having high d31 activity", *Applied Physics Letters*, vol. 108, no. 19, p. 193 903, 2016.

[48] X. Ma, H. von Seggern, G. M. Sessler, *et al.*, "High performance fluorinated polyethylene propylene ferroelectrets with an air-filled parallel-tunnel structure", *Smart Materials and Structures*, vol. 30, no. 1, p. 015 002, 2020.

[49] O. Ben Dali, P. Pondrom, G. Sessler, *et al.*, "Cantilever-based ferroelectret energy harvesting", *Applied Physics Letters*, vol. 116, no. 24, p. 243 901, 2020.

[50] O. Ben Dali, H. von Seggern, G. M. Sessler, *et al.*, "Ferroelectret energy harvesting with 3d-printed air-spaced cantilever design", *Nano Select*, vol. 3, no. 3, pp. 713–722, 2022.

[51] O. Heaviside, "Electromagnetic induction and its propagation. electrization and electrification. natural electrets", *The Electrician*, vol. 15, pp. 230–231, 1885.

[52] G. M. Sessler, “Physical principles of electrets”, in *Electrets*, ser. Topics in Applied Physics, G. M. Sessler, Ed., vol. 33, Berlin, Heidelberg: Springer Berlin Heidelberg, 1987, pp. 13–80.

[53] A. Gemant, “Lxxiii. recent investigations”, *The London, Edinburgh, and Dublin Philosophical Magazine and Journal of Science*, vol. 20, no. 136, pp. 929–952, 1935.

[54] M. Eguchi, “On the permanent electret”, *The London, Edinburgh, and Dublin Philosophical Magazine and Journal of Science*, vol. 49, no. 289, pp. 178–192, 1925.

[55] B. Hilczer and J. Malecki, “Electrets: Studies in electrical and electronic engineering”, *New York: Elsevier*, vol. 14, p. 19, 1986.

[56] F. Gutmann, “The electret”, *Reviews of Modern Physics*, vol. 20, no. 3, p. 457, 1948.

[57] B. Gross, “Static charges on dielectrics”, *British Journal of Applied Physics*, vol. 1, no. 10, p. 259, 1950.

[58] E. Fukada, “History and recent progress in piezoelectric polymers”, *IEEE Transactions on ultrasonics, ferroelectrics, and frequency control*, vol. 47, no. 6, pp. 1277–1290, 2000.

[59] S. Mikola, “Über die permanente polarisation der festen dielektrika”, *Zeitschrift für Physik*, vol. 32, no. 1, pp. 476–488, 1925.

[60] E. P. Adams, “On electrets”, *Phil. Mag*, vol. 49, p. 178, 1925.

[61] B. Gross, “Charge storage in solid dielectrics: A bibliographical review on the electret and related effects”, 1964.

[62] G. Sessler, “Bernhard gross and the evolution of modern electret research”, *Brazilian journal of physics*, vol. 29, pp. 220–225, 1999.

[63] B. i. Gross, “The electret”, *Endeavour*, vol. 30, no. 111, pp. 115–119, 1971.

[64] R. Gerhard, “Bulletin board: 50 years of international symposia on electrets from 1967 to 2017—a global history”, *IEEE Electrical Insulation Magazine*, vol. 37, no. 2, pp. 50–55, 2021.

[65] M. M. Perlman and J.-L. Meunier, “Charge decay of carnauba wax electrets”, *Journal of Applied Physics*, vol. 36, no. 2, pp. 420–427, 1965.

[66] R. Gerhard-Multhaupt, “Electrets: Dielectrics with quasi-permanent charge or polarization”, *IEEE transactions on electrical insulation*, no. 5, pp. 531–554, 1987.

[67] H. Bauser, “Ladungsspeicherung in elektronenhaftstellen in organischen isolatoren”, *Kunststoffe*, vol. 62, pp. 192–196, 1972.

[68] M. Moreira, I. Soares, Y. Assagra, *et al.*, “Piezoelectrets: A brief introduction”, *IEEE Sensors Journal*, vol. 21, no. 20, pp. 22 317–22 328, 2021.

[69] J. M. Kenney and S. C. Roth, “Room temperature poling of poly (vinylidene fluoride) with deposited metal electrodes”, *JOURNAL OF RESEARCH of the National Bureau of Standards*, vol. 84, no. 6, p. 447, 1979.

[70] S. Bamji, K. Jao, and M. Perlman, “Polymer electrets corona charged at high temperature”, *Journal of Electrostatics*, vol. 6, no. 4, pp. 373–379, 1979.

[71] M. Paajanen, M. Wegener, and R. Gerhard-Multhaupt, “Understanding the role of the gas in the voids during corona charging of cellular electret films-a way to enhance their piezoelectricity”, *Journal of Physics D: Applied Physics*, vol. 34, no. 16, p. 2482, 2001.

[72] L. Loeb, *Electrical coronas (berkeley, ca*, 1965.

[73] E. W. McDaniel and E. A. Mason, “Mobility and diffusion of ions in gases”, 1973.

[74] J. A. Giacometti, S. Fedosov, and M. M. Costa, "Corona charging of polymers: Recent advances on constant current charging", *Brazilian Journal of Physics*, vol. 29, pp. 269–279, 1999.

[75] J. Giacometti, "Radial current-density distributions and sample charge uniformity in a corona triode", *Journal of Physics D: Applied Physics*, vol. 20, no. 6, p. 675, 1987.

[76] N. Alves, G. Minami, J. Giacometti, G. L. Ferreira, and O. Oliveira Jr, "Surface potentials of corona-charged ferroelectric p (vdf-trfe) copolymer samples", *Ferroelectrics*, vol. 150, no. 1, pp. 219–226, 1993.

[77] Z. Weinberg, D. Matthies, W. Johnson, and M. Lampert, "Measurement of the steady- state potential difference across a thin insulating film in a corona discharge", *Review of Scientific Instruments*, vol. 46, no. 2, pp. 201–203, 1975.

[78] J. A. Giacometti and J. Sinézio Carvalho Campos, "Constant current corona triode with grid voltage control. application to polymer foil charging", *Review of scientific instruments*, vol. 61, no. 3, pp. 1143–1150, 1990.

[79] S. Zhukov and H. Von Seggern, "Breakdown-induced light emission and poling dynamics of porous fluoropolymers", *Journal of applied physics*, vol. 101, no. 8, p. 084 106, 2007.

[80] X. Zhang-Fu, D. Hai, Y. Guo-Mao, L. Ting-Ji, and S. Xi-Min, "Constant-current corona charging of teflon pfa", *IEEE transactions on electrical insulation*, vol. 26, no. 1, pp. 35–41, 1991.

[81] V. N. Kestelman, L. S. Pinchuk, and V. A. Goldade, *Electrets in engineering: fundamentals and applications*. Springer Science & Business Media, 2000.

[82] G. Eberle, H. Schmidt, and W. Eisenmenger, "Piezoelectric polymer electrets", *IEEE transactions on dielectrics and electrical insulation*, vol. 3, no. 5, pp. 624–646, 1996.

[83] J. Hillenbrand and G. Sessler, "Piezoelectricity in cellular electret films", *IEEE Transactions on Dielectrics and Electrical Insulation*, vol. 7, no. 4, pp. 537–542, 2000.

[84] G. M. Sessler, "Electrets: Recent developments", *Journal of Electrostatics*, vol. 51, pp. 137–145, 2001.

[85] R. Gerhard-Multhaupt, "Less can be more. holes in polymers lead to a new paradigm of piezoelectric materials for electret transducers", *IEEE Transactions on Dielectrics and Electrical Insulation*, vol. 9, no. 5, pp. 850–859, 2002.

[86] M. Wegener and S. Bauer, "Microstorms in cellular polymers: A route to soft piezoelectric transducer materials with engineered macroscopic dipoles", *ChemPhysChem*, vol. 6, no. 6, pp. 1014–1025, 2005.

[87] Y. P. Raizer and J. E. Allen, *Gas discharge physics*. Springer, 1991, vol. 1.

[88] S. Bauer, "Piezo-, pyro-and ferroelectrets: Soft transducer materials for electromechanical energy conversion", *IEEE Transactions on Dielectrics and Electrical Insulation*, vol. 13, no. 5, pp. 953–962, 2006.

[89] A. Mohebbi, F. Mighri, A. Ajji, and D. Rodrigue, "Cellular polymer ferroelectret: A review on their development and their piezoelectric properties", *Advances in Polymer Technology*, vol. 37, no. 2, pp. 468–483, 2018.

[90] M. Wegener, W. Wirges, and R. Gerhard-Multhaupt, "Piezoelectric polyethylene terephthalate (petp) foams–specifically designed and prepared ferroelectret films", *Advanced Engineering Materials*, vol. 7, no. 12, pp. 1128–1131, 2005.

[91] X. Zhang, J. Huang, J. Chen, Z. Wan, S. Wang, and Z. Xia, "Piezoelectric properties of irradiation-crosslinked polypropylene ferroelectrets", *Applied Physics Letters*, vol. 91, no. 18, p. 182 901, 2007.

[92] Z. Luo, J. Shi, and S. Beeby, "Novel thick-foam ferroelectret with engineered voids for energy harvesting applications", in *Journal of Physics: Conference Series*, IOP Publishing, vol. 773, 2016, p. 012 030.

[93] L. J. Jacobs, M. F. Kemmere, and J. T. Keurentjes, "Sustainable polymer foaming using high pressure carbon dioxide: A review on fundamentals, processes and applications", *Green Chemistry*, vol. 10, no. 7, pp. 731–738, 2008.

[94] L. Urbanczyk, C. Calberg, C. Detrembleur, C. Jerome, and M. Alexandre, "Batch foaming of san/clay nanocomposites with scco2: A very tunable way of controlling the cellular morphology", *Polymer*, vol. 51, no. 15, pp. 3520–3531, 2010.

[95] S. Zhukov, S. Fedosov, and H. von Seggern, "Piezoelectrets from sandwiched porous polytetrafluoroethylene (eptfe) films: Influence of porosity and geometry on charging properties", *Journal of Physics D: Applied Physics*, vol. 44, no. 10, p. 105 501, 2011.

[96] H. von Seggern, S. Fedosov, and S. Zhukov, "Tsd currents in corona poled fep/eptfe/fep sandwiches", in *2008 13th International Symposium on Electrets*, IEEE, 2008, B0901–B0901.

[97] Z. Xia, A. Wedel, and R. Danz, "Charge storage and its dynamics in porous polytetrafluoroethylene (ptfe) film electrets", *IEEE transactions on dielectrics and electrical insulation*, vol. 10, no. 1, pp. 102–108, 2003.

[98] S. Zhukov and H. Von Seggern, "Polarization hysteresis and piezoelectricity in open-porous fluoropolymer sandwiches", *Journal of Applied Physics*, vol. 102, no. 4, p. 044 109, 2007.

[99] X. Zhang, G. Cao, Z. Sun, and Z. Xia, "Fabrication of fluoropolymer piezoelectrets by using rigid template: Structure and thermal stability", *Journal of Applied Physics*, vol. 108, no. 6, p. 064 113, 2010.

[100] D. Flachs, F. Emmerich, G.-L. Roth, R. Hellmann, and C. Thielemann, "Laser-bonding of fep/fep interfaces for a flexible manufacturing process of ferroelectrets", in *Journal of Physics: Conference Series*, IOP Publishing, vol. 1407, 2019, p. 012 107.

[101] M. Broadhurst and G. Davis, "Piezo-and pyroelectric properties", *Electrets*, pp. 285–319, 1980.

[102] J. Yang, Q. Chen, F. Xu, *et al.*, "Epitaxy enhancement of piezoelectric properties in p (vdf-trfe) copolymer films and applications in sensing and energy harvesting", *Advanced Electronic Materials*, vol. 6, no. 10, p. 2 000 578, 2020.

[103] S. R. Anton and K. M. Farinholt, "Piezoelectret foam-based vibration energy harvester for low-power energy generation", in *Smart Materials, Adaptive Structures and Intelligent Systems*, American Society of Mechanical Engineers, vol. 45103, 2012, pp. 929–937.

[104] X. Zhang, L. Wu, and G. M. Sessler, "Energy harvesting from vibration with cross-linked polypropylene piezoelectrets", *AIP Advances*, vol. 5, no. 7, p. 077 185, 2015.

[105] X. Zhang, P. Pondrom, G. M. Sessler, and X. Ma, "Ferroelectret nanogenerator with large transverse piezoelectric activity", *Nano Energy*, vol. 50, pp. 52–61, 2018.

[106] X. Mo, H. Zhou, W. Li, *et al.*, "Piezoelectrets for wearable energy harvesters and sensors", *Nano Energy*, vol. 65, p. 104 033, 2019.

[107] T. Starner, "Human-powered wearable computing", *IBM systems Journal*, vol. 35, no. 3.4, pp. 618–629, 1996.

[108] K.-E. Byun, M.-H. Lee, Y. Cho, S.-G. Nam, H.-J. Shin, and S. Park, "Potential role of motion for enhancing maximum output energy of triboelectric nanogenerator", *APL Materials*, vol. 5, no. 7, p. 074 107, 2017.

[109] W. Li, S. Zhao, N. Wu, *et al.*, "Sensitivity-enhanced wearable active voiceprint sensor based on cellular polypropylene piezoelectret", *ACS applied materials & interfaces*, vol. 9, no. 28, pp. 23 716–23 722, 2017.

[110] S. Chen, N. Wu, L. Ma, *et al.*, "Noncontact heartbeat and respiration monitoring based on a hollow microstructured self-powered pressure sensor", *ACS applied materials & interfaces*, vol. 10, no. 4, pp. 3660–3667, 2018.

[111] B. Wang, C. Liu, Y. Xiao, *et al.*, "Ultrasensitive cellular fluorocarbon piezoelectret pressure sensor for self-powered human physiological monitoring", *Nano Energy*, vol. 32, pp. 42–49, 2017.

[112] Q. Zhong, J. Zhong, X. Cheng, *et al.*, "Paper-based active tactile sensor array", *Advanced Materials*, vol. 27, no. 44, pp. 7130–7136, 2015.

[113] W. Li, D. Torres, T. Wang, C. Wang, and N. Sepúlveda, "Flexible and biocompatible polypropylene ferroelectret nanogenerator (feng): On the path toward wearable devices powered by human motion", *Nano Energy*, vol. 30, pp. 649–657, 2016.

[114] W. Li, J. Duan, J. Zhong, *et al.*, "Flexible thv/coc piezoelectret nanogenerator for wide-range pressure sensing", *ACS applied materials & interfaces*, vol. 10, no. 35, pp. 29 675–29 683, 2018.

[115] O. Ben Dali, S. Zhukov, R. Chadda, *et al.*, "Modeling of piezoelectric coupling coefficients of soft ferroelectrets for energy harvesting", in *2019 IEEE International Ultrasonics Symposium (IUS)*, IEEE, 2019, pp. 2454–2457.

[116] S. Zhukov, H. von Seggern, X. Zhang, *et al.*, "Microenergy harvesters based on fluorinated ethylene propylene piezotubes", *Advanced Engineering Materials*, vol. 22, no. 5, p. 1 901 399, 2020.

[117] X. Zhang, H. von Seggern, G. M. Sessler, and M. Kupnik, "Mechanical energy harvesting with ferroelectrets", *IEEE Electrical Insulation Magazine*, vol. 36, no. 6, pp. 47–58, 2020.

[118] S. P. Beeby and T. O'Donnell, "Electromagnetic energy harvesting", *Energy Harvesting Technologies*, pp. 129–161, 2009.

[119] B. Maamer, A. Boughamoura, A. M. F. El-Bab, L. A. Francis, and F. Tounsi, "A review on design improvements and techniques for mechanical energy harvesting using piezoelectric and electromagnetic schemes", *Energy Conversion and Management*, vol. 199, p. 111 973, 2019.

[120] D. Briand, E. Yeatman, and S. Roundy, "Introduction to micro energy harvesting", *Edited by Danick Briand, Eric Yeatman, and Shad Roundy*, 2015.

[121] F. U. Khan and M. U. Qadir, "State-of-the-art in vibration-based electrostatic energy harvesting", *Journal of Micromechanics and Microengineering*, vol. 26, no. 10, p. 103 001, 2016.

[122] Y. Zhang, T. Wang, A. Luo, Y. Hu, X. Li, and F. Wang, "Micro electrostatic energy harvester with both broad bandwidth and high normalized power density", *Applied energy*, vol. 212, pp. 362–371, 2018.

[123] Y. Suzuki, "Recent progress in mems electret generator for energy harvesting", *IEEJ Transactions on Electrical and Electronic Engineering*, vol. 6, no. 2, pp. 101–111, 2011.

[124] E. R. Westby and E. Halvorsen, "Design and modeling of a patterned-electret-based energy harvester for tire pressure monitoring systems", *IEEE/ASME Transactions On Mechatronics*, vol. 17, no. 5, pp. 995–1005, 2011.

[125] C. Jean-Mistral, T. Vu Cong, and A. Sylvestre, "Advances for dielectric elastomer generators: Replacement of high voltage supply by electret", *Applied Physics Letters*, vol. 101, no. 16, p. 162 901, 2012.

[126] Y. Chiu and Y.-C. Lee, “Flat and robust out-of-plane vibrational electret energy harvester”, *Journal of Micromechanics and Microengineering*, vol. 23, no. 1, p. 015 012, 2012.

[127] C. Covaci and A. Gontean, “Piezoelectric energy harvesting solutions: A review”, *Sensors*, vol. 20, no. 12, p. 3512, 2020.

[128] H. Liu, J. Zhong, C. Lee, S.-W. Lee, and L. Lin, “A comprehensive review on piezoelectric energy harvesting technology: Materials, mechanisms, and applications”, *Applied Physics Reviews*, vol. 5, no. 4, p. 041 306, 2018.

[129] M. Safaei, H. A. Sodano, and S. R. Anton, “A review of energy harvesting using piezoelectric materials: State-of-the-art a decade later (2008–2018)”, *Smart Materials and Structures*, vol. 28, no. 11, p. 113 001, 2019.

[130] A. Toprak and O. Tigli, “Piezoelectric energy harvesting: State-of-the-art and challenges”, *Applied Physics Reviews*, vol. 1, no. 3, p. 031 104, 2014.

[131] S. Zhukov, D. Eder-Goy, S. Fedosov, B.-X. Xu, and H. von Seggern, “Analytical prediction of the piezoelectric d33 response of fluoropolymer arrays with tubular air channels”, *Scientific reports*, vol. 8, no. 1, pp. 1–10, 2018.

[132] O. B. Dali, “Modeling of energy harvesters based on ferroelectric materials”, M.S. thesis, 2018.

[133] C. Multiphysics and C. Module, “Comsol multiphysics user’s guide”, *Version: COMSOL Multiphysics*, vol. 3, 2014.

[134] C. B. Sawyer and C. Tower, “Rochelle salt as a dielectric”, *Physical review*, vol. 35, no. 3, p. 269, 1930.

[135] X. Qiu, L. Holländer, W. Wirges, R. Gerhard, and H. Cury Basso, “Direct hysteresis measurements on ferroelectret films by means of a modified sawyer–tower circuit”, *Journal of Applied Physics*, vol. 113, no. 22, p. 224 106, 2013.

[136] J. Fialka and P. Beneš, “Comparison of methods for the measurement of piezoelectric coefficients”, *IEEE Transactions on instrumentation and measurement*, vol. 62, no. 5, pp. 1047–1057, 2013.

[137] C. H. Sondergeld, *The rock physics handbook: Tools for seismic analysis of porous media, gary mavko, tapan mukerji, jack dvorkin, springer (2010), 84 (us),£ 48 (uk). isbn-13: 9780521861366*, 2011.

[138] M. M. Attard, “Finite strain—-isotropic hyperelasticity”, *International Journal of Solids and Structures*, vol. 40, no. 17, pp. 4353–4378, 2003.

[139] P. Pondrom, G. Sessler, J. Bös, and T. Melz, “Compact electret energy harvester with high power output”, *Applied Physics Letters*, vol. 109, no. 5, p. 053 906, 2016.

[140] H. Von Seggern and J. West, “Stabilization of positive charge in fluorinated ethylene propylene copolymer”, *Journal of applied physics*, vol. 55, no. 7, pp. 2754–2757, 1984.

[141] H. von Seggern, “A new model of isothermal charge transport for negatively corona-charged teflon”, *Journal of Applied Physics*, vol. 50, no. 11, pp. 7039–7043, 1979.

[142] J. Hillenbrand, S. Haberzettl, T. Motz, and G. Sessler, “Electret accelerometers: Physics and dynamic characterization”, *The Journal of the Acoustical Society of America*, vol. 129, no. 6, pp. 3682–3689, 2011.

[143] J. Hillenbrand, M. Kodejska, Y. Garcin, H. Von Seggern, and G. Sessler, “High-sensitivity piezoelectret-film accelerometers”, *IEEE Transactions on Dielectrics and Electrical Insulation*, vol. 17, no. 4, pp. 1021–1027, 2010.

[144] R. Kressmann, “New piezoelectric polymer for air-borne and water-borne sound transducers”, *The Journal of the Acoustical Society of America*, vol. 109, no. 4, pp. 1412–1416, 2001.

[145] Y. Wang, L. Wu, and X. Zhang, "Energy harvesting from vibration using flexible floroethylenepropylene piezoelectret films with cross-tunnel structure", *IEEE Transactions on Dielectrics and Electrical Insulation*, vol. 22, no. 3, pp. 1349–1354, 2015.

[146] J. Hillenbrand and G. Sessler, "Piezoelectret microphones with high sensitivity", in *2005 12th International Symposium on Electrets*, IEEE, 2005, pp. 125–128.

[147] X. Zhang, G. M. Sessler, Y. Xue, and X. Ma, "Audio and ultrasonic responses of laminated fluoroethylene-propylene and porous polytetrafluoroethylene films with different charge distributions", *Journal of Physics D: Applied Physics*, vol. 49, no. 20, p. 205 502, 2016.

[148] X. Zhang, X. Zhang, G. M. Sessler, and X. Gong, "Quasi-static and dynamic piezoelectric responses of layered polytetrafluoroethylene ferroelectrets", *Journal of Physics D: Applied Physics*, vol. 47, no. 1, p. 015 501, 2013.

[149] N. Lagakos, J. Jarzynski, J. Cole, and J. Bucaro, "Frequency and temperature dependence of elastic moduli of polymers", *Journal of applied physics*, vol. 59, no. 12, pp. 4017–4031, 1986.

[150] J. Hillenbrand, X. Zhang, Y. Zhang, and G. Sessler, "Pressure-treated cellular polypropylene with large piezoelectric coefficients", in *2003 Annual Report Conference on Electrical Insulation and Dielectric Phenomena*, IEEE, 2003, pp. 40–43.

[151] P. Fang, X. Qiu, W. Wirges, R. Gerhard, and L. Zirkel, "Polyethylene-naphthalate (pen) ferroelectrets: Cellular structure, piezoelectricity and thermal stability", *IEEE Transactions on Dielectrics and Electrical Insulation*, vol. 17, no. 4, pp. 1079–1087, 2010.

[152] O. Hamdi, F. Mighri, and D. Rodrigue, "Time and thermal stability improvement of polyethylene ferroelectrets", *Journal of Applied Polymer Science*, vol. 136, no. 24, p. 47 646, 2019.

[153] M. Wegener, M. Paajanen, O. Voronina, R. Schulze, W. Wirges, and R. Gerhard-Multhaupt, "Voided cyclo-olefin polymer films: Ferroelectrets with high thermal stability", in *2005 12th International Symposium on Electrets*, IEEE, 2005, pp. 47–50.

[154] H. von Seggern, "Isothermal and thermally stimulated current studies of positively corona charged polyfluoroethylenepropylene (teflon fep)", *Journal of Applied Physics*, vol. 52, no. 6, pp. 4081–4085, 1981.

[155] H. von Seggern, "Identification of tsc peaks and surface-voltage stability in teflon fep", *Journal of Applied Physics*, vol. 50, no. 4, pp. 2817–2821, 1979.

[156] T. Yovcheva, G. Mekishev, and A. Marinov, "A percolation theory analysis of surface potential decay related to corona charged polypropylene (pp) electrets", *Journal of Physics: Condensed Matter*, vol. 16, no. 3, p. 455, 2004.

[157] H. Hu, W. Zhu, D. Li, and Y. Qu, "Waterproof and low-cost piezoelectrets with high piezoelectric responses", *Journal of Physics D: Applied Physics*, vol. 54, no. 41, p. 415 502, 2021.

[158] J. Zhong, Q. Zhong, X. Zang, *et al.*, "Flexible pet/eva-based piezoelectret generator for energy harvesting in harsh environments", *Nano Energy*, vol. 37, pp. 268–274, 2017.

[159] H. Dubbel, J. Feldhusen, and K.-H. Grote, Eds., *Dubbel: Taschenbuch für den Maschinenbau*, 24., aktualisierte und erweiterte. Auflage. Berlin: Springer, 2014.

[160] T. Beléndez, C. Neipp, and A. Beléndez, "Large and small deflections of a cantilever beam", *European Journal of Physics*, vol. 23, no. 3, pp. 371–379, 2002.

[161] H. von Seggern, S. Zhukov, O. Ben Dali, C. Hartmann, G. M. Sessler, and M. Kupnik, "Highly efficient piezoelectrets through ultra-soft elastomeric spacers", *Polymers*, vol. 13, no. 21, p. 3751, 2021.

[162] O. Ben Dali, S. Zhukov, C. Hartman, H. von Seggern, G. M. Sessler, and M. Kupnik, "Biodegradable additive manufactured ferroelectret as mechanical sensor", in *2021 IEEE Sensors*, IEEE, pp. 1–4.

[163] S. Zhukov, X. Ma, H. v. Seggern, *et al.*, "Biodegradable cellular polylactic acid ferroelectrets with strong longitudinal and transverse piezoelectricity", *Applied Physics Letters*, vol. 117, no. 11, p. 112 901, 2020.

[164] O. Ben Dali, S. Zhukov, M. Rutsch, *et al.*, "Biodegradable 3d-printed ferroelectret ultrasonic transducer with large output pressure", in *2021 IEEE International Ultrasonics Symposium (IUS)*, IEEE, 2021, pp. 1–4.

[165] O. Ben Dali, S. Zhukov, R. Chadda, *et al.*, "Eco-friendly high sensitive piezoelectrets for force myography",

[166] J. Hillenbrand, G. M. Sessler, and X. Zhang, "Verification of a model for the piezoelectric d 33 coefficient of cellular electret films", *Journal of applied physics*, vol. 98, no. 6, p. 064 105, 2005.

[167] O. Hamdi, F. Mighri, and D. Rodrigue, "Piezoelectric cellular polymer films: Fabrication, properties and applications", *AIMS Mater. Sci*, vol. 5, no. 5, pp. 845–869, 2018.

[168] A. A. Bakır, R. Neshani, and S. Özerinç, "Mechanical properties of 3d-printed elastomers produced by fused deposition modeling", in *Fused Deposition Modeling Based 3D Printing*, Springer, 2021, pp. 107–130.

[169] N. Wang, R. Daniels, L. Connelly, *et al.*, "All-organic flexible ferroelectret nanogenerator with fabric-based electrodes for self-powered body area networks", *Small*, vol. 17, no. 33, p. 2 103 161, 2021.

[170] R. A. P. Altafim, D. Rychkov, W. Wirges, *et al.*, "Laminated tubular-channel ferroelectret systems from low-density polyethylene films and from fluoroethylene-propylene copolymer films-a comparison", *IEEE Transactions on Dielectrics and Electrical Insulation*, vol. 19, no. 4, pp. 1116–1123, 2012.

[171] X. Zhang, G. M. Sessler, and Y. Wang, "Fluoroethylenepropylene ferroelectret films with cross-tunnel structure for piezoelectric transducers and micro energy harvesters", *Journal of applied physics*, vol. 116, no. 7, p. 074 109, 2014.

[172] M. Lindner, S. Bauer-Gogonea, S. Bauer, M. Paajanen, and J. Raukola, "Dielectric barrier microdischarges: Mechanism for the charging of cellular piezoelectric polymers", *Journal of Applied Physics*, vol. 91, no. 8, pp. 5283–5287, 2002.

[173] C. Dias, J. Marat-Mendes, and J. Giacometti, "Effects of a corona discharge on the charge stability of teflon fep negative electrets", *Journal of physics D: Applied physics*, vol. 22, no. 5, p. 663, 1989.

[174] J. Hu, Y. Li, C. Li, W. Chen, and D. Yang, "Mechanical properties of fluorinated ethylene propylene (fep) foils in use for neutrino detector project", *Polymer Testing*, vol. 59, pp. 362–370, 2017.

[175] Y. Yanagihara, N. Osaka, S. Iimori, S. Murayama, and H. Saito, "Relationship between modulus and structure of annealed thermoplastic polyurethane", *Materials Today Communications*, vol. 2, e9–e15, 2015.

[176] W. Voigt, *Lehrbuch der kristallphysik:(mit ausschluss der kristalloptik)*. BG Teubner, 1910, vol. 34.

[177] A. Reuss, "Zamm-journal of applied mathematics and mechanics", *Zeitschrift fur Angewandte Mathematik und Mechanik*, vol. 9, no. 1, p. 49, 1929.

[178] J. Hillenbrand and G. Sessler, "Quasistatic and dynamic piezoelectric coefficients of polymer foams and polymer film systems", *IEEE Transactions on Dielectrics and Electrical Insulation*, vol. 11, no. 1, pp. 72–79, 2004.

[179] M. E. Lines and A. M. Glass, *Principles and applications of ferroelectrics and related materials*. Oxford university press, 2001.

[180] M. T. Chorsi, E. J. Curry, H. T. Chorsi, *et al.*, "Piezoelectric biomaterials for sensors and actuators", *Advanced Materials*, vol. 31, no. 1, p. 1 802 084, 2019.

[181] V. R. Feig, H. Tran, and Z. Bao, "Biodegradable polymeric materials in degradable electronic devices", *ACS central science*, vol. 4, no. 3, pp. 337–348, 2018.

[182] S. Gong, B. Zhang, J. Zhang, Z. L. Wang, and K. Ren, "Biocompatible poly (lactic acid)-based hybrid piezoelectric and electret nanogenerator for electronic skin applications", *Advanced Functional Materials*, vol. 30, no. 14, p. 1 908 724, 2020.

[183] E. J. Curry, K. Ke, M. T. Chorsi, *et al.*, "Biodegradable piezoelectric force sensor", *Proceedings of the National Academy of Sciences*, vol. 115, no. 5, pp. 909–914, 2018.

[184] R. Song, M. Murphy, C. Li, K. Ting, C. Soo, and Z. Zheng, "Current development of biodegradable polymeric materials for biomedical applications", *Drug design, development and therapy*, vol. 12, p. 3117, 2018.

[185] E. Fukada, "Piezoelectricity of biopolymers", *Biorheology*, vol. 32, no. 6, pp. 593–609, 1995.

[186] A. Guzhova and M. Galikhanov, "Charge depth in polylactic acid electret filled with fine filler", *Bulgarian Chemical Communications*, vol. 47, no. B, p. 103, 2015.

[187] A. Guzhova, M. Galikhanov, Y. A. Gorokhovatsky, *et al.*, "Improvement of polylactic acid electret properties by addition of fine barium titanate", *Journal of Electrostatics*, vol. 79, pp. 1–6, 2016.

[188] A. Guzhova, M. Galikhanov, N. Kuznetsova, V. Petrov, and R. Khairullin, "Effect of polylactic acid crystallinity on its electret properties", in *AIP Conference Proceedings*, AIP Publishing LLC, vol. 1767, 2016, p. 020 009.

[189] A. Guzhova, T. Yovcheva, and A. Viraneva, "Study of polylactic acid corona electrets", *Bulgarian Chemical Communications*, vol. 47, no. B, p. 115, 2015.

[190] A. Platko, Y. I. Sotova, Y. A. Gorokhovatskiy, E. Karulina, and M. Galikhanov, "Electret effect in biodecomposed polylactide films filled with nanoscale magnesia, st. petersburg state polytechnical university journal", *Physics and Mathematics*, vol. 11, no. 1, pp. 19–24, 2018.

[191] E. Castro-Aguirre, F. Iniguez-Franco, H. Samsudin, X. Fang, and R. Auras, "Poly (lactic acid)—mass production, processing, industrial applications, and end of life", *Advanced drug delivery reviews*, vol. 107, pp. 333–366, 2016.

[192] O. Hamdi, F. Mighri, and D. Rodrigue, "Piezoelectric property improvement of polyethylene ferroelectrets using postprocessing thermal-pressure treatment", *Polymers for Advanced Technologies*, vol. 30, no. 1, pp. 153–161, 2019.

[193] N. Behrendt, C. Greiner, F. Fischer, *et al.*, "Morphology and electret behaviour of microcellular high glass temperature films", *Applied Physics A*, vol. 85, no. 1, pp. 87–93, 2006.

[194] E. Saarimaki, M. Paajanen, A. Savijarvi, *et al.*, "Novel heat durable electromechanical film: Processing for electromechanical and electret applications", *IEEE transactions on dielectrics and electrical insulation*, vol. 13, no. 5, pp. 963–972, 2006.

[195] G. Montanari, D. Fabiani, F. Ciani, *et al.*, "Charging properties and time-temperature stability of innovative polymeric cellular ferroelectrets", *IEEE Transactions on Dielectrics and Electrical Insulation*, vol. 14, no. 1, pp. 238–248, 2007.

[196] R. Kacprzyk, E. Motyl, J. B. Gajewski, and A. Pasternak, "Piezoelectric properties of nonuniform electrets", *Journal of Electrostatics*, vol. 35, no. 2-3, pp. 161–166, 1995.

[197] P. Pondrom, J. Hillenbrand, G. M. Sessler, J. Bös, and T. Melz, "Energy harvesting with single-layer and stacked piezoelectret films", *IEEE Transactions on Dielectrics and Electrical Insulation*, vol. 22, no. 3, pp. 1470–1476, 2015.

[198] X. Zhang, J. Hillenbrand, and G. M. Sessler, "Piezoelectric d 33 coefficient of cellular polypropylene subjected to expansion by pressure treatment", *Applied physics letters*, vol. 85, no. 7, pp. 1226–1228, 2004.

[199] E. Gencheva, T. Yovcheva, M. Marudova, *et al.*, "Formation and investigation of corona charged films from polylactic acid", in *AIP Conference proceedings*, American Institute of Physics, vol. 1203, 2010, pp. 495–500.

[200] Y. Assagra, R. Altafim, R. Altafim, and J. P. Carmo, "Piezoelectrets with well–defined cavities produced from 3d–printed acrylonitrile butadiene styrene structures", *Electronics Letters*, vol. 51, no. 24, pp. 2028–2030, 2015.

[201] Y. A. O. Assagra, R. A. P. Altafim, J. P. do Carmo, *et al.*, "A new route to piezo-polymer transducers: 3d printing of polypropylene ferroelectrets", *IEEE Transactions on Dielectrics and Electrical Insulation*, vol. 27, no. 5, pp. 1668–1674, 2020.

[202] I. Kierzewski, S. S. Bedair, B. Hanrahan, H. Tsang, L. Hu, and N. Lazarus, "Adding an electroactive response to 3d printed materials: Printing a piezoelectret", *Additive Manufacturing*, vol. 31, p. 100 963, 2020.

[203] J. Shi, D. Zhu, and S. P. Beeby, "An investigation of pdms structures for optimized ferroelectret performance", *Journal of Physics: Conference Series*, vol. 557, p. 012 104, 2014.

[204] Y. A. Olivato Assagra, R. A. Correa Altafim, J. P. Pereira do Carmo, and R. A. Pisani Altafim, "Well-defined piezoelectrets fabricated with 3d printing technology", in *2016 IEEE International Conference on Dielectrics (ICD)*, IEEE, 3.07.2016 - 07.07.2016, pp. 257–259.

[205] X. Gao, L. Huang, B. Wang, *et al.*, "Natural materials assembled, biodegradable, and transparent paper-based electret nanogenerator", *ACS applied materials & interfaces*, vol. 8, no. 51, pp. 35 587–35 592, 2016.

[206] E. Gencheva, T. Yovcheva, M. Marudova, *et al.*, "Formation and investigation of corona charged films from polylactic acid", in *AIP Conference proceedings*, American Institute of Physics, vol. 1203, 2010, pp. 495–500.

[207] O. Ben Dali, Y. Sellami, S. Zhukov, *et al.*, "Ultrasensitive and low-cost insole for gait analysis using piezoelectrets", in *2022 IEEE Sensors*, IEEE.

[208] P. K. Pisharady and M. Saerbeck, "Recent methods and databases in vision-based hand gesture recognition: A review", *Computer Vision and Image Understanding*, vol. 141, pp. 152–165, 2015.

[209] M. Anvaripour and M. Saif, "Hand gesture recognition using force myography of the forearm activities and optimized features", in *2018 IEEE International Conference on Industrial Technology (ICIT)*, IEEE, 2018, pp. 187–192.

[210] Y. Choi, S. Lee, M. Sung, J. Park, S. Kim, and Y. Choi, "Development of emg-fmg based prosthesis with pvdf-film vibrational feedback control", *IEEE Sensors Journal*, vol. 21, no. 20, pp. 23 597–23 607, 2021.

[211] W. Dong, L. Yang, R. Gravina, and G. Fortino, "Soft wrist-worn multi-functional sensor array for real-time hand gesture recognition", *IEEE Sensors Journal*, 2021.

[212] N. Ha, G. P. Withanachchi, and Y. Yihun, "Performance of forearm fmg for estimating hand gestures and prosthetic hand control", *Journal of Bionic Engineering*, vol. 16, no. 1, pp. 88–98, 2019.

[213] Z. G. Xiao and C. Menon, "A review of force myography research and development", *Sensors*, vol. 19, no. 20, p. 4557, 2019.

[214] D. Esposito, E. Andreozzi, A. Fratini, *et al.*, "A piezoresistive sensor to measure muscle contraction and mechanomyography", *Sensors*, vol. 18, no. 8, p. 2553, 2018.

[215] Z. G. Xiao and C. Menon, "Towards the development of a wearable feedback system for monitoring the activities of the upper-extremities", *Journal of neuroengineering and rehabilitation*, vol. 11, no. 1, pp. 1–13, 2014.

[216] A. K. Godiyal, M. Mondal, S. D. Joshi, and D. Joshi, "Force myography based novel strategy for locomotion classification", *IEEE Transactions on Human-Machine Systems*, vol. 48, no. 6, pp. 648–657, 2018.

[217] S. Schätzle, T. Ende, T. Wüsthoff, and C. Preusche, "Vibrotac: An ergonomic and versatile usable vibrotactile feedback device", in *19th International Symposium in Robot and Human Interactive Communication*, IEEE, 2010, pp. 670–675.

[218] V. Cortes, "Cortes c., vapnik v", *Support-vector networks, Machine learning*, vol. 20, no. 3, pp. 273–297, 1995.

[219] A. Jaramillo-Yánez, M. E. Benalcázar, and E. Mena-Maldonado, "Real-time hand gesture recognition using surface electromyography and machine learning: A systematic literature review", *Sensors*, vol. 20, no. 9, p. 2467, 2020.

[220] S. Ertekin, L. Bottou, and C. L. Giles, "Nonconvex online support vector machines", *IEEE Transactions on Pattern Analysis and Machine Intelligence*, vol. 33, no. 2, pp. 368–381, 2010.

[221] A. Patle and D. S. Chouhan, "Svm kernel functions for classification", in *2013 International Conference on Advances in Technology and Engineering (ICATE)*, IEEE, 2013, pp. 1–9.

[222] C.-W. Hsu, C.-C. Chang, C.-J. Lin, *et al.*, *A practical guide to support vector classification*, 2003.

[223] S. Liang, Y. Wu, J. Chen, *et al.*, "Identification of gesture based on combination of raw semg and semg envelope using supervised learning and univariate feature selection", *Journal of Bionic Engineering*, vol. 16, no. 4, pp. 647–662, 2019.

[224] F. Pedregosa, G. Varoquaux, A. Gramfort, *et al.*, "Scikit-learn: Machine learning in python", *the Journal of machine Learning research*, vol. 12, pp. 2825–2830, 2011.

[225] G. Cicirelli, D. Impedovo, V. Dentamaro, R. Marani, G. Pirlo, and T. D'Orazio, "Human gait analysis in neurodegenerative diseases: A review", *IEEE Journal of Biomedical and Health Informatics*, 2021.

[226] M. Ntagios and R. Dahiya, "3d printed soft and flexible insole with intrinsic pressure sensing capability", *IEEE Sensors Journal*, 2022.

[227] J. S. Park, C. M. Lee, S.-M. Koo, and C. H. Kim, "Gait phase detection using force sensing resistors", *IEEE Sensors Journal*, vol. 20, no. 12, pp. 6516–6523, 2020.

[228] J. Chen, Y. Dai, S. Kang, L. Xu, and S. Gao, "A concurrent plantar stress sensing and energy harvesting technique by piezoelectric insole device and rectifying circuitry", *IEEE Sensors Journal*, vol. 21, no. 23, pp. 26 364–26 372, 2021.

[229] Y. Xin, X. Li, H. Tian, *et al.*, "Shoes-equipped piezoelectric transducer for energy harvesting: A brief review", *Ferroelectrics*, vol. 493, no. 1, pp. 12–24, 2016.

[230] E. Ziagkas, A. Loukovitis, D. X. Zekakos, T. D.-P. Chau, A. Petrelis, and G. Grouios, "A novel tool for gait analysis: Validation study of the smart insole podosmart®", *Sensors*, vol. 21, no. 17, p. 5972, 2021.

[231] Y. Dai, Y. Xie, J. Chen, S. Kang, L. Xu, and S. Gao, "A lamination-based piezoelectric insole gait analysis system for massive production for internet-of-health things", *International Journal of Distributed Sensor Networks*, vol. 16, no. 3, p. 1 550 147 720 905 431, 2020.

[232] M. W. Whittle, "Gait analysis", in *The soft tissues*, Elsevier, 1993, pp. 187–199.

[233] A. Bulling, U. Blanke, and B. Schiele, "A tutorial on human activity recognition using body-worn inertial sensors", *ACM Computing Surveys (CSUR)*, vol. 46, no. 3, pp. 1–33, 2014.

[234] D. Ravi, C. Wong, B. Lo, and G.-Z. Yang, "Deep learning for human activity recognition: A resource efficient implementation on low-power devices", in *2016 IEEE 13th international conference on wearable and implantable body sensor networks (BSN)*, IEEE, 2016, pp. 71–76.

[235] A. S. Alharthi, S. U. Yunas, and K. B. Ozanyan, "Deep learning for monitoring of human gait: A review", *IEEE Sensors Journal*, vol. 19, no. 21, pp. 9575–9591, 2019.

[236] A. Krogh, "What are artificial neural networks?", *Nature biotechnology*, vol. 26, no. 2, pp. 195–197, 2008.

[237] O. Calin, *Deep Learning Architectures*. Cham: Springer International Publishing, 2020, pp. 21–32.

[238] M. Mohammadi, A. Al-Fuqaha, S. Sorour, and M. Guizani, "Deep learning for iot big data and streaming analytics: A survey", *IEEE Communications Surveys & Tutorials*, vol. 20, no. 4, pp. 2923–2960, 2018.

[239] S. Sharma, S. Sharma, and A. Athaiya, "Activation functions in neural networks", *towards data science*, vol. 6, no. 12, pp. 310–316, 2017.

[240] R. Yamashita, M. Nishio, R. K. G. Do, and K. Togashi, "Convolutional neural networks: An overview and application in radiology", *Insights into imaging*, vol. 9, no. 4, pp. 611–629, 2018.

[241] P. Benardos and G.-C. Vosniakos, "Optimizing feedforward artificial neural network architecture", *Engineering applications of artificial intelligence*, vol. 20, no. 3, pp. 365–382, 2007.

[242] A. Zhang, Z. C. Lipton, M. Li, and A. J. Smola, "Dive into deep learning", *arXiv preprint arXiv:2106.11342*, 2021.

[243] Scikit learn, *Train_test_split*.

[244] Z. Zhang, "Improved adam optimizer for deep neural networks", in *2018 IEEE/ACM 26th International Symposium on Quality of Service (IWQoS)*, Ieee, 2018, pp. 1–2.

[245] Z. Zhang and M. Sabuncu, "Generalized cross entropy loss for training deep neural networks with noisy labels", in *Advances in Neural Information Processing Systems*, S. Bengio, H. Wallach, H. Larochelle, K. Grauman, N. Cesa-Bianchi, and R. Garnett, Eds., vol. 31, Curran Associates, Inc., 2018.

[246] G. Zaccone, M. R. Karim, and A. Menshawy, *Deep learning with TensorFlow*. Packt Publishing Ltd, 2017.

[247] N. Srivastava, G. Hinton, A. Krizhevsky, I. Sutskever, and R. Salakhutdinov, "Dropout: A simple way to prevent neural networks from overfitting", *The journal of machine learning research*, vol. 15, no. 1, pp. 1929–1958, 2014.

[248] J. Hietanen, J. Stor-Pellinen, and M. Luukkala, "A model for an electrostatic ultrasonic transducer with a grooved backplate", *Measurement Science and Technology*, vol. 3, no. 11, p. 1095, 1992.

[249] J. Hietanen, P. Mattila, J. Stor-Pellinen, *et al.*, "Factors affecting the sensitivity of electrostatic ultrasonic transducers", *Measurement Science and Technology*, vol. 4, no. 10, p. 1138, 1993.

[250] M. Kupnik, I. O. Wygant, and B. T. Khuri-Yakub, "Finite element analysis of stress stiffening effects in cmuts", in *2008 IEEE Ultrasonics Symposium*, IEEE, 2008, pp. 487–490.

[251] J. Hillenbrand, P. Pondrom, and G. Sessler, "Electret transducer for vibration-based energy harvesting", *Applied Physics Letters*, vol. 106, no. 18, p. 183 902, 2015.

[252] J. E. Ip, "Wearable devices for cardiac rhythm diagnosis and management", *Jama*, vol. 321, no. 4, pp. 337–338, 2019.

[253] H. Yin and N. K. Jha, "A health decision support system for disease diagnosis based on wearable medical sensors and machine learning ensembles", *IEEE Transactions on Multi-Scale Computing Systems*, vol. 3, no. 4, pp. 228–241, 2017.

[254] E. Rovini, C. Maremmani, and F. Cavallo, "How wearable sensors can support parkinson's disease diagnosis and treatment: A systematic review", *Frontiers in neuroscience*, vol. 11, p. 555, 2017.

[255] Y. Lee, J. Park, A. Choe, S. Cho, J. Kim, and H. Ko, "Mimicking human and biological skins for multifunctional skin electronics", *Advanced Functional Materials*, vol. 30, no. 20, p. 1 904 523, 2020.

[256] R. Nur, N. Matsuhisa, Z. Jiang, M. O. G. Nayeem, T. Yokota, and T. Someya, "A highly sensitive capacitive-type strain sensor using wrinkled ultrathin gold films", *Nano letters*, vol. 18, no. 9, pp. 5610–5617, 2018.

[257] J. Zhang, L. Wan, Y. Gao, *et al.*, "Highly stretchable and self-healable mxene/polyvinyl alcohol hydrogel electrode for wearable capacitive electronic skin", *Advanced Electronic Materials*, vol. 5, no. 7, p. 1 900 285, 2019.

[258] F. Yin, J. Yang, H. Peng, and W. Yuan, "Flexible and highly sensitive artificial electronic skin based on graphene/polyamide interlocking fabric", *Journal of Materials Chemistry C*, vol. 6, no. 25, pp. 6840–6846, 2018.

[259] C. Yang, L. Li, J. Zhao, *et al.*, "Highly sensitive wearable pressure sensors based on three-scale nested wrinkling microstructures of polypyrrole films", *ACS applied materials & interfaces*, vol. 10, no. 30, pp. 25 811–25 818, 2018.

[260] H. Chen, Y. Song, X. Cheng, and H. Zhang, "Self-powered electronic skin based on the triboelectric generator", *Nano energy*, vol. 56, pp. 252–268, 2019.

[261] G. Yao, L. Xu, X. Cheng, *et al.*, "Bioinspired triboelectric nanogenerators as self-powered electronic skin for robotic tactile sensing", *Advanced Functional Materials*, vol. 30, no. 6, p. 1 907 312, 2020.

[262] H. Yuan, T. Lei, Y. Qin, and R. Yang, "Flexible electronic skins based on piezoelectric nanogenerators and piezotronics", *Nano Energy*, vol. 59, pp. 84–90, 2019.

[263] Y. Wu, Y. Ma, H. Zheng, and S. Ramakrishna, "Piezoelectric materials for flexible and wearable electronics: A review", *Materials & Design*, p. 110 164, 2021.

[264] A. Dos Santos, E. Fortunato, R. Martins, H. Águas, and R. Igreja, "Transduction mechanisms, microstructuring techniques, and applications of electronic skin pressure sensors: A review of recent advances", *Sensors*, vol. 20, no. 16, p. 4407, 2020.

[265] Y. Tokiwa and B. P. Calabia, "Biodegradability and biodegradation of poly (lactide)", *Applied microbiology and biotechnology*, vol. 72, no. 2, pp. 244–251, 2006.